INTERFACIAL ASSEMBLY OF STAR-SHAPED POLYMERS FOR ORGANIZED ULTRATHIN FILMS

A Dissertation
Presented to
The Academic Faculty

by

Ikjun Choi

In Partial Fulfillment
of the Requirements for the Degree
Doctor of Philosophy in the
School of Materials Science and Engineering

Georgia Institute of Technology
December, 2013

INTERFACIAL ASSEMBLY OF STAR-SHAPED POLYMERS FOR ORGANIZED ULTRATHIN FILMS

Approved by:

Dr. Vladimir V. Tsukruk, Advisor
School of Materials Science and Engineering
Georgia Institute of Technology

Dr. Zhiqun Lin
School of Materials Science and Engineering
Georgia Institute of Technology

Dr. Anselm Griffin
School of Materials Science and Engineering
Georgia Institute of Technology

Dr. Seung Soon Jang
School of Materials Science and Engineering
Georgia Institute of Technology

Dr. David M. Collard
School of Chemistry and Biochemistry
Georgia Institute of Technology

Date Approved: June 4, 2013

Dedicated to my loving family

ACKNOWLEDGEMENTS

I would like to thank my advisor Prof. V. V. Tsukruk for his constant support and motivation with a clear vision and discipline during my Ph.D. I would also like to thank all Ph.D. dissertation committee members, Prof. A. Griffin, Prof. D. M. Collard, Prof. Z. Lin, and Prof. S. S. Jang for their helpful suggestions and kind willingness to take part in my dissertation committee. I would also like to offer a special thanks to Prof. A. H. X. Müller (University of Bayreuth, Germany), Prof. C. Tsitsilianis (University of Patras, Greece), and Prof. V. Shevchenko (National Academy of Sciences of Ukraine, Ukraine) for the chance to do exceptional collaborations and for their suggestions and insights.

Also I would like to thank Dr. D. D. Kulkarni, Dr. R. Kodiyath, R. Suntivich, W. Xu, S. Malak, Z. A. Combs, A. Dorokhin, C. Synatschke, Dr. F. A. Plamper, Dr. R. Gunawidjaja, Dr. M. Gupta, Prof. S. Singamaneni, Dr. Dr. O. Shchepellian, Dr. V. Kozlovskaya, Prof. E. Kharlampeiva, Dr. K. Campbell, Dr. Sehoon Chang, Dr. M. McConney, K. Hu, C. Ye, I. Drachuk, S. Young, Dr. K. D. Anderson, Dr. D. M. Lisunova, and other SEMA lab members for their significant contribution and great help in the project and technical assistance.

We thank the DOE Office of Basic Energy Sciences and Spallation Neutron Source at Oak Ridge National Laboratory for beam time, in particular Dr. J. F. Ankner and Dr. W. T. Heller for assistance to neutron experiments. Their help and contribution in the successful completion of this work cannot be overstated. Funding for this work has been

provided by the National Science Foundation; grant NSF DMR-0756273 and DMR-1002810.

I would also like to thank Prof. T. H. Yoon, Prof. T. S. Hwang, Prof. K. W. Jeong, Dr. J. H. Roh, Dr. M. S. Chun, Dr. J. W. Lee, C. H. Lee, and J. Y. Ryu for their constant supports and advises in this journey. Finally, I am deeply grateful to my parent and family for a constant source of happiness and optimism, and to all my friends.

TABLE OF CONTENTS

ACKNOWLEDGEMENTS **iv**

LIST OF TABLES **ix**

LIST OF FIGURES AND SCHEMES **x**

LIST OF SYMBOLS AND ABBREVIATIONS **xxiii**

SUMMARY **xxiv**

CHAPTER 1 INTRODUCTION **1**
1.1 Background 1
1.1.1. Supramolecular Ultrathin Films of Highly Branched Molecules 2
1.1.2. Star-Shaped Polymers: Molecular Architecture and Properties 7
1.1.3. Star-Shaped Polymers Assemblies at Interfaces 11
1.1.4. Langmuir-Blodgett Monolayers 15
1.1.5. Multilayer Assembly 20
1.2. Motivation 25

CHAPTER 2 GOALS AND OBJECTIVES **28**
2.1 Goals and Research Focuses 28
2.2 Overview of Dissertation Contents 33

CHAPTER 3 EXPERIMENTAL DETAILS **40**
3.1. Synthesis and Fabrication 40
3.1.1. Synthesis of Highly Branched Star-Shaped Polymers 40
3.1.2. LB Film Fabrication 41
3.1.3. LbL Film and Microcapsule Fabrication 42
3.2. Characterization Techniques 43
3.2.1. Ellipsometry 43
3.2.2. Atomic Force Microscopy (AFM) 44
3.2.3. Confocal Laser Scanning Microcoply (CLSM) 45
3.2.4. Transmission Electron Microscopy (TEM) 45
3.2.5. UV-Vis and Raman Spectroscopy 45
3.2.6. Small Angle Neutron Scattering (SANS) 46

CHAPTER 4 SURFACE BEHAVIOR OF $PS_n(P2VP\text{-}b\text{-}PtBA)_n$ HETEROARM STARS **48**
4.1 Introduction 48
4.2 Experimental Details 53
4.3 Results and Discussion 56
4.3.1 Chemical Composition 56
4.3.2 Surface-Pressure Isotherms at Air-Water Surface 58
4.3.3 Monolayers at Solid Subtrates 67
4.3.4 Surface Morphology of Monolayers 71

CHAPTER 5 INTERFACIAL BEHAVIOR OF pH RESPONSIVE AMPHOLYTIC HETEROARM STAR BLOCK TERPOLYMERS **80**
5.1. Introduction 80
5.2 Experimental Details 84
5.3 Results and Discussion 86
5.3.1 Chemical Structure and pH Responsive Property 86
5.3.2 Surface Morphology in the LB Films 97

CHAPTER 6 GOLD NANOPARTICLE GROWN ON STAR-SHAPED BLOCK COPOLYMER MONOLAYERS **116**
6.1 Introduction 116
6.2 Experimental Details 119
6.3 Results and Discussion 124
6.3.1 Chemical Composition 124
6.3.2 Surface-Pressure Isotherms 124
6.3.3 Surface Morphologies 126

CHAPTER 7 pH-CONTROLLED EXPONENTIAL AND LINEAR GROWING MODES OF LAYER-BY-LAYER ASSEMBLIES OF STAR POLYELECTROLYTES **142**
7.1 Introduction 142
7.2 Experimental Details 147
7.3 Results and Discussion 152
7.3.1 LbL Assembly from Star and Linear Polymers at Variable pH 152
7.3.2 Spin-Assisted vs Conventional LbL Assembly: Different Modes of Growth 159
7.3.3 Optical Properties of LbL Films 165
7.3.4 Exponential Growth for Different Star Architectures 167
7.3.5 Shear Rates and Resulting Spin-Assisted LbL Morphologies 173
7.4. Conclusions 176

CHAPTER 8 MULTICOMPARTMENTAL MICROCAPSULES FROM STAR COPOLYMER MICELLES **193**
8.1 Introduction 193
8.2 Experimental Details 196
8.3 Results and Discussion 200
8.3.1 Chemical Composition and Unimolecular Micelles 200
8.3.2 Planar Film Morphology 204
8.3.3 Hollow Microcapsule Assembly and Shell Characteristics 208
8.3.4 Porosity of LbL Shell 215

CHAPTER 9 STAR POLYMER UNIMICELLES ON GRAPHENE OXIDE FLAKES **229**
9.1 Introduction 229
9.2 Experimental Details 232
9.3 Results and Discussion 235
9.3.1 Effect of Concentration and Surface Pressure 235
9.3.2 Effect of Molecular Composition 246
9.3.3 Effect of Spreading Solvent Polarity and Subphase pH 247

CHAPTER 10 GENREAL CONCLUSIONS AND BROADER IMPACT **260**
10.1 Summary of Major Results 260
10.2. Critical Findings and Conclusions 267
10.3 Significance and Broader Impact 272

REFERENCES **279**

VITA **301**

LIST OF TABLES

Page

Table 4.1: Molecular Characteristics of Heteroarm Star Polymers. 54

Table 4.2: Monolayer Characteristics of Heteroarm Star Polymers at Different Subphase pH. 59

Table 4.3: Mophological Characteristics of monolayers as a Function of Number of Arms at Different Subphase pH. Deposited at Surface Pressure 10 mN/m. 59

Table 4.4: Aggregation Numbers of Surface Micelles. 78

Table 5.1: Molecular Characteristics of the PS_n(P2VP-*b*-PAA)$_n$ Star Block Terpolymers. 84

Table S5.1: Thickness of the LB films fabricated at different pH and surface Pressures (SP). 105

Table 6.1. Molecular Characteristics of PS_nP2VP_n Heteroarm Star Copolymers. 120

Table 6.2. Thickness of PS_nP2VP_n Composite Film and Size of Gold Nanoparticle. 131

Table 7.1: Molecular Characteristics of Polyelectrolyte Components for LbL films. 148

Table 7.2: Polymer Pair and Notation of p(AA) and p(DMAEMA) for LbL Assemblies. 151

Table 7.3: Thickness and Roughness of Spin- and Dip-Assisted LbL Films. 158

Table 7.4: Exponential Growth Rate Parameters for dip-assisted LbL. 170

Table S7.1: Thickness and Roughness of linear/star (LS) LbL FIlms at Different pH Deposition Conditions. 185

Table 8.1: Molecular Characteristics of Heteroarm PS_nP2VP_n Star Block Copolymers. 197

Table 8.2: Domain Height and Width of Star Copolymer Monolayer Films. 205

Table 8.3: Permeability of $PS_{22}P2VP_{22}$/PSS Microcapsules. 216

Table S8.1: Average Bilayer Thickness of LbL Multilayer Films. 223

Table S9.1: Molecular Characteristics of the Star Polymers. 255

LIST OF FIGURES AND SCHEMES

Page

Figure 1.1: Molecular architecture of highly-branched polymers: (a) graft, (b) brush, (c) dendrimer, (d) hyperbranched, (e) arborscent, and (f) star architectures. 4

Figure 1.2: Stimuli-responsive nano and macro structures with various geometric forms prepared via different molecular assembly techniques. 6

Figure 1.3: Representative molecular architecture of star-shaped block copolymers: (a) homoarm polymer, (b) A_nB_n type symmetri/asymmetric heteroarm copolymer, (c) $(AB)_n$ type diblock homoarm copolymer, (d) ABC type miktoarm terpolymer, and (e) $A_n(B\text{-}C)_n$ heteroarm terpolymer. 8

Figure 1.4: (a) Ultrasoft effective pair potential of star polymers at center-to-center distance *r* and (b) polymer chain conformaton in the polymer thin film (confined geometry) where thickness is less than the radius of gyration (R_g) displaying a limited interpentraton or entanglement in polymer coil pairs compared to bulk polymer melt. 10

Figure 1.5: a) $(PEO)_9$-b-$(PCL)_m$ star, (b) PS-PEO three-arm star, (c) PEO-b-PS three-arm star polymer, d) PB-b-PEO four arm star, (e) dendrimer-like PS core and PBA or PAA corona. 12

Figure 1.6: (a) Pressure-area Langmuir isotherm for surfactant molecules with different phase states, (b) LB films assembled from amphiphilic block polyelectrolyte surface micelles, (c) molecular conformational transtion from two-dimension (starfish) to quasi two-dimension (jellyfish) surface micelles on water surface, and (d) proposed two-dimensional surface micelles at air-water interface (A. hydrocarbon liquid, B. surfactant lens (left) and monolayer (right), and C. 2D associated surface micelle). 16

Figure 1.7: The surface micelle structures and aggregation behavior in the LB films of different (linear and branched) amphiphilic polymers: (a) schematic representation and TEM images of the variable surface micelles (starfish, rod, planar) of linear poly(styrene*b*-4-vinylpyridinium decyl iodide). (b) Phase transitions (AFM images) of cylindricalbrushes of poly(n-butyl acrylate) (PBA). (c) Nanofibric structures (AFM images) of amphiphilic dendritic hyperbranched polyester. (d) Circular shaped surface aggregations (AFM images) and proposed models of the domain structures of three-arm polystyrene-block-poly(ethylene oxide) stars. (e) AFM images of the surface dendritic structures of amphiphilic heteroarm poly(styene-ethylene oxide) star copolymers. 18

Figure 1.8: (a) LbL multilayer deposition process from polyanion and polycation using repeated alternating dipping and washing steps, (b) two different growth mode and structure of multilayer films (linear (left) versus exponential (right); stratified (left) versus mixed (right)), (c) preparation of hollow multilayer microcapsues by exposure of a colloidal sacrificial template to polyelectrolytes of alternating charge, and (d) proposed buildup mechansion of polyelectolyte multilayer film based on "in-and out" diffusion. 21

Scheme 2.1: (a) Star-shaped block copolymer (s-BCP): PS_nP2VP_n amphiphilic heteroam star copolymer, $PS_n(P2VP\text{-}b\text{-}PtBA)_n$ amphiphilic heteroam star terpolymer, $PS_n(P2VP\text{-}b\text{-}PtBA)_n$ amphoteric heteroam star terpolymer (n denotes arm number) (b) star-shape polyelectrolyte (s-PE): cationic $p(DMAEMA_n)_x$ star polyelectrolyte and anionic $p(AA_n)_x$ star polyelectrolyte (n denotes degree of polymerization; x denotes arm number). 29

Scheme 2.2: Conceptual diagram investigating the structure-property-assembly relationship of highly-branched star-shaped polymers. 31

Figure 4.1: a) Schematic of the multi-step synthetic procedure for the synthesis of $A_n(B\text{-}C)_n$ heteroarm star block terpolymer, * denotes active sites. b) Molecular structures of heteroarm star polymers. G I represents PS_nP2VP_n (A_nB_n) star copolymers and G II represents $PS_n(P2VP\text{-}Pt BA)_n$ star block terpolymers. 53

Figure 4.2: Surface-area isotherms of PS_nP2VP_n star copolymers (a and b) and $PS_n(P2VP\text{-}Pt BA)_n$ star block terpolymers (c and d) at different subphase pH (5.8 vs. 2.0). GI-Bn denotes PS_nP2VP_n (n is the number of arms; n = 9, 22, and 28) and GII-Tn denotes $PS_n(P2VP\text{-}Pt BA)_n$ (n = 9, 22, and 28). 57

Figure 4.3: Schematics of suggested chain conformations of star copolymers (GI) (left) and star terpolymers (GII) (right) at pH 5.8 and 2.0 at the air-water interface under lateral compression (top) and unimolecular micelle at air-water and air-solid interfaces (bottom). 61

Figure 4.4: Compression-expansion cycles of PS_nP2VP_n (a and b) and $PS_n(P2VP\text{-}Pt BA)_n$ (c and d) at different pH. The number of cycles is four. 63

Figure 4.5: a) Plot of limiting molecular area, A_0, of star polymers vs number of arms at different subphase pH 5.8 and 2.0 (PS_nP2VP_n at pH 5.8 (■) and pH 2.0 (●); $PS_n(P2VP\text{-}Pt BA)_n$ at pH 5.8 (▲) and pH 2.0 (▼). b) limiting molecular area, A_0, of star polymers vs number of 2VP monomer units at different subphase pH 5.8 and 2.0 (PS_nP2VP_n at pH 5.8 (■) and pH 2.0 (●); $PS_n(P2VP\text{-}Pt BA)_n$ at pH 5.8 (▲) and pH 2.0 (▼). c) Limiting molecular area A_0 as a function of number of arms n for PS_nP2VP_n at pH 5.8 (▲), PS_nP2VP_n at pH 2 (●), $PS_n(P2VP\text{-}Pt BA)_n$ at pH 5.8 (▼) and pH 2.0 (♦) in comparison with star polymers PS_nPEO_n (■) from ref. 183. 65

Figure 4.6: Contact angles measurements of Langmuir-Blodgett monolayers of star polymers. (●) denotes G II star terpolymers at pH 2.0 (▲) and pH 5.8; (▼), and G I star copolymers at pH 2.0 (■) and pH 5.8. 68

Figure 4.7: AFM topographical images (1 μm × 1 μm) of PS_nP2VP_n star copolymers (n = 9 for a and b; n = 22 for c and d; n = 28 for e and f) at different subphase pH: a, c and e at pH 5.8, and b, d and f at pH 2.0. The LB films were deposited at a surface pressure of 10 mN/m. G1-B_n denotes PS_nP2VP_n (number of arms, n = 9, 22, and 28). Z scale = 5 nm. 69

Figure 4.8: AFM topographical images (1 μm × 1 μm) of PS_n(P2VP-P*t*BA)$_n$ star block terpolymers (n = 9 for a and b; n = 22 for c and d; n = 28 for e and f) at different subphase pH : a, c, and e at pH 5.8, and b, d, and f at pH 2.0. The LB films were deposited at a surface pressure of 10 mN/m. G2-Tn denotes PS_n(P2VP-P*t*BA)$_n$ (n = 9, 22, and 28). Z scale = 5 nm. 70

Figure 4.9: AFM topographical images (500 nm × 500 nm) of GI-B28 ($PS_{28}P2VP_{28}$ star copolymers for a and b), GII-T28 (PS_{28}(P2VP-P*t*BA)$_{28}$ star block terpolymers for b and c), and GII-T22 (PS_{22}(P2VP-P*t*BA)$_{22}$ star block terpolymers for e and f. The LB films were deposited at surface pressure 10 mN/m at different subphase pH 5.8:(a, c and e) and at pH 2.0(b, d and f). Z scale = 5 nm. 72

Figure 4.10: AFM topographical images (1 μm × 1 μm) of PS_nP2VP_n at different surface pressures (0.5 and 20.0 mN/m) at pH 5.8. G1-B_n denotes PS_nP2VP_n (number of arms, n = 9, 22, and 28). Z scale = 5 nm. 74

Figure 4.11: AFM images (1 μm × 1 μm) of PS_n(P2VP-PtBA)$_n$ at different surface pressures (sp = 0.5 and 20.0 mN/m) at pH 5.8. GII-Tn denotes PS_n(P2VP-P*t*BA)$_n$ (n = 9, 22, and 28). Z scale = 5 nm. 75

Figure 4.12: AFM topographical images (1 μm × 1 μm) of $PS_{28}P2VP_{28}$ star copolymer as a function of surface pressure: a) 0.5 mN/m, b) 1.0, c) 5.0, d) 8.0, e) 10.0, and f) 30.0 at pH 2.0. Z scale = 5 nm. 76

Figure 4.13: AFM topographical images (1 μm × 1 μm) of PS_{28}(P2VP-P*t*BA)$_{28}$ as a function of surface pressure: a) 1.0 mN/m, b) 10.0, c) 25.0, and d) 30.0 at pH 2.0. Z scale = 5 nm. 78

Figure 5.1: The amphoteric heteroarm PS_n(P2VP-*b*-PAA)$_n$ star terpolymer with the variable ionization conditions at different pH values. 86

Figure 5.2: Zeta potentials at different pH of the H9 and H22 star terpolymers in aqueous solutions. The dashed area denotes the regions where the polymers precipitate. 87

Figure 5.3: Pressure-area isotherms of (a) H9 and (b) H22 star polymers obtained at different subphase pH values. 89

Figure 5.4. Pressure-area isotherm cycles of star terpolymers at subphase pH = 1 ((a) and (b)) and pH = 10 ((c) and (d)). The direction of compression and expansion of the monolayer is also shown. 91

Figure 5.5: Variation of the limiting molecular area (at the highest surface pressure) with subphase pH and number of arms. 94

Figure 5.6: (a) Different conformations adopted by the terpolymer at various subphase pH conditions and surface pressures (SP) at the air-water interface. (b) Unimolecular micelles which can be formed by H9 and H22 star polymers. IEP is isoelectric point. 95

Figure 5.7: AFM images of monolayer LB films of H9 [(a) and (c)] and H22 [(b) and (d)] fabricated at a subphase pH of 1 and at surface pressures of 1 mN/m (a, b) and 20 mN/m (c, d). 97

Figure 5.8: AFM images of monolayer LB films of H9 [(a) and (c)] and H22 [(b) and (d)] fabricated at a subphase pH of 3.5 and at surface pressures of 1 mN/m (a, b) and 20 mN/m (c, d). 100

Figure 5.9: AFM images of monolayer LB films of H9 [(a) and (c)] and H22 [(b) and (d)] fabricated at a subphase pH of 10 and at surface pressures of 1 mN/m (a, b) and 20 mN/m (c, d). 101

Figure 5.10. The thickness of the LB films fabricated with H9 and H22 at different surface pressures and a subphase pH of (a) 1, (b) 6 and (c) 10. 102

Figure S5.1: Pressure-area isotherm cycles of (a) H9 and (b) H22 at subphase pH of 10. 106

Figure S5.2: AFM images of monolayer LB films of H9 [(a) and (c)] and H22 [(b) and (d)] fabricated at subphase pH of 1 and different surface pressures. 107

Figure S5.3: AFM images of monolayer LB films of H9 [(a) and (c)] and H22 [(b) and (d)] fabricated at subphase pH of 3.5 and different surface pressures. 108

Figure S5.4: AFM images of monolayer LB films of H9 [(a) and (c)] and H22 [(b) and (d)] fabricated at subphase pH of 6 and different surface pressures. 109

Figure S5.5: AFM images of monolayer LB films of H9 [(a) and (c)] and H22 [(b) and (d)] fabricated at subphase pH of 6 and different surface pressures. 110

Figure S5.6: AFM images of monolayer LB films of H9 [(a) and (c)] and H22 [(b) and (d)] fabricated at subphase pH of 10 and different surface pressures. 111

Figure S5.7: AFM images of monolayer LB films of H9 fabricated at different subphase pH values and surface pressures (SP). Scale bar = 2 μm. 112

Figure S5.8: AFM images of monolayer LB films of H22 fabricated at different subphase pH values and surface pressures (SP). Scale bar = 2 μm. 113

Figure S5.9: Comparison of the roughness of the LB films fabricated with H9 and H22 at different subphase pH (a) 1, (b) 6 and (c) 10. 114

Figure 6.1: Schematic of the star PS_nP2VP_n monolayers: (A) molecular structure of the PS_nP2VP_n heteroarm star copolymer, (B) the side view of the molecule at the air-water interface, and (C) the air-solid interface as discussed in the text. 121

Figure 6.2: Growth of gold nanoparticles on the star PS_nP2VP_n monolayer. 123

Figure 6.3: Surface pressure-area isotherms of PS_9P2VP_9 and $PS_{28}P2VP_{28}$ star copolymers. 125

Figure 6.4: High resolution AFM images (height; left and phase; right) of star PS_nP2VP_n monolayer at surface pressure 0 mN/m: (A) PS_9P2VP_9 before and (B) after gold nanoparticle synthesis. (C) $PS_{28}P2VP_{28}$ before and (D) after gold nanoparticle synthesis. The scale bar is 100 nm for all images. The z-scale is 10 nm for images before the synthesis (A, C) and 40 nm for images after the synthesis (B, D). 127

Figure 6.5: TEM images (A, B) and corresponding histogram (C, D) of gold nanoparticles grown on PS_nP2VP_n heteroarm star copolymers at surface pressure 0 mN/m and gold solution concrentration, $[HAuCl_4]$ = 0.75 wt%: (A), (C) PS_9P2VP_9 and (B), (D) $PS_{28}P2VP_{28}$. 130

Figure 6.6: High resolution AFM images (height; left and phase; right) of star PS_nP2VP_n monolayer at surface pressure 10 mN/m: (A) PS_9P2VP_9 before and (B) after gold nanoparticle synthesis. (C) $PS_{28}P2VP_{28}$ before and (D) after gold nanoparticle synthesis. The scale bar is 100 nm for all images. The z-scale is 10 nm for images before the synthesis (A, C) and 50 nm for images after the synthesis (B, D). 132

Figure 6.7: TEM images and corresponding histogram of gold nanoparticles form with PS_nP2VP_n heteroarm star block copolymers at surface pressure 10 mN/m and gold solution concentration, $[HAuCl_4]$ = 0.75 wt%: (A), (C) PS_9P2VP_9 and (B),(D) $PS_{28}P2VP_{28}$. 133

Figure 6.8: AFM images (height; left and phase; right) of gold nanoparticles/ $PS_{28}P2VP_{28}$ heteroarm star copolymers at surface pressure 10 mN/m and gold solution concentration, [$HAuCl_4$] = 0.0075 wt%. The scale bar is 200 nm (A) and 100 nm (B). The z-scale is 10 nm for both A and B. 134

Figure 6.9: TEM image (left) and corresponding histogram (right) of gold nanoparticles with $PS_{28}P2VP_{28}$ heteroarm star copolymers at surface pressure 10 mN/m and gold solution concentration, [$HAuCl_4$] = 0.0075 wt%. 135

Figure 6.10: UV-Vis absorption spectra of gold nanoparticles grown on the star $PS_{28}P2VP_{28}$ monolayer with four different repeating cycles of the gold reduction. 136

Figure 6.11: Thickness of star PS_nP2VP_n monolayer film before and after reduction at surface pressure 0 mN/m (SP0) and 10 mN/m (SP10). 137

Figure 6.12: Schematic representation of the growth of gold nanoparticles in PS_nP2VP_n heteroarm star block copolymers. (A) star PS_nP2VP_n monolayer at the air-silicon interface before exposure, (B) after exposure to gold solution($AuCl_4^-$), and (C) star PS_nP2VP_n monolayer after gold reduction by sodium citrate. 138

Figure S6.1: AFM images (height; left and phase; right) of star PS_nP2VP_n monolayer at surface pressure 0 mN/m: (A) PS_9P2VP_9 before and (B) after gold nanoparticle synthesis. (C) $PS_{28}P2VP_{28}$ before and (D) after gold nanoparticle synthesis. The scale bar is 200 nm for all images. The z-scale is 10 nm for AFM images before the synthesis (A, C) and 40 nm for images after the synthesis (B, D).140

Figure S6.2: AFM images (height; left and phase; right) of star PS_nP2VP_n monolayer at surface pressure 10 mN/m: (A) PS_9P2VP_9 before and (B) after gold nanoparticle synthesis. (C) $PS_{28}P2VP_{28}$ before and (D) after gold nanoparticle synthesis. The scale bar is 200 nm for all images. The z-scale is 10 nm for images before the synthesis (A, C) and 50 nm for images after the synthesis (B, D). 141

Scheme 7.1: pH-responsive molecular conformation of (a) cationic $p(DMAEMA_n)_x$ and (b) anionic $p(AA_n)_x$ star polyelectrolyte with the chemical structure of monomer unit of star polyelectrolyte (n refers to the degree of polymerization of each arm and x denotes the number of arms). It is not set to the real length-scale for all drawings. 150

Scheme 7.2: Model structure of LbL multilayer films displaying the surface structure and expected molecular organization within the LbL assemblies: (a) spin-assisted LbL for star and (b) dip-assisted LbL for linear (top) and star (bottom) polymer at different pH condition of pH 6/6 (left) and pH 7/5 (right). Gray color-boxes represent the LbL films with different thicknesses and surface roughness, but

their values are not set to the same length-scale for all drawings. The histograms on the right hand side of each drawing show the average thickness (black, left) and roughness (gray, right) with the left y-axis (1000 nm) for thickness and right y-axis (50 nm) for roughness for 30 bilayer LbL films. The bar graphs are all on the same scale. 179

Figure 7.1: (a) Buildup curve of linear/star (LS) film versus number of bilayers prepared using spin-assisted method (3,000 rpm) at various combinations of deposition pH conditions for p(AA)/p(DMAEMA) pairs: 5/5, 5/7, 6/7, 6/6, 7/5, and 7/7. (b) Variations of thickness of LS for 6 bilayers and for 18 bilayers versus different deposition pH pairs. (c) RMS roughness for LS at different scan areas and number of bilayers: 20 μm x 20 μm of 6 bilayers (■), 1 μm x 1μm of 6 bilayers (▲), and 1 μm x 1μm of 18 bilayers (♦) (the lines are a guide to the eye). 153

Figure 7.2: AFM topography images of linear/star LbL films (LS) with 18 bilayers assembled by using spin-assisted method at different pH pairs. Scan area for all images is 1 μm × 1 μm and Z scale is 5 nm. 155

Figure 7.3: Buildup curve of the LbL multilayer assembly of varying combinations of linear and star polyelectrolytes as a function of number of bilayers (1 to 30 bilayers) at different pH conditions (a) 6/6 and (b) pH 7/5: LL (dip-assisted (■) and spin-assisted (▲)) and SS (dip-assisted (●) and spin-assisted (▼)) (the lines are a guide to the eye). 157

Figure 7.4: AFM topography images of the LbL multilayer films composed of different components with different numbers of bilayers (9, 18, and 30 bilayers): linear/linear (LL) (A-C, G-I) and star/star (SS) (D-F, J-L) assembled at pH 6 / 6 using dip-assisted (a) (A-F) and spin-assisted (b) (G-L) methods. Scale bar is 2 μm and Z scale is 10 nm for all images. 160

Figure 7.5: AFM topography images of the LbL multilayer films composed of different components with different numbers of bilayers (9, 18, and 30 bilayers): linear/linear (LL) (A-C, G-I) and star/star (SS) (D-F, J-L) assembled at pH 7/5 using dip-assisted (a) (A-F) and spin-assisted (b) (G-L) methods. Scale bar is 2 μm and Z scale is 10 nm for all images. 162

Figure 7.6: UV-Vis spectra in a reflective mode ((a) and (b)) and index of refraction ((c) and (d)) for LbL multilayer films with 30 bilayers prepared at different deposition pH pairs: pH 6/6 ((a) and (c)) and pH 7/5 ((b) and (d)). 165

Figure 7.7: Buildup curve of the LbL multilayer films assembled with varying chain topology as a function of number of bilayers assembled by dip-assisting method at different pH conditions of pH 6/6 ((a) and (b)) and pH 7/5 (c): linear/linear (LL) (■), linear/star (LS) (●), star/linear (SL) (▲), and star/star (SS) (▼). (a) Linear growth curve is obtained by fitting date in the linear

buildup region (n = 9 to 30) into a function of $d = An + B$ for pH 6/6. (b) Exponential growth rate obtained by fitting the data into a function of $d = A_0\exp(n/\tau)$ (n = 1 to 12) for pH 6/6 (b) and (n = 1 to 30) for pH 7/5 (c). 169

Figure 7.8: Variations of thickness ((a) and (b)) and RMS roughness (R_q) ((c) and (d)) of the 30 bilayered dip-assisted LbL films for different polymer pairs at pH 6/6 ((a) and (c)) and pH 7/5 ((b) and (d)). 171

Figure 7.9: AFM topography images of the LbL multilayer films with different polymer pairs assembled at pH 6/6 (A-J, left) and 7/5 (B-K, middle and C-L, right) using dip-assisted method: linear/linear (LL) (A-C), linear/star (LS) (D-F), star/linear (SL) (G-I), and star/star (SS) (J-L). Scale bar is 2 μm and Z scale is 10 nm for all images and the Z scale is 10 nm (A-J, left and B-K, middle) and 200 nm (C-L, right). 172

Figure 7.10: Buildup curve of the LbL films fabricated with dip- and spin-assisted methods for linear/linear (LL) (a) and star/star (SS) (b) polymer pairs at different spinning speeds in the range of 0 to 8,000 rpm at pH 7/5 (the lines are a guide to the eye). 174

Figure S7.1: The ellipsometric raw data of Ψ (polarized angle) and Δ (phase) of dip-assisted LbL multilayer films on silicon oxide substrate measured at three incident angles 65, 70, and 75° for wavelengths from 200 to 1000 nm. (a) Linear/linear pair at pH 6/6, (b) star/star pair at pH 6/6, (c) linear/linear pair at pH7/5, and (d) star/star pair at pH 7/5. 186

Figure S7.2. Large scale AFM topography images of linear/star LbL films (LS) with 6 bilayers assembled by using spin-assisted method at different pH pairs. Z scale is 20 nm. 187

Figure S7.3: AFM topography images of linear/star LbL films (LS) with 6 bilayers assembled by using spin-assisted method at different pH pairs. Scan area for all is 1 μm × 1 μm and Z scale is 5 nm. 188

Figure S7.4: Contact angle of the LbL multilayer films composed of different components with different numbers of bilayers (18 and 30 bilayers): linear/linear (LL) (dip-assisted (black) and spin-assisted (light gray)) and star/star (SS) (dip-assisted (dark gray) and spin-assisted (white)) at different deposition pH pairs: (a) pH 6/6 (a) and (b) pH 7/5. 189

Figure S7.5: Optical microscopy images of LbL films with 30 bilayer films assembled at pH 6/6 using dip- (A) and spin-assisted (B) methods. 190

Figure S7.6: AFM topography images of 30 bilayer LbL films: linear/linear (LL) (left) and star/star (SS) (right) assembled at different spinning speeds at pH 7/5. Scan area for all images is 10 μm × 10 μm and Z scale for height is 10 nm. 191

Figure S7.7: Variations of thickness ((a) and (b)) and RMS roughness (R_q) ((c) and (d)) of 30 bilayer LbL films of linear/linear (LL) (left) and star/star (SS) (right) polymer pairs as a function of shear rate (RPM) at pH 7 / 5 (the lines are a guide to the eye). 192

Figure 8.1: (a) Molecular structure and composition of amphiphilic heteroarm PS_nP2VP_n star block copolymers with core/corona unimolecular micelles; (b) fabrication procedure and (c) multilayer structure of assembled star polymer micelles (left) and porous shell morphology (right). 198

Figure 8.2: AFM topography image (left) and cross sectional analysis (right) of PS_nP2VP_n star block copolymer monolayer on planar silicon wafers in dry state obtained by dip-assisted deposition method at pH 3. (a) PS_9P2VP_9 in 4% DMF mixed aqueous solution. (b) $PS_{22}P2VP_{22}$ in 4% DMF mixed aqueous solution. (c) $PS_{22}P2VP_{22}$ in 4% acetone mixed aqueous solution. The z-scale of all AFM images is 10 nm. 203

Figure 8.3: High resolution AFM topography (left) and phase (right) image of $PS_{22}P2VP_{22}$ star block copolymer unimolecular micelles on planar silicon substrate in dry state deposited by dip-assisted LbL method at pH 3. The z-scale is 10 nm and 60º. 204

Figure 8.4: Build-up of PS_nP2VP_n/PSS LbL film on planar silicon wafer (9 arms (■) and 22 arm (□)). 205

Figure 8.5: (a) AFM topography images of PS_nP2VP_n/PSS LbL multilayer film as a function of number of bilayers (5 (a,d), 8 (b,e), and 11 (c,f) bilayers) on planar silicon substrate in dry state (n = 9 arms (a,b,c) and 22 arms (d,e,f)). The z-scale is 120 nm. 207

Figure 8.6: Zeta-potential measurements of $PS_{22}P2VP_{22}$/PSS LbL assemblies deposited on SiO_2 template core at pH 3. 208

Figure 8.7: CLSM images (lower resolution (a,b,c) and higher resolution (d,e,f)) of $PS_{22}P2VP_{22}$/PSS microcapsules as a function of number of bilayers (5 (a,d), 8 (b,e), and 11 (c,f)). 209

Figure 8.8: AFM topography images of PS_nP2VP_n/PSS microcapsules (9 arms (a,b,c) and 22 arms (d,e,f)) as a function of number of bilayers (5 (a,d), 8 (b,e), and 11 (c,f) bilayers) on silicon substrate in dry state. The z-scale of all images is 600 nm. 201

Figure 8.9: (a) Thickness and (b) RMS roughness of dried shell wall of PS_nP2VP_n/PSS microcapsules for different bilayers (5, 8, and 11 bilayers) compared to those of corresponding films on planar silicon wafer. 211

Figure 8.10: High resolution AFM images (topography (left) and phase (right)) of $PS_{22}P2VP_{22}$ /PSS microcapsules as a function of number of bilayers (5 (a), 8 (b), and 11 (c) bilayers) on silicon substrate in dry state. The Z scale of all images is 120 nm (topography) and 30° (phase). 212

Figure 8.11: (Top) Shell thickness and swelling ratio and (bottom) AFM images of rehydrated $PS_{22}P2VP_{22}$ /PSS LbL hollow microcapsules as a function of number of bilayers (5 (a), 8 (b), and 11 (c) bilayers) and (d) high resolution image of the surface of capsule (c) using liquid cell scan under pH3 Tris-buffer of 0.01 M. The Z scale of images is 600 nm for (a-c) and 120 nm for (d). 213

Figure 8.12: CLSM images of $PS_{22}P2VP_{22}$/PSS microcapsules (11 bilayers) using FITC-labeled dextran with varying molecular weights: (a) 20,000, (b) 150,000, (c) 500,000, and (d) 2000,000. 215

Figure 8.13: SANS data of fully hydrated $PS_{22}P2VP_{22}$/PSS microcapsules with (a) (square) 5 bilayers, (circle) 8 bilayers, and (triangle) 11 bilayers in D_2O solution that have been fitted with a power law model to determine the evolution of the fractal dimension, and (b) the 5 bilayer sample with a DAB fit. 219

Figure S8.1: (a) Zeta-potential measurements of $PS_{22}P2VP_{22}$ star block copolymer solution with varying pH conditions. (b) Variation of transparency of $PS_{22}P2VP_{22}$ star block copolymer solution with pH. 224

Figure S8.2: CLSM images of PS_9P2VP_9/PSS LbL microcapsules as a function of number of bilayers (5 (a), 8 (b), and 11 (c) bilayers). 225

Figure S8.3: Variations of the diameter of PS_nP2VP_n/PSS LbL microcapsules (n=9 (■) and 22 (●) arms) a function of number of bilayers (5, 8, and 11). 226

Figure S8.4: AFM images (topography (left) and phase (right)) of shell wall of (a) PS_9P2VP_9/PSS and (b) $PS_{22}P2VP_{22}$/PSS LbL hollow microcapsule for 8 bilayers on silicon substrate in dry state. The data scale of all images is 120 nm (topography) and 30° (phase). 227

Figure S8.5: Domain height (□) and width (■) of the shell wall of $PS_{22}P2VP_{22}$/PSS LbL multilayer microcapsule in dry state as compared to $PS_{22}P2VP_{22}$ unimolecular micelle monolayer films on silicon wafers. 228

Scheme 9.1; (a) Chemical structure of amphiphilic heteroarm $PS_{28}P2VP_{28}$ and $PS_{28}(P2VP\text{-}b\text{-}PtBA)_{28}$ star copolymers. (b) Assembly and suggested molecular conformation of star polymer surface unimicelles on graphene oxide sheets at solvent/water and air-water interfaces for different conditions on a Langmuir trough (A-C). 234

Figure 9.1: AFM topography (left) and phase (right) of GO (0.01 wt %, 0.5 ml)/$PS_{28}P2VP_{28}$ star copolymer (0.02 mg/ml in chloroform, 70 μL): (a) large area scan, (b) high resolution zoomed in image, and (c) topography height profile of corresponding image from (b) at surface pressures of 0 mN/m (a-c); (d) large area scan and (e) high resolution zoomed in for surface pressure 15 mN/m (d-e). The subphase pH was adjusted at pH 2. z-scale: 5 nm (topography) and 30° (phase) for a, d; 3 nm (topography) and 20° (phase) for b, c, e. 236

Figure 9.2: AFM topography (left, a,b,c) and phase (right, c) of GO (0.01 wt %, 0.5 ml)/$PS_{28}P2VP_{28}$ star copolymer (0.1 mg/ml in chloroform, 70 μL) at pH 2 for surface pressures of 0 mN/m. The inset in (C) indicates lattice analysis from the corresponding topography image in Figure 2c. z-scale: 5 nm (topography) and 20° (phase). 238

Figure 9.3: AFM topography (left,) and phase (right) of (a, b) GO (0.01 wt %, 0.5 ml)/$PS_{28}P2VP_{28}$ star copolymer (0.1 mg/ml in chloroform, 70 μL) at pH 2 for surface pressures of 15 mN/m; (c) The height profile of corresponding topography image; (d) FFT of domain morphologies for A and B regions from Figure 3b where A is corresponding to the center region while B, the near edge region of GO sheet. z-scale: 5 nm (topography) and 30° (phase). 241

Figure 9.4: High resolution QNM analysis of (a) topography, (b) adhesion, (c) apparent modulus, and (d) deformation for GO (0.01 wt %, 0.5 ml)/$PS_{28}P2VP_{28}$ star copolymer (0.1 mg/ml in chloroform, 70 μL) at pH 2 for surface pressures of 15 mN/m. z-scale: 4 nm (topography), 2.5 nN (adhesion), 1.61 GPa (modulus), and 1.3 nm (deformation). 243

Figure 9.5: AFM topography (left) and phase (right) of (a-c) GO (0.01 wt %, 0.5 ml)/$PS_{28}(P2VP\text{-}PtBA)_{28}$ star terpolymer (0.02 mg/ml in chloroform, 70 μL) at surface pressures of 0 mN/m, (d-e) GO (0.01 wt %, 0.5 ml)/$PS_{28}(P2VP\text{-}b\text{-}PtBA)_{28}$ star block terpolymer (0.1 mg/ml in chloroform, 70 μL) at surface pressures of 0 mN/m, (f) GO (0.01 wt %, 0.5 ml)/$PS_{28}(P2VP\text{-}b\text{-}PtBA)_{28}$ star block copolymer (0.1 mg/ml in chloroform, 70 μL) at surface pressures of 15 mN/m. All depositions were conducted at pH 2. z-scale: 5 nm (topography) for a-f and 30° for a; 20° for b, c; 10° for d-f (phase). 245

Figure 9.6: AFM topography (left) and phase (right) of GO (0.01 wt %, 0.5 ml)/$PS_{28}P2VP_{28}$ star copolymer (0.1 mg/ml, 70 μL) at pH 2 for different spreading solvents at surface pressure 0 mN/m): (a,b) toluene, (c)

dichloromethane (CH_2Cl_2), and (d) tetrahydrofuran (THF). z- scale: 5 nm for a-d (topography) and 10° for a, c, d; 30° for b (phase). 247

Figure 9.7: AFM topography images at low (a) and high (b-e) magnification images; AFM topography (left) and phase (right) of (b-e) GO (0.01 wt %, 0.5 ml)/$PS_{28}P2VP_{28}$ star copolymer (0.1 mg/ml, 70 μL) at pH 6 for surface pressure 15 mN/m. The height profile of corresponding topography image (e) is placed in bottom right. z-scale: 5 nm (topography) and 30° (phase). 249

Figure 9.8: AFM topography images at low (a) and high (b-e) magnification images; AFM topography (left) and phase (right) of GO (0.01 wt %, 0.5 ml)/$PS_{28}P2VP_{28}$ star copolymer (0.1 mg/ml, 70 μL) at pH 6 for surface pressure of 30 mN/m. The height profile of topography image is obtained from Figure 8b (bottom). z-scale: 5 nm for a; 10 nm for b (topography) and 10° for a; 20° for b (phase). 251

Figure 9.9: EFM images of GO (0.01 wt %, 0.5 ml)/$PS_{28}P2VP_{28}$ star copolymer (0.1 mg/ml, 70 μL) at pH 6 for surface pressure of 30 mN/m. z-scale: 2.5° for (a) and 2.0° for (b). 253

Figure S9.1: Pressure-area (π-A) Langmuir-isotherm versus trough area of GO (Dot, Green), $PS_{28}P2VP_{28}$ star copolymer (Dash, Red), GO/$PS_{28}P2VP_{28}$ star copolymer (Line, Black), PS_{28}(P2VP-*b*-PtBA)$_{28}$ star terpolymer (Dash-Dot, Blue), and GO/PS_{28}(P2VP-*b*-PtBA)$_{28}$ star terpolymer (Dash-Dot-Dot, Sky-Blue) at water subphase pH 2. 256

Figure S9.2: High resolution AFM topography of GO (0.01 wt %, 0.5 ml)/$PS_{28}P2VP_{28}$ star copolymer (0.1 mg/ml in chloroform, 70 μL) at pH 2 for surface pressures of 15 mN/m: (a) low magnification (20 × 20 μm), (b) high magnification (2 × 2 μm), and (c) height profile analysis of high solution image (500 × 500 nm). z-scale: 10 nm for (a), 4 nm for (b), and 4.2 nm for (c). 257

Figure S9.3: Low magnification AFM topography of GO (0.01 wt %, 0.5 ml)/$PS_{28}P2VP_{28}$ star copolymer (0.1 mg/ml, 70 μL) at pH 6 for surface pressure of 30 mN/m. z-scale: 6.5 nm. 258

Figure S9.4: Raman mapping (a) and spectra of G and D bands of GO (0.01 wt %, 0.5 ml)/$PS_{28}P2VP_{28}$ star copolymer (0.1 mg/ml, 70 μL) at pH 6 for surface pressure of 30 mN/m. 259

Scheme 10.1: Various types of novel branched functional building blocks based on star-shaped polymers (s-BCP & s-PE) for supramolecular ultrathin nanofilm assemblies. 261

Scheme 10.2: Summary I of the controlled interfacial assembly of highly-branched star-shaped polymers into organized LB monolayer films through a directed assembly at various surfaces and interfaces. 268

Scheme 10.3: Summary II of the controlled interfacial assembly of highly-branched star-shaped polymers into organized LBL multilayer films through a directed assembly at various surfaces and interfaces. 270

LIST OF SYMBOLS AND ABBREVIATIONS

R_g	Radius of gyration
GI	Group I PS_nP2VP_n heteroarm star
GII	Group II $PS_n(P2VP\text{-}b\text{-}PtBA)_n$ heteroarm stars
Φ_{P2VP}	Weight percent of P2VP blocks
A_0	limiting molecular area
A_1	Initial molecular area
π	Suface pressure
H9	Hydrolyzed $PS_n(P2VP\text{-}b\text{-}PAA)_n$ heteroam star with 9 arms
H22	Hydrolyzed $PS_n(P2VP\text{-}b\text{-}PAA)_n$ heteroam star with 22 arms
GO	Graphene oxide

SUMMARY

Surface-assisted directed assembly allows ultrasoft and replusive functional polymeric "colloids" to assemble into the organized supramolecular ultrathin films on a monomolecular level. This study aims at achieving a fundamental understanding of molecular morphology and responsive behavior of major classes of branched star-shaped polymers (star amphiphilic block copolymers and star polyelectrolytes) and their aggregation into precisely engineered functional ultrathin nanofilms. Thus, we focus on elucidating the role of molecular architecture, chemical composition, and intra/intermolecular interactions on the assembly behavior of highly-branched entities under variable environmental and confined interfacial conditions.

The inherent molecular complexity of branched architectures facilitates rich molecular conformations and phase states from the combination of responsive dynamics of flexible polymer chains (amphiphilic, ionizable arms, multiple segments, and free chain ends) and extened molecular design parameters (number of arms, arm length, and segment composition/sequence). These marcromolecular building components can be affected by external conditions (pH, salinity, solvent polarity, concentration, surface pressure, and substrate nature) and transformed into a variety of complex nanostructures, such as two-dimensional circular micelles, core/shell unimicelles, nanogel particles, pancake & brush micelles, Janus-like nanoparticles, and highly nanoporous fractal networks. The fine balance between repulsive mulitarm interactions and surface energetic effects in the various confined surfaces and interfaces enables the ability to fabricate and tailor well-organized ultrathin nanofilms. The most critical findings in this study include: (1) densely packed circular unimicelle monolayers from amphiphilic and amphoteric multiblock stars controlled by arm number, end blocks, and pH/pressure induced aggregation, (2) monolayer polymer-metal nanocomposites by *in-situ* nanoparticle growth at confined interfaces, (3) on-demand control of exponentially or linearly grown heterogeneous stratified multilayers from self-diffusive pH-sensitive star polyelectrolyte nanogels, (4) core/shell umimicelle based microcapsules with a fractal nanoporous multidomain shell morphology, and (5) preferential binding and ordering of Janus-like

unimicelles on chemically heterogeneous graphene oxide surfaces for biphasic hybrid assembly.

The advanced branched molecular design coupled with stimuli responsive conformational and compositional behavior presents an opportunity to control the lateral diffusion and phase segregation of branched compact supermolecules on the surface resulting in the generation of well-controllable monolayers with tunable ordering and complex morphology, as well as to tailor their stratified layered nanostructures with switchable morphological heterogeneity and multicompartmental architectures. These surface-driven star polymer supramolecular assemblies and interfaces will enable the design of multifunctional nanofilms as hierarchical responsive polymer materials.

CHAPTER 1

INTRODUCTION

1.1 Background

An advanced design of polymeric ultrathin film (<100 nm) devices, which is a prerequisite for soft functional bio-interfaces, high sensitive and selective sensing platforms, and fast and reliable signal transduction in actuators, still requires a fundamental and in-depth understanding of surface related assembly behavior of polymeric molecules on a single molecular level. The nanometer scale controlled ordering and organization of condensed polymer films and coatings can be obtained through a "bottom-up" self-assembly approach coupled with a sophisticated wet fabrication technology and a surface nanoengineering with enhanced spatial accuracy and specificity.[1,2,3]

Polymeric materials as a "soft matter" or "complex fluid" can offer a rich phase and dynamic behavior and thus are considered promising building blocks in organized molecular assemblies for a variety of hierarchical ordered nanostructures with a high level of mobility.[4] Molecular organization of soft polymeric units (e.g., block copolymer, polyelectrolyte, liquid crystalline polymer) is tunable through structural rearrangement triggered by responses to small environmental changes as a result of their reversible weak intermolecular interactions, such as van der Waals forces, hydrogen bonding, hydrophobic, and electrostatic interactions at mild ambient conditions. The resulting

polymeric superstructures render a rich and complex morphology, a controlled ordering, and a flexible phase behavior under external stimuli in solution, bulk, and surface states.

However, polymer assembly behavior at surfaces has remained a challenge, especially in ultrathin polymer films and on heterogeneous interfaces, exhibiting a highly confined surface effect on chain configuration and dynamics, as the film thickness become close to a single molecular level, that is, beyond a characteristic molecular dimension (i.e., the film thickness lower than the radius of gyration, R_g).[1,2] The confined polymer coils are compressed in a directon normal to the surface. The extent of confinement relies on the degree of interaction of polymer molecules with the surface, and thereby affects the chain structure and phase states of polymer molecules adsorbed onto the surfaces and interfaces of ultrathin films. In particular, branched architectures with high monomer density and interarm exclusive volume repulsions are expected to greatly reduce chain interpenetration, resulting in smaller entanglements than linear counterparts, especially in the confined geometry with a decreased pervaded volume.[3] This leads to a decreased large strain deformation of polymer thin films. Therefore, controlling the interplay between mechanical integrity and ultrasoft dynamic interactions in confined ultrathin films would be critical for developing future adaptive/responsive polymer systems.

1.1.1. Supramolecular Ultrathin Films of Highly Branched Molecules

The supramolecular organization of polymer materials through directed assembly has been adopted as an effective route to control the structural properties and effective interactions of organic ultrathin films.[1,2,5, 6,7,8,9] Self-assembled ultrathin polymer films

and coatings can significantly alter surface and interfacial properties including adsorption, friction, lubrication, adhesion, and wetting properties.[10] It is found that the aggregate behavior, morphology, spatial ordering, and orientation of the microstructure in these ultrathin films are closely related to the structural and chemical characteristics of their polymeric building blocks, such as molecular shape, size, backbone architecture, composition, and intermolecular/interfacial interactions.[11] Among them, in particular, it has been recently witnessed that molecular architecture is a key factor to determine the molecular organization and control over spatial ordering in these ultrathin films at a nano and microscale.[12,13,14,15]

Recent advances in synthetic technology (i.e., controlled living polymerization) allow for rational molecular designs, such as monomer nature, composition, and block sequence and also yield noble shape and chain configuration like non-linear highly-branched polymers, such as dendrimers, polymer brushes, hyperbranched polymers, and star-shaped polymers exhibiting intriguing structure and properties that differ from traditional linear structures (Figure 1.1).[16, 17, 18, 19] Branched polymers can be classified by the different types of joints (e.g., single core or multiple grafting backbone) at which one end of the branched arms are chemically attached in a radial, side, or tree-like fashion, and possess abundant periphery terminal end groups. The molecular shape, size, and properties can be varied as a function of the degree of branching and type/length of branched segments. Intriguing molecular characteristics, such as abundant functional end groups, globular shape, core-shell morphology and highly dense chain structure can offer a new platform for a supramolecular building component of surface science and

engineering for assemblies of dynamically stable unimolecular micelles, core/shell type nanoparticles, and nanogels.

Figure 1.1: Molecular architecture of highly-branched polymers: (a) graft, (b) brush, (c)

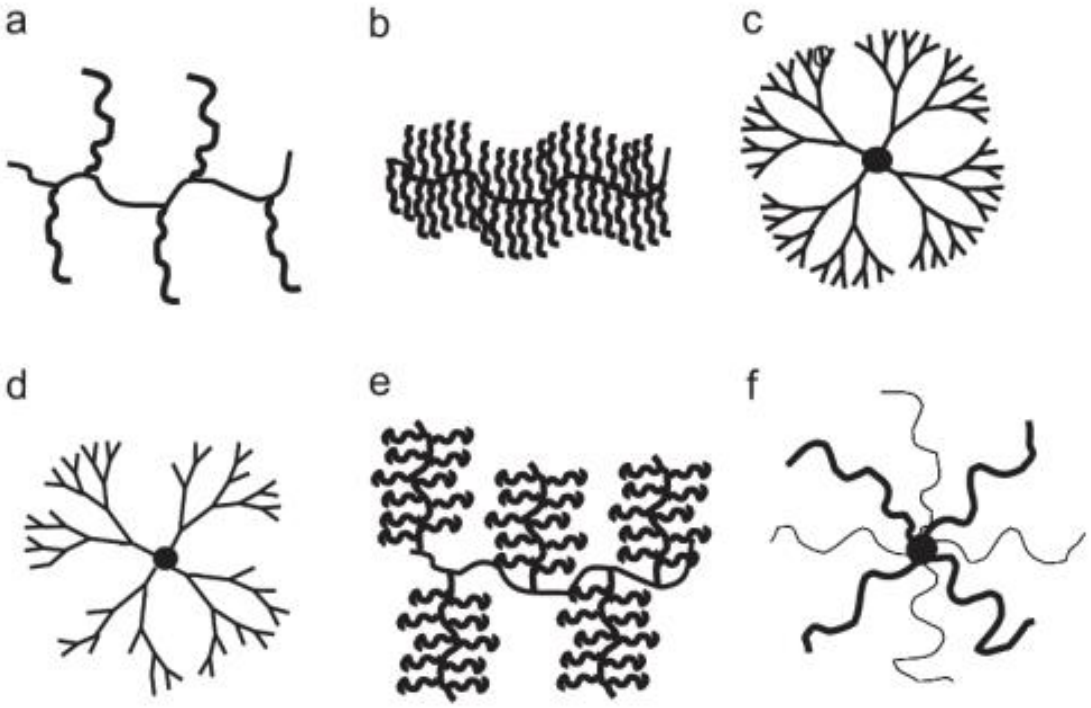

dendrimer, (d) hyperbranched, (e) arborscent, and (f) star architectures.[16]

Additional structural variables of non-linear, branched polymers provide a higher degree of freedom in molecular design and as a result render higher complexity in chain conformation, interactions, and molecular dynamics. Thus, branched polymeric systems can play an attractive role as building units in organized supramolecular assemblies. On the other hand, highly-branched polymers can also offer an active multi-functional surface and interface in a responsive/predictable manner.[20,21,22,23,24,25,26,27] Due to the high degree of free end groups and flexible side branches, more diverse conformational transformation and interactions by external stimuli (e.g. pH, temperature, and shear)

enable tunable micro and nanoscale assemblies and ordering for the design of multifunctional stimuli-responsive and adaptive thin films and coatings (Figure 1.2).[28, 29,30,31,32,33,34,35] For instance, star-shaped macromolecules, such as block copolymers and polyelectrolytes bearing pH responsive groups are considered to be a promising candidate for adaptive/responsive nanofilms due to their unique chemical properties.[36,45] Their compact and globular structures cause a distinct shift of pK_a compared to their linear counterparts due to the ionic confinement effect.[37] Such pH-responsive behaviors can be easily tuned by adjusting the charge nature of the star polyelectrolytes, as well as environmental conditions, such as pH, salinity, and multivalent counterions.

Also, the dynamic and responsive properties are closely related to the integrity and robustness of the final micro/nanostructure.[38,39] Thin polymeric films that show faster responsive behavior than bulk materials due to their favorable rearrangement, impose a challenge in maintaining mechanical stability. Thus, along with understanding their assembly behavior, quantifying these mechanical properties is critically important for validating the stability and integrity of the stimuli-responsive nanostructures. The emerging interest in smart polymer nanofilms through bottom-up approaches, such as self/directed assembly of mono/multilayers[40] can be found in biomedical and sensing applications.[41,42,43,44]

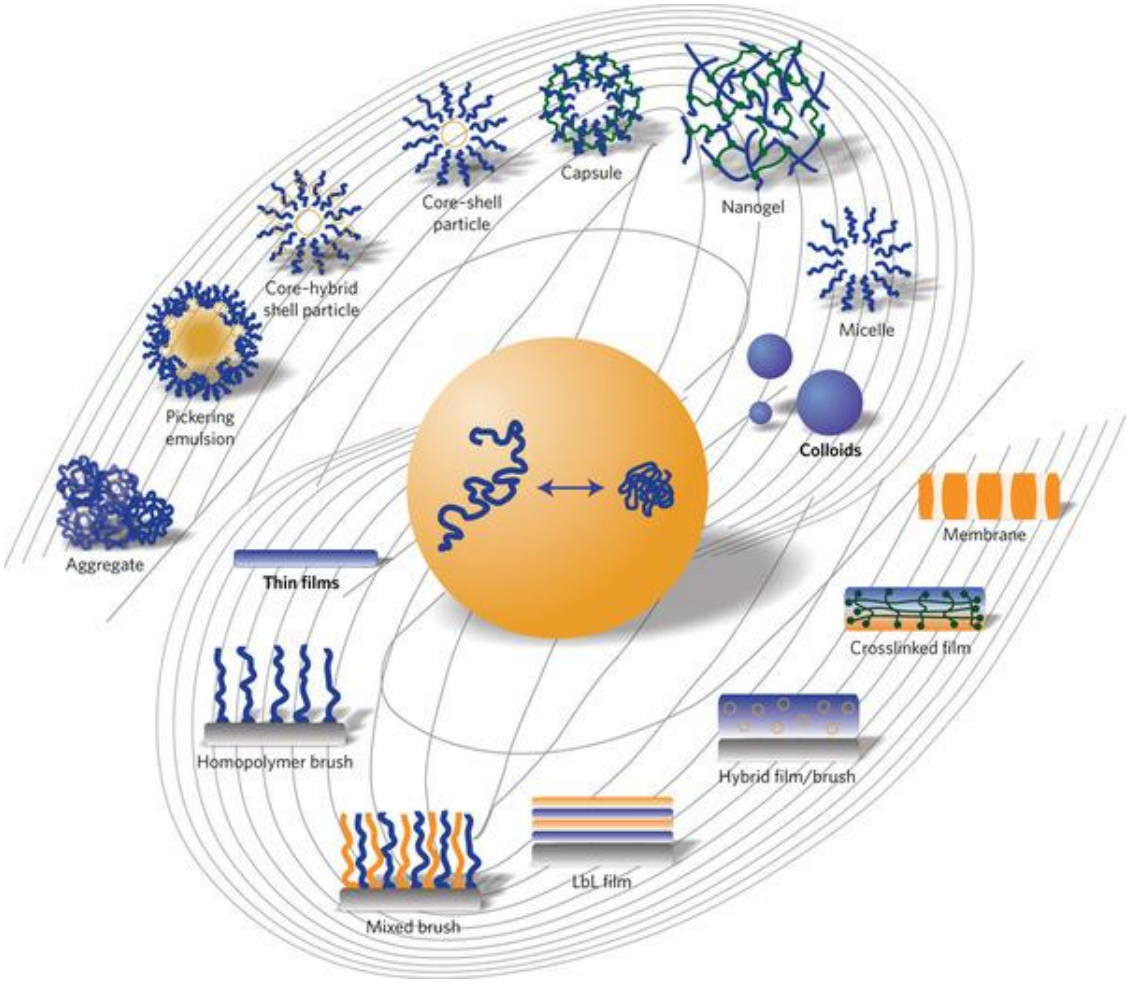

Figure 1.2: Stimuli-responsive nano and macro structures with various geometric forms prepared via different molecular assembly techniques.[28]

However, the controlled assembly of highly-branched molecules at the interface and surface still presents a considerable number of important issues due to limited entanglements, multiple functionalities, and weak intermolecular interactions. The confined branched molecular conformation in ultrathin films should produce stronger repulsive exclusive volume interactions due to their increased interarm repulsions under two-dimensional spatial constraint. This star polymer nature can provide a change for the design of ultrasensitive enviormemtal responsive polymer assemblies, but also can

deteriorate thier mechanical properties and structural integrity by preventing effective adsorption and interdigitation onto the proper substrate, in particular, in the self-assembly system from diluted solutions. Therefore, a fundamental understanding of molecular deformation and interactions of organized highly-branched polymeric ultrathin films is essentially required for the design of tunable and responsive assemblies and surfaces.

1.1.2. Star-Shaped Polymers: Molecular Architecture and Properties

The star-shaped (or star-like or star) polymer is a form of branched polymers with ideally one common join point on the microscopic level, in contrast to dendrimers with a high degree of branching (Figure 1.1). The star polymers are comprised of multiple well-defined flexible linear branches, referred to as arms that are chemically tethered onto a common central core while the other periphery ends remain free terminal groups with no steric constraints. The compact core is generally much smaller than arm length for star polymers. Star architectures are regarded as a point polymer brush with radial arms attached on substrates with extremely high curvature.[45,46,47] Star polymer also resemble polymeric micelles (also called polymeric stars) having corona arms and kinetically frozen core based on a molecular aggregation of linear amphiphilic block copolymers, or spherical brushes composed of grafted polymer arms on a colloidal particle with a large volume hard core. Thus star polymers can be considered an intermediate between linear polymer systems and soft colloidal spheres. The star structure and physical properties can be varied as a function of arm number (n): linear polymer system for n = 1 or 2, and solid colloid for n >> 1. Large number arm star polymers can behave like solid colloids with a hard core repulsion.[48,49,50]

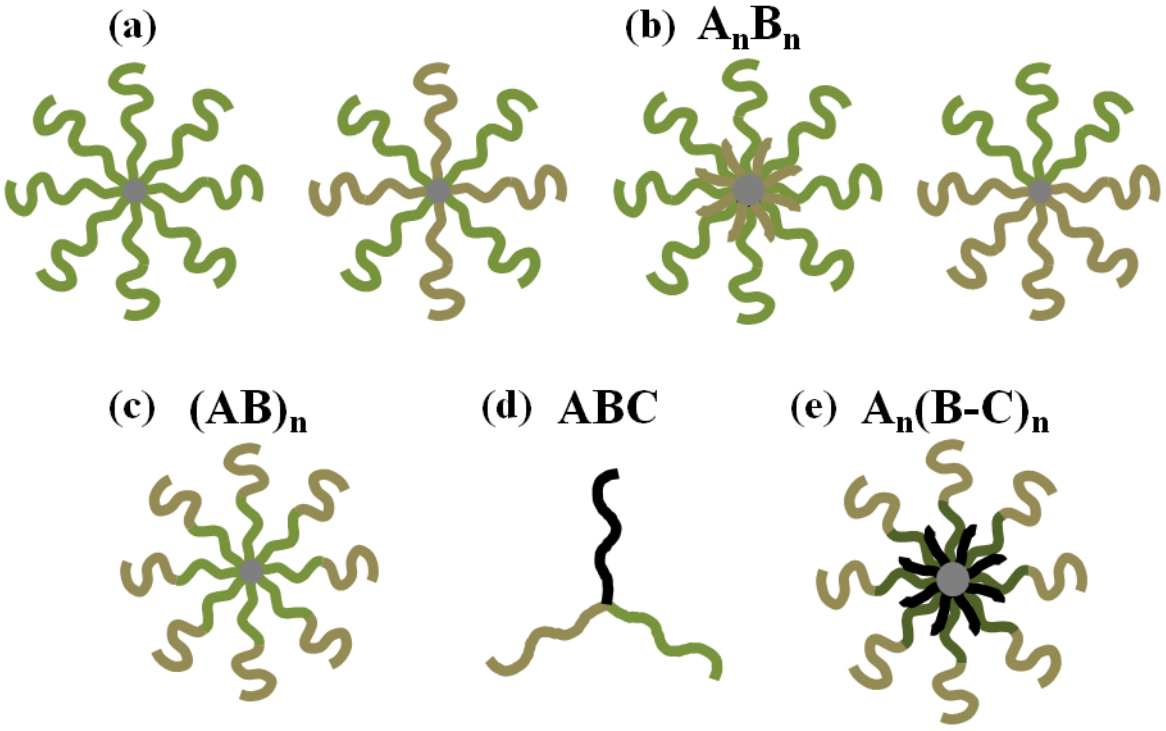

Figure 1.3: Representative molecular architecture of star-shaped block copolymers: (a) homoarm star polymer, (b) A_nB_n type symmetric or asymmetric heteroarm star copolymer, (c) $(AB)_n$ type diblock homoarm star copolymer, (d) ABC type miktoarm star terpolymer, and (e) $A_n(B\text{-}C)_n$ heteroarm star terpolymer.

The structure of star polymers can be tailored by charging arm number, composition, ionic state, degree of polymerization of arms, and block sequential arrangements. The star polymers can be divided into neutral or charged stars. Charged polymers with ionizable groups are called "polyelectrolytes", which can be further divided into strong and weak polyelectrolytes by ionization strength. The polyampholytes (amphoteric polymers) possess both acidic and basic groups and exhibit an isoelectric point where the net charge becomes zero at isoelectric pH in the case of weak polyelectrolytes.[51] The ionizable arms of polyelectrolyte stars provide a wider range of control parameters, such as pH, salinity, valence of salt, and electric potential compared to neutral stars, which are

controllable depending on solvent polarity.[52,53,54,55] The star polymers can be further classified into homoarm and heteroarm (or miktoarm) star polymers according to arm composition and topological arrangements. The homoarm star polymers are identical in arm composition and length. They have single component, or diblock or multi block arms in the form of $(AB)_n$. In the case of heteroarm star polymers, different type of arms are grafted onto the common single core and also can contain unsymmetric arms in length, for example, as represented by A_nB_n , ABC, or $A_n(B\text{-}C)_n$ (Figure 1.3).[47]

Star-shaped amphiphilic block copolymers are an interesting design, especially with ionic blocks containing amphiphilic polyelectrolytes as a candidate for core/shell micelle like structure with respect to different solvent conditions. The microstructure and phase segregation state is dependent on the solubility of polymer segments in solvents used for dispersion. A good solvent for all polymer blocks, often referred to as a "non-selective solvent," can render a swollen coiled structure with a corona-corona configuration, while in certain solvents that have different miscibility for specific block, called "selective solvents," polymer chain of amphiphiles take a form composed of collapsed core and stretched corona or swollen shell, which is similar to conventional polymer micelles.[52,53,54,55] Thus the quality of the solvent can determine molecular conformation and interactions of amphiphilic block copolymers and this solution property affects adsorption and assembly behavior on surfaces upon deposition or spreading. Recent theoretical study has demonstrated the phase behavior of diblock arm star polyelectrolytes and showed a dramatic switch of molecular conformation and dimension with response to the solvent, pH, and salt concentration.[55]

Star polymers can exhibit intriguing dynamic characteristics including polymer-like relaxation as well as colloidal-like self-diffusion because of their hybrid polymer-colloid character. For example, Likos et al. proposed an effective pair potential between star polymers showing ultrasoft effective interaction in concentrated solution by logarithmic repulsion for short distance in contrast to exponential decay in the potential for diluted condition.[48] Multiarm stars can behave like colloidal particles suggesting the ability to form ordered structures at high concentration, and for large arm star there is a gelation transition in the star polymer solution (Figure 1.4).[49,50]

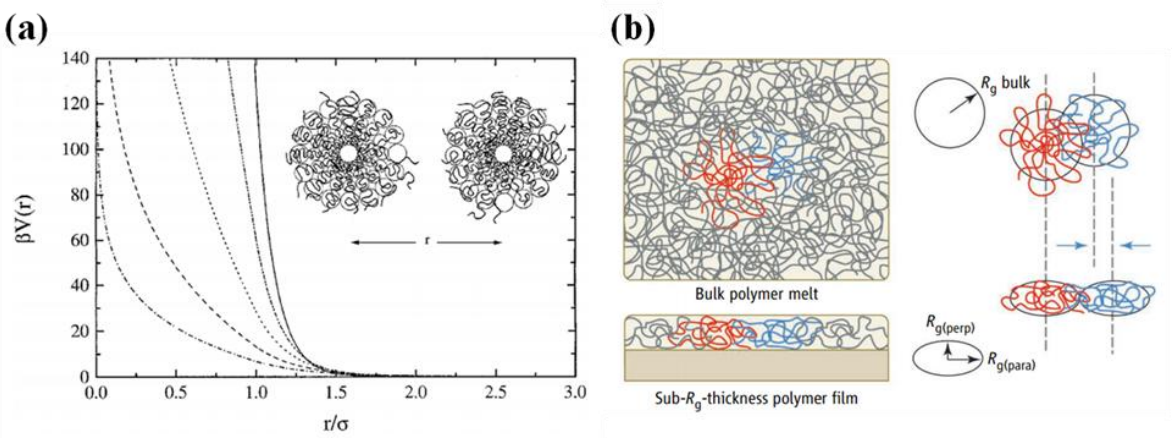

Figure 1.4. (a) Ultrasoft effective pair potential of star polymers at varying center-to-center distance r [48] and (b) polymer chain conformaton in the polymer thin film (confined geometry) where thickness is less than the radius of gyration (R_g) displaying a limited interpentraton or entanglement in polymer coil pairs compared to bulk polymer melt.[3]

At a certain pH, star polyelectrolytes have more stretched arms than neutral stars due to either electrostatic or steric repulsions between arms or osmotic pressure induced from confined counterions. The counterion confinement leads to a reduction of electrostatic

energy by decreased charge on the star polymers. When the counterion condensation occurs on the arm, decreased repulsion leads to less stretched conformation. Star polyelectrolytes have been theoretically demonstrated to be able to become dense in the overlap concentration region, and further transition into the interdigitated state at higher concentration. In the overlap case, the chains of two polyelectrolyte stars retract as modeled by "fused spheres" and have stronger interactions than neutral stars for a lower number of arms.[48,49,50,52,53]

The effective interactions of two adsorbed star polymers at the surface have been studied by simulation and analytical theory.[56] When soft star polymers are strongly adsorbed on a surface, this confinement makes a dramatic change in chain conformations showing more stretched arms and leading to stronger repulsive interactions compared to the three dimensional state (Figure 1.4). These two dimensional star polymers are expected to have higher ordering behvaior due to strong entropic repulsion, and their chain conformations can be controlled depending on the strength of adsorption onto the substrate.[1,2,49,57,58]

1.1.3. Star-Shaped Polymers Assemblies at Interface

Star-shaped polymers have been synthesized in a variety of chemical architectures and compositions and show a range of unique physical properties (see Figure 1.5).[59] Among recent studies, He et al.[60] reported an assembly behavior of extended unimers, based on novel multiarm block copolymer of poly(ethylene oxide)-b-poly(methacrylic acid) (PEO-b-PMMA) block copolymers. At high pH these block copolymers can self-assemble into

the unimers due to negatively charged carboxylate groups and hydrophilic PEO, whereas the star polymer forms micelles at low pH. Such a pH-responsive star block copolymer containing PEO blocks grafted to PMAA chains can stabilize the polymer complex for potential use in drug delivery due to a high density of pH-responsive functional groups. These polyacidic star copolymers were observed to induce the aggregation necessary to produce larger nanostructures.[61]

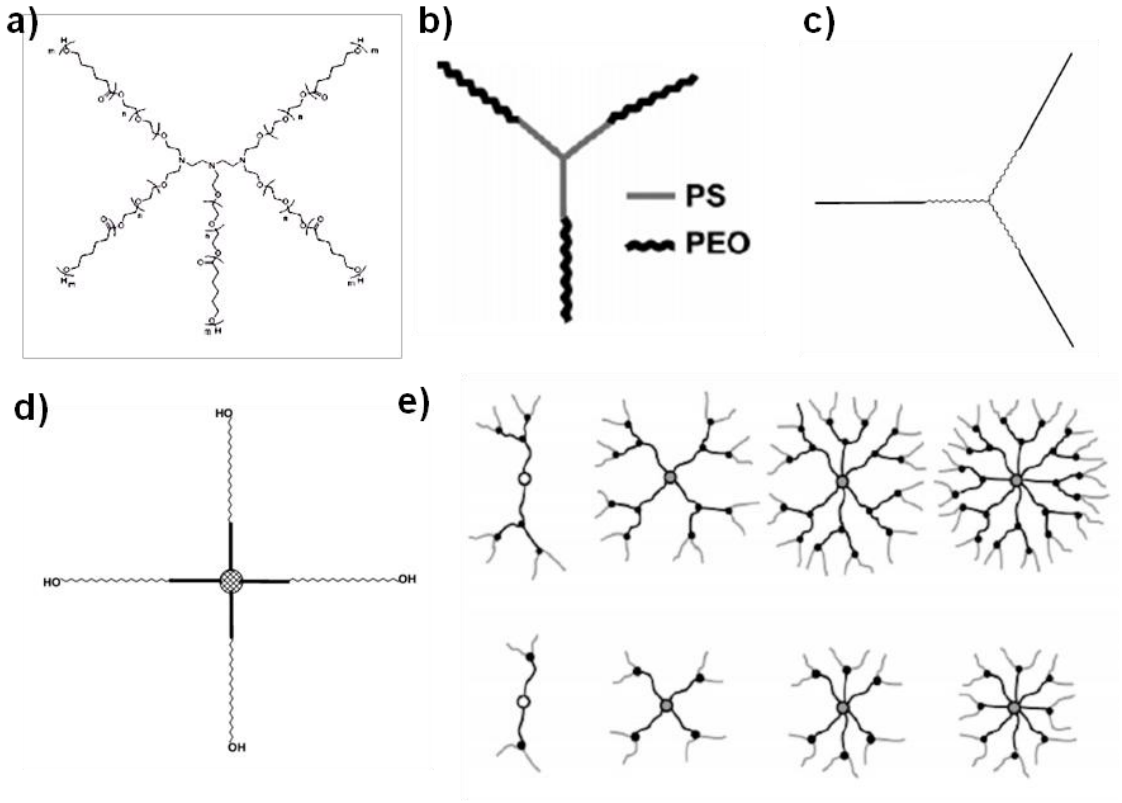

Figure 1.5: a) $(PEO)_9$-b-$(PCL)_m$ star, (b) PS-PEO three-arm star, (c) PEO-b-PS three-arm star polymer, d) PB-b-PEO four arm star, (e) dendrimer-like PS core and PBA or PAA corona.

The various porous morphologies were observed to be formed by changing dendritic end groups such as hydrophobic acetonide, which subsequently deprotected to a hydroxyl-

functionalized star. Dong *et al.*[62] showed the honeycomb-structured microporous films were self-assembled based on novel hyperbranched poly(3-ethyl-3-oxetanemethanol)-star-polystyrene (HBPO-star-PS). These porous films exhibited isolated hexagonal pores which are easily controlled by changing the solvent, molecular weight, and concentration of the polymer. Luke et al.[63] demonstrated that highly ordered, porous honeycomb films can be prepared from dendron-functionalized star polymers.

Hammond *et al.* have observed pH-responsive changes in all-star polyelectrolyte multilayer film, but not in films of linear polyelectrolytes.[64] This difference was attributed to the lower degree of ionic cross-linking, and hence greater free-volume within all-star polyelectrolyte films. Tsitsilianis *et al.*[65] and Sheiko *et al.*[66] demonstrated that increasing the grafting density of branched polymer greatly reduced its micellar aggregation number as a result of mitigated chain entanglement. Such polymers can exist as unimolecular micelles with their conformation significantly changed as a function of selective solvents and adsorbing surfaces.[67]

Morphology of single crystals and thin films of star-branched polyesters with poly(ε-caprolactone) (PCL) arms were studied by Nunez *et al.*[68] The dendritic core of star-branched polymers, enables the study of pronounced effects, such as slow crystal rearrangement, higher equilibrium melting point and higher fold surface energy, caused by retarded crystal rearrangement of the star branched polymer, which is attributed to low chain mobility of fixed arms. Stavrouli *et al.*[69] explored the novel multi-arm star-shaped terpolymers, $(ABC)_n$. These star terpolymers composed of nonionic, hydrophilic

methoxy hexa(ethylene glycol) methacrylate, ionizable hydrophilic 2-(dimethylamino)ethyl methacrylate, and hydrophobic methyl methacrylate were found to form unimolecular micelles. They can provide stable, multi-compartmental soft nanoparticles, which can not be obtained from their linear counterparts. Stavrouli and coworkers[70] reported that a novel heteroarm star block terpolymer was synthesized using an extending "in-out" method. Muller *et al*. reported on several ionic star block-copolymers capable of assembling in cylindrical shaped micelles under external stimuli.[71,72]

An amphiphilic $A_n(B\text{-}b\text{-}C)_n$ heteroarm star terpolymer constituted of PS and poly(2-vinyl pyridine)-block-poly(acrylic acid) (P2VP-*b*-PAA) as an ampholyte shows pH-dependent phase behavior which causes the system to form a reversible hydrogel material based on the solvent induced sol/gel transition (see Figure 1.5).[73] According to Hammond *et al*.,[74] these heteroarm star block terpolymers also offer the macromolecular template for hierarchical self-organization in polyelectrolyte-surfactant complexes. Unique phase behavior of these complexes in solution was observed as a function of pH due to the ampholytic nature of P2VP-b-PAA segments. Several interesting morphological features have been observed for star block copolymers with novel architectures.[75,76,77,78] Unlike the usual AB block systems, no spherical domains were observed for low PCL content $(PS)_9\text{-}b\text{-}(PCL)_m$ stars but the crystallizable PCL chains aggregated to form dendritic and needlelike domains.[79] Similarly, extreme crowding of linear polymeric arms at a single junction point for $PS_{20}\text{-}PEO_{20}$ star polymer yielded dendritic morphology.

In another study, the responsive PS_7-$P2VP_7$ star polymers were grafted to the surface and were demonstrated to adopt various molecular conformations when exposed to selective solvents.[65,80] It was shown that the chain crowding increases the stability of the spherical domains as the arm number increases. Other P2VP-based star macromolecules were demonstrated to be pH-responsive with arm conformation directly visualized.[81] Moreover, metallized stars have been created by additional exposure to metal salt solutions. Rich morphologies have been reported for ABC star copolymer.[82] Some of these unique morphologies include core/shell and helix/cylinder morphologies for PS-*b*-P2VP-*b*-poly(*tert*-butyl methacrylate).[83] The influence of nanoparticles geometry and microdomain dimensions has also been explored theoretically by Balaz *et al.*[84] and studied by Thomas and co-workers.[85] A uniform dispersion of nanoparticles within periodic block copolymer structures requires at least one of the characteristic dimensions of the nanoparticles to be on the order of the length scale of the copolymer microstructure (spacing and dimension).

1.1.4. Langmuir-Bldogett Monolayers

Wet molecular fabrication methods have been widely employed for supramolecular ultrathin film assemblies and immobilization on appropriate substrates. Directed assembly approaches including Langmuir-Blodgett (LB) technique and layer-by-layer (LbL) assembly are useful methodologies to enable directed molecular level organization based on self-assembly in the range of a monolayer to hierarchical multilayer films with highly ordered and organized structure by a repeated deposition process. For star block-copolymers with an amphiphilic nature, we study the surface behavior under variable

surface areas by utilizing a well-known LB approach widely explored for understanding surface behavior.[4, 86] Water-soluble star block copolymer and star polyelectrolyte nanostructures with ionic arms are assembled via the LbL approach which relies on fine ionic interactions between anionic-cationic species.[87,88]

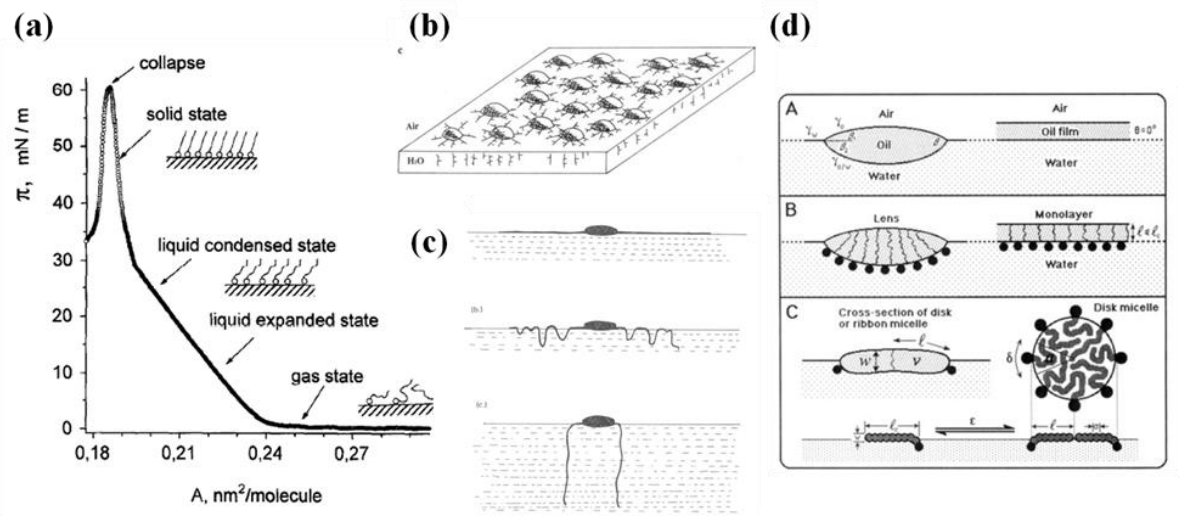

Figure 1.6: (a) Pressure-area Langmuir isotherm for surfactant molecules with different phase states,[4] (b) LB films assembled from amphiphilic block polyelectrolyte surface micelles,[92] (c) molecular conformational transtion from two-dimension (starfish) to quasi two-dimension (jellyfish) surface micelles on water surface,[93] and (d) proposed two-dimensional surface micelles at air-water interface (A. hydrocarbon liquid, B. surfactant lens (left) and monolayer (right), and C. 2D associated surface micelle).[96]

LB is a versatile and powerful method that allows the study of assembly behavior (i.e., phase transition) of amphiphile molecules as a function of pressure and temperature at air-water and air-solid interfaces. Upon deposition of diluted amphiphilic molecules by the aid of a volatile polar organic solvent, the molecular phase state can be transformed from a gas state, expanded liquid, condensed liquid, solid and collapsed state by lateral pressure on the LB trough, as represented by the two-dimensional isotherm profile

(pressure-area Langmuir isotherm) (Figure 1.6).[4,46] The monolayer (so called, Langmuir film) on the water surface at the air-water interface can transfer onto solid substrates by vertical dipping (Langmuir-Blodgett film) or horizontal liftoff (Langmuir-Schaefer film) at varying desirable deposition conditions, where the molecular density and spatial ordering of spread molecules is controlled by lateral compression with a barrier while monitoring the variation of surface pressure using a Wilhelmy plate. It is known that the surface pressure is the difference in the surface tension of pure water exposed to air and the water contact with the spread polymer phase. The molecular orientation, ordering, and packing of the LB monolayer is determined by the extent of lateral compression and deposited molecular characteristics.[89]

For diverse amphiphilic block copolymers, from linear to branch structure (e.g., brush, star, hyperbranched polymers), the surface aggregation behavior at air-water interfaces have been demonstrated (Figure 1.7).[34,75, 90 ,94,164] It is known that the polymeric amphiphiles associate into a variety of micelles (i.e., sphere, rod, and lamella) depending on molecular composition and relative block length on the water surface, which is called a surface micelle (Figure 1.6 and 1.7). Upon deposition of polymer amphiphiles, the hydrophilic chains dissolve or spread at the air-water interface depending on varying pressures, while collapsed hydrophobic chains on top of hydrophilic domains continue submerging molecules into the water subphase by anchoring on water surface.

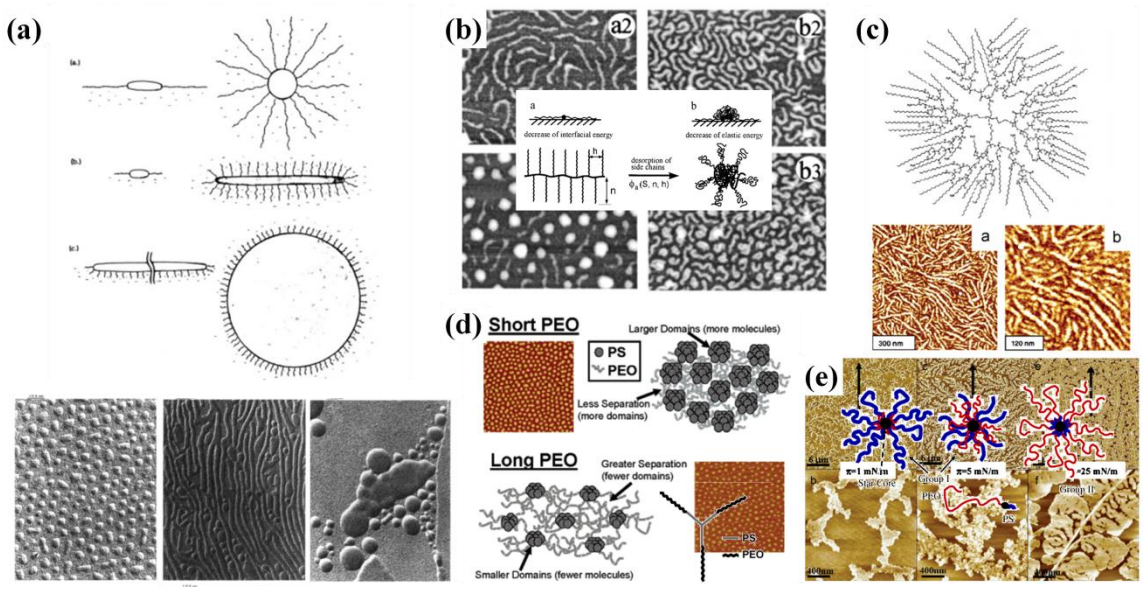

Figure 1.7: The surface micelle structures and aggregation behavior in the LB films of different (linear and branched) amphiphilic polymers: (a) schematic representation and TEM images of the variable surface micelles (starfish, rod, planar) of linear poly(styrene*b*-4-vinylpyridinium decyl iodide).[94] (b) Phase transitions (AFM images) of cylindricalbrushes of poly(n-butyl acrylate) (PBA).[90] (c) Nanofibric structures (AFM images) of amphiphilic dendritic hyperbranched polyester.[34] (d) Circular shaped surface aggregations (AFM images) and proposed models of the domain structures of three-arm polystyrene-block-poly(ethylene oxide) stars.[75] (e) AFM images of the surface dendritic structures of amphiphilic heteroarm poly(styene-ethylene oxide) star copolymers.[164]

The interesting molecular transition from "pancake" (or starfish) to "brush" (jellyfish) of the surface micelles as indicated by a broaden breadth of the plateau on the 2D isotherms was of intensive research interest for different molecular parameters, such as composition, hydrophobic-hydrophilic balance, and block ratio at varying surface pressures. In this regime, it was experimentally and theoretically demonstrated that the formation of quasi-two dimensional structures from two dimensional surface micelles is an entropically favorable process in molecular conformation.[91,92,93,94,95,96] For polymer brushes, for example, poly(butyl acrylate) cylindrical brushes, intriguing molecular transitions were investigated as a function of arm length and density, and spreading coefficient at certain

surface pressures. The rod-like to globular conformational transition depend upon the degree of desorption of side branches at the interface and was more pronounced for a high grafting density and long side arms.[97]

Langmuir isotherms allow for the elucidation of local conformation of ionic blocks at the air-water interface as a function of the surface area available. The formation of vertically and laterally segregated nanostructures can be revealed by in-situ X-ray and neutron reflectivity as was probed for branched nanoparticles and monodendrons.[98,99] Langmuir isotherms and molecular area are collected and analyzed as the function of the number of arms and block sequences at different pHs. We expect that a decrease in the surface area available for the molecules at the interface should result in reorganization of the molecular conformation from partially submerged and spread P2VP blocks surrounding aggregated PS blocks. Crowding of the chains attached to a single point should modify surface behavior as compared to linear block copolymers and extend a condensed state of the monolayer. Although phase diagrams for star block copolymers have been found to be similar to those of linear block copolymers, as shown by Milner,[100] phase boundaries can be significantly shifted, promoting the formation of non-traditional morphologies at unusual compositions. These phenomena as well as the role of collapsed or expanded ionic chains are considered, taking into account various possible scenarios.

To this end, we consider amphiphilic star copolymers residing at the air-water interface which tend to adopt molecular conformations with ionic chains in close contact with the water sub-phase and hydrophobic arms forming individual elevated domains. For a star

polymer, ionic chains with modest water solubility can be spread on the water surface in a randomly coiled conformation beneath/next to hydrophobic domains or can be submerged into the water subphase. The occurrence of one of the two scenarios is controlled by chemical composition, the length of chains, the presence of specific terminal groups, the surface pressure, and pH environment. For example, hydrophilic end-functional groups allow the arms to "sink" into the water sub-phase, under even low surface pressure. Forced submerging of hydrophilic arms at high surface pressure could result in complete transformation of the microdomain morphology. The suppressed lateral aggregation of hydrophobic domains in star macromolecules and the reduction of their effective interfacial content due to their submerging should promote the formation of a circular morphology, even at unfavorable compositions. In addition, the ionization of the arms at the proper pH could result in additional arm sinking, which further promotes the formation of different morphologies.

1.1.5. Multilayer Assembly

Layer-by-Layer (LbL) assembly is a simple and versatile method for multilayer preparation from mutually interactive species. While LB assembly is limited to amphiphilic molecules, the LbL depositions are applicable to more diverse building components including polyelectolytes, nanoparticles, biomolecules, carbon materials, and micelles. LbL multilayers have well-defined thicknesses and "fuzzy" yet periodic layer structure through repeated alternating deposition of a pair of building elements by dipping, spin coating, or spraying without an expensive apparatus (Figure 1.8).[101]

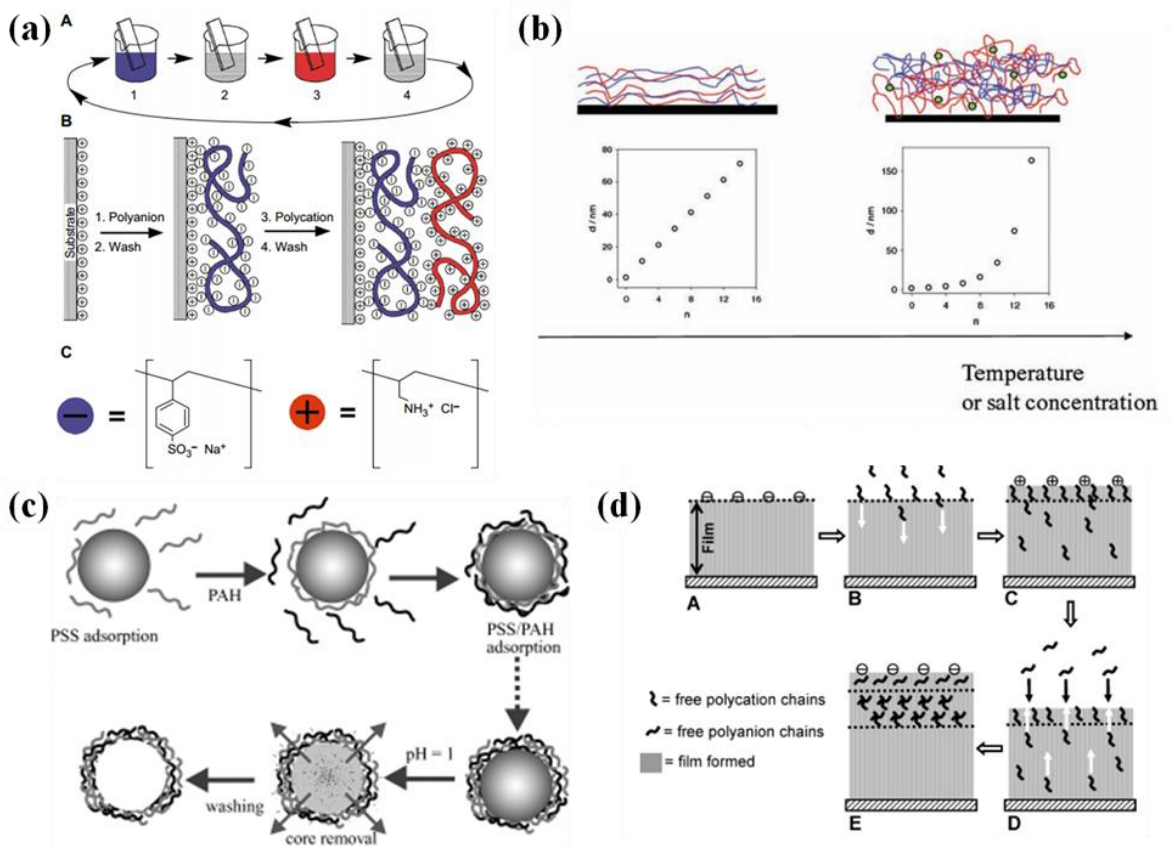

Figure 1.8: (a) LbL multilayer deposition process from polyanion and polycation using repeated alternating dipping and washing steps,[101] (b) two different growth mode and structure of multilayer films (linear (left) versus exponential (right); stratified (left) versus mixed (right)),[40] (c) preparation of hollow multilayer microcapsues by exposure colloidal sacrificial template to polyelectrolytes of alternating charge,[109] and (d) proposed of a buildup mechansion of polyelectolyte multilayer film based on "in-and out" diffusion.[105]

For example, the LbL films based on oppositely charged polyelectrolyte pairs can be buildup by sequential deposition of diluted polyelectrolyte solutions on desired substrates with rinsing steps after adsorption until a required thickness is achieved. It is known that the electrostatic LbL film growth can be made through charge overcompensation and reversal. Various interaction states and components have been used for LbL assembly

via electrostatic interaction, hydrogen bonding, metal coordinating interaction, charge transfer, click reaction, and step wised sol-gel reaction. LbL assembly can be extended from flat solid substrates to curved non-planar or porous solid substrates, for example, silica or polymeric microspheres for hollow multilayer microcapsules.[102]

The thicknesses of LbL films have been observed to grow in two different modes, known as linear or exponential buildup (Figure 1.8). The exponentially growing films show much thicker films at the same number of deposition cycles compared to linear growing films. A possible explanation is that linear growth occurs because complexation only occurs at the outer layer of the film whereas for exponentially growth, the adsorption occurs through the whole film thickness by diffusion in and out of films.[103,104] The diffusion can be driven by electrochemical potential difference in and out of films and such a fast exponential increase in mass is proportional to the accumulated mass prior to adsorption.

There is another critical issue that the exponentially growing films undergo a transition into a linear growth mode during LbL assembly due to the limited diffusion in certain regime of the film, not through the whole film thickness by a given deposition and rinsing time. The linear growing film exhibited a more stratified layered internal structure that was selectively permeable in contrast to the intermixed exponentially growing films exhibiting highly hydrated and porous properties.[40,105,106] The LbL thin films can find a variety of application including biomaterial coatings, membranes, biosensors, energy

conversion devices, and ultrastrong films. Also, the controlled growth modes and interactions will allow for the preparation of responsive and dynamic LbL films.

LbL films can also be prepared on non-planar substrates with different shapes or porosity. In particular, LbL microcapsules from spherical scarificial substrates offer an interesting material plateform (Figure 1.8).[107] The variety of sacrificial templates, which require a complete removal after deposition under mild dissolution conditions, include polystyrene latex, melamine formaldehyde, SiO_2, carbonate particles, and biological cells. The shell wall thickness is easily tailorable by varying deposition layer numbers and further functionalized by incorporating magnetic/metal nanoparticles, fluorescent dyes, and biomolecules. The shell permeability and porosity of the capsules can be tunable by pH, ionic strength, solvent, and shell thickness etc. The capsules consisted of a multilayer shell wall and the inner core can be used as a catalysis reservoir, carrier, or microreactor for applications in bioanotechnology, and medicine.[108,109]

LbL multilayered structures are assembled from star polymers by utilizing anionic and cationic star counterparts. We pay special attention to the lateral segregation in these structures with a chance to form ordered supramolecular microdomain networks for LbL films assembled from large, multiarmed star polyelectrolytes or star block copolymers with electrolyte arms. As known, LbL films usually demonstrate either uniform or random heterogeneous morphologies.[102] Ionic chain-containing star block copolymers with the ability to form ordered microdomain morphology are promising candidates for

forming ultrathin films. To induce lateral ordering in the course of LbL assembly, we considered the assembly of laterally segregated LbL films by incorporating hetero-armed star block copolymers as unimolecular micelles and a stabilized microdomain network by metallization within ionic blocks (e.g., gold nanoparticles reduction within P2VP blocks).[110,111,112,113]

To date, very few LbL films were reported for star polymers with weak ionic strength such as poly(acrylic acid) (PAA) and poly[2-(dimethylamino)ethyl methacrylate] (PDMAEMA). Multilayer thin films, using brush polymer as a building block, have been reported to have been fabricated from linear poly(vinylpyrrolidone) (PVPON) and a spherical polymer brush of PAA with an inorganic precursor core for hair chains based on hydrogen bonded LbL.[114] Qia et al. presented PAA star polymer LbL assemblies with pH-responsive behavior.[115] Recently, Hammond and coworkers have demonstrated star/star polyelectrolyte LbL multilayers from PDMAEMA and PAA stars.[64] However, the resulting star/star LbL films showed non-uniform morphologies and dewetting due to weak ionic cross-linking which might be overcome by the selection of a larger number of arms and increasing their length.

LbL multilayers are considered a promising multifunctional material concept. However, some challenges in theoretical and practical applications still need to be solved: The viscoelastic properties related to mechanical strength and stability, dynamic exchange process and growth mechansim, and predictable charge potential of the interface in

design of multiresponsive materials for use in self-healing coatings or reversible nanovalves. For the multilayer microcapsules, we need to address critical questions involving the fine tuning of permeability for controlled encapsulation and release of active functional payloads, biocompatible or biodegradable, and control over core-shape, and enhanced specific recognition and adhesion of capsule surfaces towards biomimetic multicompartmentalized carriers or cages of DNA, and templates for polymerization or biomineralization.[44,116]

1.2. Motivation

The integration of multiple functionalities within organic and inorganic nanostructures promotes the manufacturing of complex branched nanomaterials with unmatched properties.[117] The unique properties seen in highly branched molecular systems, such as star, dendrimers, and hyperbranched molecules, arise from their molecular characteristics caused by chain-crowding and confinements, few entanglements, an available internal-cavity, and abundant terminal groups.[118]

Star block-copolymers, representing the popular form of branched architecture, are composed of linear chains tethered to a single junction point with the grafting density characterized by the number of arms. In contrast, dendrimers possess tree-like architecture, with sizes that are defined by their generation number. Finally, hyperbranches are a class of one-pot synthesized branched molecules that have less-defined molecular structure and a high polydispersity. Novel properties in polymeric systems are associated with branched architectures where branching can have interesting

effects on their bulk structures, surface behavior, and phase separation in multi-component systems.

Research activities in the field of branched polymers, centered around designing new architectures, resulted in the appearance of a wide spectrum of novel highly branched molecules including dendrimers, star block copolymers, branched brushes, hyperbranched molecules, and different combinations of branched and linear fragments (dendronized rods, discs, and stems).[119] The critical role of chemical architecture has been demonstrated by comparing dendritic or branched structures to linear polymers.[120] Currently, the focus of the research has somewhat shifted from synthetic efforts towards a deeper understanding of the physical properties and structures of these molecules particularly at surfaces and interfaces.[45] An understanding of the behavior of branched polymers at engineered surfaces and interfaces is ultimately beneficial for optimum designs in energy harvesting organic solar cells, organic light emitting diodes, and high-performance nanocomposites.[121,122,123] For example of solar cell applications, a high number of light absorbing or photoactive units at the periphery results in greater light-to-energy conversion and an introduction of branching can be beneficial for light emission.[124] For light-emitting materials, the presence of a branching point as a point-defect interrupting the backbone conjugation has been suggested as an efficient way to diminish intra/intermolecular charge transfer in order to increase photoluminescent efficiency.[125]

Highly-branched polymer has recently emerged as a promising building block for adaptive/responsive functional coatings and films to create miniaturized polymer thin film devices. Integral and robust nanostructures from branched architectures, however, require their controlled spatial ordering and precise physical/chemical modulation at the surface and interface. This approach will present a promising strategy to fabricate organized ultrathin polymer film and coating materials for future applications in bio-interface, sensing and actuator platforms.

CHAPTER 2

GOALS AND OBJECTIVES

2.1. Goals and Research Focuses

In this study, we focus the directed assembly of star-shaped polymers (star block copolymers and star polyelectrolytes) and primarily discuss their chain structure and phase transformation in nanoscale ultrathin films at various surfaces and interfaces, such as air-water, air-solid, water-polymer, air-polymer, polymer-polymer, and polymer-graphene oxide interfaces. The aggregation behavior, morphological properties, and microstucture of star polymer-based mono/multilayer ultrathin films are explored with an emphasis on surface effects and molecular confinement using LB and LbL deposition techniques. A comprehensive surface analysis would enable us to establish a structure-property-assembly relationship for these complex architectures. The responsive assembly behavior is studied from the viewpoint of adsorption, diffusion, and conformation of highly-branched molecular architectures as a function of morphology, number of arms, arm length, and nature of interactions. These efforts are expected to offer a design strategy for fabrication of stimuli-responsive functional ultrathin nanostructures for prospective applications in biosensing, self-healing coatings, drug delivery, tunable catalysts, and imaging.

The ultimate goal of the work presented in this dissertation is to understand the fundamental principles of the directed assembly of novel star-shaped polymers with a focus on complex architectures with ionic blocks capable of dramatic conformational

changes under external stimuli. Specifically, we study two different classes of star-shaped polymers, including star amphiphilic block copolymers (s-BCP) and star polyelectrolytes (s-PE) at various surfaces and interfaces as presented in detailed in Scheme 2.1.

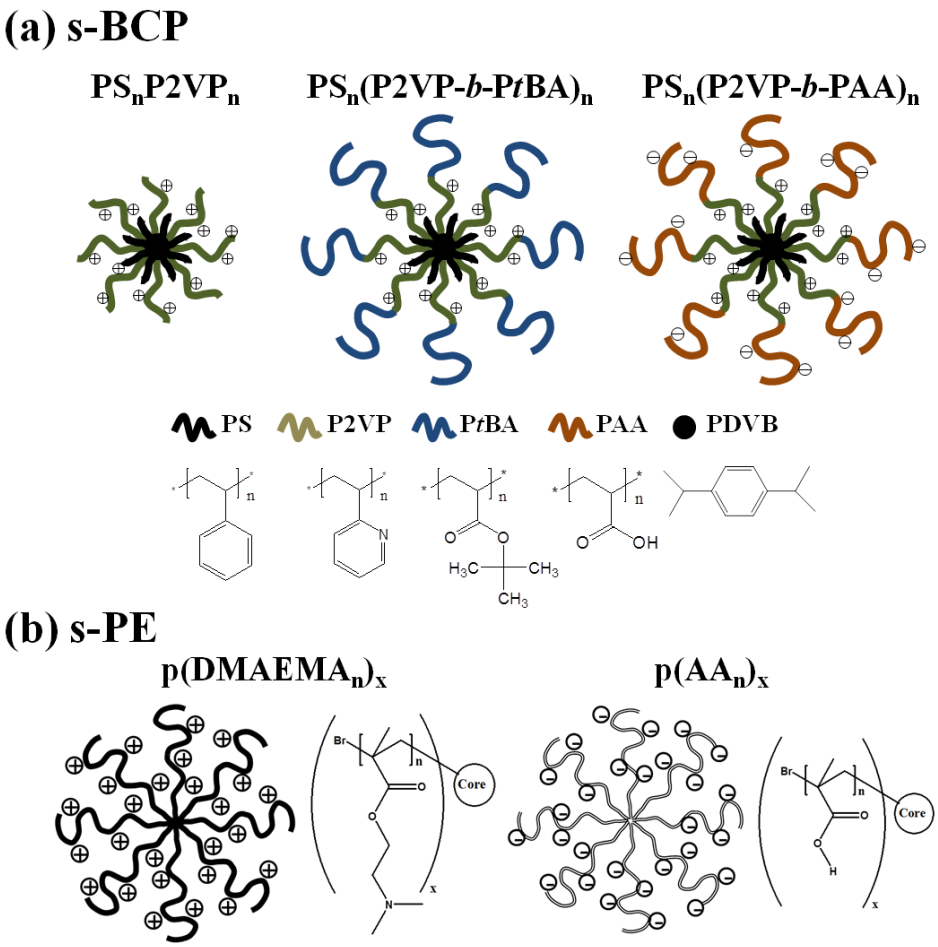

Scheme 2.1: (a) Star-shaped block copolymer (s-BCP): PS_nP2VP_n amphiphilic heteroam star copolymer, $PS_n(P2VP\text{-}b\text{-}PtBA)_n$ amphiphilic heteroam star terpolymer, $PS_n(P2VP\text{-}b\text{-}PtBA)_n$ amphoteric heteroam star terpolymer (n denotes arm number) (b) star-shape polyelectrolyte (s-PE): cationic $p(DMAEMA_n)_x$ star polyelectrolyte and anionic $p(AA_n)_x$ star polyelectrolyte (n denotes degree of polymerization; x denotes arm number).

A set of star polymers studied here includes pH-sensitive amphiphilic heteroarm star copolymers, star block terpolymers with hydrophobic ends, and star polyampholytes possessing zwitteric diblock arms, and pH and salinity responsive weak polycationic and polyanionic star polyelectrolytes. These star polymers can be forced through molecular phase segregation and intermolecular interactions into well-defined ultrasoft nanoparticles, nanogels, quasi two dimensional circular micelles, core/shell type single molecular micelles, pancake & brush micelles or Janus-like molecular particles in assembled ultrathin films as will be discussed later.

The significance and novelty of this approach is in elucidating the effects of surface and interface energetics and confinements on the molecular conformation and interaction of these highly-branched well-defined supermolecules with a crowding compact structure. The advanced branch and multicompositional molecular design, in combination with integrated adaptive/responsive chain segments, represents a powerful approach to control the lateral diffusion and phase segregation of novel functional branched building blocks on the surface resulting in generating tunable and ordered complex structural nanodomains in monomolecular thin films, as well as to tailor their stratified layered nanostructures with capabilities for switchable morphological heterogeneity and multicompartmental structures.

As compared to traditional linear polymers, however, the limited interdiffusion and entanglement, compact structure, multiple free ends, and repulsive interactions of stronger stretched arms of non-linear highly-branched molecular architectures, in

particular when confined at surface, pose a great challenge facing the construction of flexible but stable two-dimensional (2D) supramolecular assembly in quasi-equilibrated thermodynamic system. In this respect, the profound understanding of chain conformation, interaction, and phase transformation in the ultrathin films (from monomolecular to multilayer assembly) is of great necessity in order to realize structural hierarchy and responsive property.

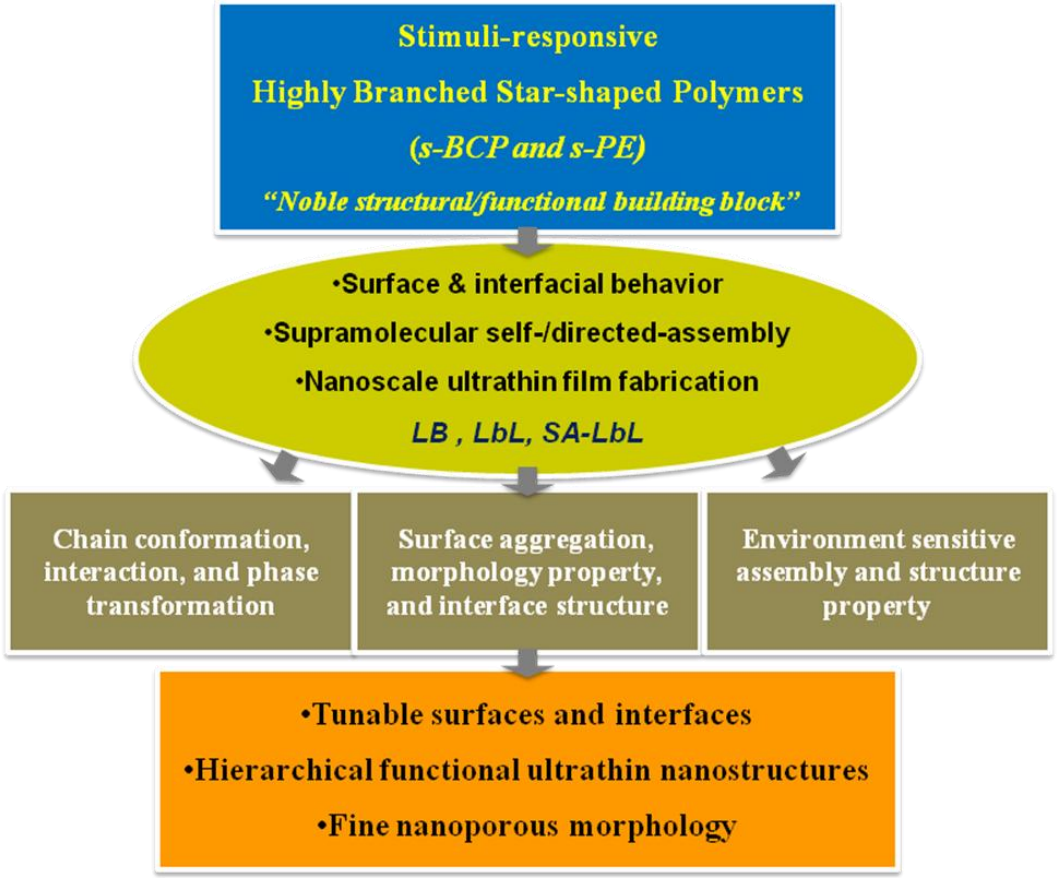

Scheme 2.2: Conceptual diagram investigating the structure-property-assembly relationship of highly-branched star-shaped polymers.

Therefore, we address a fundamental question of *how the* ***chemical composition*** *and* ***architecture*** *of different highly-branched entities influence their* ***assembly behavior*** *and*

intra/intermolecular interactions *under variable environmental and confined interfacial conditions. The* ***self-/directed-assembly behavior*** *of stimuli-sensitive highly-branched molecules at the interface has been explored with a focus on the* ***controlled interfacial organization*** *and* ***tunable complex morphology*** *for the fabrication of hierarchical functional nanofilms (Scheme 2.2).*

The key technical focuses of the work presented are:

1. Morphology, microstructure, and microdomain organization of ionic and non-ionic blocks grafted to a single center in star block copolymers at air-water and air-solid interfaces as a function of the number of arms, chemical composition, environmental conditions, and star architecture;
2. Surface behavior of star block copolymers which differ in architecture, molecular weight, arm length, nature of ionization, and number of arms on planar and templated functionalized surfaces with tailored intermolecular interactions and topography under variable environmental conditions (pH variation and salt-initiated formation of nanoparticles), which can tune the conformation of ionic blocks;
3. Understanding interfacial aggregation behavior and intra/intermolecular interaction of amphoteric arm containing star terpolymer amphiphiles for an extended pH region at the air-water and air-solid interface;
4. Examination of the feasibility of *in-situ* gold nanoparticle growth at the confined liquid-solid interface using ionizable pyridine containing heteroarm star copolymers as a template;

5. pH-tunable LbL growth behavior of star polycationic polyelectrolytes with variable molecular weights and number of arms as compared to their corresponding linear counterparts as a function of deposition pH, number of layers, and the method of assembly;
6. Fabrication of multilayer hollow microcapsules prepared from star polymer core/corona unimicelles using a sacrificial template with a curved surface and characterization of the porous shell structure and permeability using confocal fluorescence microscopy and small angle neutron scattering;
7. Study of adsorption, spreading, and assembly properties of star unimicelles, and demonstrate confinement of branched arms on heterogeneous graphene oxide surfaces compared to water surfaces by investigation of molecular transformation and interactions on a Langmuir trough.

2.2. Overview of Dissertation Contents

Chapter 1 presents a critical review of the literature relevant to the field of surpramolecular assembly of highly branched molecules and responsive surface behavior. The chapter highlights the significance of current issues to be addressed and and raises fundamental questions that need further investigation.

The current chapter (**Chapter 2**) addresses the ultimate goals and specific technical objectives in this dissertation. It also includes an overview and organization of the entire dissertation.

Chapter 3 describes key experimental characterization techniques employed in this dissertation in detail. Characterization methods in these studies presented here include ellipsometry, atomic force microscopy, confocal laser scanning microscopy, and small angle neutron scattering, and transmission electron microscopy. Specific experimental techniques used and detailed experimental description are further included for the particular chapter presented.

Chapter 4 presents the surface behavior and morphologies of two series of pH-responsive amphiphilic heteroarm star block copolymers. In this respect, we studied polystyrene/poly(2-vinylpyridine)/poly(*tert*-butylacrylate), $PS_n(P2VP\text{-}Pt BA)_n$, heteroarm star block terpolymers and their precursors, PS_nP2VP_n, star copolymers. These star block polymers differ in architecture (copolymer vs terpolymer), block topology and arm length (molecular weight of P*t*BA segments varies from 8 900 and up to 15 250), and number of arms (n = 9, 22, and 28). The π-A isotherms at different subphase pH (pH = 5.8 and 2.0) exhibited strong pH dependence leading to different limiting molecular area and surface micelle stability. Due to the pH-induced ionization of the P2VP block, the surface morphology of star copolymers bearing the free P2VP arms was strongly dependent on the pH of the subphase, while the star terpolymers containing the protonated hydrophilic P2VP block as midblocks maintained the same circular morphology at low pH and high pressures. The surface morphologies suggested that the high number of arms promoted the formation of unimolecular micelles which are stable under different fabrication conditions.

Chapter 5 describes the pH-controlled surface behavior of amphiphilic heteroarm star block terpolymers, (n = number of arms, 9 and 22), bearing amphoteric diblock arms with varying polyvalent ionic charges (i.e. negative, positive, and zwitterionic) at the air-water and air-solid interfaces. We investigated the assembly of these pH-sensitive star terpolymers in Langmuir and LB monolayers under different pH conditions of the subphase. The π-A isotherms acquired at variable pH conditions revealed a distinct aggregation behavior of surface micelles which is dependent on the ionization of the polyelectrolyte blocks and the number of arms. The star block copolymer with a small number of arms (n=9) was found to exhibit a strong pH-dependent phase transformation under compression. The pH responsive (zwitterionic) behavior results in changes in surface morphologies from circular micelles to complex labyrinth structures. In contrast, star polymers with a larger number of arms (22) and a crowded branched architecture show stable circular domain morphology without the internal reorganization under variable conditions. The observed variety of surface behaviors is attributed to the fine balance of intramolecular interactions caused by the highly branched chain architecture composed of both acidic and basic blocks.

In **chapter 6**, we report on the growth of gold nanoparticles in polystyrene/poly(2-vinyl pyridine) (PS/P2VP) star-shaped block copolymer monolayers. These amphiphilic PS_nP2VP_n heteroarm star copolymers differ in molecular weight (149 000 and 529 000 Da) and number of arms (9 and 28 arms). LB deposition was utilized to control the spatial arrangement of P2VP arms and their ability to reduce gold nanoparticles. The PS_nP2VP_n monolayer acted as a template for the gold nanoparticle growth due to their

high micellar stability at the liquid-solid interface, uniform domain morphology, and ability to adsorb Au ions from the water subphase. UV-vis spectra, AFM, and TEM images confirmed the formation of the individual gold nanoparticles with an average size of 6 ± 1 nm in P2VP-rich outer phase. This facile strategy is critical for the formation of ultrathin polymers-gold nanocomposite layers at large surface areas with confined, one-sided positioning of gold nanoparticles in an outer P2VP phase at polymer-silicon interfaces.

The unique LbL assembly behavior of pH-sensitive star-shaped polyelectrolytes with both linear and exponential growth modes controlled by star architecture and assembly conditions is addressed in **chapter 7**. We demonstrated the LbL growth behavior of cationic poly[2-(dimethylamino)ethyl methacrylate] and anionic poly(acrylic acid) stars as a function of deposition pH (ranging from 5 to 7), number of layers (up to 30 bilayers), and the method of assembly (dip- vs spin-assisted LbL). The spin-assisted LbL assembly makes it possible to render smoother and thinner LbL films with parameters controlled by the shear rate and pH conditions. In contrast, for dip-assisted LbL assembly, the pH-dependent exponential growth was observed for both linear and star polyelectrolytes. In the case of linear/linear pair, the exponential buildup was accompanied with a notable surface segregation which resulted in dramatic surface non-uniformity, "worm-like" heterogeneous morphology, and dramatic surface roughening. In contrast, star/linear and star/star LbL films showed very uniform and smooth surface morphology (roughness below 2.0 nm on the scale 10 μm x 10 μm) with much larger thickness reaching up to 1.0 μm for 30 bilayers and rich optical interference effects. Star polyelectrolytes with

partially screened charges and high mobility caused by compact branched architecture appear to facilitate fast diffusion and exponential buildup of LbL films.

Chapter 8 presents the LbL assembly of amphiphilic heteroarm pH-sensitive star-shaped polystyrene/poly(2-pyridine) (PS_nP2VP_n) block copolymers to fabricate porous and multicompartmental microcapsules. Pyridine-containing star molecules forming a hydrophobic core/hydrophilic corona unimolecular micelle in acidic solution (pH 3) were alternately deposited with oppositely charged linear sulfonated polystyrene (PSS), yielding microcapsules with LbL shells containing hydrophobic domains. The surface morphology and internal nanopore structure of the hollow microcapsules was comparatively investigated for shells formed from star polymers with a different numbers of arms (9 versus 22) and varied shell thickness (5, 8, and 11 bilayers). The successful integration of star unimers into the LbL shells was demonstrated by probing their buildup, surface segregation behavior, and porosity. The larger arm star copolymer with stretched conformation showed a higher increment in shell thickness due to the effective ionic complexation whereas a compact, uniform grainy morphology was observed regardless of the number of deposition cycles and arm numbers. Small angle neutron scattering (SANS) revealed that microcapsules with hydrophobic domains showed different fractal properties depending upon the number of bilayers with a surface fractal morphology observed for the thinnest shells and a mass fractal morphology for the completed shells formed with the larger number of bilayers. Moreover, SANS provides support for the presence of relatively large pores (about 25 nm across) for the thinnest shells as suggested from permeability experiments. The formation of robust microcapsules with

nanoporous shells composed of a hydrophilic polyelectrolyte with a densely packed hydrophobic nanoscale domain based on star amphiphiles represents an intriguing and novel case of compartmentalized microcapsules with an ability to simultaneously store different hydrophilic, charged, and hydrophobic components within shells.

In **Chapter 9**, we discuss the interfacial assembly of amphiphilic heteroarm star copolymers (PS_nP2VP_n and $PS_n(P2VP\text{-}b\text{-}PtBA)_n$ (n = 28 arms)) on graphene oxide flakes assembled at the air/water interface. Probing spreading, adsorption, and ordering of star polymer surface micelles on the basal plane and edge of in-plane amphiphilic monolayer graphene oxide was investigated by sequential deposition on a Langmuir trough. This interface-mediated assembly approach resulted in polymer micelle decorated graphene oxide platelets with controlled binding and organized morphology as revealed by high resolution AFM. We found that the unique surface activity of solvated graphene oxide sheets enables star polymer surfactants to subsequently adsorb on the pre-suspended graphene oxide sheets, thereby producing a bilayer hybrid nanofilm. The positively charged heterocyclic pyridine containing star polymers exhibited strong affinity onto the basal plane and edge of graphene oxide, leading to a well-organized discrete micelle assembly with no large scale aggregation. The preferred binding behavior and extent of coverage was tuned by controlling assembly parameters such as concentration and solvent polarity, as well as dependent upon multi-arms conformation. The surface unimicelles on the basal plane of graphene oxide remained incompressible under lateral compression in contrast to ones on the water surface due to limited arm transformation on the attractive surface of graphene oxide. The densely packed, stable biphase tile-like

morphology was evident suggesting the interfacially stable and mechanically stiff nature of graphene oxide sheets. This non-covalent assembly at fluid interface represents a facile route for the control and fabrication of graphene oxide-inclusive ultrathin hybrid films for catalyst template and sensing platform.

Chapter 10 finalizes the dissertation work with general discussion and conclusions, and further addresses research impact and future perspectives.

CHAPTER 3

EXPERIMENTAL DETAILS

This chapter provides an overview of experimental details related to sample preparation procedure, characterization techniques, and instruments used throughout this work. Specific experimental techniques and procedures are presented in more detailed in the following each chapter.

3.1. Synthesis and Fabrication

3.1.1. Synthesis of Highly Branched Star-Shaped Polymers

The $PS_n(P2VP\text{-}Pt BA)_n$ heteroarm star block terpolymers were synthesized by a multi-step, one pot, sequential anionic living polymerization procedure following the "in-out method" by Tsitsilianis group (University of Patras, Greece) [126,127] According to this routine, the first generation of PS arms were formed in the first step by reacting sBuLi with styrene. These "living" linear PS chains were used in a subsequent step to initiate the polymerization of a given amount of divinylbenzene (DVB) acting as a crosslinking agent. A living PS star-shaped polymer was thus formed bearing within its polyDVB core, an equal number of active sites with its arms. In the third step, a second generation of arms was grown from the core upon the addition of 2VP. Part of the reaction medium was sampled out and the PS_nP2VP_n precursor was isolated and characterized. In the remaining solution, the sites located now at the ends of the second generation of P2VP arms are "living" and was used to polymerize the third monomer (*t*-BA) leading to $PS_n(P2VP\text{-}Pt BA)_n$ heteroarm star block terpolymer. All samples have been characterized

by a combination of gel permeation chromatography, ^{1}H NMR, and light scattering in accordance with the approach published elsewhere.[74] The $PS_n(P2VP\text{-}b\text{-}PAA)_n$ heteroarm star block terpolymers were synthesized according to a previous procedure reported elsewhere [46,70,128]

Star-shaped p(DMAEMA) and p(AA) were synthesized via ATRP in a core-first approach by Müller group (Univeristy of Bayreuth, Germany).[37, 129, 130] As multifunctional initiators either saccharose-, cyclodextrin-, or silsesquioxane-based cores functionalized with 2-bromoisobutyryl groups were used. The detailed synthesis and characterization of these initiator molecules is given in the above references. For the linear polymers we used ethyl 2-bromoisobutyrate (EBIB) as the initiator. The number of arms was determined by cleaving off the arms from the core.[37] For this experimental research, all star polymer samples were provided from collaboration works.

3.1.2. LB Film Fabrication

The LB studies are conducted using a KSV2000 mini-trough, according to the standard procedure adapted in our lab.[131] 40-120 µL solutions (usually, chloroform (HPLC grade)) are prepared and dispersed evenly onto the surface of the water. Compression of the monolayers is conducted at a speed of 5 mm/min. The limiting cross sectional area A_0 is determined by the steepest rise in the surface pressure which evidenced the formation of a condensed monolayer.[132] Monolayers at the air-water interface can be transferred onto a substrate for further characterizations.

A 0.5-0.10 mg/ml concentration of solution composed of a star polymer sample dissolved in a nonselective solvent of chloroform/methanol mixture (90/10 % in vol/vol) (HPLC grade) was prepared. The LB minitrough was next filled with Nanopure water. The pH of the water subphase was adjusted by using hydrochloric acid without a buffer system. The 60-120 μL polymer solution was dispersed in several droplets evenly onto the surface of the water. It was then left for 30 minutes to allow for the evaporation of the chloroform. Compression of the monolayers was conducted at a speed of 5 mm/min. The Langmuir monolayers were transferred from the air-water interface by vertically pulling out the substrate submerged in the water subphase at a rate of 2 mm/min. The limiting cross sectional area A_0 was determined by the steepest tangent rise in the surface pressure, which evidenced the formation of a condensed monolayer.[132]

3.1.2. LbL Film and Microcapsule Fabrication

LbL assembly will be applied to fabricate multilayered films from water-soluble star block copolymers with ionic-blocks.[39] Spin-assisted LbL films were prepared by using sequential spin-casting at different rpm for 20 sec and rinsed twice between depositions of polyelectrolyte solution under the same condition in accordance with usual procedure in our lab.[133,134] Subsequently, LbL films were spun for 1 min to remove water under dry nitrogen and further dried at room temperature for 48 hrs before experimental measurements. The dip-assisted LbL process was performed by alternate immersion of the substrates in polyelectrolyte solutions for 10 min, followed by rinsing three times with the same pH buffer solution. The LbL hollow microcapsules were prepared using silica microsphere core (4.0 ± 0.2 μm in diameter, Polyscience, Inc.) as a sacrificial

template. The silica cores were alternately immersed in 0.2 mg/ml polymer solution at pH 3 via repeated deposition cycles. The assembly of each polymer layer was conducted for 15 min with constant shaking. The microcapsules were precipitated by centrifugation at 2,000 rpm for 2 min to separate solid and supernatant, and then the collected capsules were rinsed three times with 0.01 M TrisHCl buffer solution at the same pH. The assembly/washing cycle was repeated until a desirable thickness of the capsule was obtained. The silica cores were removed using diluted 0.2 M hydrofluoric acid (HF) at pH 3. To obtain hollow capsules the core dissolution process was repeated three times to ensure that the silica core was completely removed.

3.2. Characterization Techniques

A wide range of characterization techniques are employed for the comprehensive surface and structure analysis to study the relevant physical and chemical properties of prepared ultrathin films.

3.2.1. Ellipsometry

Measurement of the film thicknesses and refractive indices were carried out with a Woollam M2000U (J.A. Woollam Co, Inc., Lincoln, NE) multiangle spectroscopic ellipsometer with a WVASE32 analysis software for three incident angles 65, 70, and 75°. The Ψ (polarized angle) and Δ (phase) values were measured and used to construct a Cauchy model to determine the optical constants *n* and *k* over wavelengths 245 to 1000 nm (Figure S1). These data were used to determine the thickness of the LbL films by fitting the data to the Cauchy approximation using a multilayer structure model composed

of silicon, silicon oxide, and the LbL film of interest. The thickness of silicon and silicon oxide (n = 1.46, native thickness 2.0 nm) was predetermined prior to deposition of polyelectrolyte LbL film from the well known reflective index. The LbL film thickness data was fit to the Cauchy model where the reflective index is given as $n(\lambda) = A_n + B_n/\lambda^2 + C_n/\lambda^4$ with A_n= 1.45, B_n= 0.01, and C_n= 0.0 as a function of λ. For sufficiently thick films, thickness (>300 nm thickness) was determined using fitted Cauchy constants obtained from Ψ and Δ of measured films. The mean squared error (MSE) for data fitting was in range of 5-25. Thickness measurements were conducted on at least three different homogeneous surfaces for each sample showing standard deviation within ±8% level.

3.2.2. Atomic Force Microscopy (AFM)

The morphology of ultrathin films were probed under ambient conditions in air using a Dimension 3000 atomic force microscope (AFM) (Veeco Inc.). For quantitative analysis of surface topography, AFM images were obtained in the "light" tapping mode with an amplitude ratio within 0.90-1.00 to avoid surface damage and deformation.[135,136] The AFM cantilevers had spring constants in the range of 40-60 N/m. Scanning rates were between 1.0-2.0 Hz, depending on the scan area which ranged from 10 μm x 10 μm to 1 μm × 1 μm.[137] Electrostatic force images were obtained with a Bruker Icon AFM using a p-doped silicon cantilever with a spring constant of 3N/m and resonant frequency of 65KHz.[138] Adhesion maps, modulus and deformation maps were obtained using the 'Quantitative Nanomechanical Measurements' (QNM) mode on the Bruker Icon AFM using similar probes as used for EFM measurements.[139]

3.2.3. Confocal Laser Scanning Microcoply (CLSM)

Confocal images of LbL hollow microcapsules were acquired by a LSM 510 VLS META inverted confocal laser scanning microscope equipped with a 63 × 1.4 oil immersion objective lens (Zeiss). Excitation/emission wavelengths of 488/515 nm were used. A small volume of a dispersion of hollow capsules were placed into Lab-Tek chambers (Electron Microscopy Sciences) and then analyzed after they settled. To investigate capsule permeability to FITC-dextrans, hollow capsules were added to several Lab-Tek chambers, which were then half-filled and mixed with FITC-dextran solutions. To confirm the alternating assembly of polymer pairs on the silica core, the surface potentials were monitored on Zetasizer Nano-ZS equipment (Malvern).

3.2.4. Transmission Electron Microscopy (TEM)

TEM was performed on JEOL 100CX-2 electron microscope and operated at 100 kV to analyze characteristic of the gold nanoparticles. The samples for TEM have been prepared by using LB technique on gold grids coated with a carbon support layer. The particle size was calculated from TEM images using ImageJ 1.43u software (National Institute of Health) by following regular image analysis procedure.

3.2.5. UV-Vis and Raman Spectroscopy

UV-vis spectroscopy measurements were conducted on a Craic QDI 202 microscope spectrophotometer attached to a Leica microscope (Leica DM4000M) with a 50x objective or with a UV-2450 spectrophotometer (Shimadzu). The Raman mapping was

performed with a WITec (Alpha 300R) confocal Raman microscope using an Ar + ion laser (λ = 514.5 nm) as an excitation source according to usual procedure. The spectrum was obtained using a 600 grooves mm^{-1} grating with a spectral resolution of 5 cm^{-1}.[140]

3.2.6. Small Angle Neutron Scattering (SANS)

Small-angle neutron scattering (SANS) and neutron reflectivity at Oak Ridge National Lab (ORNL) were utilized to reveal inner organization of hybrid nanostructures. To reveal information about the compact or swollen states of branched nanostructures (expected diameter from 3 nm to 100 nm), we applied SANS in mixed, variable contrast aqueous-deuterated solutions. The feasibility of SANS to study the complex nanostructures is supported by earlier studies. For instance, SANS was applied for characterization of silver nanoparticles[141] and for gold nanoparticles formed inside dendrimers.[142,143] SANS allows the study of polymer chain conformation in aqueous solutions *e.g.*, the PEO or PAA or P2VP chains of star block copolymers.[144] SANS provides an insight into the polymer/polymer interactions in a range of physical states as demonstrated by Melnichenko *et al*.[145]

All samples were measured in D_2O to minimize the incoherent backscattering and increase contrast for hydrogenated shells.[146] For the 22 arm star polymer, the microcapsules with different shell thickness (5, 8, and 11 bilayers) in hydrogenated water were treated with deuterated water (D_2O) that was adjusted to pH3 using 0.1 M HCl. To minimize the mixing of H_2O, the D_2O exchange was repeated three times using the centrifugation method. The final capsule concentration was sufficiently dilute to

minimize capsule-capsule scattering effects. This reduces the complexity of data fitting by eliminating the effects of a structure factor (i.e. $S(q) \approx 1$). Samples were loaded into 1mm path length 'banjo' style quartz cuvettes (Hellma USA, Plainview, NY). All SANS measurements were made at room temperature (22°) on the Extended-Q Small Angle Neutron Scattering (EQ-SANS) instrument of the Spallation Source at Oak Ridge National Lab (ORNL).[147]

The time-of-flight instrument was operated in 30 Hz (frameskipping) mode using a minimum wavelength, λ, of 2.5 Å, yielding two bands of neutrons (2.5-6.1 Å and 9.4-13.4 Å). A sample to detector distance of 4 m was used, resulting in a q-range of approximately 0.0035 to 0.45 $Å^{-1}$, where "q" is the momentum transfer vector defined as $q = (4\pi/\lambda)\sin(\theta/2)$ and θ is the scattering angle, which probes dimensions on the order of 10-1500 Å (distance = $2\pi/q$). Data correction for proton charge normalization, wavelength-dependent flux and sample transmission, background, detector sensitivity and instrument dark current (cosmic radiation and electronic noise) followed the standard procedures implemented in MantidPlot (http://www.mantidproject.org/). Azimuthally-averaged intensity profiles from the two neutron bands employed were merged using the routine implemented in MantidPlot. To convert the data into absolute units (1/cm) an absolute intensity calibration was conducted using a calibrated standard, which in this case was Porasil B in a 1 mm pathlength quartz cuvette.[148] Non-linear fitting of experimental data was conducted using the SANSView (http://danse.chem.utk.edu/sansview.html).

CHAPTER 4

SURFACE BEHAVIOR OF PS_n(P2VP-*b*-P*t*BA)$_n$ HETEROARM STARS

4.1. Introduction

Branched macromolecules have been widely used for studying ultrathin films because of their unique and diverse chain architectures as compared to their corresponding linear counterparts. Star-shaped polymers belong to the class of branched organic materials which includes dendrimers, hyperbranched, and dendronic molecules.[16] They have a molecular structure composed of a number of peripheral arms chemically bonded to a single core.[149,150, 151] Recently, star shaped block copolymers have gained a considerable attention in terms of micelle aggregation and microphase separation in bulk, solution, and at the surface and interface as a result of their well-defined macromolecular architecture.[152, 153, 154, 155] For example, heteroarm star copolymers, (also called miktoarm polymers) consist of an equal number of two different pure arms (A_nB_n).[128,126,127,156, 157, 158] The crowding of chains and multiple chain ends of these star copolymers account for their unique micellization behavior with diverse physical and chemical properties. [159, 160, 161, 162, 163, 164, 165]

The surface morphology of star block copolymers is controlled by a variety of factors such as the number of arms, degree of polymerization, composition, and chain architecture.[163,164,165] Accordingly, studies on their interfacial properties can offer more information on the structure-property-assembly relationship of ultrathin film formation.

In the end, such an effort will lead to their potential applications in advanced functional systems such as ultrathin coatings, sensors, and drug carriers, for which responsive properties to external stimuli (e.g. pH, thermo, and shear) are required.[80]

Polystyrene/poly(2-vinylpyridine) (PS_nP2VP_n) heteroarm star copolymers synthesized via the "in-out method" with pH sensitive ionizable P2VP segments showed associative properties in the solution state in the presence of toluene, which acts as a selective solvent. They were considered to be unimolecular micelles below the critical micelle concentration (cmc) and formed supermicelles above the cmc adopting a spherical shape with a core-shell structure.[157, 127] When compared with corresponding linear counterparts, these heteroarm star copolymers showed three orders of magnitude higher cmc and an order of magnitude lower aggregation number. This was attributed to thermodynamically less favorable conditions to form micellar associates as indicated by a positive Gibbs energy at higher temperatures. The effect of the length of insoluble arms in PS_nP2VP_n heteroarm star polymers on their aggregation behavior in toluene was also considered.

The aggregation behavior of these amphiphilic PS_nP2VP_n star polymers was also examined in acidic aqueous solution where the P2VP arms are protonated, exhibiting polyelectrolyte characteristics.[127,128] Single molecular conformations and dimensions of core-shell structure of unimolecular and multimolecular micelles of PS_7P2VP_7 stars were studied in various solvents, at different pH, and concentration conditions using atomic force microscopy (AFM) with improved contrast through metallization.[65,166] Yu *et al.* prepared an asymmetric amphiphilic PS-P2VP heteroam star copolymer via atom transfer

radical polymerization (ATRP) and demonstrated the morphology change of polymolecular micelles of star polymer in a tetrahydrofuran and methanol mixed solvents.[167] The results revealed a change in morphology from irregular spherical and short rod-like aggregates (10 % methanol) to rod like micelles (90 % methanol) by increasing the methanol concentration, which is a poor solvent for PS arms.

The systematic study of quasi two dimensional surface micelles based on linear amphiphilic diblock copolymers was reported by Eisenberg *et al.* [91] Since then, the surface aggregation behavior of macromolecules has offered an insight into the formation mechanism of ultrathin monolayers and their structural characteristics.[92,93,94,95] Various parameters such as aggregation number, geometric dimensions of surface micelles, and their shape have been explored through pressure-area isotherms and by transmission electron microscopy (TEM) and AFM of Langmuir-Blodgett monolayers. Final aggregation behavior depends on the composition, degree of polymerization, hydrophilic/hydrophobic balance, arm length, concentration of spreading solution, solvent polarity, and subphase pH and ionic strength. These surface micelles can be formed in solution, or are compression induced, or can form spontaneously upon spreading at the air-water interface. [168] More recently, there have been reports on surface micelles, chain conformations, and morphologies of amphiphilic A_nB_n binary heteroam star copolymers having symmetric or asymmetric chain structure, (e.g. polystyrene-star-poly(ethylene oxide) (PS_nPEO_n), polystyrene-star-poly(2-vinyl pyridine), polystyrene-star-poly(acrylic acid) (PS_nPAA_n), and poly(ethylene oxide)-star-poly(ε-caprolactone)).[76,79, 169,162, 165]

Recently, novel star-shaped $A_n(B\text{-}C)_n$ multisegmental block terpolymers bearing PS, P2VP, and PAA blocks were synthesized through an extended "in-out method" and were explored in aqueous media. These star terpolymers consist of pure PS arms and an equal number of P2VP-*b*-PAA diblock copolymer arms, $PS_n(P2VP\text{-}b\text{-}PAA)_n$, named heteroarm star block terpolymers. Hammond *et al.* demonstrated their hierarchical self-organization of such a complex structures with small surfactants.[74] The ampholytic nature of this novel star block terpolymer allowed for complexation to be carried out on either the P2VP blocks (with negatively-charged surfactants) or on the PAA blocks (with positively-charged surfactants), depending on the pH at which the complexation reaction was carried out. Addition of surfactants to one block versus the other results in dramatically different morphologies and when the P2VP blocks are complexed, close-packed spheres are observed. On the other hand, when the PAA blocks are complexed, the molecules form core-shell cylinders (PS and P2VP composing the core and shell, respectively) in a matrix of PAA (surfactant).

However, studies of the surface micelles of $A_n(B\text{-}C)_n$ star terpolymers are still rare. Moreover, triblock ABC copolymers offer diverse morphologies with over 30 phases in the solution and bulk state because of the introduction of a third block. Such diverse morphologies cannot be observed in binary AB diblock or ABA triblock systems.[170, 171] Therefore, it is intriguing whether these $A_n(B\text{-}C)_n$ star terpolymers can provide diverse surface supramolecular nanostructures with various core-shell-corona structures such as

spherical, worm-like, vesicles, toroids, and Janus micelles, as observed with ABC linear counterparts.[172, 173, 174, 175, 176, 177]

In this chapter, we explore the surface behavior and morphologies of a series of pH-responsive amphiphilic star block terpolymers, $PS_n(P2VP\text{-}Pt\text{BA})_n$, and their precursors, heteroarm star copolymers, PS_nP2VP_n, with a high asymmetry in arm length. The focus of this work is on the effect of pH on the morphology of these amphiphilic star-shaped multiblock polymers which differ in architecture (copolymers and terpolymers), arm/block length (molecular weight of P2VP segments), and number of arms (n = 9, 22, and 28). To investigate the molecular aggregation and microphase separation of complex amphiphiles at the air-water/air-solid interface, we focused on morphological studies at different subphase pH (pH = 5.8 and 2.0). Our results demonstrate a strong pH dependence of the surface aggregation leading to different limiting molecular areas and surface morphologies for stars with different chemical compositions.

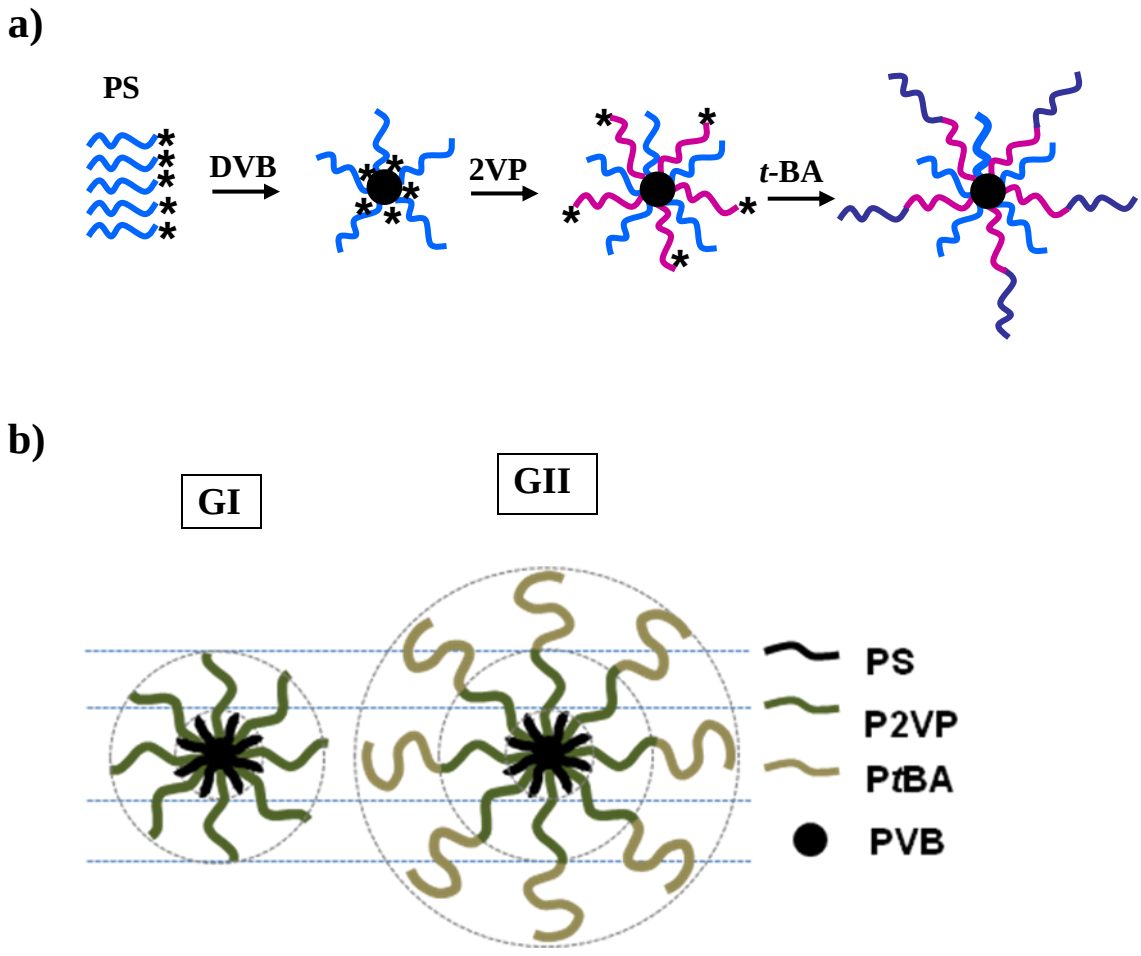

Figure 4.1: a) Schematic of the multi-step synthetic procedure for the synthesis of $A_n(B\text{-}C)_n$ heteroarm star block terpolymer, * denotes active sites. b) Molecular structures of heteroarm star polymers. G I represents PS_nP2VP_n (A_nB_n) star copolymers and G II represents $PS_n(P2VP\text{-}PtBA)_n$ star block terpolymers.

4.2. Experimental Details

Materials. The $PS_n(P2VP\text{-}PtBA)_n$ heteroarm star block terpolymers were synthesized by a multi-step, one pot, sequential anionic living polymerization procedure following the "in-out method" (Figure 4.1(a)).[126,127] All samples have been characterized by a

combination of gel permeation chromatography, ^{1}H NMR, and light scattering in accordance with the approach published elsewhere and summarized in Table 4.1.[74]

Table 4.1. Molecular Characteristics of Heteroarm Star Polymers.

Sample	Chemical structures	Number of arms		A		B		C		Φ_{P2VP} [a]	$M_{w,tot}$
		N	Total	M_w	N_{PS}	M_w	N_{P2VP}	M_w	N_{PtBA}		
GI-B9	PS_nP2VP_n	9	18	3,400	33	13,200	126			0.80	149,000
GI-B22		22	44	3,500	34	14,300	136			0.80	386,000
GI-B28		28	56	3,000	29	16,000	152			0.84	529,000
GII-T9	PS_n(P2VP-P*t*BA)$_n$	9	18	3,400	33	13,200	126	8,900	69	0.52	235,000
GII-T22		22	44	3,500	34	14,300	136	15,250	119	0.44	717,000
GII-T28		28	56	3,000	29	16,000	152	11,000	86	0.53	843,000

[a] weight fraction of P2VP.

Substrate preparation. Freshly cut silicon substrates with dimensions 1 cm x 2 cm and [100] orientation (Semiconductor Processing) and a native silicon dioxide layer having a 1.6 nm thickness were cleaned with piranha solution (3 : 1 concentrated sulfuric acid and hydrogen peroxide mixture) in accordance with usual procedure.[178] Subsequently, it was abundantly rinsed with Nanopure water (18.2 MΩ cm) and dried with a dry nitrogen stream. Pretreated substrates served as a hydrophilic base for film deposition.

Fabrication and characterization of monolayers. The Langmuir-Blodgett studies were conducted using a KSV2000 minitrough at room temperature, according to the usual procedure adapted in our lab.[131] A 0.5-0.10 mg/ml concentration of solution, composed of a star polymer sample dissolved in a nonselective solvent of chloroform/methanol

mixture (90/10 % in vol/vol) (HPLC grade) was prepared. The LB minitrough was next filled with Nanopure water. The pH of the water subphase was adjusted by using hydrochloric acid without a buffer system. The 60-120 µL polymer solution was dispersed in several droplets evenly onto the surface of the water. It was then left for 30 minutes to allow for the evaporation of the chloroform. Compression of the monolayers was conducted at a speed of 5 mm/min. The Langmuir monolayers were transferred from the air-water interface by vertically pulling out the substrate submerged in the water subphase at a rate of 2 mm/min. The limiting cross sectional area A_0 was determined by the steepest tangent rise in the surface pressure, which evidenced the formation of a condensed monolayer.[132]

Effective monolayer thicknesses were obtained with a M-2000 U spectroscopic ellipsometer with WVASE32 analysis software. AFM images were obtained with a Dimension-3000 atomic force microscope. AFM images were generated in the "light" tapping mode with an amplitude ratio within 0.90-1.00 to avoid monolayer damage.[135,136] Measurement of the contact angles were undertaken with a KSV CAM101 setup by dropping Nanopure water at three different locations for each sample.

4.3. Results and Discussion

4.3.1. Chemical composition.

Two groups of star polymers with different compositions, chain architectures, block topologies and the number of arms were used in this study. Group I includes heteroarm star copolymers composed of PS and P2VP arms (PS_nP2VP_n), where n denotes the number of each arm (Figure 4.1). The Group II, represented as $PS_n(P2VP\text{-}Pt BA)_n$, are star polymers composed of three kinds of blocks, which bear P*t*BA blocks as another hydrophobic component directly connected to the end of the P2VP arms. In both stars, the arms are linked on the same polydivinylbenzene (PDVB) core (Table 4.1 and Figure 4.1). Group I heteroarm star copolymers and Group II heteroarm star block terpolymers will be abbreviated as G I and G II respectively throughout this manuscript.

Figure 4.1(b) represents the general macromolecular architecture of the heteroarm star polymers studied here. For the sake of brevity the PS_nP2VP_n are termed as star copolymers and the $PS_n(P2VP\text{-}Pt BA)_n$ as star terpolymers. The two groups have a different number of arms (n = 9, 22, and 28 respectively) and the total arm number is 18, 44, and 56 per single star polymer, respectively (Table 4.1). Φ_{P2VP} presents the weight percent of P2VP blocks indicating the hydrophilicity of the star polymers in the condition that pyridine groups in P2VP are ionizable. Overall the star copolymers, PS_nP2VP_n ($\Phi_{P2VP} = 0.8$), are more hydrophilic than the star terpolymers, $PS_n(P2VP\text{-}Bt BA)_n$ (Φ_{P2VP} = 0.4-0.5).

Based on the ionization constant of pyridine (pK_a = 5.2) in solution, P2VP remains highly protonated under acidic conditions at pH 2.0 (adjusted by hydrochloric acid) whereas it is

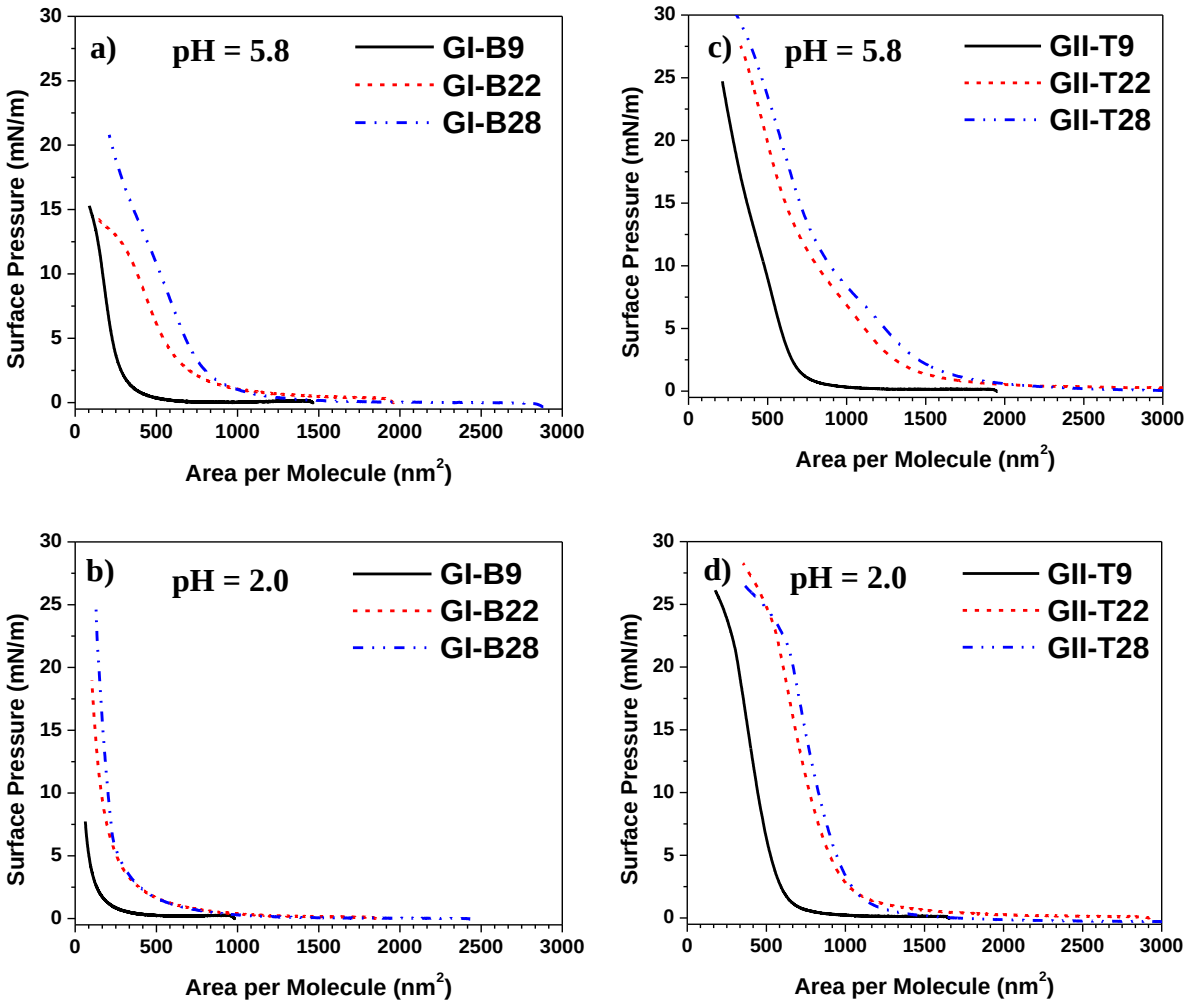

Figure 4.2: Surface-area isotherms of PS_nP2VP_n star copolymers (a and b) and $PS_n(P2VP\text{-}PtBA)_n$ star block terpolymers (c and d) at different subphase pH (5.8 vs. 2.0). GI-Bn denotes PS_nP2VP_n (n is the number of arms; n = 9, 22, and 28) and GII-Tn denotes $PS_n(P2VP\text{-}PtBA)_n$ (n = 9, 22, and 28).

only partially ionized at pH 5.8 (Nanopure water without pH adjustment).[183] However, the effective pK_a value of the star polymer is expected to be lower (less than 5.2) than the

linear counterpart due to ionic confinement phenomena, which leads to high osmotic pressure within the star architecture.[64] Li *et al.* reported that P*t*BA homopolymer and PS-*b*-PtBA linear block colymer spread at the air-water interface whereas PS homopolymer does not.[179] P*t*BA chain ends in star terpolymer thus seem to be surface-active and form surface aggregates. However, they are likely to be classified as hydrophobic based on their hydrophilic/hydrophopobic balance.

4.3.2. Surface-pressure isotherms at air-water surface.

Figure 4.2 shows the pressure-area isotherms (π-A) of G I star copolymers and G II star terpolymers as a function of the number of arms and at different subphase pH. The initial molecular area A_1, defined as the starting lift-up point of the surface pressure from zero pressure, depends on the number of arms (their molecular weight) at both pH conditions (Table 4.2). The π-A isotherm plots show a large range of high compressibility at the low pressure region until they start to dramatically increase. This gradual build up in pressure is due to the higher occupancy required for a larger number of arms which are initially stretched at the air-water interface, but sink to the water subphase with modest lateral compression. The heteroarm star polymers studied here have very large initial area, A_1, in a gas state at which star polymers exist as unimers with little interaction between them resembling their state in solution below the cmc. Cross-sectional areas of initial gas states depend on the number of arms and the subphase pH for both groups. In the condensed state region, limiting molecular area, A_0 also shows similar change in terms of number of arms for both G I and G II groups (Table 4.2). The limiting molecular areas of

all star polymers were determined by extrapolating the tangential line at the steepest rise to zero surface pressure in the range of surface pressures 5-20 mN/m.

Table 4.2: Monolayer Characteristics of Heteroarm Star Polymers at Different Subphase pH.

	A_0, (nm^2)		A_1, (nm^2)		Effective thickness (nm)					
					P = 0.50 (mN/m)		P = 10.0 (mN/m)		P = 20.0 (mN/m)	
Sample	pH 5.8	pH 2.0	pH 5.8	pH 2.0	pH 5.8	pH 2.0	pH 5.8	pH 2.0	pH 5.8	pH 2.0
GI-B9	340	120	1400	900	0.0	0.2	1.0	2.3	3.6	
GI-B22	750	260	1900	1800	0.6		1.4	3.0	4.1	
GI-B28	820	300	2800	2500	0.8	0.5	2.1	3.7	3.5	
GII-T9	750	580	1900	1800	0.4		1.1	1.1	2.0	
GII-T22	900	950	3400	2900	0.5		1.3	1.3	1.9	
GII-T28	1100	1100	3900	3400	0.6		1.6	1.3	1.9	2.0

Table 4.3: Mophological Characteristics of monolayers as a Function of Number of Arms at Different Subphase pH. Deposited at Surface Pressure 10 mN/m.

	Average domain height (nm)		Domain area coverage (%)		RMS Roughness	
Sample	pH 5.8	pH 2.0	pH 5.8	pH 2.0	pH 5.8	pH 2.0
G1-B9	0.8	0.8	48.0	48.0	0.20	0.22
G1-B22	1.0	0.9	48.0	48.0	0.24	0.25
G1-B28	1.1	1.4	45.0	53.0	0.33	0.39
G2-T9	2.5	1.7	51.0	49.3	0.60	0.30
G2-T22	1.3	1.6	48.0	46.6	0.38	0.35
G2-T28	1.3	1.4	50.0	49.0	0.42	0.38

The initial surface areas of compounds from G II group are larger than those of G I compounds (Table 4.2). This effect could be attributed to the higher hydrophobic block content in the star terpolymers. At acidic conditions, A_1 shows a smaller decrease as

compared to that at neutral pH (Table 4.3). This difference can be caused by the fact that the ionized P2VP chain segments remain anchored to the air-water interface in a star fish shape with few submerged P2VP segments under these conditions (see Figure 4.3 and more discussion below).

On the other hand, G I and G II star polymers displayed distinct pH-sensitive surface pressure behavior. At acidic pH (2.0) condition, the values of A_1 and A_0 decrease for G I, but stay constant for G II polymers. This distinct dependence on pH seems to be due to the difference in chain topology for these different groups. The relatively hydrophobic P*t*BA end blocks of G II compounds influence the chain conformation change at the air-water interface unlike G I compounds with pH sensitive P2VP arms (Figure 4.1). In particular, we found that the shape of π-A isotherms at acidic pH condition is similar to that for linear PS-P2VP block copolymers and PS-P2VP with incorporated alkyl groups.[93,183]

The pH-dependence of surface isotherms reveals that G I compounds have notably smaller A_0 at neutral pH (pH = 5.8) than that at acidic pH (2.0) condition if compared to G II star terpolymers (Table 4.3). At acidic pH, pyridine moieties (pK_a = 5.2) on P2VP blocks are ionized with a positive charge. The G I group shows a dramatic reduction in A_0 without any transition shoulder on the isotherms while A_0 for G II compounds remains the same under the highly ionized condition (Figure 4.2). This behavior can be explained by the well-known characteristic transition model, that is, from "star fish" to "jelly fish" transition (see Figure 4.3 and more discussion below).[91,93] At higher surface pressure, the

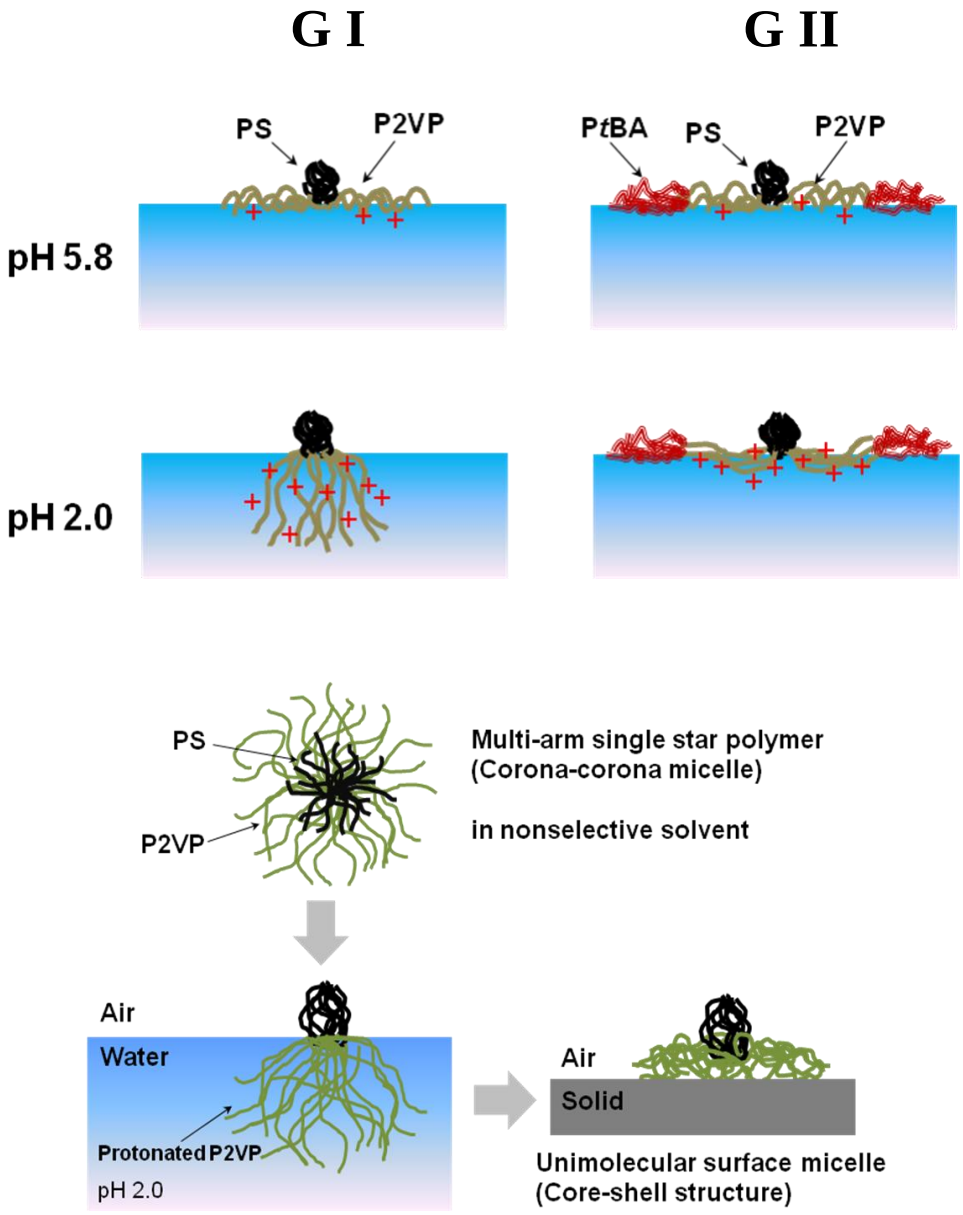

Figure 4.3: Schematics of suggested chain conformations of star copolymers (GI) (left) and star terpolymers (GII) (right) at pH 5.8 and 2.0 at the air-water interface under lateral compression (top) and unimolecular micelle at air-water and air-solid interfaces (bottom).

submersion of pyridinium chains into the water subphase occurs upon compression. Indeed, it has recently been found that the highly ionized P2VP arms of linear PS-P2VP

diblocks might sink into the water subphase with increasing lateral compression depending upon the degree of ionization of pyridine groups without quaterization.[183] On the other hand, the hydrophobized version of PVP, alkylated PVP, remains adsorbed at the water surface without undergoing the conformation change and the chain submersion in the water subphase.[180]

However, the G II star terpolymers do not show any noticeable decrease in A_0 with pH change contrary to the G I star copolymer precursors (Figure 4.2). π-A isotherms of G II compounds show a weak transition shoulder in the range of 3 mN/m to 10 mN/m. At pH 2.0, the surface pressure undergoes a sharper transition in a solid state (Figure 4.2). However, A_0 of G II compounds remain the same at both pH conditions except for star polymers with a lower number of arms (GI-T9) (Table 4.2). This fact suggests that the P2VP-P*t*BA arms of G II star terpolymers reside in the adsorbed state on the water surface without a phase transition from the "star-fish" to "jelly-fish" conformation for both neutral and acidic pH (Figure 4.3). It is apparent that the hydrophobic P*t*BA chain ends, which are attached to P2VP arms, keep these diblock arms adsorbed onto the

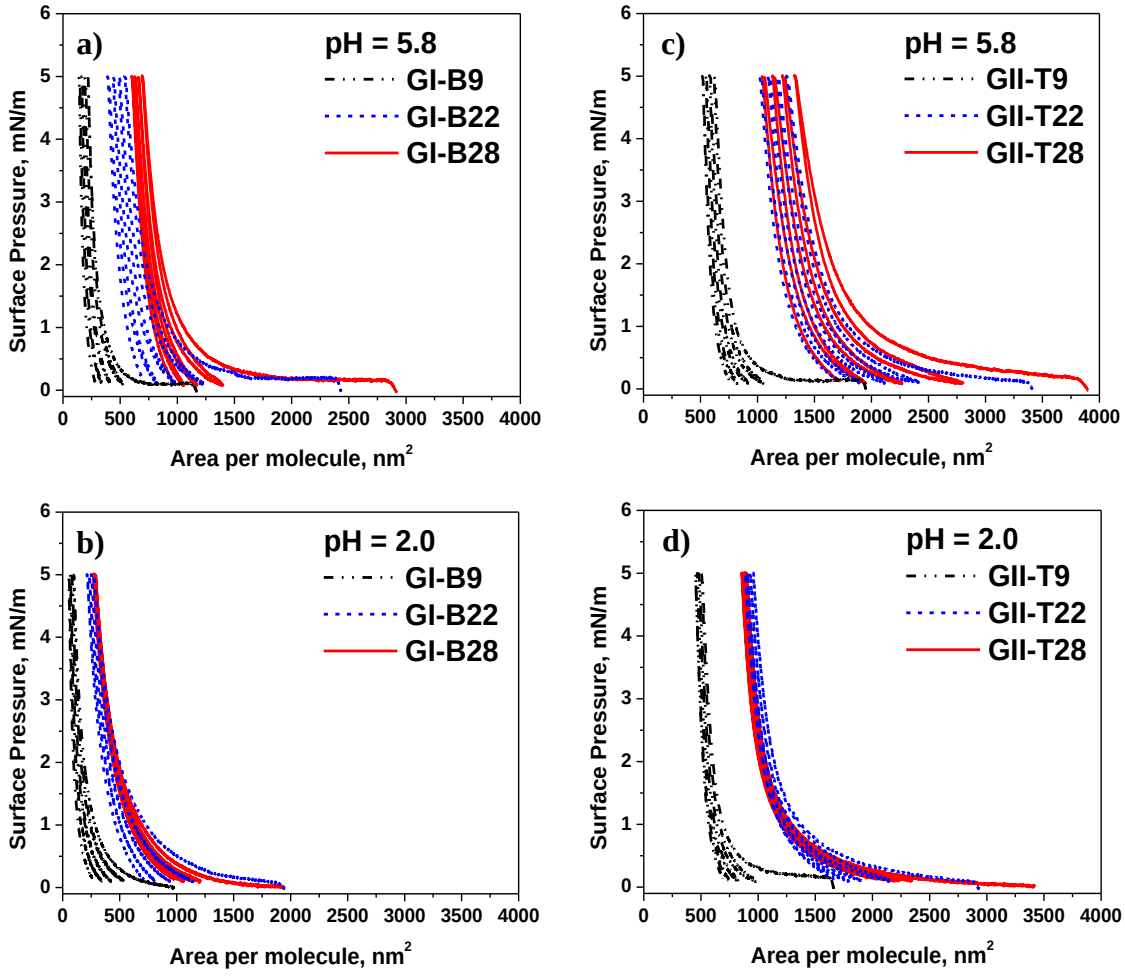

Figure 4.4: Compression-expansion cycles of PS_nP2VP_n (a and b) and $PS_n(P2VP\text{-}Pt\text{BA})_n$ (c and d) at different pH. The number of cycles is four.

interface and not completely submerged into the water subphase. At pH 5.8, pyridine is partially protonated and remains adsorbed at the air-water interface due to the strong ionic repulsion, which causes the chain to be stretched along the interface. This intermolecular repulsion leads to a weak shoulder transition on the surface pressure isotherms for GII-T22 and GII-T28 at pH 5.8. At pH 2.0, the increased solubility of the fully protonated P2VP segments allows the chains to easily submerged into the water

subphase (Figure 4.3). As a result, star molecules can be more highly compressed at pH 2.0 than at pH 5.8.

Compression-expansion isotherm cycles at different pH were conducted to measure the monolayer stability and the reversibility of surface aggregation (Figure 4.4). Langmuir monolayers were compressed up to 5.0 mN/m and subsequently expanded to 0.1 mN/m. The results show mostly reversible behavior of the compression-expansion cycle for G I and G II compounds at varying pH conditions in this compression range. Both G I and G II compounds exhibit higher hysteresis at pH 5.8 than at pH 2.0. G II compounds show a larger hysteresis, especially, at pH 5.8.

In addition, for both G I and G II groups, the hysteresis at pH 5.8 increases with the number of arms, while at pH 2.0 this trend does not depend upon the number of arms within the same group. In the case of pH 5.8, higher hysteresis implies loose initial packing at the air-water interface, which can be ascribed to higher electrostatic repulsion between surface aggregates. We suggest that partially ionized P2VP segments, which are absorbed at the air-water interface, become reorganized, resulting in the transformation into a different chain conformation (Figure 4.3). This different conformation at pH 5.0 can be explained by the varying charge distribution on the partially ionized P2VP segments serving as a kinetic barrier.[95,181] The hydrophobic P*t*BA end blocks anchored to the surface act as additional elastic barrier, thereby preventing the close packing of the molecules. P*t*BA segments seem to sustain the ionized P2VP chains floating at the air-water interface by hindering the submersion of P2VP block into the water subphase.

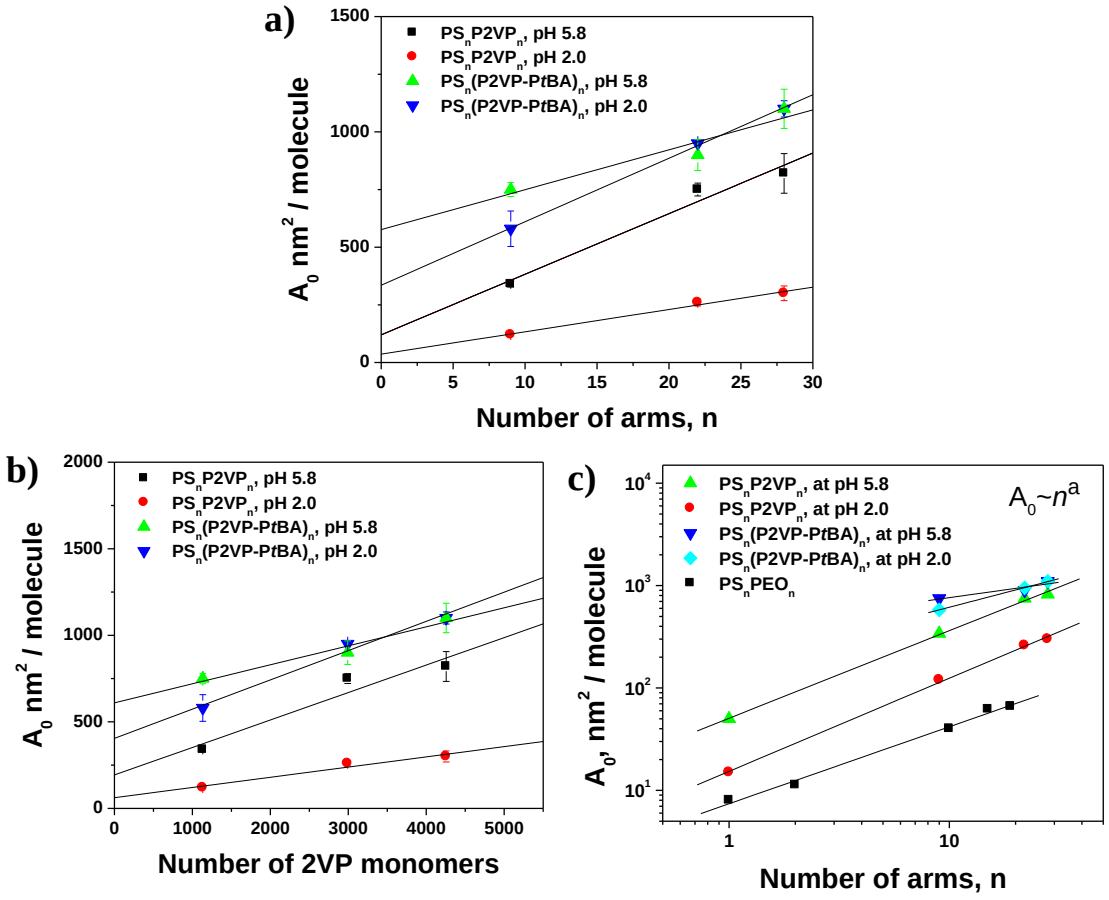

Figure 4.5: a) Plot of limiting molecular area, A_0, of star polymers vs number of arms at different subphase pH 5.8 and 2.0 (PS_nP2VP_n at pH 5.8 (■) and pH 2.0 (●); PS_n(P2VP-P*t*BA)$_n$ at pH 5.8 (▲) and pH 2.0 (▼). b) limiting molecular area, A_0, of star polymers vs number of 2VP monomer units at different subphase pH 5.8 and 2.0 (PS_nP2VP_n at pH 5.8 (■) and pH 2.0 (●); PS_n(P2VP-P*t*BA)$_n$ at pH 5.8 (▲) and pH 2.0 (▼). c) Limiting molecular area A_0 as a function of number of arms n for PS_nP2VP_n at pH 5.8 (▲), PS_nP2VP_n at pH 2 (●), PS_n(P2VP-P*t*BA)$_n$ at pH 5.8 (▼) and pH 2.0 (♦) in comparison with star polymers PS_nPEO_n (■) from ref. 164 and PS_2-PEO_2 from ref. 162(c). For n=1, the data for corresponding diblock copolymer of PS-P2VP was taken from ref. 183.

Limiting molecular area, A_0, varies linearly with the number of arms and the number of pyridine monomer units although this conclusion is made with a limited number of data points (Figure 4.5). Extrapolating the limiting molecular area to zero P2VP monomers characterizes the micelle structure based on the contribution of each block to the surface area at the air-water interface. Previous reports on the limiting molecular area of surface

micelles composed of linear block copolymers at neutral pH conditions, showed a zero intercept as the number of surface-anchored fragments decreased.[182,183] However, a non-zero intercept indicates that the PS cores contribute to the surface area at the air-water interface at low pH condition (15 nm^2 at pH 1.8).[183] G I group with free hydrophilic P2VP arms showed a lower intercept than G II group with two hydrophobic segments, PS and P*t*BA. In the case of G I compounds, PS arms and P2VP arms remaining at the air-water interface account for the non-zero intercept. The relatively higher intercept for G II compounds is due to the contribution of additional long P*t*BA end blocks to the limiting molecular area. The higher intercept of these compounds at pH 5.8 than at pH 2.0 indicates that PS and P2VP arms of star polymer micelles contribute to their surface area, implying incompletely-segregated chain-like structures at the air-water interface. The slope of the plots represents the area of each arm or the 2VP monomer unit at the air-water interface. G I shows a change in area of 2VP monomer unit from 0.16 nm^2 at pH 5.8 to 0.06 nm^2 at pH 2.0 whereas the slope for G II is similar at different pH conditions (0.11 nm^2 at pH 5.8 and 0.17 nm^2 at pH 2.0). These results reflect that the chain conformation of P2VP in G1 is more sensitive to pH than G II.

Figure 4.5(c) shows a linear variation of the number of arms with limiting molecular area under log-log scale suggesting the power law dependence of the variables i.e. $A_0 \sim n^{\alpha}$ in the range of parameters studied here. Therefore we can speculate that this dependence suggests that the surface aggregation behavior of our star polymer at the interface is analogues to the aggregation number dependency on the degree of polymerization of the different block copolymers in solution state.[184] The analysis shows that the α value for G

I group is within 0.85-0.90 but decreases to 0.30-0.56 for G II group. These values can be compared with data for PS-PEO star block copolymer from our previous studies with exponential value $\alpha = 0.75$ (Figure 4.5c). Larger α value implies the higher contribution of each arm to molecular area at the air-water interface. From comparison with surface behavior of linear counterpart, we suggest that star architectures hinder the rearrangement of arms at the interface since they have the restriction of chain conformation due to confined and highly crowd chain structure around core. On the other hand, a significant drop of α for G II group can be related to already high initial molecular area caused by the contribution from additional hydrophobic ends.

4.3.3. Monolayers at solid substrates.

The effective thickness of Langmuir monolayers deposited at the surface pressure of 10 mN/m increases with the number of arms for both G I and G II groups (Table 4.2). At varying surface pressure, the effective monolayer thickness increases with increasing compression for the same number of arms. G I heteroarm star copolymers exhibit pH-dependent behavior of thicknesses (Table 4.2). At acidic pH (2.0) condition, the effective thickness is three times higher than that at neutral pH. This result supports the suggestion made above that pressure induces chain reorientation in the vertical direction, which contributes to the monolayer thickness (Figure 4.3). The drastic increase in thickness at acidic conditions can be attributed to the swelling of the P2VP chain segment at acidic conditions due to intramolecular ionic repulsion, which leads to the expanded chain conformation. Moreover, the lateral compression provides smaller surface area per molecule, thus forcing the ionized P2VP chains to further stretch in a vertical direction.

In contrast, the effective thickness of the LB monolayer for G II star terpolymers undergoes no pronounced changes at different pH (Tables 4.2, 4.3). Moreover, they exhibited similar thicknesses with group G I star copolymers despite much longer arm lengths. We suggest that hydrophobic block, P*t*BA, at chain ends plays a critical role in the stabilization of the lateral organization and the prevention of their star fish conformation even at acidic pH conditions (Figure 4.3). This behavior underlines the critical role of the nature of the end groups in the overall conformation of the star molecules at interfaces and their behavior at different pH conditions.

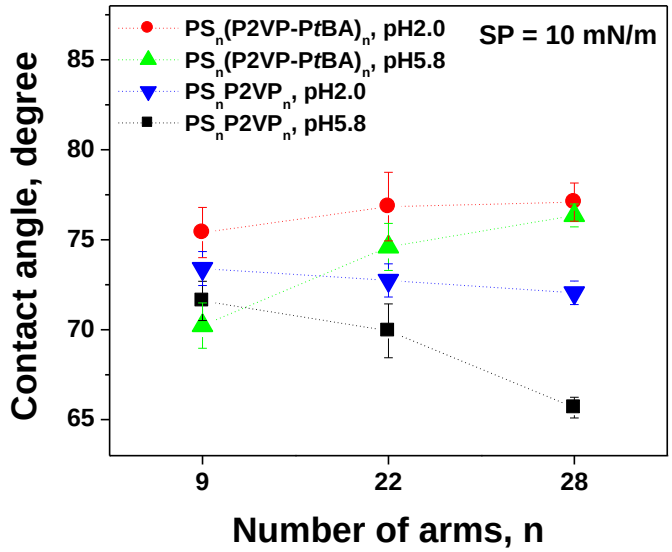

Figure 4.6: Contact angles measurements of Langmuir-Blodgett monolayers of star polymers. (●) denotes G II star terpolymers at pH 2.0 (▲) and pH 5.8; (▼), and G I star copolymers at pH 2.0 (■) and pH 5.8.

For LB monolayers formed with both groups of star polymers, the contact angle was within 65-77^o (Figure 4.6) indicating the modestly hydrophobic composition of the topmost surface layer and confirming the preferential surface location of PS and PtBA

blocks in accordance with models discussed above (Figure 4.3). A higher contact angle was

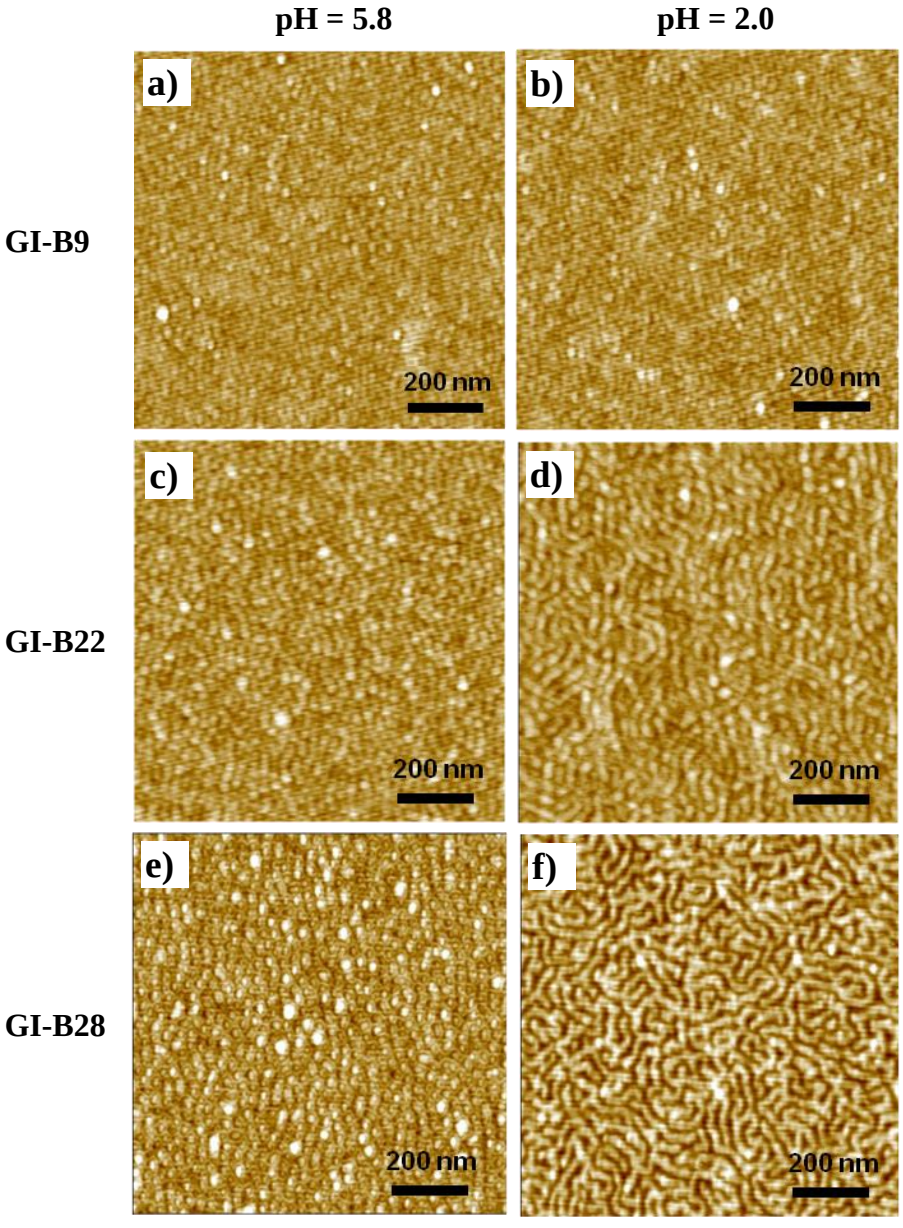

Figure 4.7: AFM topographical images (1 μm × 1 μm) of PS_nP2VP_n star copolymers (n = 9 for a and b; n = 22 for c and d; n = 28 for e and f) at different subphase pH: a, c and e at pH 5.8, and b, d and f at pH 2.0. The LB films were deposited at a surface pressure of 10 mN/m. G1-B_n denotes PS_nP2VP_n (number of arms, n = 9, 22, and 28). Z scale = 5 nm.

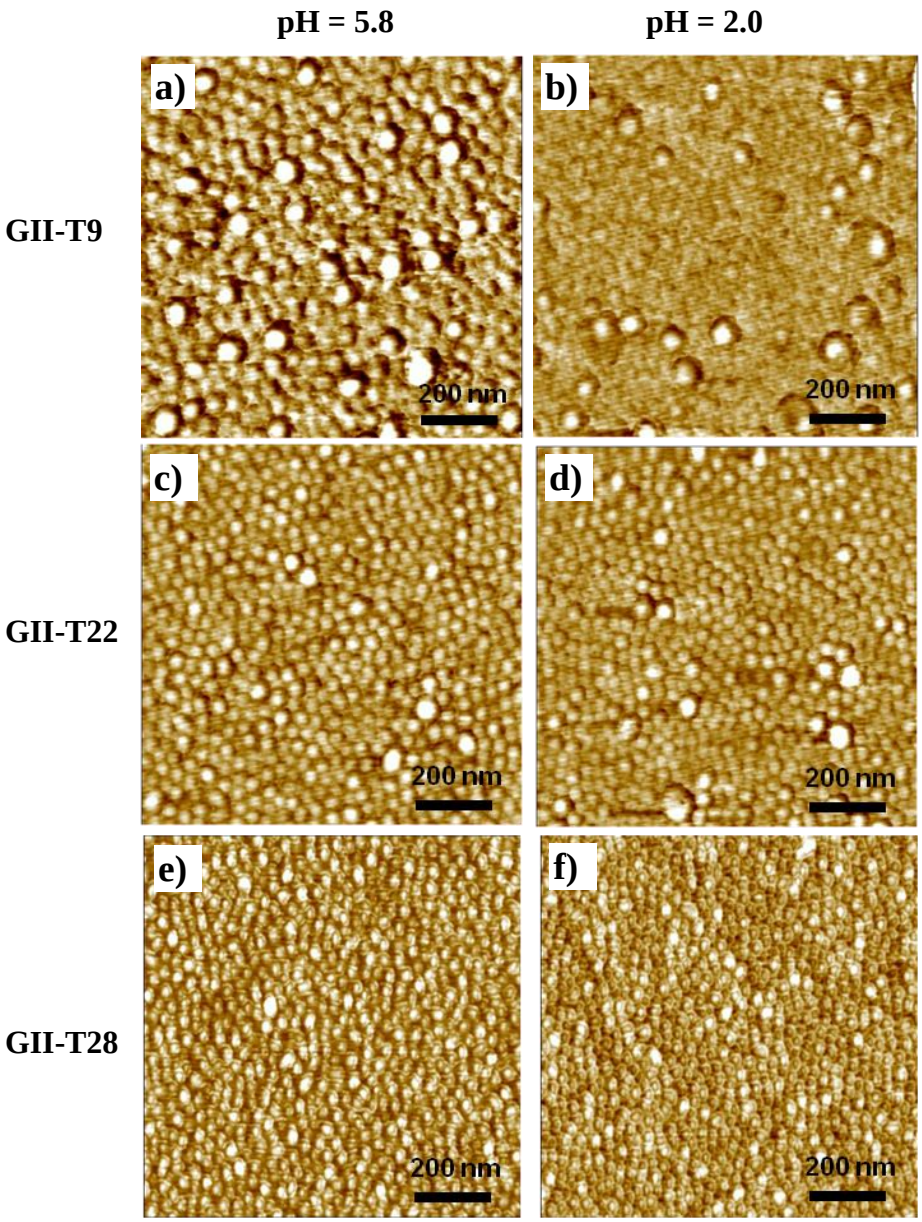

Figure 4.8. AFM topographical images (1 μm × 1 μm) of $PS_n(P2VP\text{-}Pt BA)_n$ star block terpolymers (n = 9 for a and b; n = 22 for c and d; n = 28 for e and f) at different subphase pH : a, c, and e at pH 5.8, and b, d, and f at pH 2.0. The LB films were deposited at a surface pressure of 10 mN/m. G2-Tn denotes $PS_n(P2VP\text{-}Pt BA)_n$ (n = 9, 22, and 28). Z scale = 5 nm.

observed for LB monolayers deposited at acidic conditions (Figure 4.6). The increasing contact angles at acidic pH suggest that the ionized P2VP blocks stretch out beneath the

topmost PS phase resulting in the enhanced vertical chain segregation of hydrophobic PS and hydrophilic P2VP blocks. The presence of the additional PtBA blocks in the G II star terpolymers results in a slightly higher contact angle (Figure 4.6). The contact angle of G I star polymers increases with the number of arms in contrast to the G II group, which can be related to different surface morphologies and microroughness as will be discussed in the next section (Table 4.3).

4.3.4. Surface morphology of monolayers.

Figure 4.7 shows the surface morphology of LB monolayers of G I star polymers formed at different pH and at a surface pressure of 10 mN/m. The surface morphology changes from regular circular micelles at pH 5.8 to ribbon-shaped aggregates at pH 2.0. For a higher number of arms (GI-B22), a distinct labyrinth pattern was observed instead of a long ribbon or rod structure as previously reported for star block copolymers.[93,94] On the other hand, the circular micelles of PS-P2VP can be compressed up to high surface pressure and tend to form a labyrinth pattern caused by the fusing of PS cores into short rods.[181] This transformation provides further evidence for the submersion of ionized P2VP blocks (transition from star fish to jelly fish) at the air-water interface (Figure 4.3). It is noteworthy that at pH 2.0 the labyrinth pattern becomes more prominent with an increase in the number of arms. In the case of GI-B28, the surface aggregates are more curved and branched as compared to GI-B9 and GI-B22. However, at this pressure, inter-micellar distance remains similar for many star polymers regardless of pH conditions.

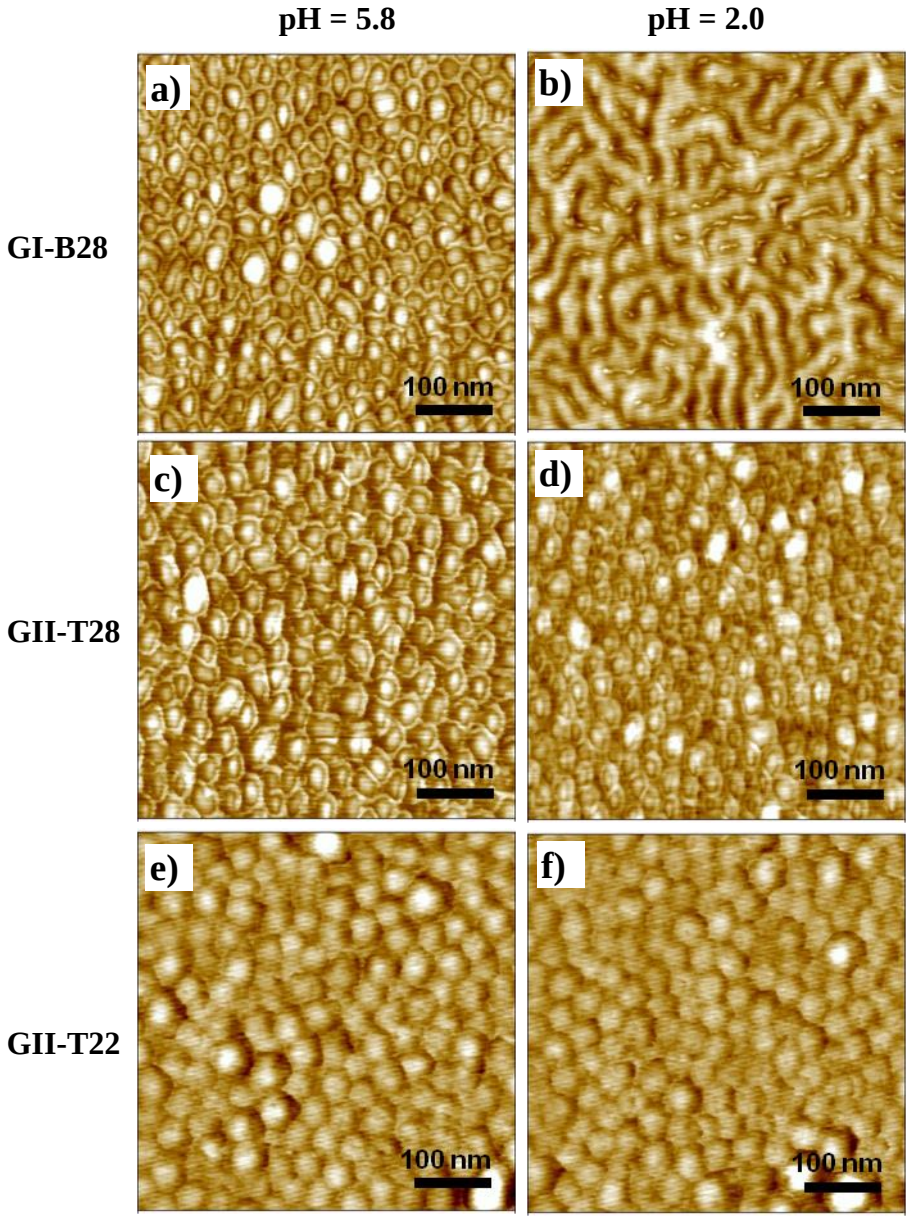

Figure 4.9: AFM topographical images (500 nm × 500 nm) of GI-B28 ($PS_{28}P2VP_{28}$ star copolymers for a and b), GII-T28 (PS_{28}(P2VP-P*t*BA)$_{28}$ star block terpolymers for b and c), and GII-T22 (PS_{22}(P2VP-P*t*BA)$_{22}$ star block terpolymers for e and f. The LB films were deposited at surface pressure 10 mN/m at different subphase pH 5.8:(a, c and e) and at pH 2.0(b, d and f). Z scale = 5 nm.

In contrast, the G II star terpolymers show no significant pH-dependent transformations of surface morphology (Figure 4.8). The well-defined circular surface micelles with

large diameters were maintained regardless of the variation of arm number with little change in the surface texture. However, GII-T9 exhibited smoother surfaces at neutral pH. The hydrophobic P*t*BA blocks appear to keep the ionized P2VP blocks floating even at acidic pH thereby suppressing the transformation of the molecular state from star fish into jelly fish (Figure 4.3).

In contrast to the G I group, whose micelle size increases with the number of arms for different pH, the size of micelles of the G II group decreases with increasing number of arms as can be seen in high resolution AFM images in Figure 4.9. For instance, GI-B9 compound with a smaller number of arms shows larger and more irregular micelles with an average diameter of 55 ± 5 nm. On the other hand, diameters of domains for GII-T22 are slightly lower (45 ± 5 nm) and there is an even further decrease for GII-T28 to 38 ± 5 nm. Such shrinking can be caused by the co-aggregation of PS and P*t*BA hydrophobic blocks in more crowded stars resulting in a more condensed state.

Next, to elucidate the pH effect on the surface morphology and its transformations, the LB monolayers were compared at different surface pressures, particularly at 0.5 and 20.0 mN/m at neutral pH as illustrated in Figures 4.10 and 4.11. At the low surface pressure of 0.5 mN/m, a more loose packing of circular surface aggregates is observed for both G I and G II groups. For compounds with lowest number of arms, such as GI-B9, no clear micellar structures are observed. Moreover, increasing the number of arms effectively makes the micelle aggregates more defined and more separated. In particular, the G II-T28 compound shows a large uniform space between surface micelles.

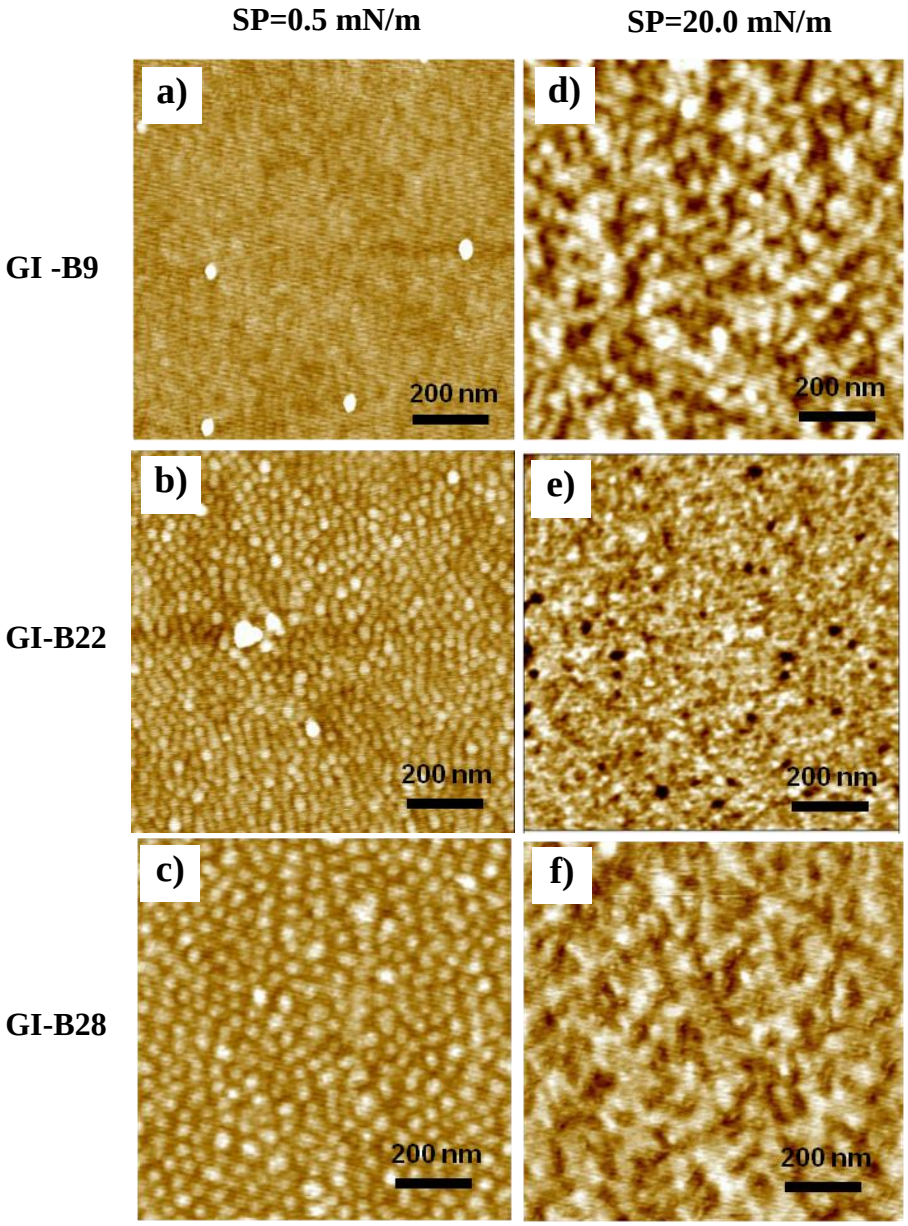

Figure 4.10: AFM topographical images (1 μm × 1 μm) of PS_nP2VP_n at different surface pressures (0.5 and 20.0 mN/m) at pH 5.8. G1-B_n denotes PS_nP2VP_n (number of arms, n = 9, 22, and 28). Z scale = 5 nm.

On the other hand, at the higher surface pressure of 20 mN/m, the G I group shows coarse texture and collapsed monolayers contrary to the transformation from circular to lamellar morphology at acidic pH (Figure 4.7). However, G II compounds maintain the circular micellar structures at higher pressure and neutral pH showing higher stability without

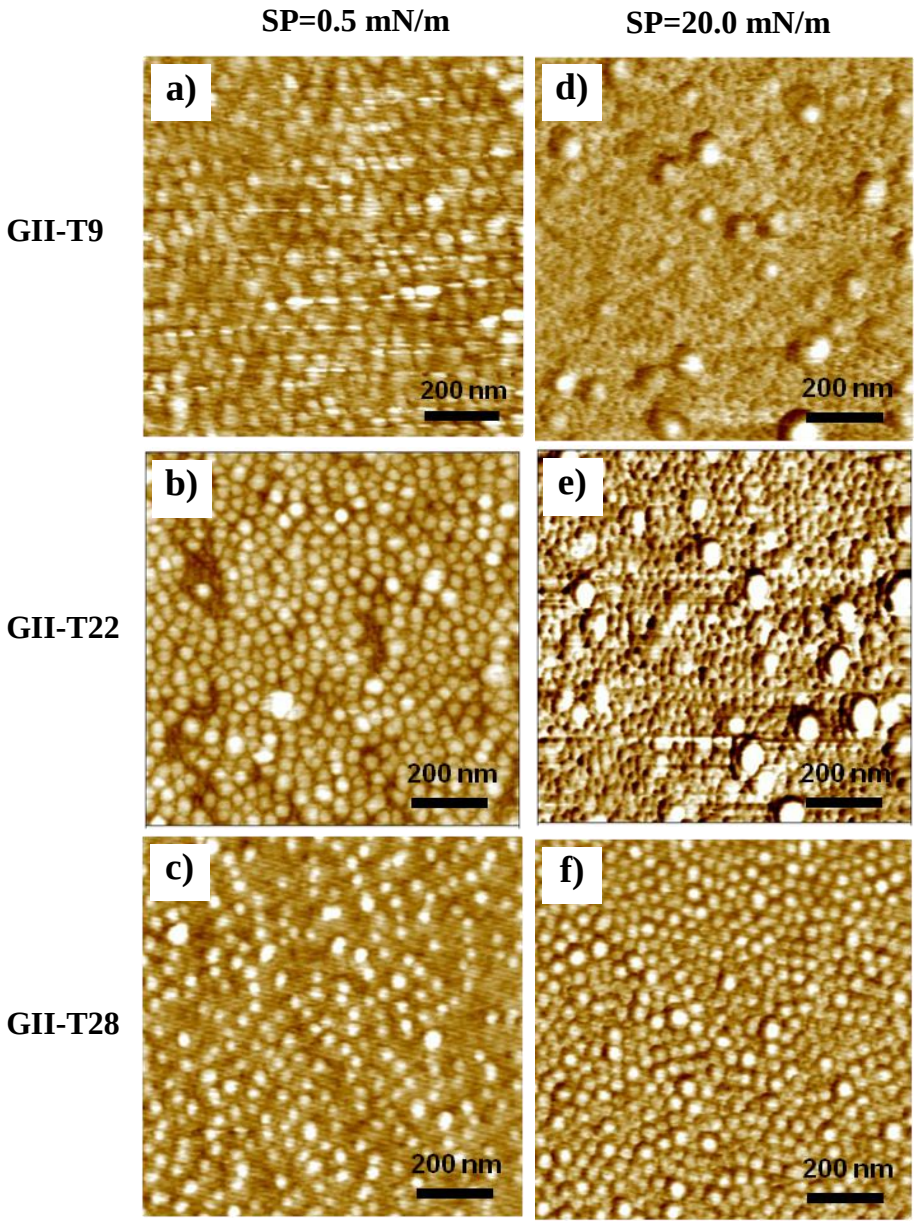

Figure 4.11: AFM images (1 μm × 1 μm) of $PS_n(P2VP\text{-}PtBA)_n$ at different surface pressures (sp = 0.5 and 20.0 mN/m) at pH 5.8. GII-Tn denotes $PS_n(P2VP\text{-}P\textit{t}BA)_n$ (n = 9, 22, and 28). Z scale = 5 nm.

collapsing as displayed in Figure 4.11d,e,f. In particular, G II-T28, with a larger number of arms, exhibits a higher stability compared to compounds with a lower number of arms (GII-T9 and GII-T22). This observation confirms conclusions made base upon π-A

isotherm analysis and suggest that the hydrophobic P*t*BA corona serves as a more effective barrier under higher lateral compression than the hydrophilic corona of G I compounds, thus preventing collapse and preventing the circular micellar morphology.

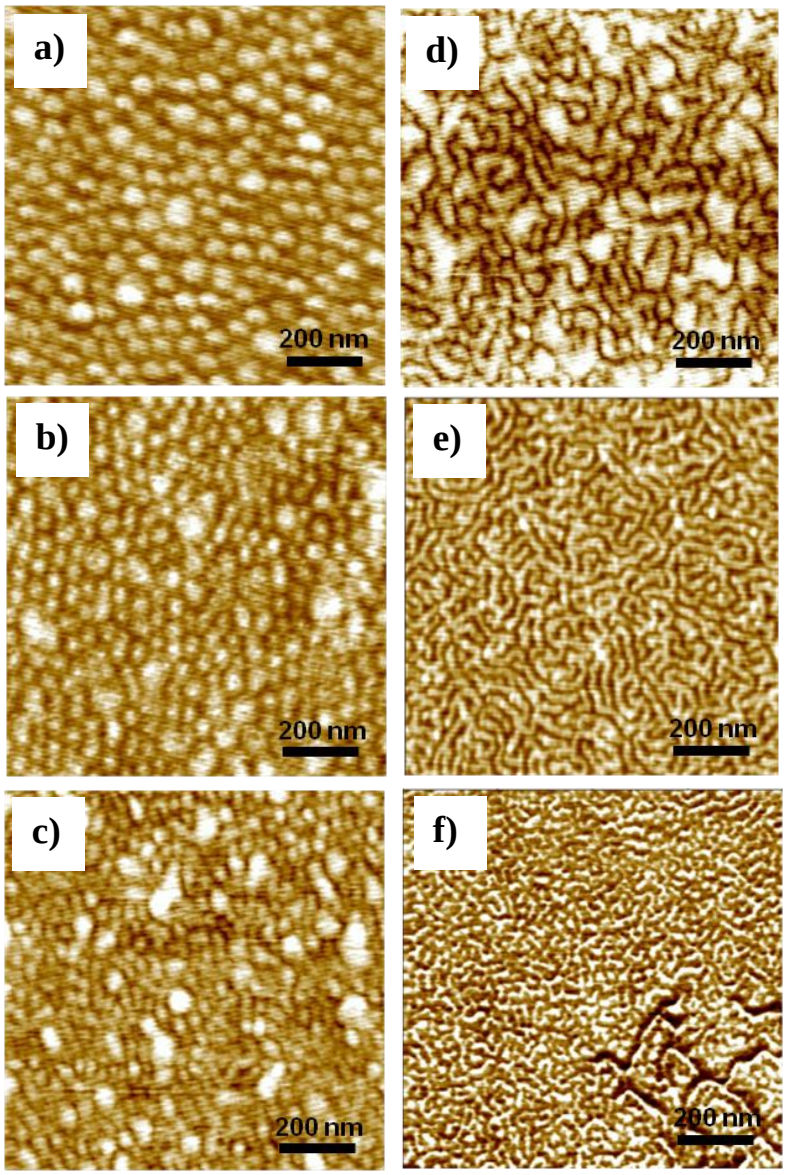

Figure 4.12. AFM topographical images (1 μm × 1 μm) of $PS_{28}P2VP_{28}$ star copolymer as a function of surface pressure: a) 0.5 mN/m, b) 1.0, c) 5.0, d) 8.0, e) 10.0, and f) 30.0 at pH 2.0. Z scale = 5 nm.

To consider the formation of the labyrinth morphology at acidic pH (2.0) condition, LB films were examined at different surface pressures (0.5, 1.0, 5.0, 8.0, 10.0, and 30.0 mN/m) for selected compounds. We selected long arm star copolymers from G I group (GI-B9, n = 28) and from Group II (GII-T9, n = 28) (Figures 4.12, 4.13). AFM imaging demonstrates that the labyrinth morphology has indeed originated from the transition from the initial circular structures observed at very low surface pressure (Figure 4.12a). As the lateral compression increased (1.0-5.0 mN/m), the surface morphology began a gradual transformation to with compressed and coalesced circular domains (Figure 4.12b,c). At the intermediate state, a mixture of condensed circular and short ribbon, is observed (Figure 4.12d). When compressed further up to 10.0 mN/m, the surface morphology finally converts into fine, interwoven ribbon structures constituting the labyrinth morphology (Figure 4.12e). This morphology remains stable, although with much finer elements, up to the highest pressure (30.0 mN/m), close to the monolayer collapse. Thus, the G I compound could readily undergo the conformation transformation from flattened arms (star fish) at the air-water surface into submerged P2VP blocks (jelly fish) under high surface pressure, leading to the easier collapse of these monolayers (Figure 4.3).

In contrast to the $PS_{28}P2VP_{28}$ compound discussed above, no significant changes of the labyrinth morphology composed of branched ribbons were observed for the G II star terpolymers with an identical number of arms at the same pH conditions (Figure 4.13). $PS_{28}(P2VP\text{-}Pt\text{BA})_{28}$ sustains the stable circular structures, confirming that the hydrophobic P*t*BA end blocks prevent the aggregation/transformation by acting as natural

barriers which can endure the compression forces such as suggested above (Figure 4.3). Finally, the monolayer collapse resulted in disorganized local regions of coalesced domains without any signs of labyrinth morphology (Figure 4.13d).

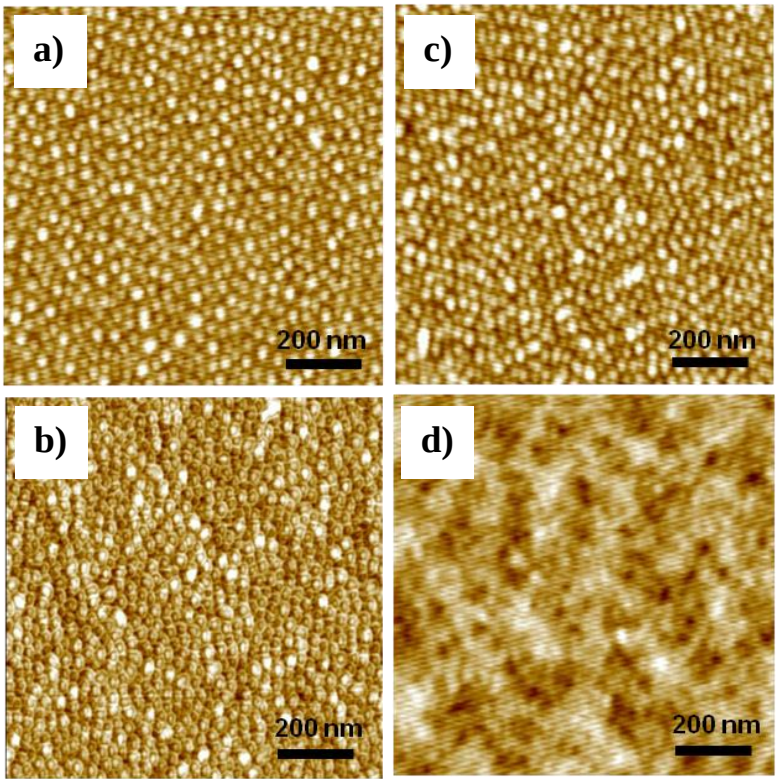

Figure 4.13. AFM topographical images (1 μm × 1 μm) of $PS_{28}(P2VP\text{-}Pt\text{BA})_{28}$ as a function of surface pressure: a) 1.0 mN/m, b) 10.0, c) 25.0, and d) 30.0 at pH 2.0. Z scale = 5 nm.

Table 4.4: Aggregation Numbers of Surface Micelles.

Sample	pH	SP[a] (mN/m)	A_{mol}[b] (nm^2 / molecule)	N_{micel}[c] (n)	A_{micel}[d] (nm^2 / micelle)	N_{agg}[e] (n)
GI-B28	5.8	0.1	1723	21 ± 2	2976 ± 0.5	1.7 ± 0.5
	5.8	10.0	520	74 ± 4	845 ± 0.3	1.6 ± 0.3
GII-T28	5.8	10.0	897	48 ± 5	1302 ± 0.2	1.5 ± 1.0
	2.0	10.0	829	60 ± 7	1042 ± 0.4	1.3 ± 0.8

a. Surface pressure. b. Molecular area from surface-area isotherms. c. Number of micelle estimated from AFM images (250 × 250 nm^2). d. Micelle area. e. Aggregation number.

To quantitatively characterize the domain morphology for the star polymers with the largest number of arms (28) we derived the aggregation number (N_{agg}) from AFM images according to the known procedure.[91] The number of aggregates per selected surface area (A_{micel}) was compared with the molecular area (A_{mol}) from the limiting cross-section area, A_0, to derive N_{agg} (Table 4.4). Remarkably, it is found that the star polymers with a larger number of arms possess a very low aggregation number, around 1.5, at different pressures and pH. This fact indicates that domain structures in these star block copolymers are predominantly *uni-molecular micelles.* This conclusion is in agreement with the models suggested above (Figure 4.3). Apparently, the over-crowding of the outer shell of the star molecules with a large number of long arms causes *intramolecular aggregation* and microphase separation and prevents the aggregation of multiple molecules into a single micelle. The formation of stable unimolecular aggregates is in contrast with regular, compositionally-similar linear block copolymers, which show a large aggregation number.[127]

In summary, the surface behavior and morphologies of two series of novel pH-responsive amphiphilic heteroarm star polymers, which differ in architecture, block topology, arm lengths, and number of arms, have been presented. Due to the pH-sensitive ionization of P2VP block, the morphology of star copolymers bearing the free P2VP arms was strongly dependent on the pH of the subphase, while the star terpolymer containing the protonated hydrophilic P2VP block as midblocks and terminal hydrophobic P*t*BA blocks, maintained nearly constant organization at low pH.

CHPATER 5

INTERFACIAL BEHAVIOR OF pH RESPONSIVE AMPHOLYTIC HETEROARM STAR BLOCK TERPOLYMERS

5.1. Introduction

Recently, star-shaped polymers with different blocks confined to a single core, named heteroarm or miktoarm star copolymers, have attracted significant attention because of their well defined macromolecular architectures and can be considered as model branched systems with colloidal and polymeric properties.[152,153,154,166,185,186,187] As a result of their star-shaped chain architecture, they can show peculiar micelle aggregation in bulk, solution, and at interfaces. In fact, star copolymers show a critical micellar concentration which is a few orders of magnitude higher that of linear counter parts while the association number is significantly lower than that observed for linear counterparts.[127,162,163,188]

Star copolymers bearing chemically different arms possess a variety of morphologies such as spherical micelles, stripes, and disk-like micelles depending upon the copolymer composition and solvent selectivity.[162,174,189,190] For instance, the assembly of amphiphilic heteroarm star polymers composed of hydrophobic and hydrophilic arms polystyrene/poly(2-vinylpyridine) (PS_nP2VP_n) in organic solvents like toluene, as well as in acidic aqueous solutions, was demonstrated utilizing the responsive nature of the blocks present in the star polymer.[155] In another study, spherical to rod-like micelles were obtained by simply changing the polarity of the solvent which is selective for one of the arms of asymmetric PS_nP2VP_m heteroarm star copolymer.[167] Assembly and aggregation behavior of

amphiphilic star polymers of different chain architectures such as, poly(ethylene oxide)/polystyrene (asymmetric PEO-PS_n and symmetric PEO_nPS_n heteroarm stars) at air-water and solid-air interfaces demonstrated a variety of surface morphologies.[164,191]

Heteroarm star block terpolymers of the type $A_n(B\text{-}b\text{-}C)_n$, which can be synthesized using the in-out synthetic route, have attracted much attention very recently due to the intra- and intermolecular interactions that lead to interesting assemblies.[192,193] These star polymers can be considered to be a hybrid between the known A_nB_n heteroarm star copolymer and a $(BC)_n$ star block copolymer.[194] Tuning these blocks makes the system responsive to external stimulus such as pH, temperature, and shear. Star polymers composed of poly acid/base blocks exhibit an isoelectric point over a certain pH range depending on the ionization of the blocks. The polymer then precipitates in this region due to intra/inter molecular electrostatic interaction; however, their self-assembly in other pH region leads to various interesting morphologies.[196,197,195] Recently, attention has been given to terpolymers constituted of hydrophobic polystyrene (PS) and the hydrophilic diblock copolymer poly(2-vinyl-pyridine)-*b*-poly(acrylic acid) (P2VP-*b*-PAA) since the individual blocks show strong pH dependence over a wide range of pH values. Various nanostructures can be obtained by tuning the interaction between the hydrophilic groups (P2VP and PAA) within or between the polymer chains.[192,193] Polyampholytes that contain cationic and anionic moieties in the same macromolecules have several potential applications in drug delivery and water-born formulations due to their pH-sensitive behavior.[196,197]

The LB method allows to fabricate ultrathin films with a firm control over the molecular organization and composition. Assembly of the amphiphilic polymers at the air-water interface and in ultrathin films can be controlled by a variety of factors such as molecular are, chain architecture, composition, and interactions between the substrate and the star polymer.[132] Tailoring these properties allows for the development of ultrathin films for applications in advanced functional systems such as coatings, sensors, and drug carriers.[80,198] Assembly of pH responsive $PS_n(P2VP\text{-}b\text{-}PtBA)_n$ star terpolymer and its heteroarm star copolymer precursors PS_nP2VP_n, was studied in both the Langmuir and LB films [199]. The star polymer PS_nP2VP_n containing free P2VP segments, shows a strong pH dependency and forms different morphologies such as unimolecular circular micelles and labyrinth structures at different pH values and surface pressures. These surface micelles are formed around PS cores with P2VP arms radiating outward in a star-fish like fashion. However, $PS_n(P2VP\text{-}b\text{-}PtBA)_n$ with P2VP as the midblock maintained the same circular morphology regardless of the pH and surface pressures. In another study, surface micelles formed in the LB monolayer of star PS_nP2VP_n with different numbers of arms and composition were utilized as a template to grow gold nanoparticles at the solid-air interfaces and showed that the particle size distribution can be varied by changing the number of arms of the star polymers. [200]

The terpolymers, constituted of weak polyelectrolytes, P2VP and PAA segments, in the diblock, are expected to show strong pH responses over a wide pH range in contrast to $PS_n(P2VP\text{-}b\text{-}PtBA)_n$ with hydrophobic P*t*BA end block as previously demonstrated.[199] The amphoteric nature of the arms, which is a distinct and novel feature of these star polymers,

is expected to make available diverse supramolecular structures through a variable balance of H-bonding and electrostatic interactions over a wide range of pH values (1-10). Even though there are some reports on pH dependant surface morphologies of LB films of star polymers of different types, such as PS_nP2VP_n, and $PS_n(P2VP\text{-}b\text{-}PtBA)_n$, most of these studies are limited to a small range of pH due to the presence of only one type of pH responsive block or non-responsive block at the end of the arms. Even though the assembly of the star terpolymers in solution has been studied extensively,[70,74,192,193] their surface behavior at the air-water interface has not been studied rigorously.

In this chapter, we focus on the pH-dependent behavior of novel, pH-sensitive amphoteric $PS_n(P2VP\text{-}b\text{-}PAA)_n$ star terpolymers possessing different numbers of arms i.e. n = 9 (H9) and 22 (H22) at the air-water interface at four subphase pH values: 1, 3.5, 6, and 10. We addressed the question how local architecture of star macromolecules with different crowding conditions as well as their local conformation at different pHs affect their behavior and morphology at interfaces. We observed that the pressure–area (π–A) isotherms and the morphology of the LB film are strongly dependent upon pH and surface pressure conditions and are very different for star polymers with different number of arms. The star block copolymer with a small number of arms (n=9) was found to exhibit strong pH-dependent phase transformation from circular micelles to complex labyrinth structures in contrast to the star polymer with a larger number of arms (n=22) in which the crowded branched architecture prevents the internal reorganization under variable external conditions.

5.2 Experimental Details

Materials. The PS_n(P2VP-*b*-PAA)$_n$ heteroarm star block terpolymers were synthesized according to a previous procedure reported elsewhere.[69,70,126,128] All samples have been characterized by a combination of gel permeation chromatography and static light scattering (SLS) and are summarized in Table 5.1.

Table 5.1: Molecular Characteristics of the PS_n(P2VP-*b*-PAA)$_n$ Star Block Terpolymers.

sample	Number of arms	PS		P2VP		PAA		Φ_{P2VP} [e]	$M_{w,\,tot}$ [f]
	n [a]	M_w [b]	N_{PS}	M_w [c]	N_{P2VP}	M_w [d]	N_{PAA}		
H9	9.2	3,400	33	13,200	126	4968	69	0.61	199 000
H22	21.7	3,500	34	14,300	136	8568	119	0.54	572 000

[a] average number of arms of each kind by SLS, [b] by SEC, [c] calculated by subtracting the M_w of the PS_n from that of PS_nP2VP_n and dividing by the number of arms n, [d] calculated, by subtracting the M_w of the PS_nP2VP_n from that of PS_n(P2VP-*b*-PtBA)$_n$ and dividing by n, considering quantitative hydrolysis of tBA to AA, [e] P2VP weight fraction. [f] M_w of heteroarm star terpolymer (calculated).

Zeta-potential measurements were carried out at 25°C by means of a NanoZetasizer, Nano ZS Malvern apparatus. The excitation light source was a 4 mW He-Ne laser at 633 nm and the intensity of the scattered light was measured at 173°. Aqueous solutions of H9 and H22 at different pH values ranging from 1 to 12 at a concentration of 0.2 wt% were prepared for the electrophoresis measurements.

Fabrication and characterization of monolayers. π-A isotherms of the star terpolymers at the air-water interface were recorded on a KSV2000 mini trough equipped with a Wilhelmy plate for pressure sensing. Nanopure water (Nanopure system, Barnstead, resistivity ≥ 18.2 MΩ. cm) was used as the subphase.[131] All experiments were carried out at a constant temperature of 25°C in a clean environment. The pH of the water subphase was adjusted within the range of pH 1-10 by using hydrochloric acid and sodium hydroxide without a buffer system. Solutions of 0.1-0.5 mg/ml of a star polymer was dissolved in a non-selective solvent mixture of dimethylsulfoxide/dimethylformamide/chloroform ((DMSO/DMF/$CHCl_3$), HPLC grade) and spread 80-100 μL of the polymer solution uniformly at the air-water interface. The Langmuir film was then allowed to equilibrate for 30 minutes at the air-water interface. Compression of the monolayers was conducted at a speed of 5 mm/min. The Langmuir monolayers were then transferred onto a silicon wafer by a vertical dipping method at a dipping rate of 2 mm/min and different surface pressures (1, 5, 10 and 20 mN/m) which represent different phase states.

5.3. Results and Discussion

5.3.1. Chemical structure and pH responsive property:

To understand and explore the effects of molecular architecture and subphase pH on the assembly behavior of star terpolymer at the air-water interface and in LB films, we have synthesized and studied two different star terpolymers with different numbers of arms (H9 and H22) and focus on their comparative studies. Although the synthesis and solution behavior have been reported earlier[46,47] the surface behavior of these star polymers have not been studied.

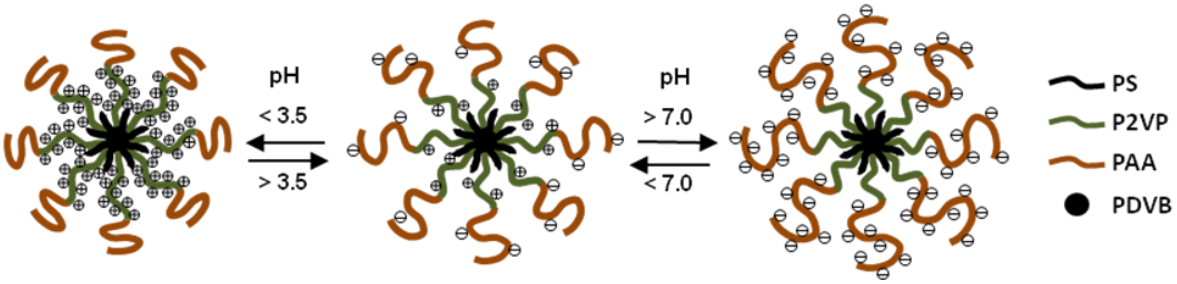

Figure 5.1: The amphoteric heteroarm $PS_n(P2VP\text{-}b\text{-}PAA)_n$ star terpolymer with the variable ionization conditions at different pH values.

The amphoteric star terpolymers investigated in this study have a heteroarm structure composed of the same number of hydrophobic PS segments and P2VP-*b*-PAA diblocks anchored to polydivinyl (PDVB) core (Figure 5.1). The number of arms can be defined by either the PS arms or P2VP-*b*-PAA diblock arms. The ratio of the degree of polymerization of PAA to P2VP is in the range of 0.5 to 0.9 (see the detail characteristics

in Table 5.1). Nevertheless the different acid to base molar ratio does not change the isoelectric point position.

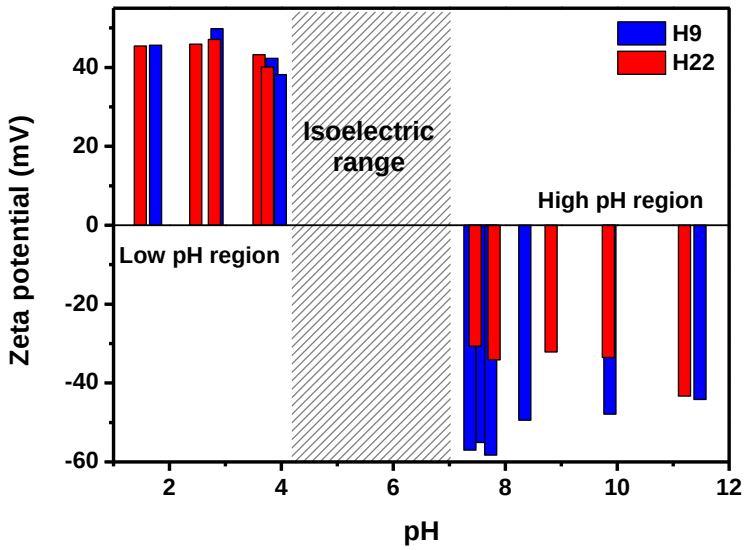

Figure 5.2: Zeta potentials at different pH of the H9 and H22 star terpolymers in aqueous solutions. The dashed area denotes the regions where the polymers precipitate.

The P2VP-*b*-PAA di-block arm undergoes ionization to a different extent depending on the pH of the subphase. As a result of the amphoteric nature of the arms, a variety of supramolecular assemblies can be obtained by the star polymer at the air-water interfaces as well as in LB films depending upon the ionization conditions which depends upon their pK_a. As expected, P2VP had a pK_a value of 5 while PAA had a value of 5.5 (Figure 5.2).[192]

It is known that P2VP blocks are expected to be protonated at lower pH while the PAA blocks remain unionized. Thus the polymer behaves like a cationic polyelectrolyte at

lower pH values. As the pH increases, the PAA units start to undergo ionization (deprotonation) that leads to the formation of a zwitterionic structure in the star polymer 3<pH<6. The polymers were found to be precipitate in the region 4.2<pH<7 due to charge neutralization and the transformation of P2VP to hydrophobic. This pH range is considered to be *the isoelectric region* (IEP) of the star polymers. Further increase in pH (pH>7) leads to a complete deprotonation of the PAA blocks causing them to behave like a negatively charged polyelectrolyte (Figure 5.2). Thus a variety of intra and inter molecular associations are possible at different pH conditions, in contrast to traditional star block copolymers with one type of polyelectrolyte arms.

Indeed, as is well known, at the extreme pH conditions used in this study (pH= 1 and 10) one of the blocks in the diblock arm is ionized and the charge on the polymer is determined by the pH of the subphase. At low pH, the P2VP blocks are protonated (ionized) and the PAA are marginally soluble in water while PS segments exist as hydrophobic moieties. Thus intermolecular association is possible through hydrophobic interactions between the polymers. In addition to this, due to the presence of carboxyl group, the polymers can associate through intermolecular hydrogen bonding. At higher pH, most of the carboxyl groups are ionized and therefore hydrophobic interactions through PS and P2VP segments predominate. However in the isoelectric region, electrostatic interactions between the oppositely charged polymer chains are expected to occur and hence strong inter or intra molecular interactions arise depending on the number of arms present in the star terpolymer.

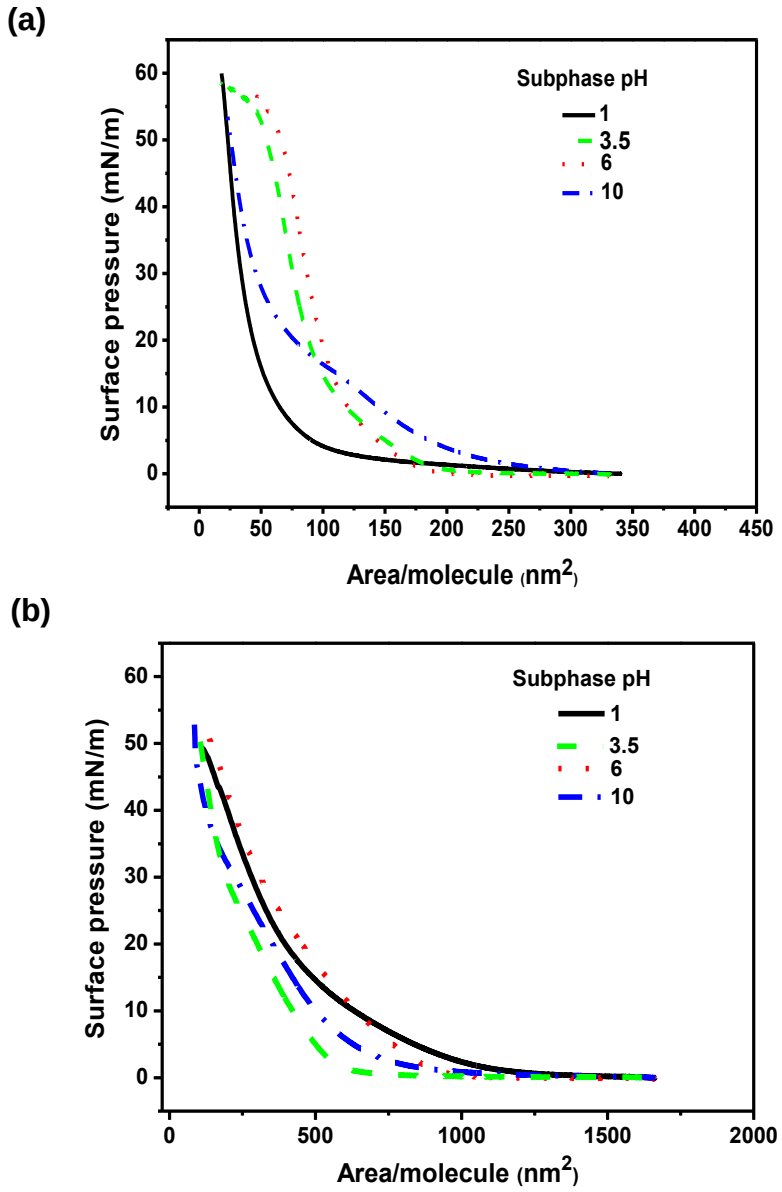

Figure 5.3: Pressure-area isotherms of (a) H9 and (b) H22 star polymers obtained at different subphase pH values.

The π-A isotherms obtained for the two star polymers with different number of arms, H9 and H22, are shown in Figure 5.3. As evident from these isotherms, the two star polymers form a monolayer at the air-water interface. For this deposition, the solvent

mixture (DMSO/DMF/$CHCl_3$) with a low concentration (0.10-0.50 mg/ml) was chosen in order to prevent the formation of multistar micelles in the solution. The aprotic polar solvent dissociates the strong complexation of the P2VP and PAA block that occurred during the hydrolysis process. A higher percentage of chloroform (60%) in the solution mixture facilitates the fast spread of the polymers to the air-water interface.

In order to investigate the assembly behavior at different pH conditions, four different subphase pH conditions (1, 3.5, 6, and 10) were chosen (Figure 5.3a). The choice of these pH values were made based on the zeta potential measurements and pK_a values of the pH responsive blocks present in the star terpolymers. We did not investigate the assembly behavior for higher pH values (> 10) because entire ionization of the PAA moieties are attained at pH=10 [201]. The π-A isotherms show gradual increases in the surface pressure as the compression progresses. The pressure starts to increase at a molecular area of 170 nm^2 (obtained by extrapolating the high pressure region of the π-A isotherm). A steep pressure increase at lower molecular area suggests a close packed assembly of the star polymers at higher compression.

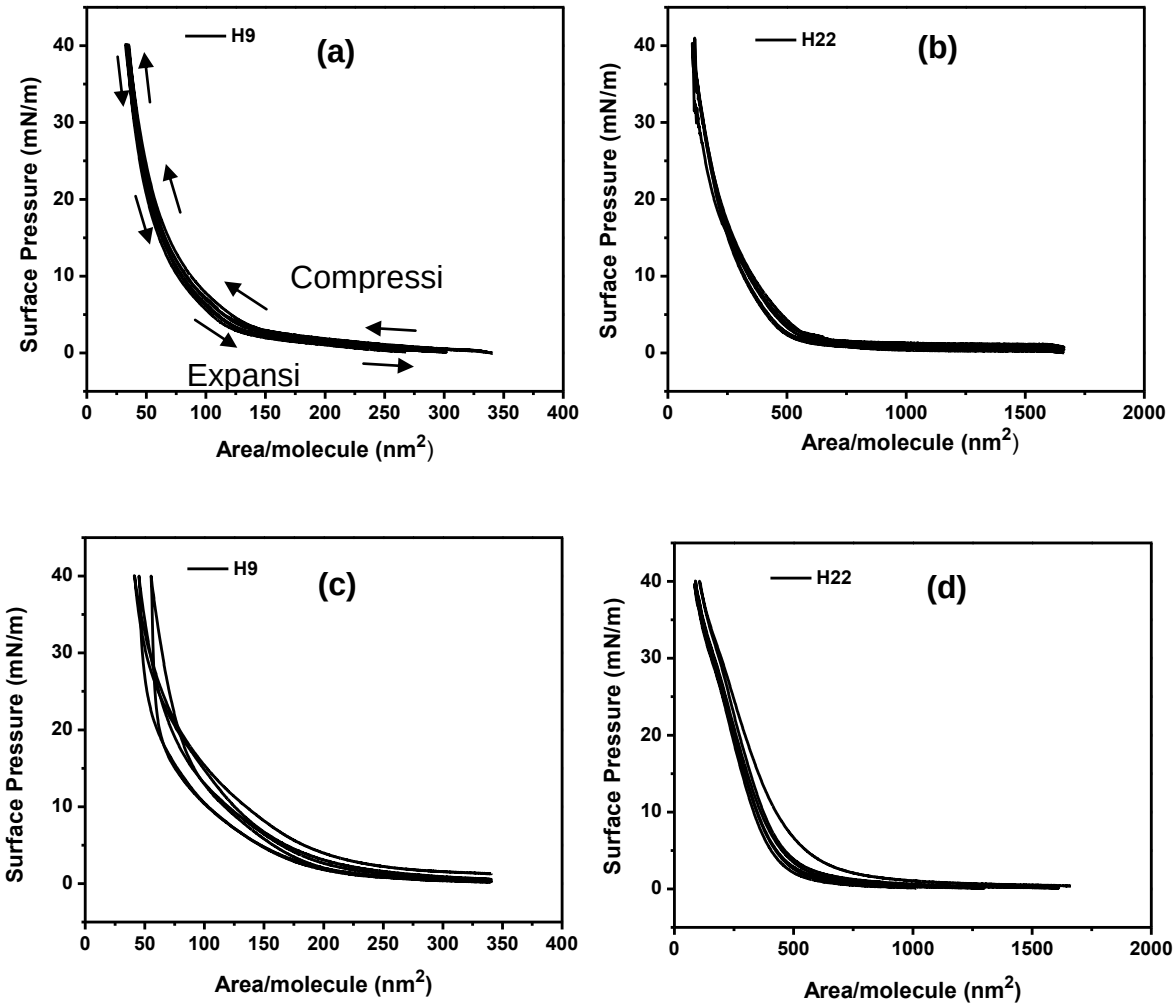

Figure 5.4. Pressure-area isotherm cycles of star terpolymers at subphase pH = 1 ((a) and (b)) and pH = 10 ((c) and (d)). The direction of compression and expansion of the monolayer is also shown.

Star polymer H9 behaves differently under various pH conditions of the subphase, suggesting that H9 adopts different conformations at the interface. Interestingly, at pH=1 the steep rise in pressure commences at a lower molecular area compared to what occurs for other pH conditions. This behavior may be caused by the high solubility of P2VP chains in the aqueous phase and cannot be considered as surface active chain at pH=1.[202] However, the presence of hydrophobic PS and PAA blocks assures the amphiphilic

balance and thus the star polymer forms a stable monolayer at the air-water interface. The area per molecule for H9 at pH=1 is approximately 50 nm^2 which is considerably lower than that observed for pH = 3.5, 6, and 10 (102, 130, and 85 nm^2, respectively).

Furthermore, the stability of the Langmuir film was investigated by performing π-A isotherm cycles experiments. The repeated π-A isotherm cycles (3 cycles) up to surface pressure of 40 mN/m for H9 and H22 for pH=1 and 10 are shown in Figure 5.4. The monolayer was compressed to the target pressure (40 mN/m) and then expanded the film without holding at the target pressure. The π-A isotherm cycles show a highly reproducible compression-expansion cycle with small hysteresis, indicative of a reversible and stable Langmuir film at the interface. In particular it is found that isotherm curves show a steep drop in surface pressure at the beginning of the expansion cycle and the difference between compression and expansion curve appears to be decreased at pH=1. However, a hysteresis was observed for H9 at subphase pH =10 (Figure 5.4c). This phenomenon may be due to the strong affinity of completely ionized PAA segments (hydrophilic) with the subphase and consequent delay in chain reorganization during the expansion of the monolayer. It should be noted that for pH=1 and pH=10, the π-A isotherm of H22 reveals a minimum deviation between compression and expansion curves, which suggests that the larger arm star terpolymers remain as an individual surface micelle with higher colloidal stability which prevents high domain aggregation under compression (Figure S5.1). The small difference in the area of the isotherm cycles for H22 compared to that shown in Figure 5.3 is likely due to the inherent experimental variability associated with different solution preparation and the deposition.

Figure 5.3b shows the π-A isotherm obtained for H22 for different subphase pH conditions. Even though H22 shows pH responsive behavior, a dramatic change in its interfacial behavior was not observed. As expected, H22 exhibits a larger area per molecule compared to that of H9. This difference can be attributed to the higher number of arms present in the terpolymer. All the π-A isotherms of H22 show very low surface pressure over large molecular area, as seen in Figure 5.3b. This indicates that there are well separated polymer domains at the air-water interface during the initial compression of the monolayer. The slope of the π-A isotherms were found to be smaller than that observed for H9 which indicates that the film is more compressible at the interface. This difference may be due to the fact that the area exhibited by H22 (higher molecular weight) indeed includes the trapped or dead area which is significantly higher than that exhibited by H9 (lower molecular weight).

The area/molecule obtained for the two polymers at different pH conditions are shown in Figure 5.5. As expected, H22 shows a much higher limiting area for all subphase pH values, likely due to the larger number of arms resulting in more extended chain conformations for star polymers with larger arms. These arms restrict chain reorganization within the polymer by steric hindrance or reduced internal space. The higher content of PAA segments in the H22 facilitates a stronger interaction with the water surface at higher pH values, causing a closed packing (Figure 5.3b). Interestingly, a minor transition is observed around 30 mN/m which is not as significant as that observed for H9 at pH=10 as discussed in detail below.

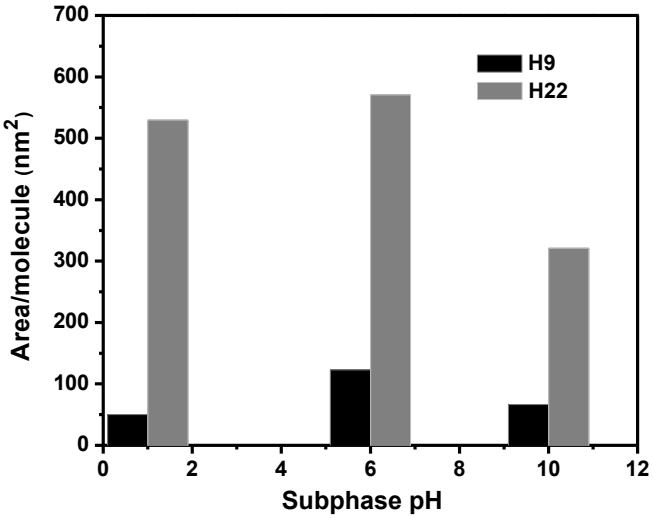

Figure 5.5: Variation of the limiting molecular area (at the highest surface pressure) with subphase pH and number of arms.

To gain insight into the area occupied by star polymers with different chain conformations, we estimated the dimensions of the star polymer with extended and random chains for diblock (P2VP-*b*-PAA) arm using usual contour length calculations assuming theta solvent conditions.[203] The area per molecule was estimated to be about 6375 and 12000 nm^2 for H9 and H22, respectively, if the diblock arm adopts a fully extended conformation. However, these values are much higher than that obtained from pressure-area isotherms (Figure 5.5). The estimation was done by assuming that the star polymers form a 2D assembly (circular) at the air-water interface. On the other hand, the area/molecule calculation, assuming random coil conformation, from the radius of gyration yields values of 14 nm^2 and 23 nm^2, for H9 and H22, respectively [203]. We assume that, at pH=1, the P2VP chains are submerged in the subphase and thus the area/molecule observed is the area occupied by the collapsed PAA chains at the interface.

These area/molecule values are well below those obtained from the π-A isotherms which indicates that both star polymers are spread at the air-water interface but this spreading does not reach the fully extended state.

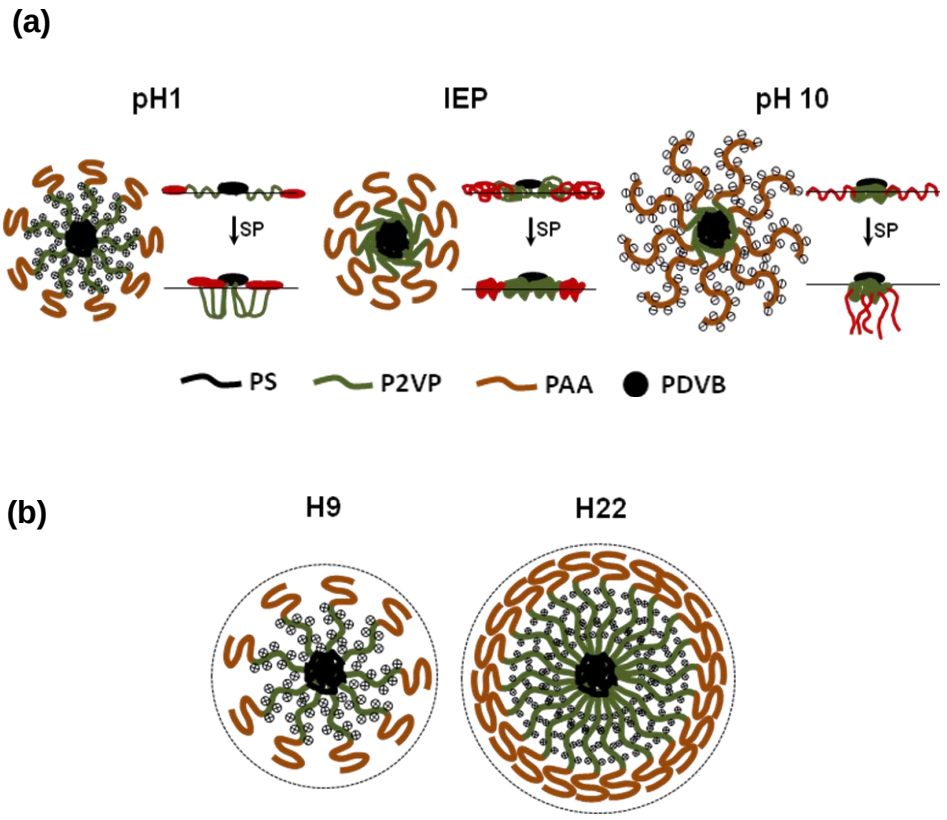

Figure 5.6: (a) Different conformations adopted by the terpolymer at various subphase pH conditions and surface pressures (SP) at the air-water interface. (b) Unimolecular micelles which can be formed by H9 and H22 star polymers. IEP is isoelectric point.

The star polymers tend to aggregate in the isoelectric region mainly because of the reduced charge-related repulsion that eventually decreases the colloidal stability. As a result, the surface activity of the polymer is expected to be reduced in the isoelectric range and the surface micelles likely remain confined at the air-water interface which leads to a higher molecular area. Thus we suggest that in the isoelectric region, the star polymers form pancake like structure with arms widely spread at the interface (Figure

5.6a). The changes in the surface area per molecule at different pH values is ascribed to different molecular conformations adopted by the polymer at various subphase pH values (Figure 5.6a).

In contrast, at pH=10, the anionic PAA chains submerge in water to minimize the repulsive force between negatively charged PAA segments. It is expected that as the pH increases, the polymer transforms from bis-hydrophilic (P2VP, PAA hydrophilic segments) to bis-hydrophobic (PS, P2VP) that alter the amphiphilic balance of the terpolymer. The highly ionized PAA arms are susceptible to external compression due to their enhanced hydrophilicity which allows them to submerge into water as the compression proceeds (Figure 5.6a). The isotherm shows a small transition around 15 mN/m suggesting a shift from a pancake form to a more vertical reorganization of the chains at the air-water interface.[204] The isotherm shows a reduced surface area per molecule under these conditions suggesting a transition from pancake to a more compressed organization of the chains at the air-water interface (Figure 5.5). This difference suggests that the PAA blocks submerge in water and that the P2VP and PS chains collapse at the interface as the compression progresses. In order to verify this reorganization at the air-water interface, we conducted AFM imaging of Langmuir monolayers after transferring them to a hydrophilic substrate at different pH conditions.

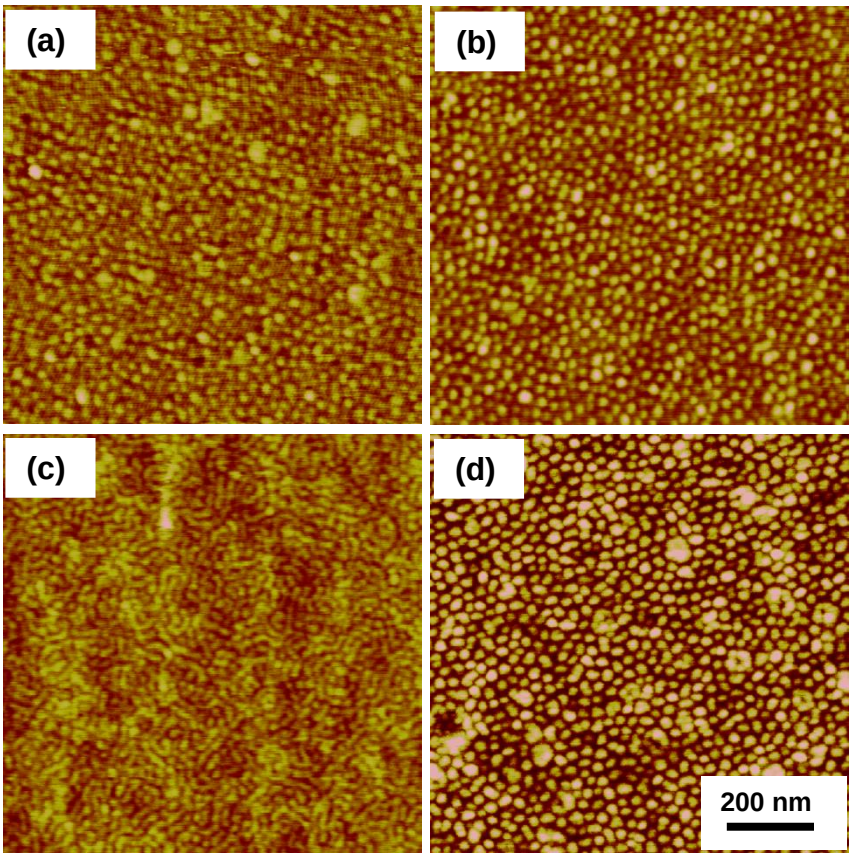

Figure 5.7: AFM images of monolayer LB films of H9 [(a) and (c)] and H22 [(b) and (d)] fabricated at a subphase pH of 1 and at surface pressures of 1 mN/m (a, b) and 20 mN/m (c, d).

5.3.2. Surface morphology in the LB films:

LB monolayers were obtained by transferring the Langmuir film onto hydrophilic substrates at different pressures (1, 5, 10, and 20 mN/m) and subphase pH (1, 3.5, 6, and 10) and studied with AFM. Only LB films that showed appreciable transfer (90% or above) under different conditions are considered in the present study. Based on AFM imaging of the LB films at different surface pressures and the good correlation between pressure-area isotherm and morphology evolution, we suggest that the star polymer retains its morphology in the LB films even though the interactions at the interface may be slightly different on hydrophilic silicon wafer in accordance with well-know and

accepted paradigm.[164,191] Figure 5.7 shows the AFM images of the H9 monolayer fabricated at different surface pressures with a subphase pH=1. The star polymer shows formation of circular micelles at a very low surface pressure (1 mN/m). As the pressure increases, the circular micelles seem to interact with each other to form closer packed structures (Figure S5.1, S5.7, and S5.8).

At a higher surface pressure (20 mN/m), most of the circular structures have deformed and associated together to form the labyrinth patterns that were observed earlier for the star block copolymer precursor (Figure 5.7c, S5.1).[199] The formation of the labyrinth pattern is ascribed to the aggregation of the hydrophobic PS core micelles. In addition, the presence of unionized PAA segments in the terpolymer offer intermolecular interactions through hydrogen bonding at lower pH which is also responsible for the association of circular micelles at high surface pressures. The average film thickness was found to increase from 1.5 to 3.2 nm as the surface pressure increased to 20 mN/m (Table S5.1). This trend clearly suggests that the H9 star polymer undergoes a transition from pancake morphology to brush morphology where most of the P2VP chains are submerged in the subphase as the compression of the monolayer continues and thus allow for further merging of hydrophobic blocks as suggested by isotherm-based models (Figure 5.6). The lateral dimension of the circular micelles, estimated from AFM cross-sections, is close to 15 nm (after correction for tip dilation) for both star polymers in the expanded state (pressure 1 mN/m) which is close to the estimated molecular diameter of H9 and smaller than that for molecules with a larger number of arms. The comparison of the molecular and micelle volumes leads to the conclusion that the H22 star polymer forms truly

unimolecular surface micelles whereas 3-4 molecules are included in the surface micelles formed by the H9 star polymer.

Moreover, in contrast to H9, a dramatic change in morphology with surface pressure was not observed for H22 star polymer with larger number of arms (Figure 5.7b, d). Similar to H9, at low surface pressure the polymer forms a circular micellar structures. However, increasing the number of arms and the aggregation number makes the micelles more stable and well separated. The circular micellar structures become closely packed as the surface pressure increases. Even though some minor association of the circular structure is observed at higher surface pressures, most of the circular micelles maintain their original shape (Figure 5.6b). We suggest that the intermolecular association through hydrophobic PS arm interactions is hindered as a result of the limited interpenetration and suppressed entanglement associated with dense shells formed by multiple arms in the H22 star polymer (Figure 5.6). The morphology difference at pH=1 is likely due to the difference in PAA chain length in the two star terpolymers. The circular to labyrinth morphology transition was observed only for H9 and can be attributed to lower PAA chain length, which seems to enable short PAA chains to submerge in the subphase along with highly protonated P2VP segments upon compression. However, this is not observed for H22 due to higher segment density, longer PAA chain length, and the H-bonding they may develop.

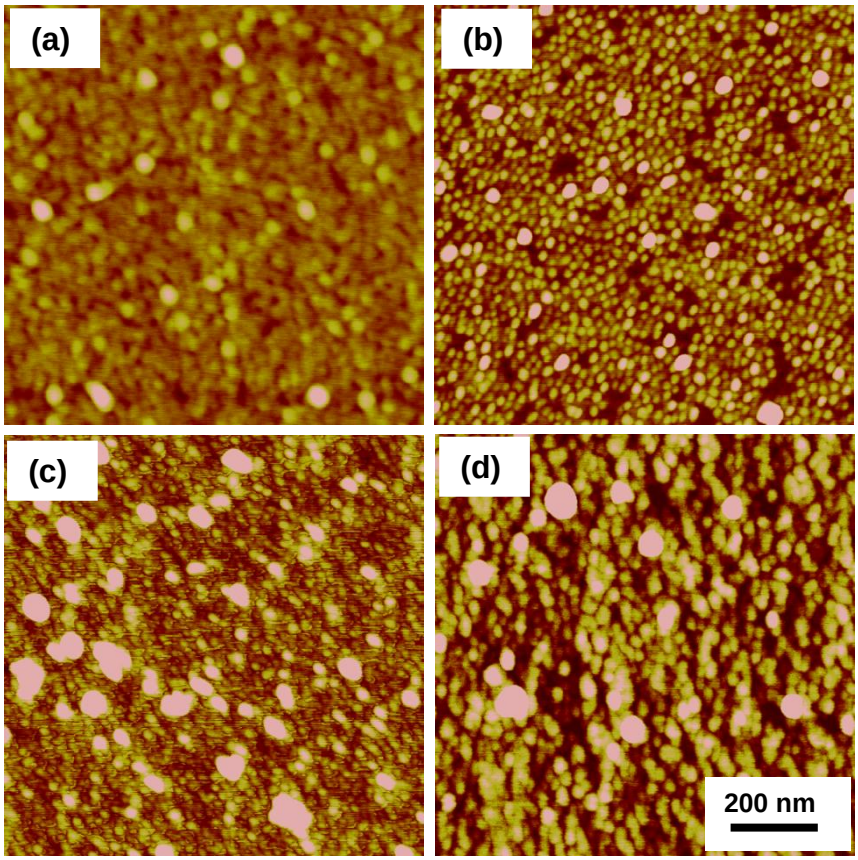

Figure 5.8: AFM images of monolayer LB films of H9 [(a) and (c)] and H22 [(b) and (d)] fabricated at a subphase pH of 3.5 and at surface pressures of 1 mN/m (a, b) and 20 mN/m (c, d).

Figures 5.8 and S5.2 show AFM images of the LB films fabricated with a subphase pH of 3.5. As clearly seen from the AFM images, H9 forms circular micelles with a larger amount of aggregation that are found to be close packed as the surface pressure increases (Figure 5.8c). As a result of the ampholytic character or zwitterionic structure (due to partial ionization of the segments), an electrostatic interaction between the oppositely charged blocks is expected which results in the association of the polymers even at very low surface pressures. As suggested by the π-A isotherms, the H9 polymer adopts very different molecular conformations in Langmuir films with a subphase pH of 3.5. As the

subphase pH increases, the degree of ionization of the acid/base blocks of the polymer is expected to vary, and hence, a variety of inter or intra molecular interactions are expected to occur. At pH=3.5, the number of protonated pyridine groups must be lower than that at pH=1 while the extent of ionization of the PAA segments increases as the pH increases, which leads to star precipitation in the pH range of 4.2 to 7 (isoelectric range).[201,205]

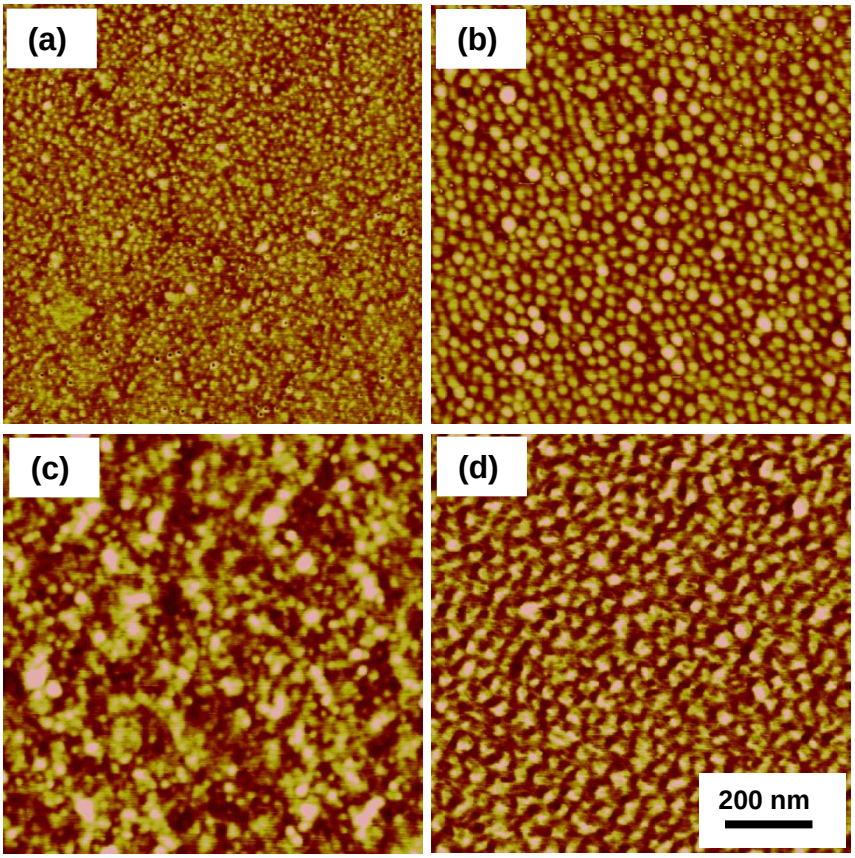

Figure 5.9: AFM images of monolayer LB films of H9 [(a) and (c)] and H22 [(b) and (d)] fabricated at a subphase pH of 10 and at surface pressures of 1 mN/m (a, b) and 20 mN/m (c, d).

Well defined circular micelles with some aggregates are observed for H22 at lower surface pressure as well (Figure 5.8). At higher surface pressure, modest association of the unimolecular micelles is observed but without forming continuous morphologies

(Figure 5.8b, d). For the higher number of arm star polymer, the original circular structures are preserved at higher compression due to steric hindrances which restrict chain reorganization The AFM images of the LB films fabricated at a subphase pH of 6 are shown in Figure S5.4 and S5.5. Similar to pH=3.5, larger aggregates are formed mainly because of the hydrophobic interactions of the neutral polymer chains.

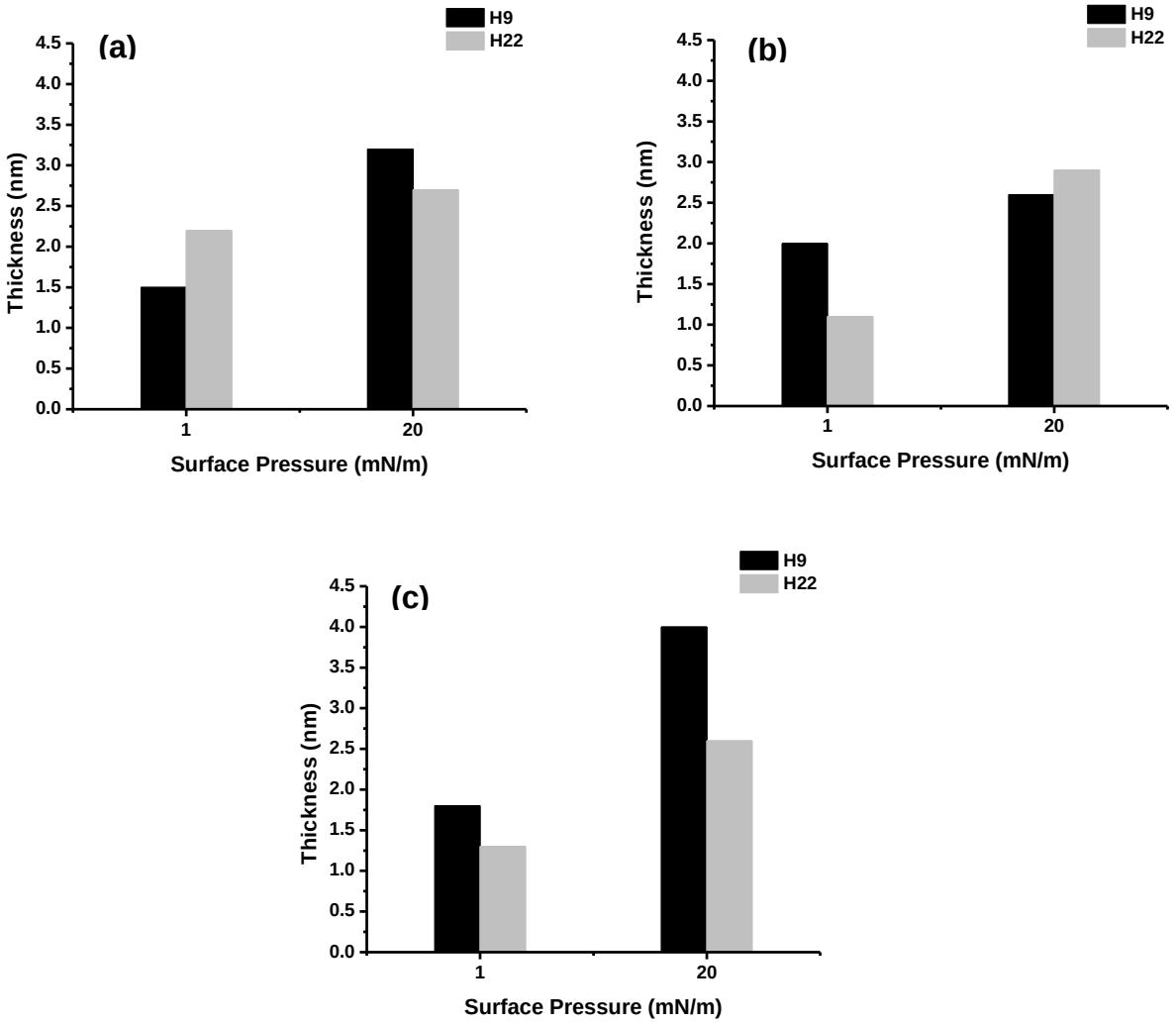

Figure 5.10: The thickness of the LB films fabricated with H9 and H22 at different surface pressures and a subphase pH of (a) 1, (b) 6 and (c) 10.

At pH=10, all the PAA segments are expected to be ionized completely and the polymer transforms from bis-hydrophilic to mono-hydrophilic. The AFM images for the monolayer LB film fabricated at pH=10 are shown in Figure 5.9 and S5.6. Circular micellar structure formation was observed for H9 at a low surface pressure (Figure 5.9a). At lower surface pressure (1mN/m), the polymer is expected to form a multicompartment hydrophobic (PS/P2VP) core with a negatively charged PAA corona [192,193]. At a surface pressure of 1 mN/m, H9 adopts a circular micellar structure where the hydrophobic chains collapse to form the core of the micelle while the corona of the micelles consists of negatively charged PAA segments spread at the interface and are submerged partially in the subphase. As the surface pressure increases, the polymer forms brush like structure as suggested by the transition point observed in the π-A isotherm. This brush structure formation is further confirmed by the increase in thickness of the dry, collapsed LB films with surface pressure. The thickness of the film was found to increase from 1.8 to 4 nm when the surface pressure increased from 1 to 20 mN/m (Figure 5.10, Table S5.1). To validate this measured thickness, we estimated the thickness of the film using the molecular weight of the polymer and the area/molecule that corresponds to the surface pressure of 20 mN/m. The estimated thickness was found to be around 6 nm which suggests a partial collapse of the polymer chains in the dry LB films. On the other hand, as the surface pressure increases, surface micelles merge to form continuous labyrinth morphology (Figure 5.9 and S5.6). A similar increase in monolayer thickness is observed for the H22 star polymer indicating some submergence of arms but the initial circular morphology remains intact even at the highest surface pressure attained. However, the film thickness of H9 is higher than that of H22 although the P2VP-PAA arm length is

lower. The star with higher segment density (H22) hinders the easy submerging of PAA units in the subphase even at pH 10. This can be attributed to the lower ionization ability of H22 due to its lower negative zeta potential (see Figure 5.2), as expected for dense stars (high arm number).[242]

In summary, the interfacial behavior of complex amphiphilic and amphoteric star-shaped terpolymers, namely $PS_n(P2VP\text{-}PAA)_n$ at the air-water interface as well as in LB films as a function of subphase pH. The presence of two oppositely ionizable polyelectrolytes blocks in the same diblock arms led to variety of inter/intra molecular interactions triggered by changing the pH of the subphase. The effect of pH on the assembly behavior was more distinct for the polymer with smaller arm density because of easy chain reorganization feasible in the polymer. In contrast, star copolymer with large number of arms exhibit a similar molecular area at the air-water interface and hence retained their circular micellar structure in the LB films at different subphase pH and surface pressures due to the restriction of chain reorganization in the polymer.

Appendix. Supplementary Information: additional information as noted in the text and AFM images of large area scans for all samples (Table S5.1, Figure S5.1-S5.9)

Table S5.1: Thickness of the LB films fabricated at different pH and surface Pressures (SP)

System	pH	Thickness (nm)			
		SP=1 mN/m	SP=5 mN/m	SP=10 mN/m	SP=20 mN/m
H9	1	1.5	2.0	3.2	3.2
	6	2	2.8	2.3	2.6
	3.5	1.7	1.9	2.0	2.2
	10	1.8	2.1	2.2	4.0
H22	1	2.2	1.8	2.2	2.7
	3.5	1.3	1.5	2.1	2.4
	6	1.1	1.7	2.1	2.9
	10	1.3	1.8	1.8	2.6

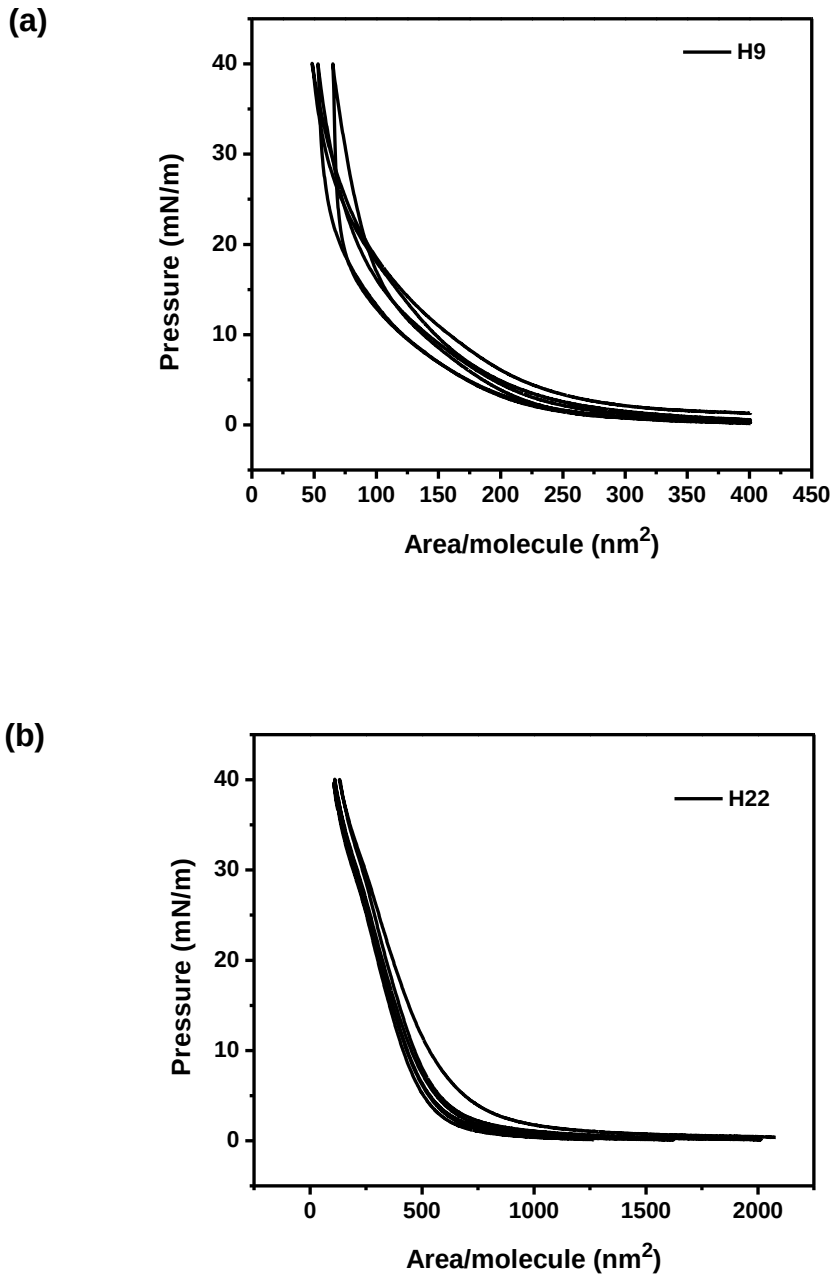

Figure S5.1: Pressure-area isotherm cycles of (a) H9 and (b) H22 at subphase pH of 10.

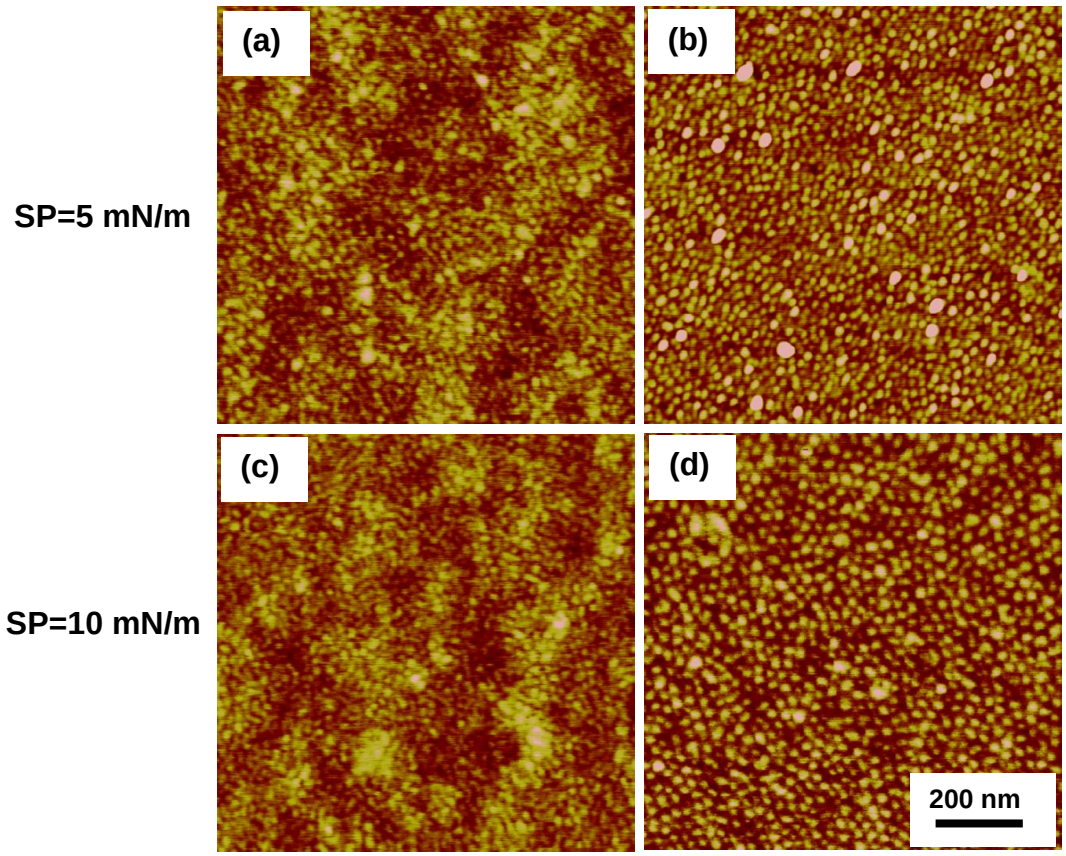

Figure S5.2: AFM images of monolayer LB films of H9 [(a) and (c)] and H22 [(b) and (d)] fabricated at subphase pH of 1 and different surface pressures.

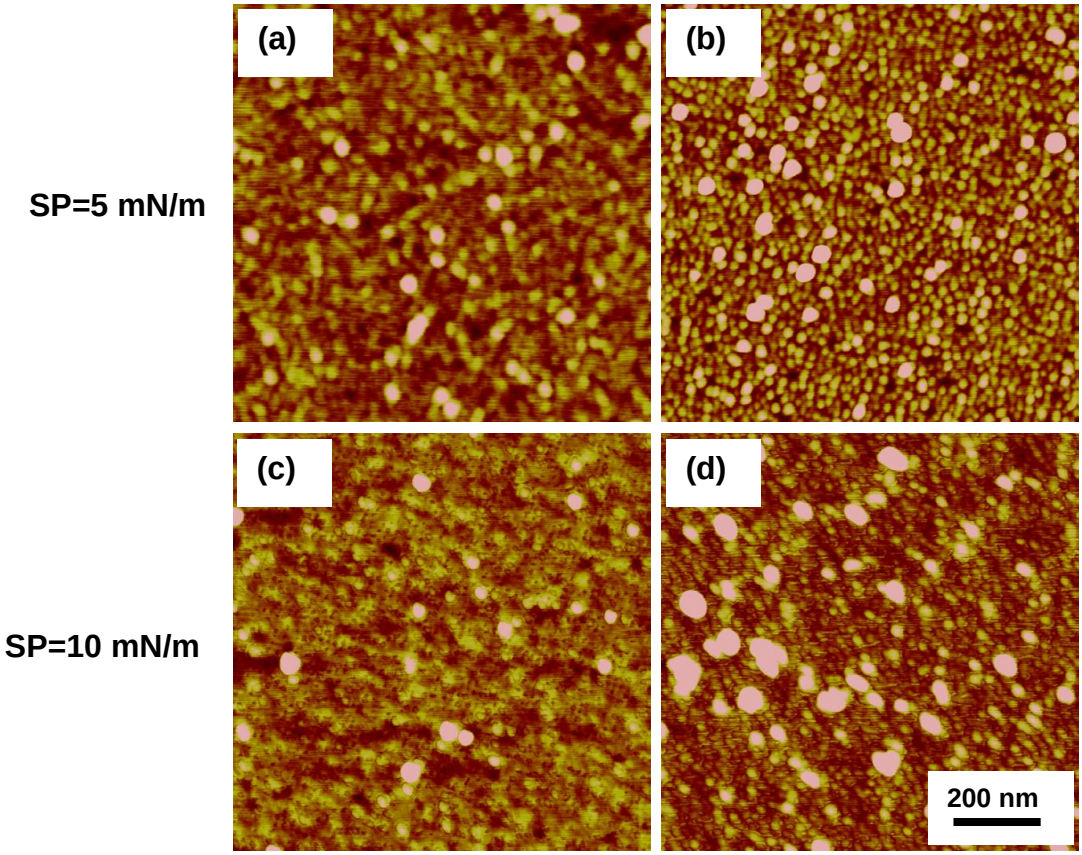

Figure S5.3: AFM images of monolayer LB films of H9 [(a) and (c)] and H22 [(b) and (d)] fabricated at subphase pH of 3.5 and different surface pressures.

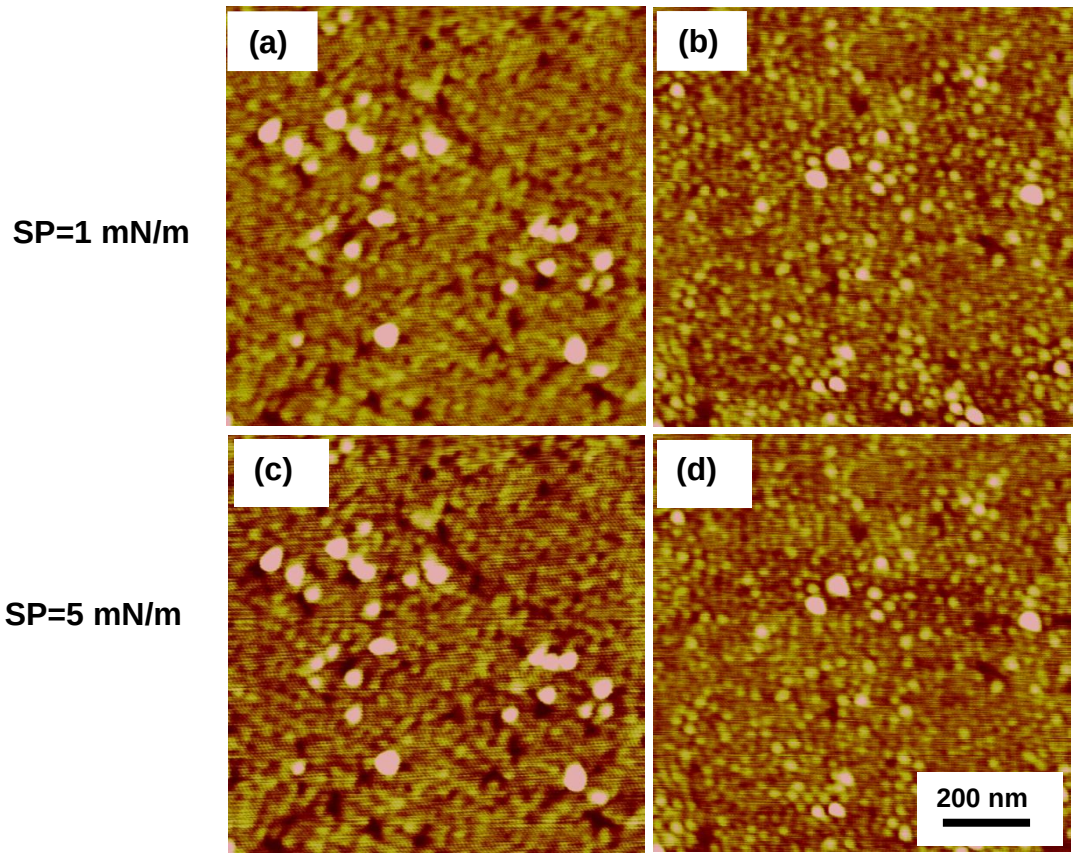

Figure S5.4: AFM images of monolayer LB films of H9 [(a) and (c)] and H22 [(b) and (d)] fabricated at subphase pH of 6 and different surface pressures.

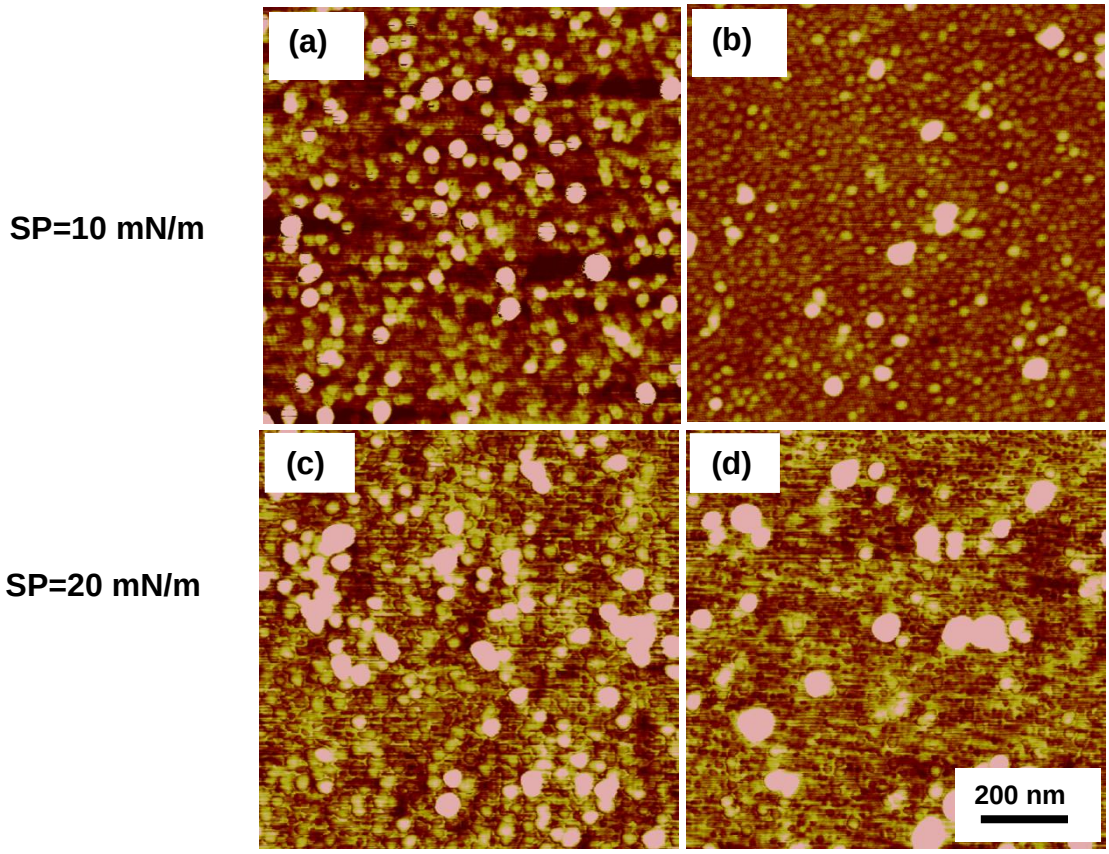

Figure S5.5: AFM images of monolayer LB films of H9 [(a) and (c)] and H22 [(b) and (d)] fabricated at subphase pH of 6 and different surface pressures.

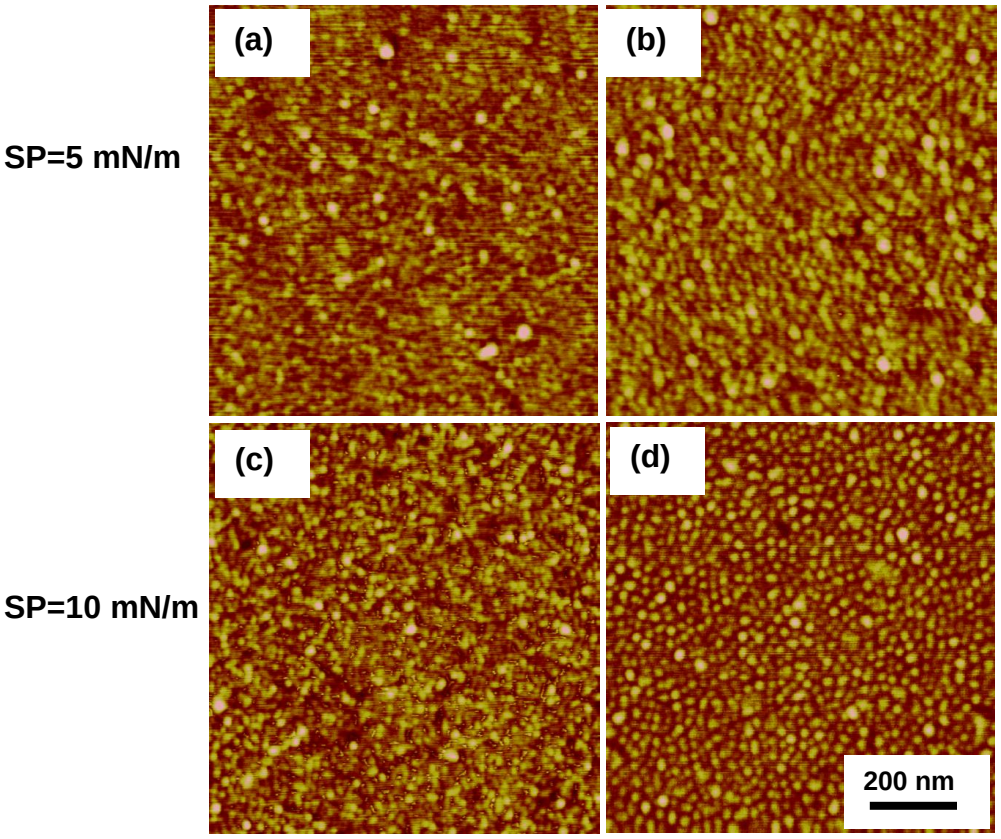

Figure S5.6: AFM images of monolayer LB films of H9 [(a) and (c)] and H22 [(b) and (d)] fabricated at subphase pH of 10 and different surface pressures.

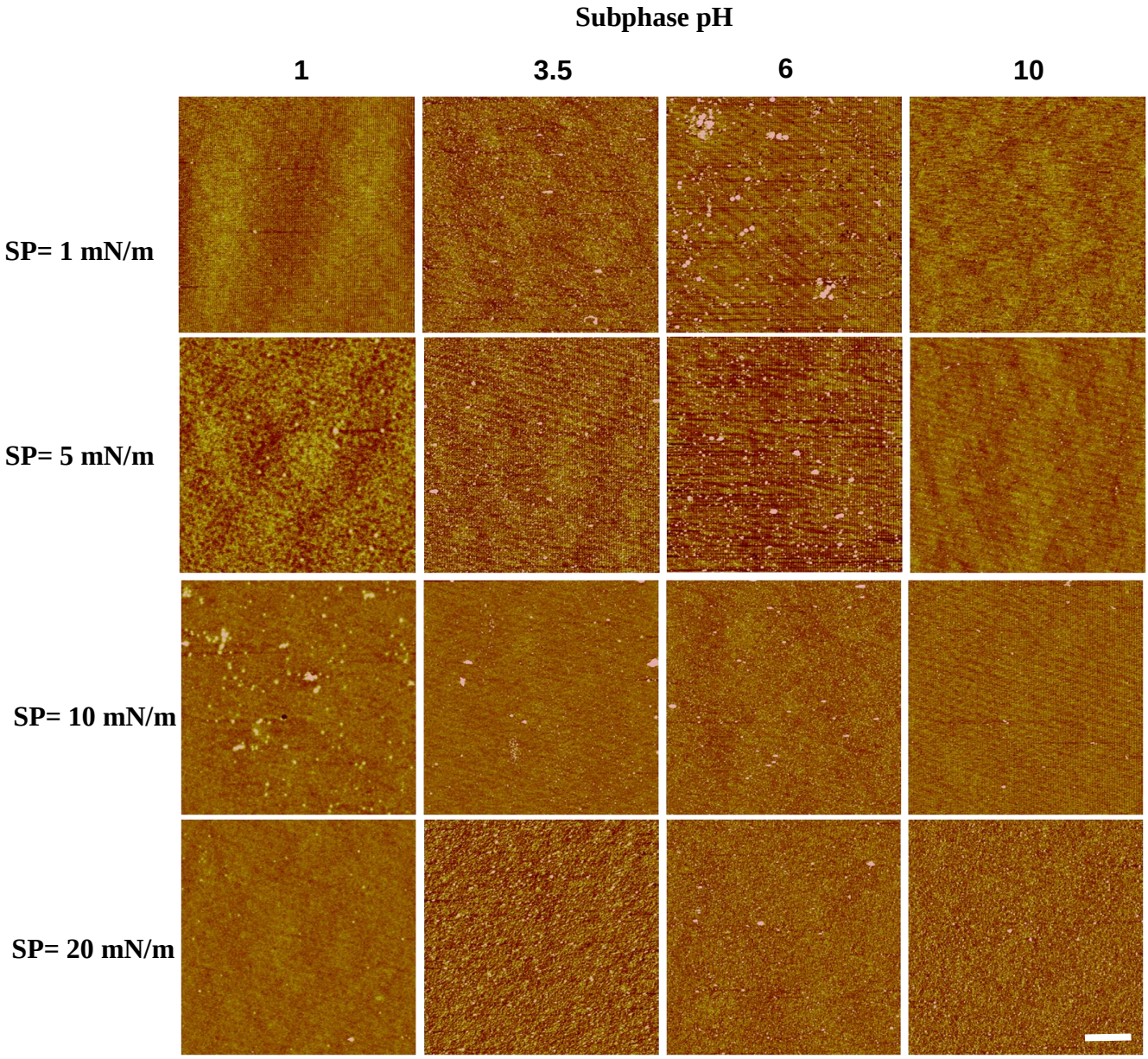

Figure S5.7: AFM images of monolayer LB films of H9 fabricated at different subphase pH values and surface pressures (SP). Scale bar = 2 µm.

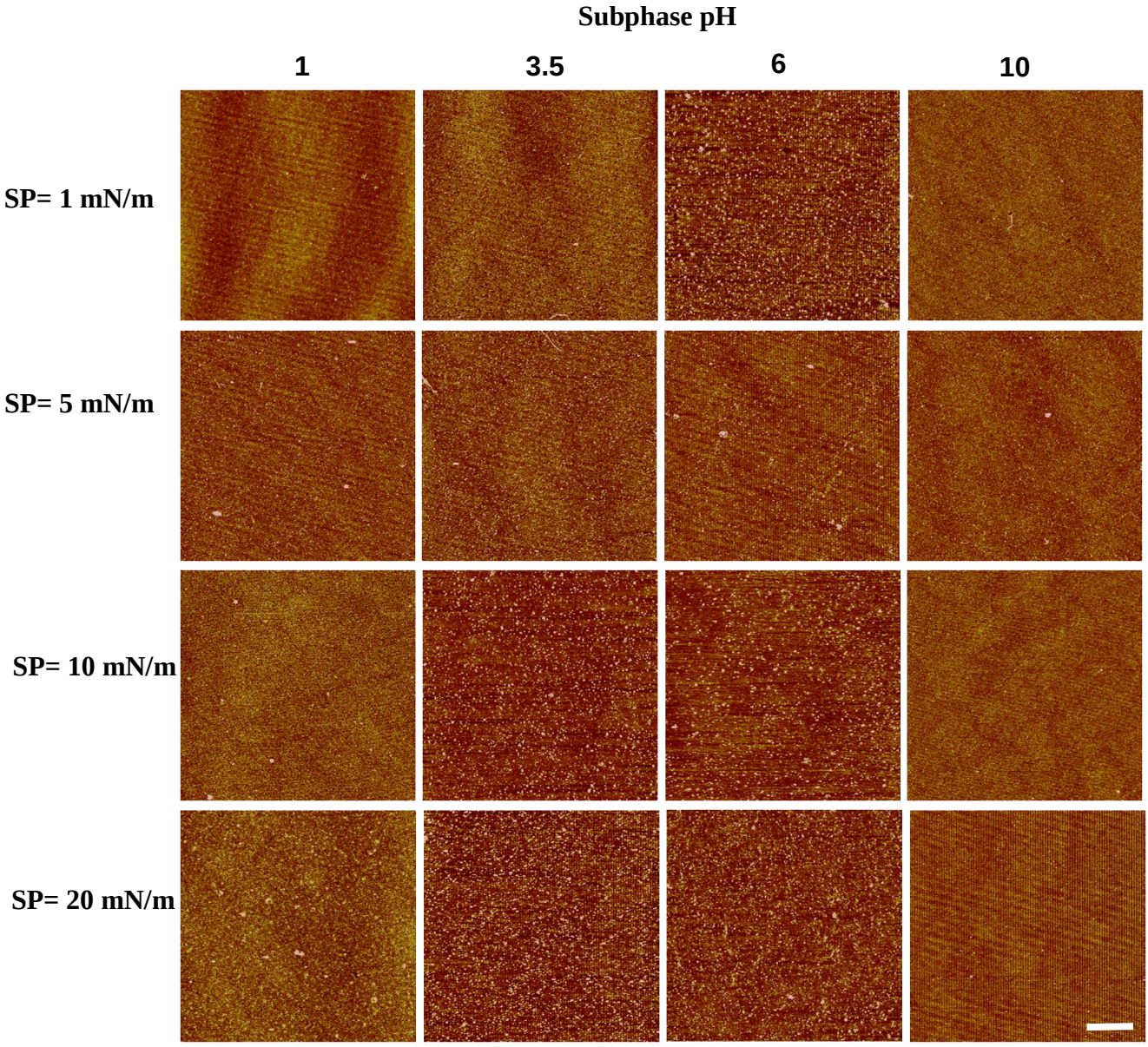

Figure S5.8: AFM images of monolayer LB films of H22 fabricated at different subphase pH values and surface pressures (SP). Scale bar = 2 μm.

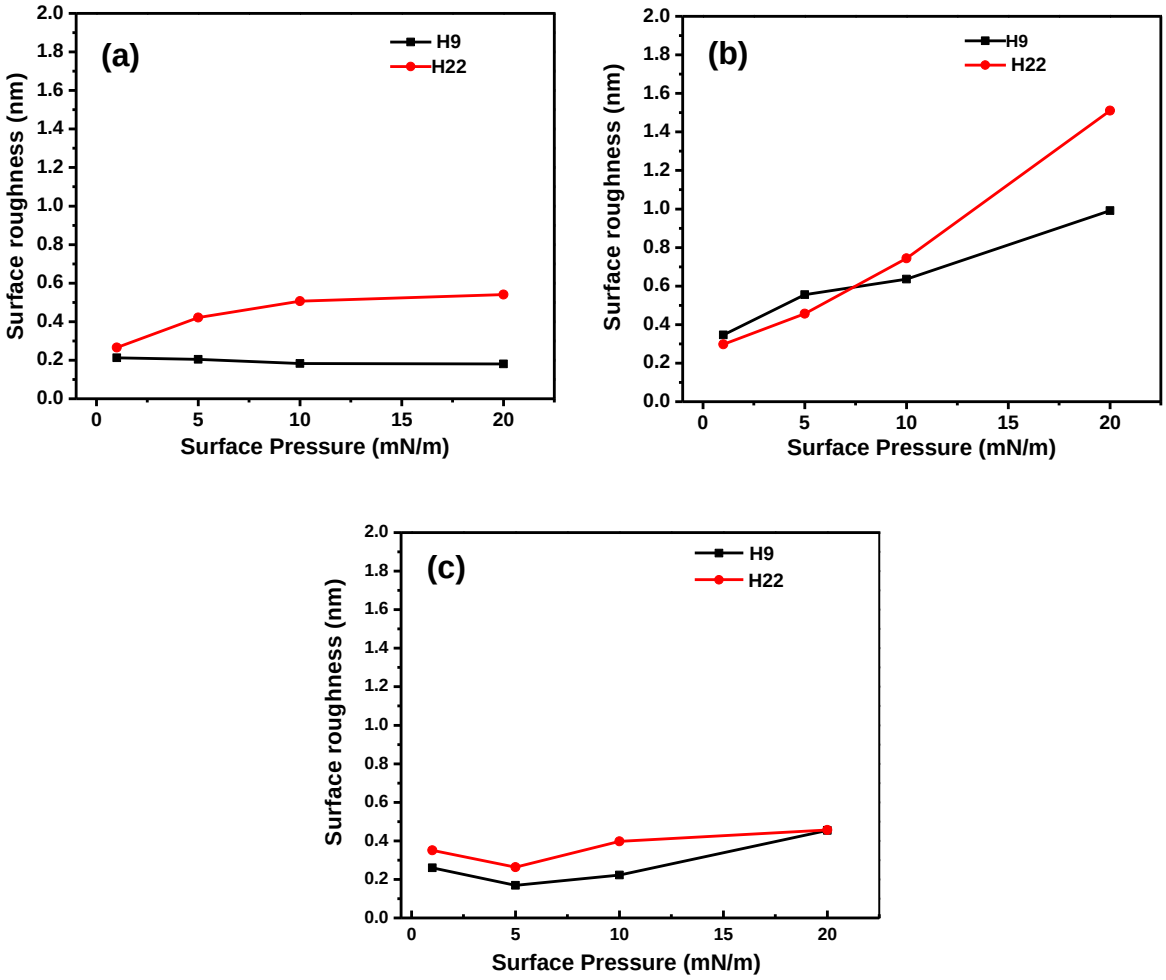

Figure S5.9. Comparison of the roughness of the LB films fabricated with H9 and H22 at different subphase pH (a) 1, (b) 6 and (c) 10.

In order to get further insight into the assembly behavior, we have estimated the surface roughness of the LB films. The variation of the film roughness with the surface pressures and subphase pH is shown in Figure S5.9. As evident from this figure, LB films of H9 form a smoother film with all different experimental conditions even though the difference is small. Interestingly, the surface roughness was found to be several times higher for the films fabricated at pH=6. This is clearly an indication of larger particles formation due to the aggregation of polymer in the film. The roughness analysis of the films also suggests that both H9 and H22 form smooth LB films for the subphase pH of 1 and 10. At these pH conditions, only one block of the diblock arms ionizes and the electrostatic interaction between the polymer which is responsible for the aggregation is minimized. As a result, smooth and continuous film formation was observed for both polymers. This study clearly demonstrates the effect of macromolecular engineering and architecture on the assembly of star block copolymer at interfaces.

CHAPTER 6

GOLD NANOPARTICLE GROWN ON STAR-SHAPED BLOCK COPOLYMER MONOLAYERS

6.1. Introduction

Growth of metal nanoparticles on organic, biological, and polymeric templates under ambient conditions is a versatile approach for the formation of organic-inorganic nanocomposites.[112,206,207,208,209,210,211,212,213,214,215] Nanocomposites containing gold nanoparticles have strong potential to be useful in many future applications in areas such as electronic devices, sensors, catalysts, or cancer therapy.[216,217,218,219] Among recent examples of polymeric templates for inorganic nanoparticle formation are histidine and tyrosine-rich proteins and synthetic amino acids for titania and gold nanoparticle formation on organic films via plasma enhance chemical vapor deposition.[220,221] Additionally, polystyrene-polyvinylpyridine block copolymer (PS-*b*-PVP) and 2-(4′-hydroxybenzeneazo)benzoic acid (HABA) have been used to facilitate nanotemplates and control the orientation of metal such as Ni nanodots and nanowires.[222] Polyvinylpyridine (PVP) is widely used to synthesize nanoparticles by itself as well as in combination with other polymers.[223] However, block copolymers with the ability to form stable micelles in solution and at interfaces are excellent candidates for preparation of gold nanoparticles with narrow size distribution and long-term stability.[224]

Polystyrene-*block*-poly(2-vinyl pyridine) (PS-*b*-P2VP) is a block copolymer commonly explored for the gold nanoparticle preparation since the pyridine functional group in

P2VP can stabilize $AuCl_4^-$ which is gold nanoparticle precursor. Adding a chemical reducing agent or using UV irradiation will reduce the complex metal ion. The reduction causes metal atom formation, aggregation of the clusters and finally growth of gold nanoparticles.[225]

The size and distribution of metal nanoparticles grown on polymeric templates can be changed by many factors such as the initial molar ratio of the metal to amine group, film thickness, and temperature. The amine groups in polymer chains can serve to bind gold ions and stabilize gold nanoparticles. Therefore, gold nanoparticles can be formed with narrow size distribution at high amine to gold ion ratio.[226,227,228] Film thickness and temperature affect the size and shape of gold nanoparticles, when synthesized by thermal decomposition of $HAuCl_4$ in a solution of linear PS-*b*-P2VP copolymers.[229] Also, the size of gold nanoparticles increases significantly when synthesized in thicker polymer films. Unfortunately, nanoparticles that synthesized at lower temperature possess a wide size distribution because of slow reaction that leads the poorly controlled nucleation and growth.[230,231,232]

Linear PS-*b*-P2VP form micelles with a P2VP core in toluene and can be used as templates to synthesize gold nanoparticles by mixing $HAuCl_4$ in the solution and subsequently adding a reducing agent.[233] In this approach, the size of the gold particles is controlled by the concentration of the gold precursor. In addition, the stability of individual gold nanoparticles depends on the stability of the micelle template. However, linear block copolymers do not excel in precisely controlling the size of nanoparticles

formed and their aggregation.[234] Particularly, the low stability of the micelle template in solution is a major challenge in using linear block copolymers. Linear PS-*b*-P2VP cannot form spherical nanoparticles if the block copolymer concentration is below the critical micelle concentration and their poor stability leads to the growth of irregular gold nanoclusters in solution and on solid substrates.[235,236]

Branched polymers such as dendrimers, hyperbranched polymers, and star-shaped block copolymers with distinct supramolecular structures have also been widely investigated as templates for inorganic nanoparticle formation.[188, 237 , 238 , 239] Dendrimers and functionalized hyperbranched macromolecules have been demonstrated to be peculiar templates for nanoparticle formation such as nanofibrillar discrete spherical, interconnected ring-shape, and structures.[237,240,241] The advantage of the star copolymers is their stability due to covalently bond of core segments. Star copolymer is one type of branched polymers which has unique morphology and lower aggregation number.[164] In addition, star polymers still remain solvent responsive and can be synthesized with narrow size distribution.[65,149,242] Star-shaped PS-P2VP block copolymers can be utilized as a robust template for the formation of gold nanoparticles in solution state.[224,234] In toluene, 5 nm gold nanoparticles can be synthesized inside star PS-P2VP molecule having PS-*b*-P2VP diblock arms, which forms hydrophilic P2VP core and PS shell structure. Minko et al. demonstrated the metallization of different arms for adsorbed PS_nP2VP_n heteroarm star copolymers.[166,243]

In recent studies, various linear and star P2VP macromolecules in the inner core of

micelles were used as a template for synthesis of gold nanoparticles.[207,213,238] However, there is no report about gold nanoparticle synthesis with P2VP chains acting as an outer phase. Synthesis of gold nanoparticles within P2VP thin outer layer instead of inner P2VP cores offers an opportunity to explore a new route towards synthesis of ultrathin nanocomposite films with one-sided confinement of gold nanoparticles.

In this chapter, we demonstrate the gold nanoparticle synthesis at liquid-solid interface by using amphiphilic PS_nP2VP_n heteroarm star block copolymer with P2VP phase forming an outer layer at the film-water interface. We revealed how the number of arms and chain conformation of star copolymers affect nanoparticle dimensions. The PS_nP2VP_n LB monolayer fabricated here acted as a template for the gold nanoparticle growth due to its uniform domain structure with high stability at the air-water interface and LB monolayer. UV-vis spectroscopy, atomic force microscopy (AFM), and transmission electron microscopy (TEM) all have been used to confirm the formation of the gold nanoparticles with an average size of 6 ± 1 nm in P2VP-rich side of the interface.

6.2. Experimental Details

Materials and Substrates. Amphiphilic PS_nP2VP_n heteroarm star copolymers were synthesized by the "in-out" method through anionic "living" polymerization in a multistep, one pot reaction as described previously.[126] Molecular characteristics are summarized in Table 6.1, chemical structures and schematics are presented in Figure 6.1A.

Table 6.1. Molecular Characteristics of PS_nP2VP_n Heteroarm Star Copolymers[199]

Composition	Number of arms		PS		P2VP		Φ_{P2VP} [g]	$M_{w,tot}$ [h]
	N [a]	Total [b]	M_w [c]	N_{PS} [d]	M_w [e]	N_{P2VP} [f]		
PS_9P2VP_9	9	18	3,400	33	13,200	126	0.8	149,000
$PS_{28}P2VP_{28}$	28	56	3,000	29	16,000	152	0.84	529,000

[a.] number of each PS and P2VP arm. [b.] total number of arms for individual star copolymer including PS and P2VP arm. [c.] weight average molecular weight of single PS arm. [d.] degree of polymerization of single PS arm. [e.] weight average molecular weight of single P2VP arm. [f.] degree of polymerization of single P2VP arm. [g.] weight fraction of P2VP in single star copolymer. [h.] total weight average molecular weight of star copolymer.

$HAuCl_4$ (99.99% trace metals basis) solution and sodium citrate (99 wt%) were purchased from Sigma- Aldrich. [100] silicon substrates and glass substrates were cut freshly in 1x2 cm^2 pieces. Piranha solution (3:1 concentrated sulfuric acid and hydrogen peroxide mixture) was used to clean the substrate according to the normal procedure (*warning: hazardous solution*).[178,244,245] Consequently, the silicon substrates were rinsed with Nanopure water (18.2 MΩ cm) and dried with a dry nitrogen stream.

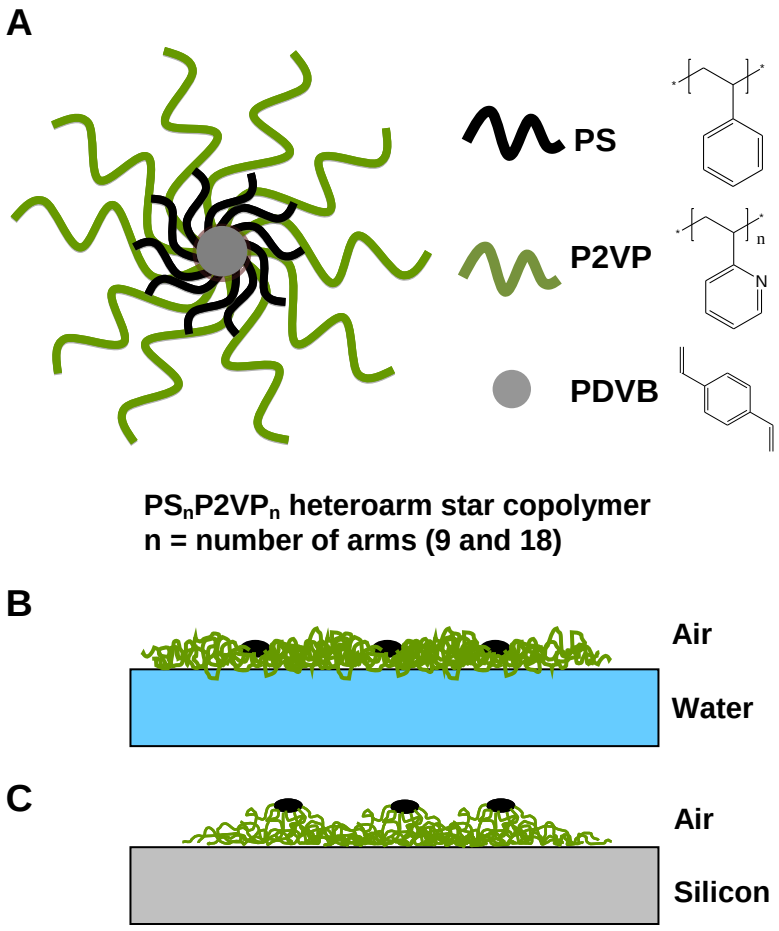

Figure 6.1: Schematic of the star PS_nP2VP_n monolayers: (A) molecular structure of the PS_nP2VP_n heteroarm star copolymer, (B) the side view of the molecule at the air-water interface, and (C) the air-solid interface as discussed in the text.

Fabrication of the Langmuir-Blodgett Monolayers. The PS_nP2VP_n monolayers have been prepared on silicon substrates with the LB technique.[246] We utilized a KSV2000 minitrough at room temperature according to the normal process. The star polymers were dissolved in a non-selective solvent (chloroform/methanol = 90/10 in vol.) with the concentration 0.001-0.1 mg/ml. The LB minitrough was filled with Nanopure water at pH 6. The silicon substrate was submerged into water phase for monolayer preparation. The 20-90 μl polymer solution was dropped gently with several droplets to disperse

evenly on the water surface. The system was left around 30 min until the solvent completely evaporates. The monolayer compression was conducted at 5 mm/min after the evaporation to reach the desire surface pressure. The monolayer of the polymer was transferred from air-water interface by pulling up the silicon substrate vertically at a rate of 2 mm/min.

Growth of gold nanoparticles within the star PS_nP2VP_n monolayers. Figure 6.2 shows the procedure for the fabrication of LB monolayers and growth of gold nanoparticles from subphase. First, the PS_nP2VP_n monolayer film was deposited on a silicon substrate and submerged into two different concentrations of $HAuCl_4$ solution, 0.75 wt% or 0.0075 wt%, for 24 hr. Consequently, $HAuCl_4$ formed a complex with the star copolymer monolayer on the solid substrate by protonating pyridine groups in the PS_nP2VP_n monolayer with H^+ from $HAuCl_4$ and the remaining $AuCl_4^-$ binding to the protonated pyridine units. Then, the substrate was washed with Nanopure water to remove unbound $HAuCl_4$ and the sample was submerged into 0.15 wt% sodium citrate solution for 12 hr at 70^oC to synthesize gold nanoparticles.[113] The sodium citrate will reduce Au ions to Au^0, which finally aggregate to form gold nanoparticles stabilized by the pyridine groups in the PS_nP2VP_n monolayer. Finally, the sample was washed with Nanopure water again to remove excessive sodium citrate and salts.

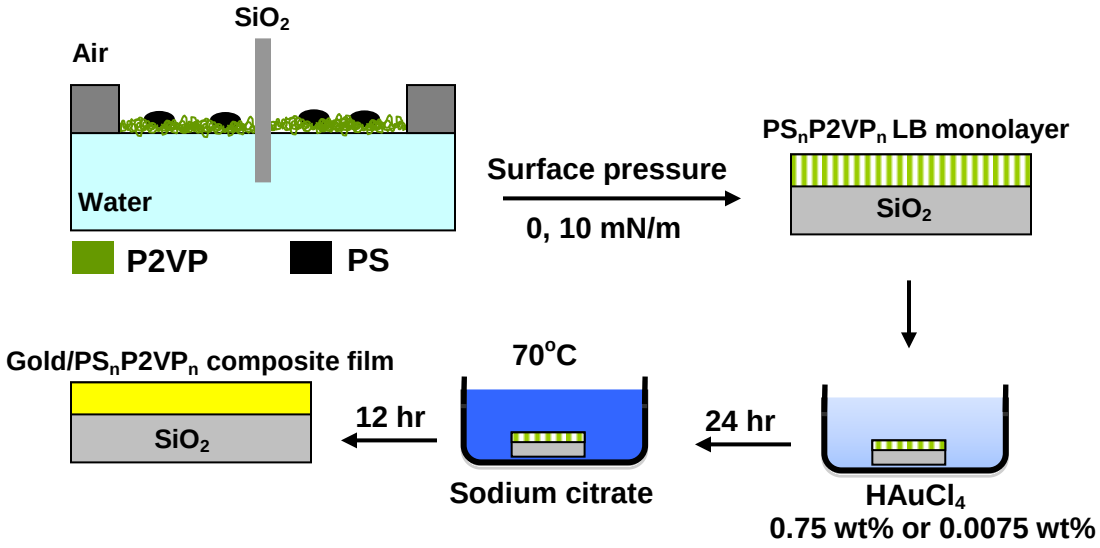

Figure 6.2: Growth of gold nanoparticles on the star PS_nP2VP_n monolayer.

Characterization. The surface morphology of the PS_nP2VP_n monolayers was characterized by AFM. The AFM images were obtained with a Multimode microscope with the "light" tapping mode according to usual procedure.[135,136] The thickness of the monolayer was obtained from scratching test. The height difference between bare silicon and the top of the film was taken to determine the thickness of the film. Also a M-2000U spectroscopic ellipsometer with WVASE32 analysis software was utilized to further confirm the film thickness. TEM was performed on JEOL 100CX-2 electron microscope and operated at 100 kV to analyze characteristic of the gold nanoparticles. The samples for TEM have been prepared by using LB technique on gold grids coated with a carbon support layer. The particle size was calculated from TEM images using ImageJ 1.43u software (National Institute of Health) by following regular image analysis procedure.

The UV-visible spectra of gold- star PS_nP2VP_n hybrid can be obtained by using UV-2450 spectrophotometer (Shimadzu). The samples for UV-visible measurements have been prepared by depositing LB monolayers on a glass substrate. The monolayer has been submerged in 0.75 wt%$HAuCl_4$ solution for 24 hrs and followed by reduction with sodium citrate for 12 hrs at 70^{o}C. The submersion and reduction were repeated up to four times to increase nanoparticle density.

6.3. Results and discussion

6.3.1. Chemical Composition.

Two types of PS_nP2VP_n heteroarm star copolymers with similar in P2VP weight fraction but different number of arms and molecular weights were used in this study (Table 6.1). PS_9P2VP_9 represents star copolymer with 9 PS and 9 P2VP arms and $PS_{28}P2VP_{28}$ with total 28 arms each. PS domains are hydrophobic while P2VP chains are relatively hydrophilic because of ionizable pyridine groups which are protonated in acidic conditions (pK_a ~ 4.5).[193,199,247,248] The weight percent of P2VP blocks of both PS_9P2VP_9 and $PS_{28}P2VP_{28}$ (0.8 and 0.84 respectively) signifies that the major fractional component of both star copolymers is P2VP phase. Although both PS_9P2VP_9 and $PS_{28}P2VP_{28}$ are similar in chemical composition, PS_9P2VP_9 exhibits remarkably less monomer density and less charge density upon protonation than $PS_{28}P2VP_{28}$ due to lower arm density.

6.3.2. Surface-pressure isotherms

The pressure-area isotherms of PS_nP2VP_n heteroarm star copolymers shown in Figure 6.3 were measured to explore the surface assembly behavior of amphiphilic star copolymers

and their ability to a complexation with gold precursor as described in detail elsewhere.[199] As known, at the air-water interface, the hydrophobic PS form collapsed domain on top of the hydrophilic P2VP arms forming underlayer in the contact with water (Figure 6.1B).[183,183] At higher surface pressure, the PS_nP2VP_n heteroarm star copolymers form uniform and dense monolayer whereas the star polymers show gas-like phase at low surface pressure (nominally, no compression). After transferring to a silicon substrate, P2VP arms spread in the bottom part and form intimate contact with the hydrophilic substrate and the PS phase aggregates in the center of the micelle (Figure 6.1C) as will be discussed later.

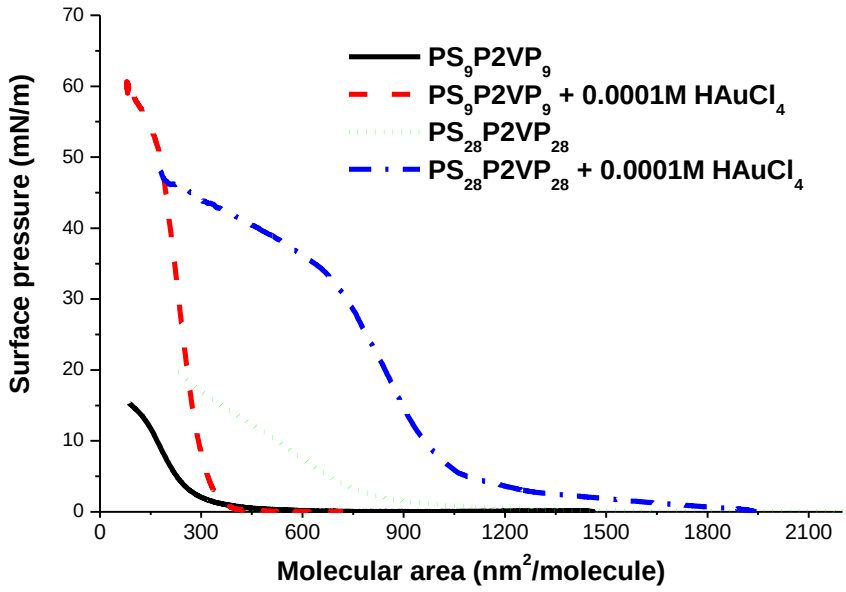

Figure 6.3: Surface pressure-area isotherms of PS_9P2VP_9 and $PS_{28}P2VP_{28}$ star copolymers.

Adding $HAuCl_4$ in the subphase resulted in the formation of uniform complexation between $HAuCl_4$ in the subphase and PS_nP2VP_n heteroarm star copolymers at the air-water surface due to higher affinity of the pyridine functional group with gold ion via

electrostatic interaction. Notably the isotherm in Figure 6.3 shows the change in molecular area both PS_9P2VP_9 and $PS_{28}P2VP_{28}$ after adding $HAuCl_4$ in the LB trough. The increase of molecular area of the monolayer film on water interface both PS_9P2VP_9 and $PS_{28}P2VP_{28}$ indicates the ion adsorption of polar P2VP domains.[98,249] The change in molecular area of $PS_{28}P2VP_{28}$ is higher than PS_9P2VP_9 due to higher amount of amine groups and hence greater capacity to bind Au ions that can be ascribed to high chain density of multi-arm star architecture (Table 6.1). The highly compact structure of star polymer is known to affect ionization and condensation with a counterion as well as osmotic pressure inside macromolecules. As shown for PS_9P2VP_9 heteroarm star copolymers, the surface pressure reached up to 50 mN/m after forming complex with Au ions. This increased monolayer stability suggests the change in chain conformation at higher surface pressure due to the interaction between Au ions and P2VP arms. Similarly, the $PS_{28}P2VP_{28}$ heteroarm star copolymers were also found to undergo pronounced phase transition at a higher surface pressure from 20 mN/m to 35 mN/m indicating the variation of chain conformation influenced by gold ions.[239,250]

6.3.3. Surface morphologies

To investigate the growth of nanoparticle and stability of LB monolayer, we examined the variation of surface morphology before and after reduction of gold nanoparticles. In this study, we focus on gold nanoparticle synthesis at the liquid-solid interface with

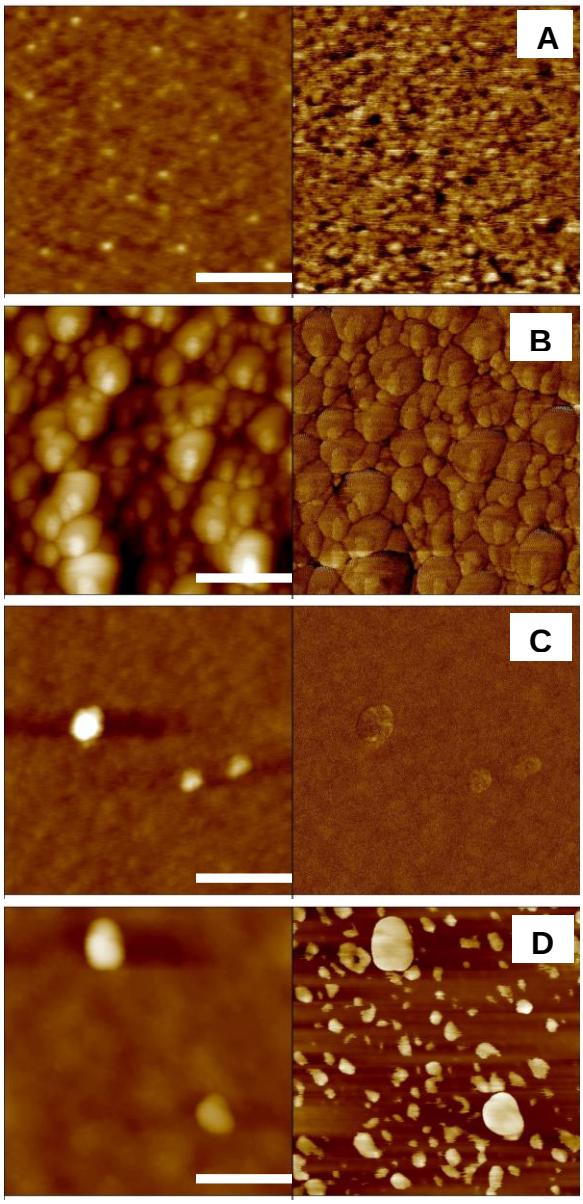

Figure 6.4: High resolution AFM images (height; left and phase; right) of star PS_nP2VP_n monolayer at surface pressure 0 mN/m: (A) PS_9P2VP_9 before and (B) after gold nanoparticle synthesis. (C) $PS_{28}P2VP_{28}$ before and (D) after gold nanoparticle synthesis. The scale bar is 100 nm for all images. The z-scale is 10 nm for images before the synthesis (A, C) and 40 nm for images after the synthesis (B, D).

ionizable pyridine containing PS_nP2VP_n heteroarm star copolymers as a template allowing for the stabilization of gold ion on a silicon substrate. We expose the PS_nP2VP_n monolayer transferred from air-water interface to $HAuCl_4$ solution at pH 1.0 to enable the binding of $AuCl_4^-$ with protonated PS_nP2VP_n monolayer and subsequently reduce $AuCl_4^-$ ions with sodium citrate to promote the formation of gold nanoparticles.

The surface morphologies of the LB monolayers of PS_9P2VP_9 and $PS_{28}P2VP_{28}$ heteroarm star copolymers at the lowest surface pressure (nominally, 0 mN/m) are shown in Figures 6.4 (See supporting information, Figure S6.1 for large area scans). The AFM images (both topography and phase) show individual dots representing star copolymer micelles in the gas-like phase at the lowest surface pressure and low concentration of polymer solution. For PS_9P2VP_9, the size of individual P2VP domains on the silicon substrate is about 1.5 nm in height and 20 nm in the lateral dimension. P2VP aggregates of $PS_{28}P2VP_{28}$ are larger than those of PS_9P2VP_9 because of higher number of arms and total molecular weight (Table 6.1). From Figure 6.4C, the average P2VP domain in the copolymer is around 4.5 nm in height and 39 nm in dimension, which corresponds well to previous reports.[166,251,359]

To explore the effect of change in surface aggregation on the growth of gold nanoparticle, we compared the surface morphology at different surface pressures (0 and 10 mN/m). At 0 mN/m, the surface morphology of the original monolayers was changed dramatically after exposure to gold salt. PS_9P2VP_9, block copolymers with gold nanoparticles possess several layers of nanoparticles (Figures 6.4B). In contrast, $PS_{28}P2VP_{28}$ monolayer

contains individual nanoparticles after gold reduction (Figures 6.4D). The PS_nP2VP_n heteroarm star copolymers, both PS_9P2VP_9 and $PS_{28}P2VP_{28}$, are swelled after exposure to $HAuCl_4$ due to the electrostatic repulsion from the protonated P2VP arms.[252,359] After reduction with sodium citrate, gold nanoparticles are formed inside the PS_nP2VP_n monolayer and retain the swelled structure. For PS_9P2VP_9, it is possible those P2VP domains may swell and partially overlap because of close distance between neighbor micelles. In contrast to PS_9P2VP_9, the surface morphology of $PS_{28}P2VP_{28}$ still shows individual dots on the silicon substrate both before and after gold reduction. Figure 6.4C indicate the distance between each $PS_{28}P2VP_{28}$ micelles is higher than the micelle size of $PS_{28}P2VP_{28}$ that prevents partial overlapping of P2VP chains from the swelled neighbor micelles. As the result, the $PS_{28}P2VP_{28}$ retained separated micelles even after gold reduction.

AFM images do not reflect the actual dimension of gold nanoparticle because the height measured includes contribution from the star polymer templates (Figure 6.12C). Thus, the shape and size of the gold nanoparticles were independently determined by TEM. Aggregation of the nanoparticles seen in some areas can be due to the swelling effect of the PS_nP2VP_n LB film. However, to reduce the error in the particle size measurement due to the present of aggregates, we utilized ImageJ program to analyze the gold nanoparticle size and selected only individual dots to calculate the gold nanoparticle size because the overlap structures prevent the observation of actual perimeter of the nanoparticles. The number of individual nanoparticles in each TEM images is more than 50 units and is sufficient to calculate the particle size reliably. The analysis result was

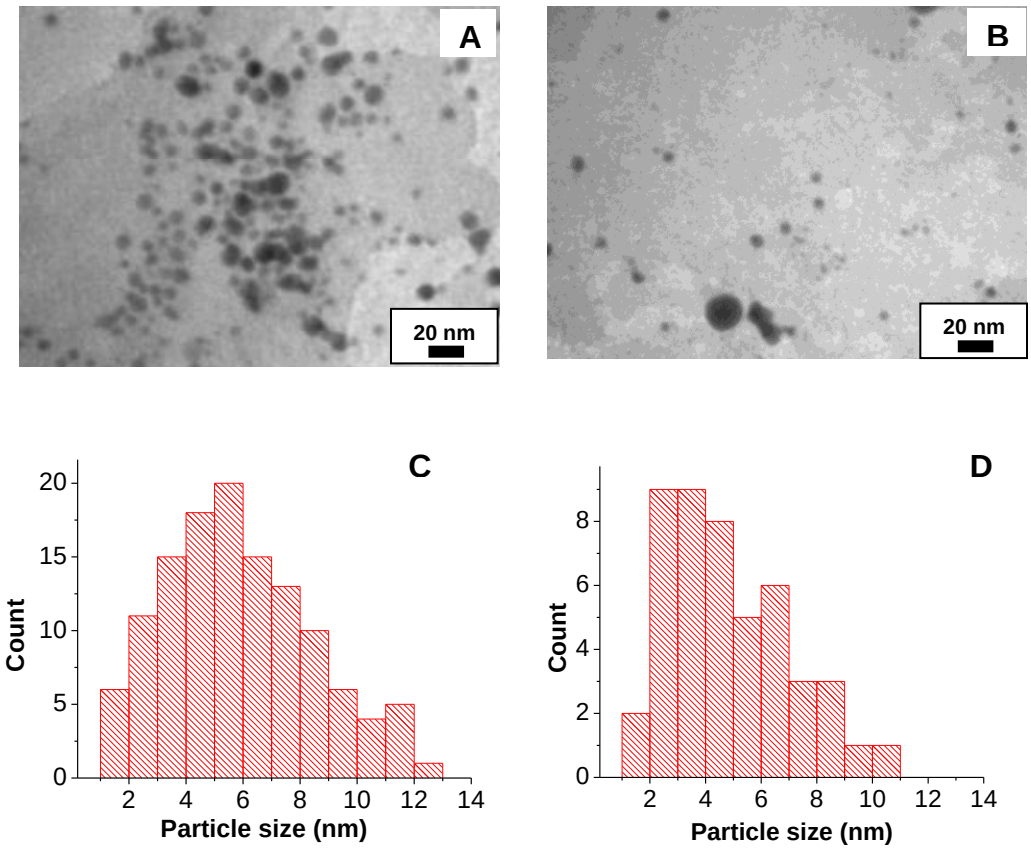

Figure 6.5: TEM images (A, B) and corresponding histogram (C, D) of gold nanoparticles grown on PS_nP2VP_n heteroarm star copolymers at surface pressure 0 mN/m and gold solution concrentration, [$HAuCl_4$] = 0.75 wt%: (A), (C) PS_9P2VP_9 and (B), (D) $PS_{28}P2VP_{28}$.

reproducible and was consistent over the different areas. Figure 6.5 shows TEM images of star PS_nP2VP_n/gold nanoparticles monolayer at the lowest surface pressure along with histograms of size distribution calculated from these images. As clear from these images, gold nanoparticles are spherical with the average particle size somewhat similar for both star block copolymers: 6.0 nm and 4.9 nm for PS_9P2VP_9 and $PS_{28}P2VP_{28}$, respectively (Table 6.2). The histograms show that PS_9P2VP_9 monolayer possesses a broader size distribution of gold nanoparticles, which imply the less stringent confined conditions for nanoparticle formation. Indeed, the PS_9P2VP_9 monolayer contains lower ratio P2VP

phase to gold ion, which stabilizes gold nanoparticles, than $PS_{28}P2VP_{28}$ monolayer. Higher concentration of amine groups is critical for the prevention of agglomeration and growth of smaller nanoparticles.[253]

Table 6.2. Thickness of PS_nP2VP_n Composite Film and Size of Gold Nanoparticle.

Composition	Surface pressure (mN/m)	[$HAuCl_4$] %	Film thickness (nm)[a]		Particle size[b] (nm)
			star monolayer	Gold-star polymer composite	
PS_9P2VP_9	10	0.75	1.6 ± 0.28	6.3 ± 0.45	7.1 ± 1.9
	0	0.75	1.0 ± 0.18	7.2 ± 1.17	6.0 ± 2.8
$PS_{28}P2VP_{28}$	10	0.75	2.0 ± 0.37	24.6 ± 5.49	6.5 ± 1.7
	10	0.0075	2.0 ± 0.31	7.3 ± 0.87	7.0 ± 1.8
	0	0.75	3.1 ± 0.35	10.9 ± 1.53	4.9 ± 2.2

[a] Measured from scratched film by AFM. [b] Measured by TEM.

Figures 6.6 (See supporting information, Figure S6.2 for large area scans) present AFM images of PS_9P2VP_9 and $PS_{28}P2VP_{28}$ on silicon substrate at higher surface pressure of 10 mN/m. At this pressure, both star block copolymers form dense monolayer at the air-water interface under these conditions with densely packed micelles. AFM images in Figure 6.6A and 6.6C shows uniform morphology of the transferred star copolymer from the air-water interface. The uniformity of this structure on exposing the polymer film to $HAuCl_4$ solution and on further reduction with sodium citrate is significantly affected due to swelling effects. Also, Langmuir-Blodgett monolayer composed of interconnected P2VP chains may have uneven gold ion absorption among P2VP layer, leading to partial aggregation and a broad size distribution of the gold nanoparticles.

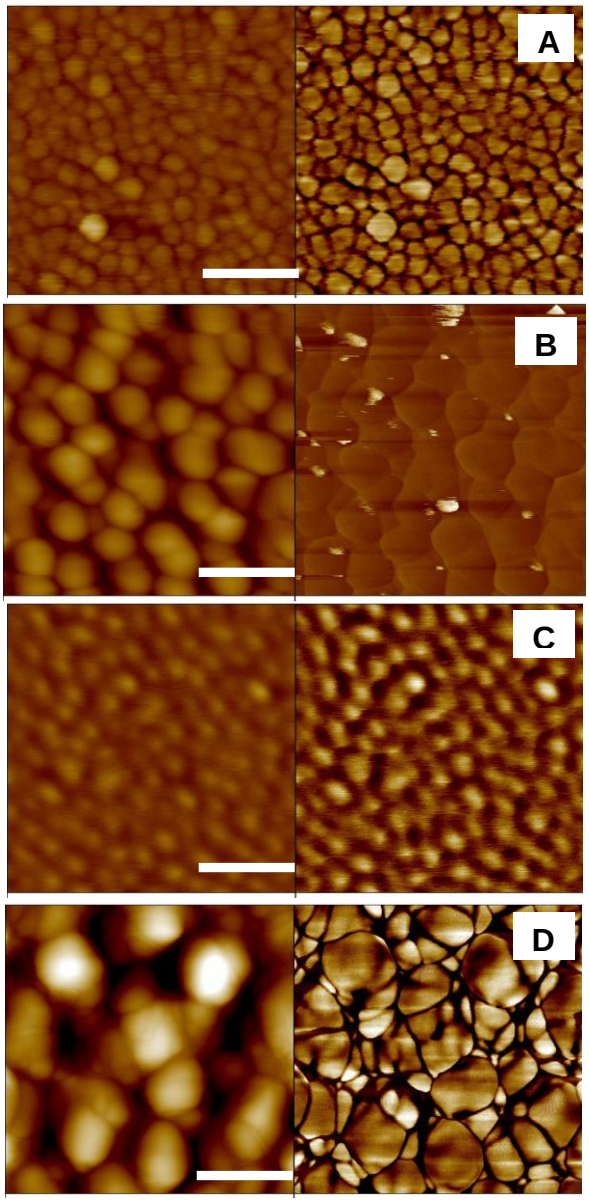

Figure 6.6: High resolution AFM images (height; left and phase; right) of star PS_nP2VP_n monolayer at surface pressure 10 mN/m: (A) PS_9P2VP_9 before and (B) after gold nanoparticle synthesis. (C) $PS_{28}P2VP_{28}$ before and (D) after gold nanoparticle synthesis. The scale bar is 100 nm for all images. The z-scale is 10 nm for images before the synthesis (A, C) and 50 nm for images after the synthesis (B, D).

AFM and TEM images appear different results because the AFM images display spherical micellar structure of PS_nP2VP_n heteroarm star copolymers encompassing the gold nanoparticles whereas the TEM images only exhibit gold nanoparticles in the LB

film. However, both AFM and TEM images demonstrate a trend in the gold nanoparticle distribution. At the lowest surface pressure after gold reduction, PS_nP2VP_n monolayer exhibits the partially aggregated and swelled micelles after gold reduction as shown in AFM images (Figure 6.4B), which thereby likely lead to unevenly distributed gold nanoparticle as shown in the TEM image (Figure 6.5A). This result can be attributed to the insufficient stabilization of gold nanoparticle by P2VP star copolymer micelles. At high surface pressure, the monolayer exhibit denser micelle organization with more uniform distribution (AFM in Figure 6.6), which is compatible with highly dense nanoparticle morphology as demonstrated in the TEM image (Figure 6.7).

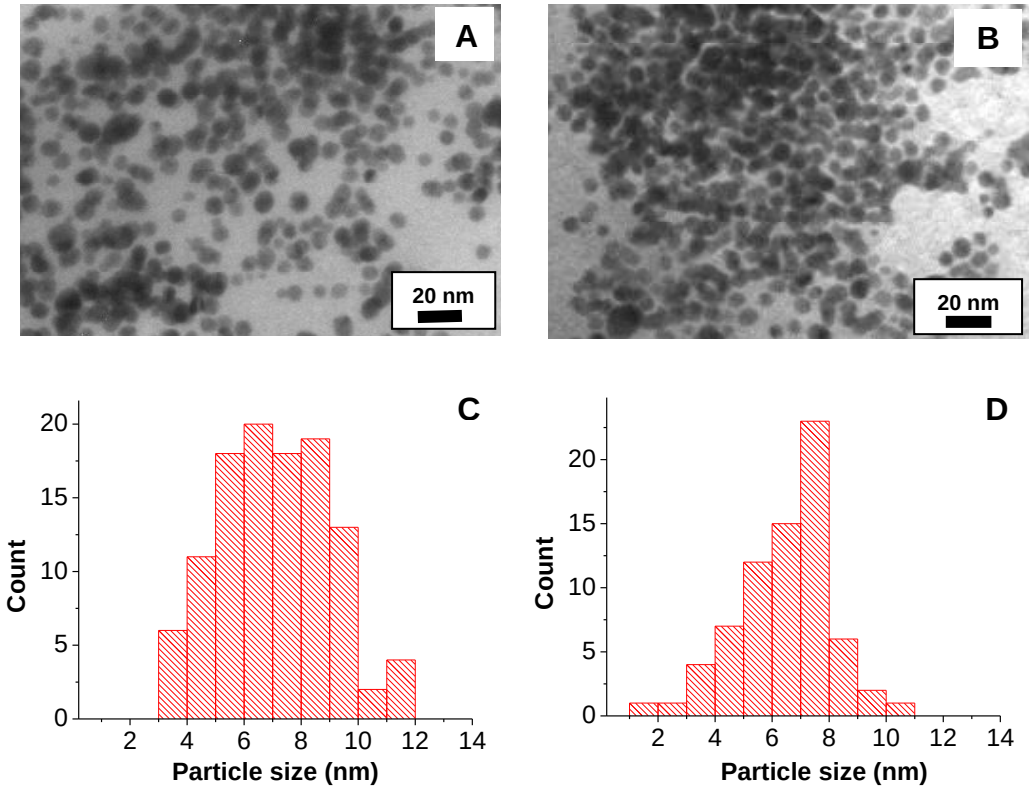

Figure 6.7: TEM images and corresponding histogram of gold nanoparticles form with PS_nP2VP_n heteroarm star block copolymers at surface pressure 10 mN/m and gold solution concentration, $[HAuCl_4]$ = 0.75 wt%: (A), (C) PS_9P2VP_9 and (B),(D) $PS_{28}P2VP_{28}$.

The thickness of polymer film before and after gold reduction provides further information to understand formation behavior of gold nanoparticles within the polymer film. Figure 6.6A and 6.6C confirm the uniformity of the polymer film on silicon substrate. The thickness of the PS_nP2VP_n monolayer film in Table 6.2 is measured using AFM with a scratch test on the polymer deposited on silicon substrates (not from TEM samples). The film thickness was measured from more than three different areas in large area AFM scans (20 um size). As shown, the standard deviation values tend to increase with increasing in film thickness and the standard deviation are within 20%.

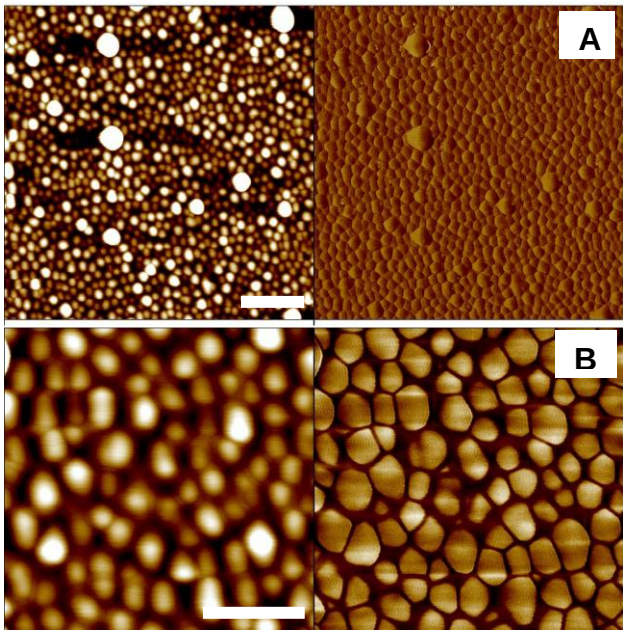

Figure 6.8: AFM images (height; left and phase; right) of gold nanoparticles/ $PS_{28}P2VP_{28}$ heteroarm star copolymers at surface pressure 10 mN/m and gold solution concentration, $[HAuCl_4]$ = 0.0075 wt%. The scale bar is 200 nm (A) and 100 nm (B). The z-scale is 10 nm for both A and B.

At high surface pressure, the film thickness of PS_9P2VP_9 and $PS_{28}P2VP_{28}$ film before the gold incorporation is around 1.6 nm and 3.1 nm, respectively, that are much higher than

that for the PS_nP2VP_n monolayer at the lowest surface pressure (Table 6.2). The film thickness from AFM scratch tests is in good agreement with that obtained by ellipsometer (Table 6.2). The film thickness of PS_9P2VP_9 monolayer increases to 6 nm after gold nanoparticles formation. It indicates the formation of the individual gold nanoparticles in PS_9P2VP_9 ultrathin film. In contrast to PS_9P2VP_9, the thickness of $PS_{28}P2VP_{28}$ increases dramatically from 2 nm to 25 nm after gold nanoparticles formation (Table 6.2). Such a thickness increase is observed even the size of the gold nanoparticles in $PS_{28}P2VP_{28}$ monolayer is only 6.5 nm. This difference suggests that the gold nanoparticles form multilayer aggregates within the monolayer of $PS_{28}P2VP_{28}$. This high concentration of nanoparticles formed is due to high concentration of amine groups available for gold reduction in continuous P2VP phase. Moreover, the size distribution of gold nanoparticles for densely packed star block copolymers (at 10 mN/m) becomes more narrow (Table 6.2). .

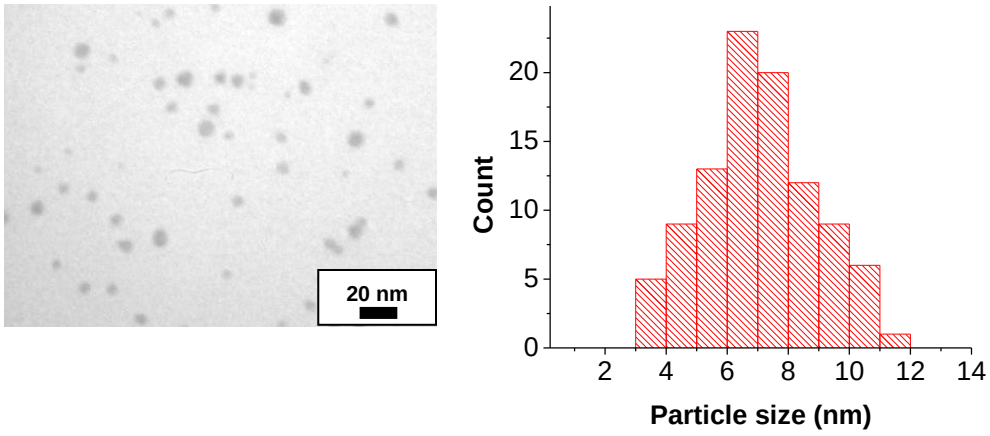

Figure 6.9: TEM image (left) and corresponding histogram (right) of gold nanoparticles with $PS_{28}P2VP_{28}$ heteroarm star copolymers at surface pressure 10 mN/m and gold solution concentration, $[HAuCl_4]$ = 0.0075 wt%.

As a next step, we applied $HAuCl_4$ at two different concentrations, 0.75 wt% and 0.0075 wt% to compare the effect of gold ion concentration on nanoparticle formation. The AFM images in Figure 6.8 indicates that the gold nanoparticles formed at the 0.0075 wt% $HAuCl_4$ form a monolayer while larger aggregates of gold nanoparticles are formed at 0.75 wt% $HAuCl_4$ concentration. At 0.0075 wt% $HAuCl_4$ a much higher ratio of P2VP group is available to stabilize the gold nanoparticle and facilitate narrow size distribution. TEM image in Figure 6.9 clearly shows much lower gold nanoparticle density compare to

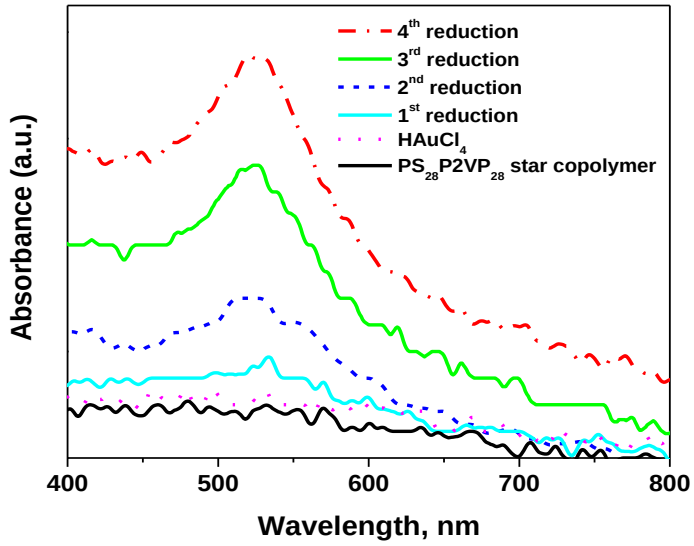

Figure 6.10: UV-Vis absorption spectra of gold nanoparticles grown on the star $PS_{28}P2VP_{28}$ monolayer with four different repeating cycles of the gold reduction.

the 0.75 wt% $HAuCl_4$ due to lower number of gold ions available for reduction. The diluted $HAuCl_4$ solution provides fewer $AuCl_4^-$ ions to bind with $PS_{28}P2VP_{28}$ and causes low density of gold nanoparticles within the star copolymer template. In contrast to the diluted $HAuCl_4$, 0.75 wt% $HAuCl_4$ has larger number of gold ions to grow high density nanoparticle and even their layering in $PS_{28}P2VP_{28}$. Finally, it is worth to note that adding 0.0001M $HAuCl_4$ in the subphase does not affect significantly the surface

morphology and dimensions of gold nanoparticles formed (see Figure 6.3 for isotherms, data not shown).

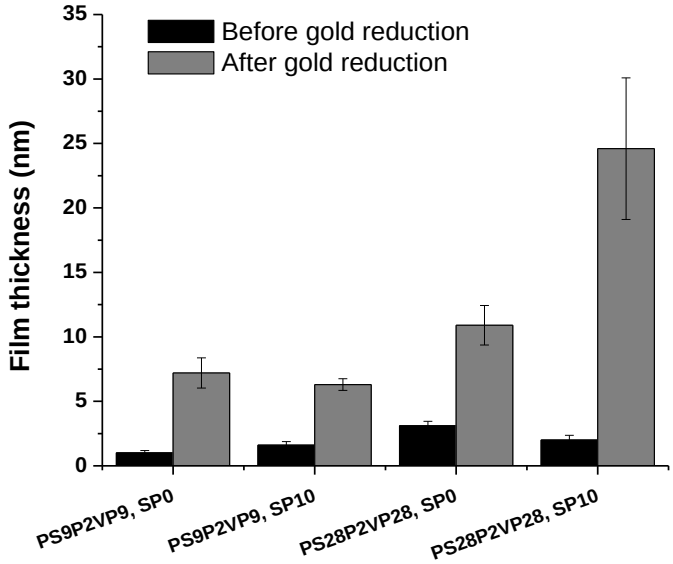

Figure 6.11: Thickness of star PS_nP2VP_n monolayer film before and after reduction at surface pressure 0 mN/m (SP0) and 10 mN/m (SP10).

Independent confirmation of the gold nanoparticle formation and information on their aggregation status can be obtained from the UV-Vis spectra of gold nanoparticles grown in star copolymer templates (Figure 6.10). The samples for UV-Vis measurement are prepared by deposition of star $PS_{28}P2VP_{28}$ copolymers on a clean glass substrate at the surface pressure of 10 mN/m. The gold reduction procedure was repeated several times to increase the density of gold nanoparticles. After repeating the gold reduction procedure an absorption band at 530 nm appeared that corresponds to gold nanoparticles Plasmon band.[254,255,256] The peak position agrees with the formation of 3-7 nm gold nanoparticles known in literature and thus confirms out TEM observations.[224,234] The absorption bands are located at the same position irrespective of the number of times the

reduction was repeated and the absorption intensity increased with the corresponding increase in nanoparticle density. The constant peak position indicates uniformity in the size of gold nanoparticles without larger aggregates.

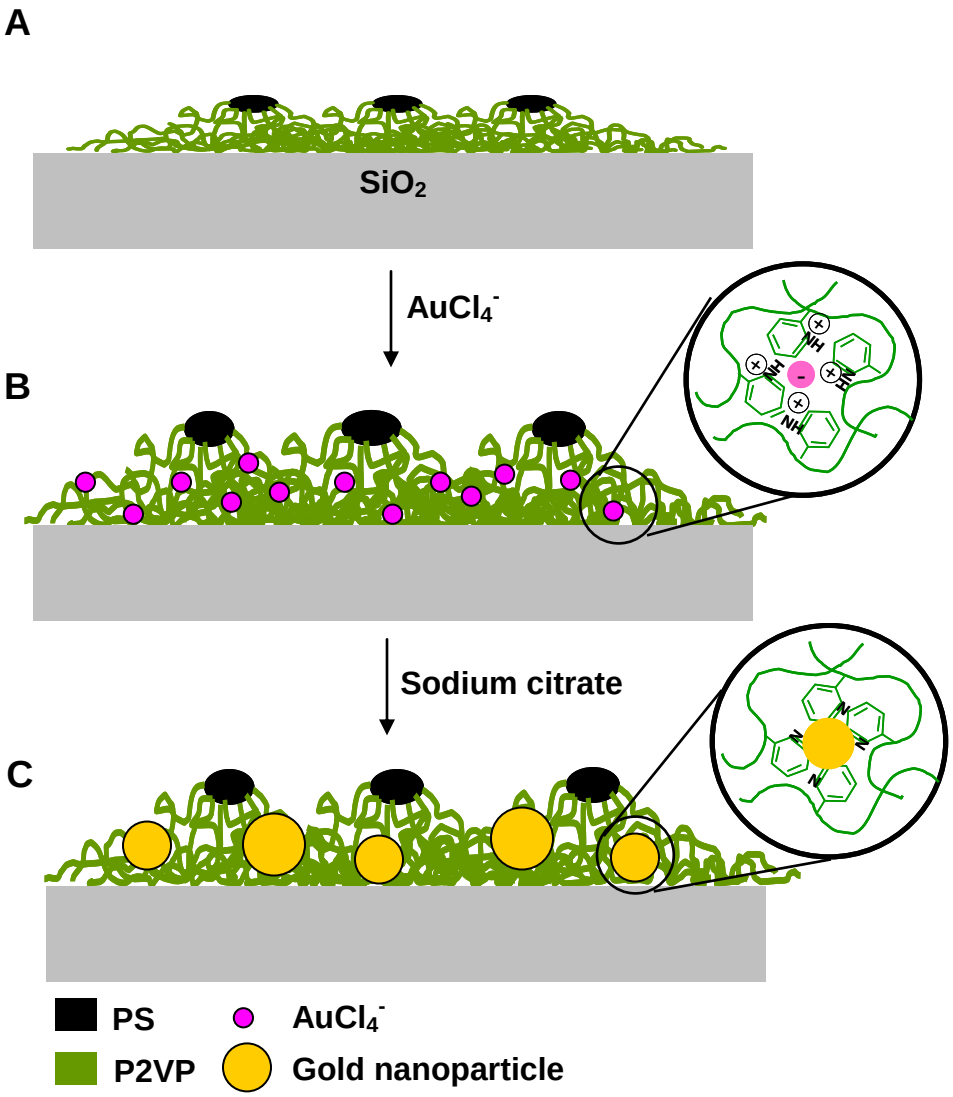

Figure 6.12: Schematic representation of the growth of gold nanoparticles in PS_nP2VP_n heteroarm star block copolymers. (A) star PS_nP2VP_n monolayer at the air-silicon interface before exposure, (B) after exposure to gold solution($AuCl_4^-$), and (C) star PS_nP2VP_n monolayer after gold reduction by sodium citrate.

Summary of all monolayer thickness variation under different fabrication conditions is presented in Figure 6.11. As apparent from results discussed above, the P2VP chains conformation and the state of microphase separation play very important role in controlling gold nanoparticle size distribution. For our systems, P2VP domains form an underneath layer to interact with hydrophilic surfaces such as water subphase and silicon substrate (Figure 6.12A). The $AuCl_4^-$ are bounded with the underneath P2VP layer on the silicon substrate with protonated pyridine units.[113, 257] The particle size distribution depends on the number of P2VP units and gold ion concentration but nanoparticles dimensions always stay with 5-7 nm, which could be attributed to the confinement of P2VP domain structure of star polymer considering the film thickness (Figures 6.12B and 12C). Such the distinct micellar stability and suppression of nanoparticles aggregation common in solution-based reduction are likely due to the dense chain state in multi-arm star architecture in contrast to conventional micelles composed of linear block copolymers.

To summarize, we studied *in situ* synthesis of individual gold nanoparticles on monolayers of PS_nP2VP_n star copolymers at the liquid-solid interface and demonstrated that LB monolayer comprised of star copolymer surface micelles can act as a template for nanoparticle growth in one-sided P2VP microphase as a function of surface pressure, $HAuCl_4$ concentration, domain morphology, and the number of P2VP arms.

Appendix. Supplementary Information: AFM images for large scan areas in Figure S6.1. and S6.2.)

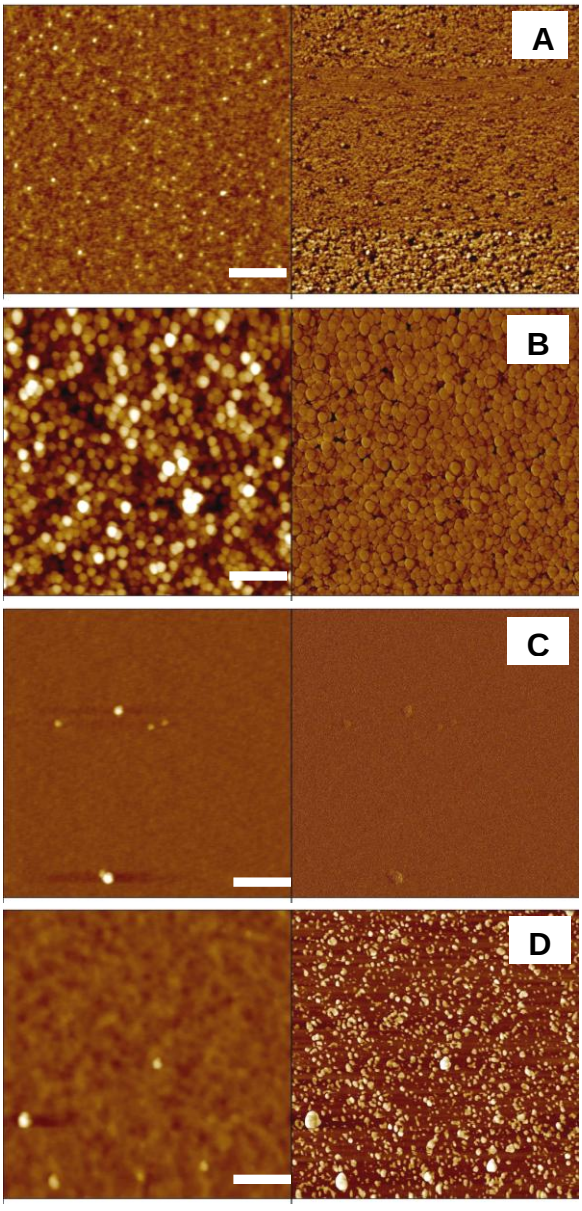

Figure S6.1: AFM images (height; left and phase; right) of star PS_nP2VP_n monolayer at surface pressure 0 mN/m: (A) PS_9P2VP_9 before and (B) after gold nanoparticle synthesis. (C) $PS_{28}P2VP_{28}$ before and (D) after gold nanoparticle synthesis. The scale bar is 200 nm for all images. The z-scale is 10 nm for AFM images before the synthesis (A, C) and 40 nm for images after the synthesis (B, D).

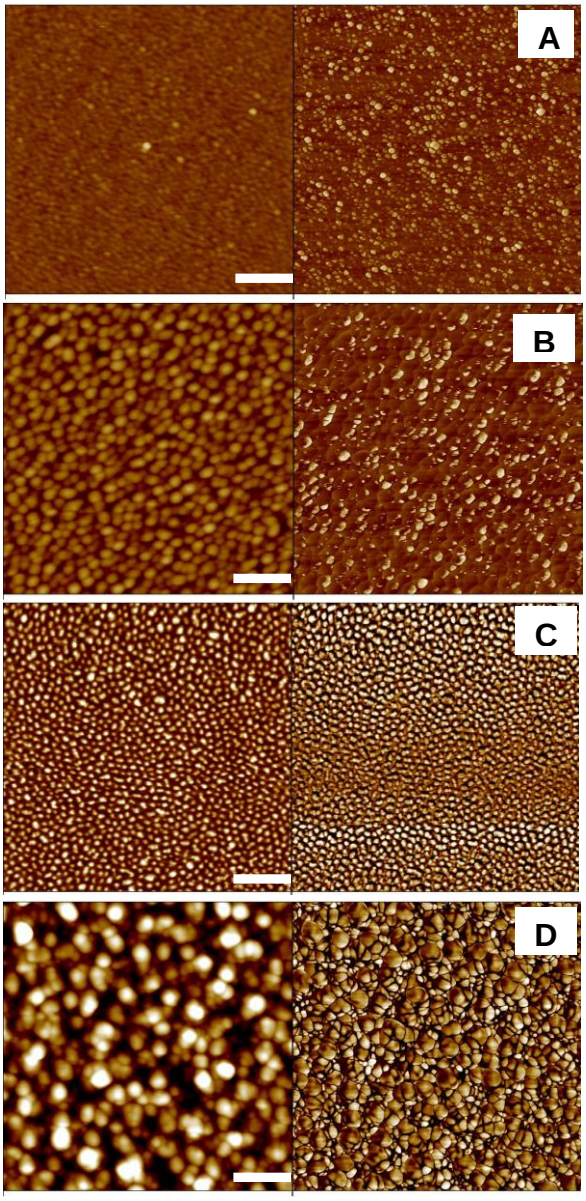

Figure S6.2: AFM images (height; left and phase; right) of star PS_nP2VP_n monolayer at surface pressure 10 mN/m: (A) PS_9P2VP_9 before and (B) after gold nanoparticle synthesis. (C) $PS_{28}P2VP_{28}$ before and (D) after gold nanoparticle synthesis. The scale bar is 200 nm for all images. The z-scale is 10 nm for images before the synthesis (A, C) and 50 nm for images after the synthesis (B, D).

CHAPTER 7

pH-CONTROLLED EXPONENTIAL AND LINEAR GROWING MODES OF LAYER-BY-LAYER ASSEMBLIES OF STAR POLYELECTROLYTES

7.1. Introduction

LbL multilayer assembly[101,102, 258 , 259] is an intriguing subject of continuous interest because it can offer a variety of functional organized nanomaterials for various applications.[41,42,43,44, 260 , 261 , 262 , 263 , 264 , 265 , 266 , 267 , 268] The LbL assembly consists of successively adsorbed macromolecular or nanoparticulate layers bonded via electrostatic,[101] hydrogen bonding, [269] and hydrophobic interaction [270] by controlling various parameters such as pH, ionic strength, temperature, and concentration, which affect the integrity and strength of LbL films.[10,102,260,271] Recently, much effort has been made to design weakly bonded stimuli-responsive thin films and microcapsules from LbL multilayer assemblies.[28,40,214,272,273,274] In particular, the LbL multilayer assemblies based on weak polyelectrolytes such as poly(acrylic acid) (p(AA)), poly(allylamine hydrochloride) (p(AH)), or poly(methacrylic acid) (p(MAA)) exhibit various pH-responsive behaviors, which can be tuned by the adjustment of the ionic strength and charge density of the polyelectrolytes, as well as environmental conditions such as pH, salinity, and multivalent counterions.[275,276,277] Owing to pH-triggered volume phase transformations (i.e. “coil to globular” chain conformational transition), weak polyelectrolytes have been recognized as a promising building component for the effective manipulation of the chemical and structural properties of LbL

assemblies.[28,39,,278] However, the LbL multilayer growth mechanism in exponential mode has not been completely understood yet, especially for complex polyelectrolyte architectures such as star polyelectrolytes.

Recent advancements in controlled/living polymerization methods, especially atom transfer radical polymerization (ATRP), allow for an intense research on branched polymers with novel architectures such as star-shaped block copolymers and polyelectrolytes.[279,280,281,282,283,284] The architecture of such branched polymers features compact, globular chain conformation, and multiple chain ends. This molecular structure leads to diverse physical and chemical properties in bulk, solution, and at interfaces due to the reduced hydrodynamic volume compared to the linear counterpart with an equivalent molecular weight. For instance, it has been observed that amphiphilic branched block copolymers exhibit peculiar surface morphologies of their thin films at the interface.[162,163,164,188,191] In particular, pH-sensitive star-shaped polyelectrolytes and dendrimers are considered to be an intriguing component for LbL films because of their unique chemical properties such as high charge density and multiple reactive sites of terminal groups.[4,36,285] Interestingly, the highly branched polyamidoamine (PAMAM) dendrimer was found to interdiffuse in multilayers at lower critical degree of ionization (55%).[286,287] In addition, weak star polyelectrolytes exhibit a distinct shift of pK_a value as compared to linear ones.[71,130] This phenomenon is caused by an ionic confinement effect due to the highly crowded chain structure of star polymers because of the increased osmotic pressure inside star polymers.[37]

Apart from the properties of polyelectrolytes such as ionic strength, charge density, and molecular weight and structure, assembly techniques such as dip-[41], spray-,[288] or spin-assisted[289,290,291,292] methods play a critical role in determining the mode of growth, intermixing state, and final morphology and physical properties of LbL films as controlled by balance of adsorption, diffusion, the presence of nanostructures, and the degree of hydration.[293,294,295,296,297,298,299,300,301,302,303] A recent comparative study of spray- and dip-assisted methods has shown that a spray-assisted LbL allows thinner, less dense, and rougher films than a dip-assisted method.[304] Spin-assisted LbL assembly rapidly provides highly mechanically robust and stratified LbL films by controlling shear force and solvent evaporation.[38,289,305] The shear effect can promote mass transfer enhancing intermolecular interaction as well as preventing interlayer mixing due to the limited diffusion by quick solvent removal.[289,290,306] To date, however, it is not clear how different LbL assembling approaches can allow for growing much thicker (microns) films by utilizing an exponential mode of LbL growth.

Indeed, since the first report of the exponential growth of polylysine and polyalginate,[103,105,307,308] both regular (linear) and exponential (nonlinear) growing modes were observed for LbL films from a variety of linear polyelectrolytes. As is known, the exponential growth of LbL films can be caused by the increasing roughness of adsorbed polyelectrolytes with low charge density which undergo surface-assisted microphase separation as well as excessive adsorption of components facilitated by the "in-and-out" diffusion of polymer chains. Specifically, weakly bonded free polymer chains diffuse across the hydrated swollen film during endothermic complexation in the course of the

adsorption process. Recently, a three-zone model was suggested and "exponential-to-linear" transition in LbL assembly was experimentally demonstrated and discussed.[106,296] Also, the interdiffusion and dynamic exchange of weak polycations within LbL multilayers was found to occur at a critical ionization of around 70% for different chain topologies (linear, branched, and dendrimer).

Despite the intriguing architecture of star polyelectrolytes, they have rarely been explored for building LbL assemblies because of their complex interfacial behavior. Recently, Yang et al. discussed composite thin films composed of a star-shaped poly(acrylic acid) (p(AA)) polymer brush having a poly(methylsilsesquioxane) (PSQ) core with poly(vinylpyrrolidone) (p(VPON) via hydrogen bonding interactions.[114] Thin films showing reversible morphological transitions that were assembled from pH-responsive star p(AA) and linear p(AH) were explored by Connal et al.[115] Distinct morphological changes under post-pH treatment were also observed by Kim et al. in LbL films from star-shaped and pH responsive poly[2-(dimethylamino)ethyl methacrylate] (p(DMAEMA)) and p(AA).[64] They proposed the unique compact structure of the star polymer and a resulting limited interpenetration of the polymers to be responsible for those changes. A recent study by Guo et al. demonstrated that LbL films of star p(DMAEMA)/poly(sodium 4-styrenesulfonate) (p(SS)) showed exponential growth as a function of arm length and number of arms.[309] Still, no systematic study on the modes of growth of star polyelectrolytes has been conducted to date. It is unclear how the incorporation of star polyelectrolytes can facilitate a fast exponential mode of LbL

growth and provide for responsive properties and if the mode of LbL growth can be tuned with pH control during assembling process.

Here, we report pH-tunable LbL growth modes of pH-sensitive stars, p(DMAEMA) with variable molecular weights and number of arms, which are consecutively deposited with p(AA) stars and corresponding linear counterparts at varying pH conditions. To understand the effect of ionic states on LbL assembly, both dip-assisted and spin-assisted LbL assemblies were explored to build LbL films with the number of bilayers reaching 30 at various pH (from 5 to 7). Moreover, different pairs of combinations including linear-star, star-linear, and star-star were also used to understand the role of molecular architecture on the LbL assembly. We suggest that in the exponential mode fast buildup prevents long-range lateral diffusion of polyelectrolyte star components which hinders microphase separation, and leads to thick, smooth, uniform, transparent, and colorful films from star polyelectrolytes in contrast to traditional linear counterparts.

In this chapter, we demonstrate the pH-tunable exponential/linear growth behavior of star polyelectrolytes in the course of LbL assembly. We found a distinct evolution of surface morphology of star polyelectrolytes during LbL buildup which is different from that known for linear counterparts. The fast exponential growth observed at certain assembly conditions suggests that the vertical diffusion of star polyelectrolytes within LbL films occurs efficiently in spite of their large molecular weights. We suggest that globular and compact molecular conformations play a pivotal role in facilitating high mobility and interdiffusion needed for exponential mode of growth. In order to further elucidate the

LbL growth mechanisms, the LbL assembly conditions are systematically explored for various combinations such as linear/linear, linear/star, star/linear, and star/star polyelectrolyte pairs. These efforts clearly reveal that both linear and exponential growth modes result in LbL films with varying thicknesses and morphologies. The growth modes can be finely tuned with pH conditions which in turn affect the interplay of various parameters such as charge density, degree of hydration, and molecular diffusion as discussed below.

7.2. Experimental Details

Materials. Linear p(AA_{1400}) (M_W = 100 kDa), p(SS_{380}) (M_W = 70 kDa), and p(AH_{600}) (M_W = 56 kDa) (the index indicating the degree of polymerization) were obtained from Aldrich and were used as-received. 1.0M TRIS HCl was purchased from Rockland and was diluted to 0.01M in Nanopure water for use. 0.1M HCl (99.5% purity) and 0.1M NaOH (99.5%) solutions were utilized to adjust the pH of polyelectrolyte solutions.

Synthesis of the star and linear polyelectrolytes. In short, star-shaped p(DMAEMA) and p(AA) were synthesized by ATRP in a core-first approach. [37,129,130] The molecular characterization of the polymers is summarized in Table 7.1, where the subscripts n and x of the formula p($NAME_n$)$_x$ denote the average degree of polymerization of each arm and the number of arms, respectively.

Table 7.1: Molecular Characteristics of Polyelectrolyte Components for LbL films.

Entry	Formula	Initiator	PDI[a]	$M_{n,star}$ × 10^{-3} [g / mol][b]	$M_{n,arm}$ × 10^{-3} [g / mol][c]	pK_a[d]
1	$p(AH_{600})$	commercial	-	56	-	-
2	$p(DMAEMA_{880})$	EBIB	1.9	139	-	6.2
3	$p(DMAEMA_{170})_{5.6}$	saccharose[130]	1.2	146	27	6.0
4	$p(DMAEMA_{170})_{18}$	silsesquioxane[130]	1.4	490	27	5.8
5	$p(SS_{320})$	commercial	-	70	-	-
6	$p(AA_{1400})$	commercial	~1.1	100	-	6.2
7	$p(AA_{125})_{21}$	cyclodextrin[23]	1.1	190	9	6.7

[a]calculated from the NMR conversion data together with the initiator concentration. [b]determined by GPC in THF (containing 0.25 wt% TBAB for cationic polyelectrolytes) and polystyrene standards. [c]calculated by dividing the total molecular weight of star by the number of arms. [d] apparent value measured as pH at degree of neutralization $\alpha = 0.5$, 1g/L in pure water.[37]

Preparation of LbL multilayer assemblies. Polyelectrolytes were dissolved in Nanopure water (18.2 MΩ cm) or in 0.01M Tris HCl buffer solution. 0.2 wt% (2.0 mg/ml) of p(AH) and p(SS) were used for the precursor layer by the deposition of 2.5 bilayers of (PAH / $PSS)_{2.5}$ to improve initial adhesion and to obtain the same initial condition prior to the assembly of the main p(AA) and p(DMAEMA) LbL multilayer film. Polyelectrolyte solutions of p(AA) and p(DMAEMA) were prepared to 0.02 wt% (0.2 mg/ml) in concentration with 0.01M Tris HCl buffer solution. The pH of all the solutions was

adjusted by the addition of 0.1 M HCl or 0.1 M NaOH aqueous solution to control the charge density of polyelectrolytes.

Freshly cut silicon substrates with dimensions 1 cm x 2 cm and the [100] orientation (Semiconductor Processing) and a native silicon oxide layer having a 1.6 nm thickness were cleaned with piranha solution (3:1 concentrated sulfuric acid and hydrogen peroxide mixture, *Cautions!*) in accordance with usual procedure.[178,244] Subsequently, it was abundantly rinsed with Nanopure water and dried with a dry nitrogen stream. Pretreated fresh wafers served as hydrophilic substrates for LbL film deposition.

Spin-assisted LbL films were prepared by using sequential spin-casting at different rpm for 20 sec and rinsed twice between depositions of polyelectrolyte solution under the same condition in accordance with usual procedure in our lab.[133,134] Subsequently, LbL films were spun for 1 min to remove water under dry nitrogen and further dried at room temperature for 48 hrs before experimental measurements. The p(AA) and p(DMAEMA) layers were deposited alternately up to 30 bilayers. The dip-assisted LbL process was performed by alternate immersion of the substrates in polyelectrolyte solutions for 10 min, followed by rinsing three times with the same pH buffer solution.

***Characterization of LbL films*.** Measurement of the film thicknesses and refractive indices were carried out with a Woollam M2000U (J.A. Woollam Co, Inc., Lincoln, NE) multiangle spectroscopic ellipsometer with a WVASE32 analysis software for three incident angles 65, 70, and 75°. The LbL film thickness data was fit to the Cauchy model

where the reflective index is given as $n(\lambda) = A_n + B_n/\lambda^2 + C_n/\lambda^4$ with A_n= 1.45, B_n= 0.01, and C_n= 0.0 as a function of λ. For sufficiently thick films, thickness (>300 nm thickness) was determined using fitted Cauchy constants obtained from Ψ and Δ of measured films. The mean squared error (MSE) for data fitting was in range of 5-25. Thickness measurements were conducted on at least three different homogeneous surfaces for each sample showing standard deviation within ±8% level.

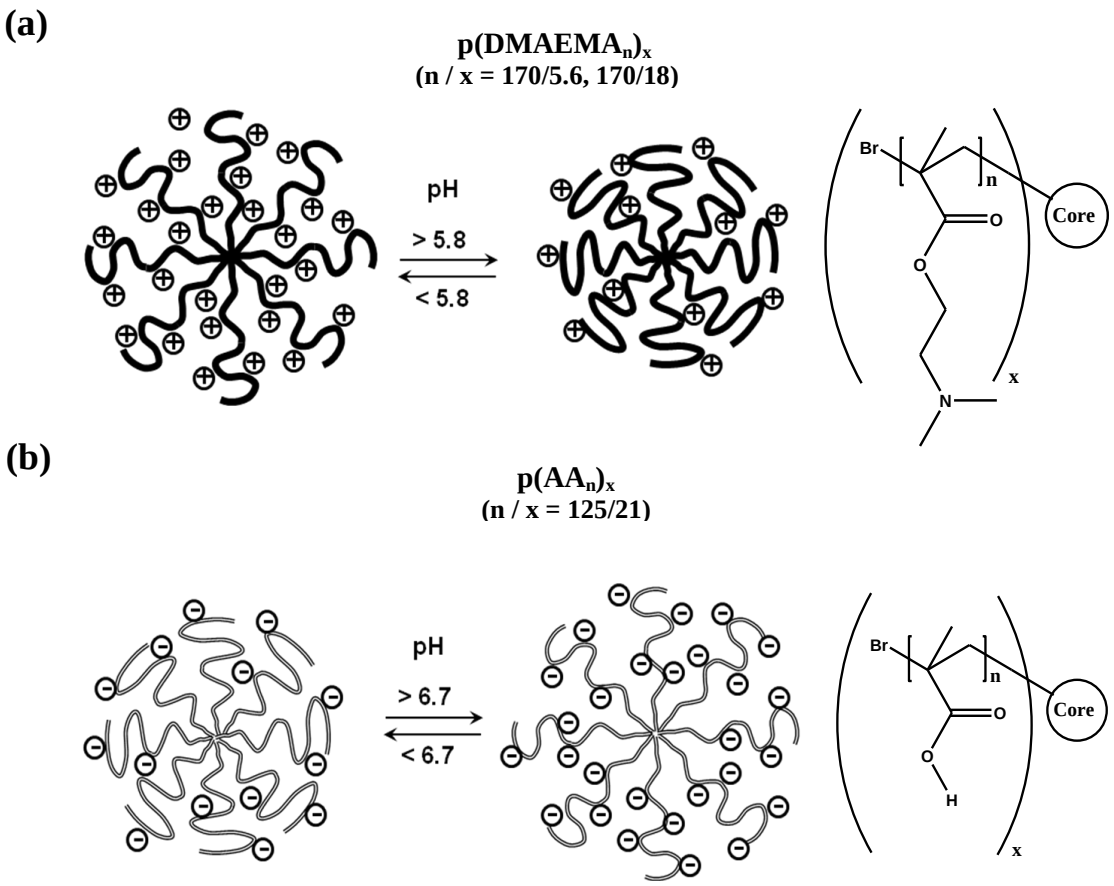

Scheme 7.1: pH-responsive molecular conformation of (a) cationic p(DMAEMA$_n$)$_x$ and (b) anionic p(AA$_n$)$_x$ star polyelectrolyte with the chemical structure of monomer unit of star polyelectrolyte (n refers to the degree of polymerization of each arm and x denotes the number of arms). It is not set to the real length-scale for all drawings.

AFM images were obtained with a Dimension-3000 in the "light" tapping mode with an amplitude ratio, within 0.90-1.00 to avoid surface damage and film deformation.[135,136] The AFM cantilevers had spring constants in the range of 40-60 N/m. Scanning rates were between 1.0-2.0 Hz, depending on the scan area that ranged from 40 x 40 μm^2 down to 1 x 1 μm^2.[137] The large area optical microscope images were collected by optical microscopy operating in the bright field mode (Leica DM4000M). UV-vis spectroscopy was conducted on a Craic QDI 202 microscope spectrophotometer attached to a Leica microscope with a 50x objective. Measurement of contact angles were undertaken with a KSV CAM101 at three different locations for each sample.

Table 7.2: Polymer Pair and Notation of p(AA) and p(DMAEMA) for LbL Assemblies.

Polymer pair		DP[a] of arm (n) / Number of arms (x)		Molecular weight ($\times 10^{-3}$ g/mol)
p(AA) / p(DMAEMA)	Notation	$p(AA_n)_x$	$p(DMAEMA_n)_x$	$M_{n,p(AA)}$ / $M_{n,p(DMAEMA)}$
Linear / Linear	LL	1400 / 1	880 / 1	100 / 139
Linear / Star	LS	1400/ 1	170 / 5.6	100 / 146
Star / Linear	SL	125 / 21	880 / 1	190 / 139
Star / Star	SS	125 / 21	170 / 18	190 / 490

[a]DP refers to the degree of polymerization.

7.3. Results and Discussion

7.3.1 LbL assembly from star and linear polymers at variable pH.

pH-sensitive p(DMAEMA) and p(AA) polymers are weak polyelectrolytes which can be ionized depending on pH with respect to the pK_a of p(DMAEMA) and p(AA) (Table 7.1, Scheme 7.1). The apparent value of pK_a is defined as the pH when 50% neutralization of total ionic monomer units occurs in a titration curve. The pK_a shift of polyelectrolyte star compared to the linear polymer has been known to be caused by the increased confinement of counterions within the macroion.[115,310] This results in a higher osmotic pressure within the star polymers which constrains the neutralization. The shifts are dependent on not only the degree of neutralization, but also the number of arms and arm length due to the variation of mean segment density within the star.[37,130] The pH-dependence of weak polyelectrolytes has a significant influence on the molecular conformation in solution and at the interface by undergoing the "coil-to-globule" phase transitions.[311] Cationic p(DMAEMA) stars having a different number of arms (5.6 and 18) with the same degree of polymerization of each arm employed to evaluate the effect of the number of arms (see characteristics of all components in Table 7.1).

Then, we chose and compared different polymer pairs to assemble LbL films based on star (S) or linear (L) p(DMAEMA) and p(AA) polyelectrolytes (Table 7.2). Four different pairs were selected for LbL assembly to represent components with different numbers of arms and degrees of polymerization of each arm (Scheme 7.1). For convenience, the same notation (LL, SL, LS, and SS, see Table 7.2) referring to each LbL pair will be utilized throughout this manuscript. A bilayer is defined as a polyelectrolyte

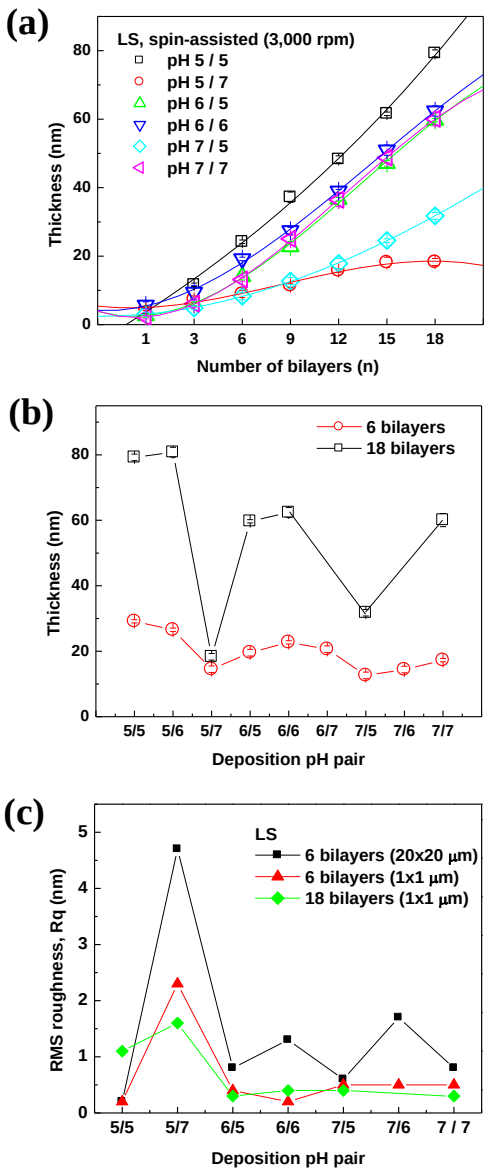

Figure 7.1: (a) Buildup curve of linear/star (LS) film versus number of bilayers prepared using spin-assisted method (3,000 rpm) at various combinations of deposition pH conditions for p(AA)/p(DMAEMA) pairs: 5/5, 5/7, 6/7, 6/6, 7/5, and 7/7. (b) Variations of thickness of LS for 6 bilayers and for 18 bilayers versus different deposition pH pairs. (c) RMS roughness for LS at different scan areas and number of bilayers: 20 μm x 20 μm of 6 bilayers (■), 1 μm x 1μm of 6 bilayers (▲), and 1 μm x 1μm of 18 bilayers (♦) (the lines are a guide to the eye).

pair composed of one polyanionic p(AA) layer and one polycationic p(DMAEMA) layer. Two and a half (2.5) bilayers of $(p(AH)/p(SS))_{2.5}$ with p(AH) as the topmost layer were employed to improve the initial adhesion and provide the same initial condition prior to assembling the main p(AA) and p(DMAEMA) LbL multilayer film.

Both spin-assisted and dip-assisted LbL methods were employed at various assembly pH conditions such as pH 5/5, 5/7, 6/5, 6/6, 7/5, and 7/7 to explore the pH-sensitive assembly behavior of weak linear/star polyelectrolytes. In this pH notation the first figure refers to the solution pH of the p(AA) component and the second one is the pH of the p(DMAEMA) solution. The pH region ranging from 5 to 7 is chosen here because it covers the pK_a of both p(DMAEMA) and p(AA) that are considered to give different interactions between polymer pairs (Table 7.1) and ensures stable LbL growth. We also explored more acidic (down to 2) and basic (up to 8) conditions. However, these conditions led to extremely non-uniform and unstable films and thus were not studied in detail further.

In the selected pH region ranging from 5 to 7, the variation of the LbL film thickness shows a high dependency on the dipping solution pH condition (Figure 7.1). A lower pH than 5 for p(AA) and a higher pH than 7 for p(DMAEMA) appears to induce the desorption of the LbL film during the spin-assisted LbL assembly due to insufficient ionic charge density as will be discussed later. Considering the pK_a of both components are within 5.8-6.7, the pH combinations represent pairs with the weakest electrostatic interactions (5/5, 6/6, and 7/7) in contrast to pairs with the strongest interactions of

components at 7/5 and 7/6. Moreover, the expectation is that p(AA) is in a compact shape and p(DMAEMA) is in an expanded state for lower pH (5 and 6) and vice versa for higher pH (7) although variation of molecular dimensions of the star components is much less pronounced than that for the linear counterparts.[37,64,115]

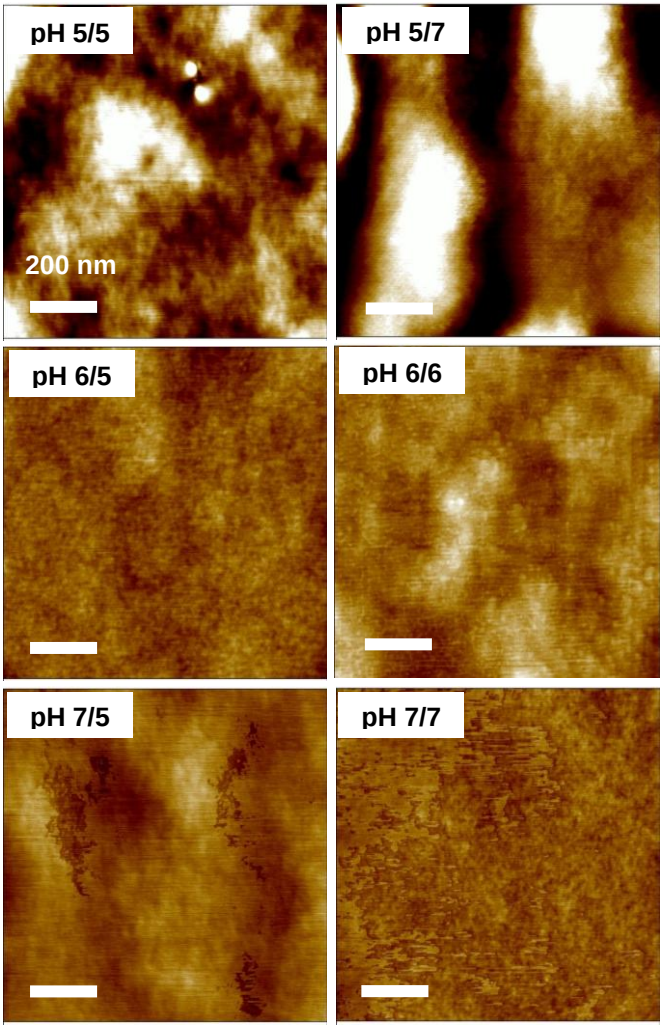

Figure 7.2: AFM topography images of linear/star LbL films (LS) with 18 bilayers assembled by using spin-assisted method at different pH pairs. Scan area for all images is 1 μm × 1 μm and Z scale is 5 nm.

For the linear p(AA) and star p(DMAEMA) pair (LS, Table 7.2), we examined the spin-assisted LbL growth at variable pH conditions by measuring the thickness of LbL films

with an increasing number of bilayers (Figure 7.1(a)). The results revealed that the LbL assembly behavior appears to be close to the linear buildup profile in all cases.

It is clear that the growth of LbL films depends upon the assembly pH conditions: at pH 7/5 and 5/7, the resulting thickness observed was the lowest while at pH 5/5 and 6/6, the thickest LbL films were shown (Figure 7.1, Table S7.1). Thickness variations are similar for 6 and 18 bilayer films within 50-100% variation for thin films which increases to 200-300% for thicker LbL films (18 bilayers) (Figure 7.1).

AFM topography images of these films, presented in Figure 7.2 (see Supporting Information, Figures S7.2, S7.3 for 6 bilayers), show clear differences in surface morphologies at different pH at both large- and fine-scales. A smooth morphology was observed for all specimens except LbL films assembled at 5/7 conditions. Indeed, surface roughness was within 0.2-1.7 nm at a 20 μm x 20 μm surface area with higher values for modestly phase separated films at 6/6 and 7/6 (Table S7.1). Surface roughness below 0.5 nm for 1 μm x 1 μm surface area is also characteristic of uniform, molecularly-smooth LbL films grown in a linear regime (Figure 7.1(c), Table S7.1). The formation of polyelectrolyte complexes in most of the cases would lead to a smooth surface due to a "ladder-like" architecture with a stretched conformation whereas partially ionized chains can adopt a "scrambled salt conformation" composed of a high percentage of "loops" and "tails" which results in odd surface morphology.[260]

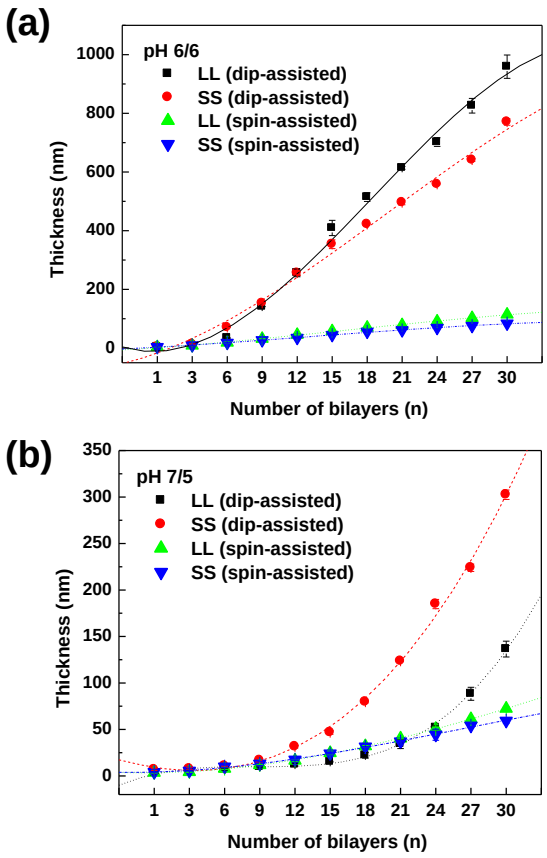

Figure 7.3: Buildup curve of the LbL multilayer assembly of varying combinations of linear and star polyelectrolytes as a function of number of bilayers (1 to 30 bilayers) at different pH conditions (a) 6/6 and (b) pH 7/5: LL (dip-assisted (■) and spin-assisted (▲)) and SS (dip-assisted (●) and spin-assisted (▼)) (the lines are a guide to the eye).

In the case of pH 5/5, the LbL film thickness is the highest, but the surface appears to be very even showing a smooth morphology as compared to that of pH 5/7 (Figure 7.2, S7.3). This result indicates that at lower pH conditions more ionized arms of p(DMAEMA) should form a smooth surface by adopting a stretched conformation.[312,313] In contrast, AFM images of 5/7 LbL films show very uneven surface morphology with surface corrugation at micron and sub-micron scales and developed surface roughness as

high as 4.7 nm at large surface areas (20 μm × 20 μm) and 2.3 nm for fine surface areas (1 μm × 1 μm) (Figure 7.1(c)).

Table 7.3: Thickness and Roughness of Spin- and Dip-Assisted LbL Films.

pH	Method	Polymer pair	Thickness (nm) Number of bilayers (n) 9[a]	18[a]	30[a]	30[b]	30[c]	RMS roughness (nm)[d] Number of bilayers (n) 9	18	30
6/6	Dip	LL	141.3 ± 0.5	514.6 ± 15.0	959.1 ± 39.7	1032.5 ± 8.0	790	2.9	29.7	49.8
		SS	152.6 ± 2.0	422.0 ± 2.0	770.4 ± 10.9	797.6 ± 3.0	757	2.1	3	1.7
	Spin	LL	31.6 ± 1.5	70.0 ± 1.0	114.5 ± 0.3	117.0 ± 4.0	-	0.5	0.6	0.7
		SS	26.7 ± 1.0	56.0 ± 2.0	83.7 ± 3.0	92.0 ± 7.0	-	0.8	1.1	1.7
7/5	Dip	LL	9.7 ± 1.0	22.1 ± 3.0	136.4 ± 8.5	144.9 ± 6.0	-	0.6	0.9	46.0
		SS	16.8 ± 2.0	79.6 ± 1.0	302.5 ± 5.0	307.5 ± 2.0	-	1.7	3.4	6.7
	Spin	LL	13.1 ± 2.0	31.5 ± 0.1	59.3 ± 3.0	60.2 ± 2.0	-	0.4	0.8	0.6
		SS	11.8 ± 0.7	32.1 ± 0.6	72.4 ± 2.0	80.5 ± 4.0	-	0.5	0.8	1.7

[a] obtained by fitting the ellipsometry data to the Cauchy model. [b] measured using a scratching method by AFM height analysis. [c] thickness values were obtained from UV-Vis interference fringe data by plotting l/2 versus n/λ using the equation of $l/2 = 2d \times (n/\lambda)$ where l/2 is the interference order, d, the thickness, n, the refractive index, and λ, the wavelength.[317] [d] all RMS roughness values were collected from AFM image of 10 μm × 10 μm.

This uneven surface morphology can be an indication that a stable complexation cannot be successfully realized due to the weak electrostatic interactions at this pH condition.[312,313] Indeed, both p(AA) and p(DMAEMA) components are weakly charged under these conditions with the collapsed state of linear p(AA) further promoting local phase separation. The overall trends in thickness and roughness variation are similar for 6 and 18 bilayer LbL films with more pronounced roughening visible for 5/5 LbL films (Figure 7.2).

7.3.2. Spin-assisted vs conventional LbL assembly: different modes of growth.

The different LbL assembly methods are known to define the morphology of LbL films due to distinct mass flow, drying rate, and diffusion characteristics.[289,320] In order to investigate this aspect, we selected two different assembly pH conditions which generated the highest adsorbed amount at pH 6/6 and the lowest growth rate at 7/5. Under these conditions, the growth curve of linear- and star-based LbL multilayers was examined for up to 30 deposited bilayers (60 deposition cycles) (Figure 7.3).

The linear growth of spin-assisted LbL films at pH 6/6 showed a low increment of 3.8 nm/bilayer for the linear/linear pair, and even lower, 2.8 nm increment, for the star/star pair (Table 7.3, Figure 7.3). The thicknesses of 30 bilayers, 117 nm for linear/linear film and 92 nm for star/star film, determined from ellipsometry and from AFM scratch tests are virtually identical indicating the uniformity of the films. The same trend is observed for pH 7/5 deposition conditions with the growth increment further decreasing to 2.0 nm/bilayer for the linear/linear pair and to 2.4 nm for the star/star pair (Figure 7.3).

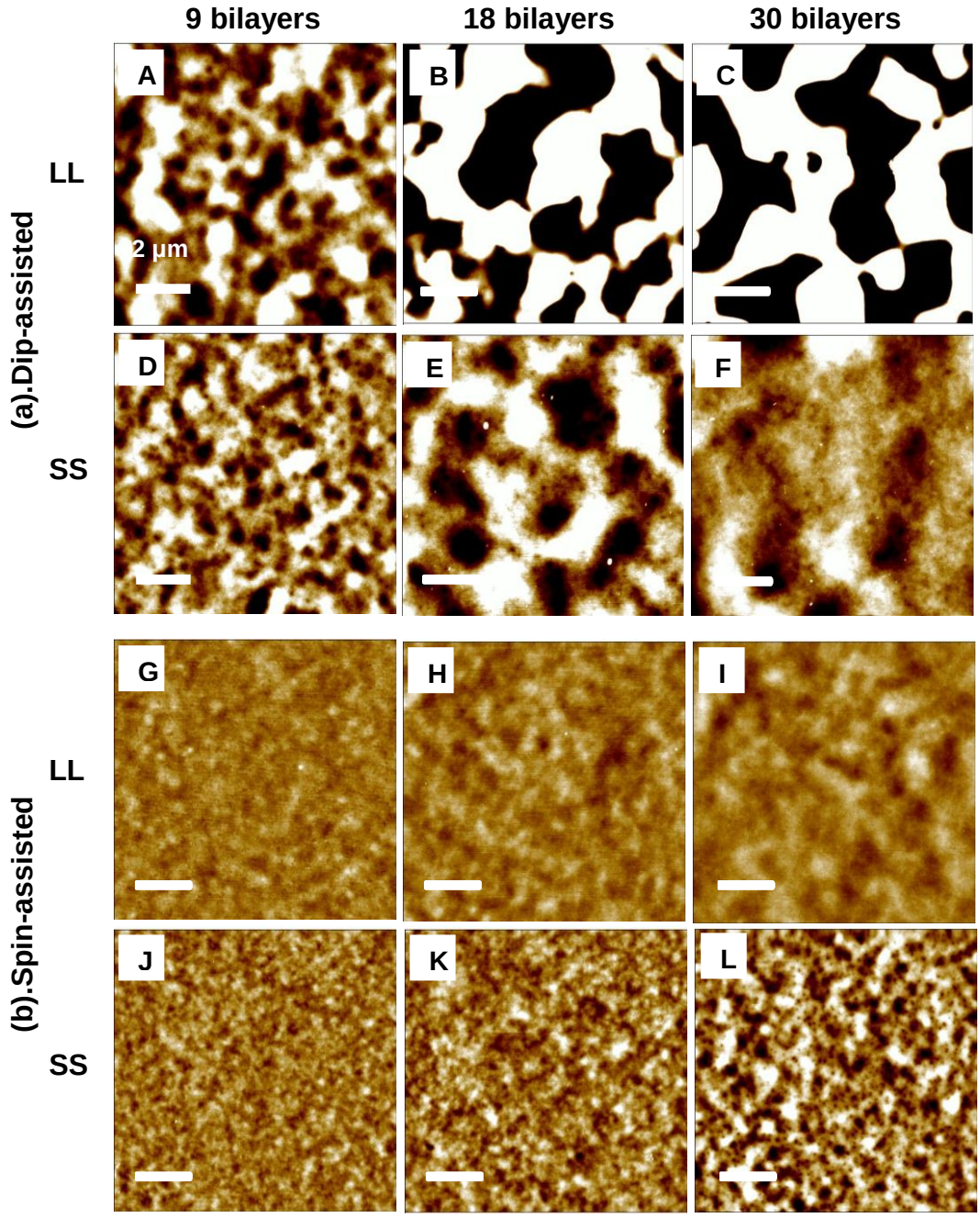

Figure 7.4: AFM topography images of the LbL multilayer films composed of different components with different numbers of bilayers (9, 18, and 30 bilayers): linear/linear (LL) (A-C, G-I) and star/star (SS) (D-F, J-L) assembled at pH 6 / 6 using dip-assisted (a) (A-F) and spin-assisted (b) (G-L) methods. Scale bar is 2 µm and Z scale is 10 nm for all images.

For linear/linear pairs (pH 6/6 and 7/5) prepared by the dip-assisted method, the increased surface roughness (roughness up to 50 nm for 30 bilayers) of LbL film with increasing numbers of bilayers was observed to reduce reflectivity of the film due to light scattering. However, the intensity of reflected light was sufficiently high for determining the film thickness (raw data of Ψ and Δ was added in Supporting information, Figure S7.1) indicating the LbL films remain optically transparent and uniform despite increased surface roughness.

Since the ellipsometry measurement give a relative thickness value, AFM height analysis was used to confirm the thickness of the LbL film. The thickness from ellipsometry was in agreement with the thickness obtained from the height difference seen between bare silicon and the top of the film during an AFM scratch test.[260,273,314,315] This result clearly showed that the increased surface roughness (up to 50 nm) has no significant effect on the accuracy of thickness measurement by ellipsometry due to the fact that the total thickness of LbL films is much (around ten-fold) higher than the surface inhomogeneities. However, the error in thickness measurement tends to be increased with increase in thickness and surface roughness. In contrast, the LbL films obtained by the dip-assisted method grow at a much higher rate (Figure 7.3). At pH 6/6 the initial exponential growth for a number of bilayers 3 to 12 is replaced with a linear growth with a high increment of around 30 nm/bilayer. A similar trend is observed for both linear/linear and star/star pair LbL assemblies obtained with the dip-assisted method. The overall LbL thickness approached 1 μm for only 30 bilayers (Table 7.3).

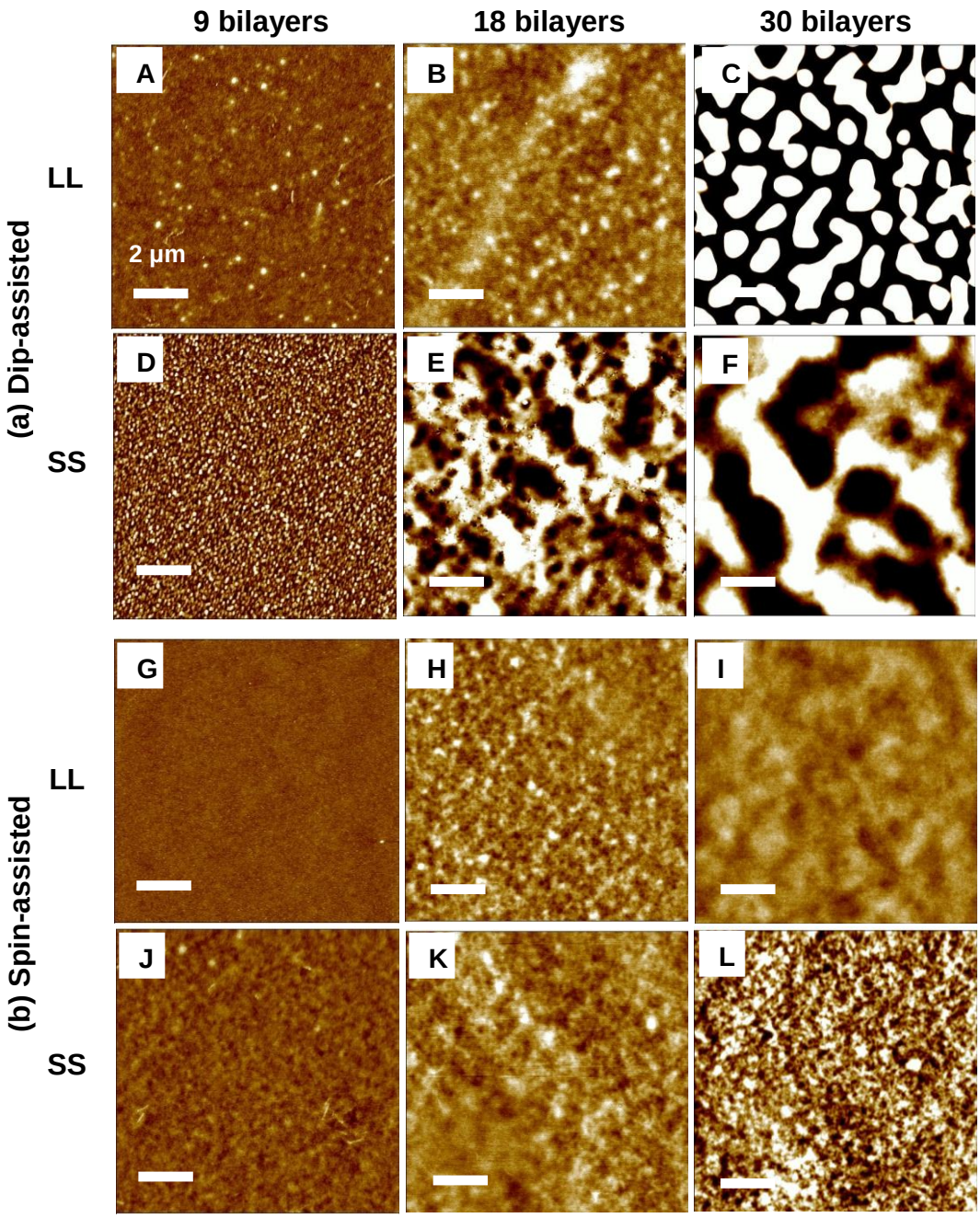

Figure 7.5. AFM topography images of the LbL multilayer films composed of different components with different numbers of bilayers (9, 18, and 30 bilayers): linear/linear (LL) (A-C, G-I) and star/star (SS) (D-F, J-L) assembled at pH 7/5 using dip-assisted (a) (A-F) and spin-assisted (b) (G-L) methods. Scale bar is 2 μm and Z scale is 10 nm for all images.

Remarkably, under different assembly conditions, at pH 7/5 we observed exponential growth for both linear/linear and star/star LbL assemblies with the number of bilayers above 9 (Figure 7.3). In this mode, the rate of growth is the highest at the latest stage of growth reaching 50 nm/bilayer for n = 20-30 and far exceeding the average increment of around 30 nm for dip-assisted 6/6 LbL films and around 3 nm for spin-assisted LbL films (Figure 7.3). To further explore the evolution of the surface morphology of LbL growth behavior, AFM images were compared for the different number of bilayers (9, 18, 30) for pH 6/6 and 7/5 (Figure 7.4, 7.5). As presented in Figures 7.4(B,C) and 7.5(C), a distinct large surface domain morphology (domain height reaching 150 nm) was observed at both 6/6 and 7/5.

The distinct surface corrugation appears to occur at microscopic length scales throughout the samples. The surface roughness on the scale 10 μm x 10 μm increases with increasing number of bilayers (Table 7.3). We note that at pH 6/6 and pH 7/5 linear/linear LbL films display a rougher surface than star/star for the dip-assisted method in contrast to the results of the spin-assisted LbL which showed opposite trend (Figures 7.4, 7.5). Star/star spin-assisted LbL films show significant increase in roughness on the scale 10 μm x 10 μm compared to linear/linear counterpart. Overall, spin-assisted LbL films show smoother morphology and lower roughness on the 10 μm x 10 μm than dip-assisted films for all combinations studied here.

This difference suggests that star polymers with large molecular weight can be distributed unevenly and accumulate as larger aggregates due to progressing phase separation with

an increasing number of bilayers deposited and time available for diffusion and rearrangement (hours) although the shear force and short processing times of the spin-assisted method make them transform into a smooth morphology with very fine roughness on the 10 μm x 10 μm. It appears that for the linear/linear pairs, the spin-assisted LbL method prevents intermixing within the multilayers due to limited diffusion time induced by the quick solvent removal. In contrast, for the case of the star/star pairs, shearing is believed to allow transformation of spherical star polyelectrolyte macromolecules into a flattened pancake-like shape.[320]

Contact angle measurements were further performed to monitor the change in surface wettability of LbL films with a topmost layer of p(DMAEMA (Figure S7.4). Overall, a contact angle within 50-70° indicated a modestly hydrophobic surface which is within the range reported for ultrathin surface layers of the p(DMAEMA) component (65°).[316] Some modest variation for different LbL films can be related to variable surface roughness, drying conditions, and minor exposure of the underlying, less hydrophobic p(AA) component with an effective contact angle of below 10°.[312,313] Thicker 30 bilayer films demonstrate more uniform values of contact angles across all LbL films with different compositions. For LbL films at pH 6/6 with 30 bilayers we observed a slightly lower contact angle of 57° ± 3 than 63° ± 3 for 7/5 LbL films, which can be related to a more collapsed topmost layer of p(DMAEMA) due to the surface diffusion of the p(AA) layer (Figure S7.4).

7.3.3. Optical properties of LbL films.

Optical microscopy images of the 30 bilayer linear/linear dip-assisted LbL films show large-scale non-uniform patterns of different intensity in contrast to the uniform spin-assisted LbL films (Figure S7.5). This surface inhomogeneity is indicative of the occurrence of dramatic phase changes caused by phase separation during the assembly process. A more notable rough surface was observed for linear-linear pairs fabricated by the dip-assisted method confirming the AFM data discussed above. Star/star pairing resulted in much more uniform films on an optical scale (Figure S7.5).

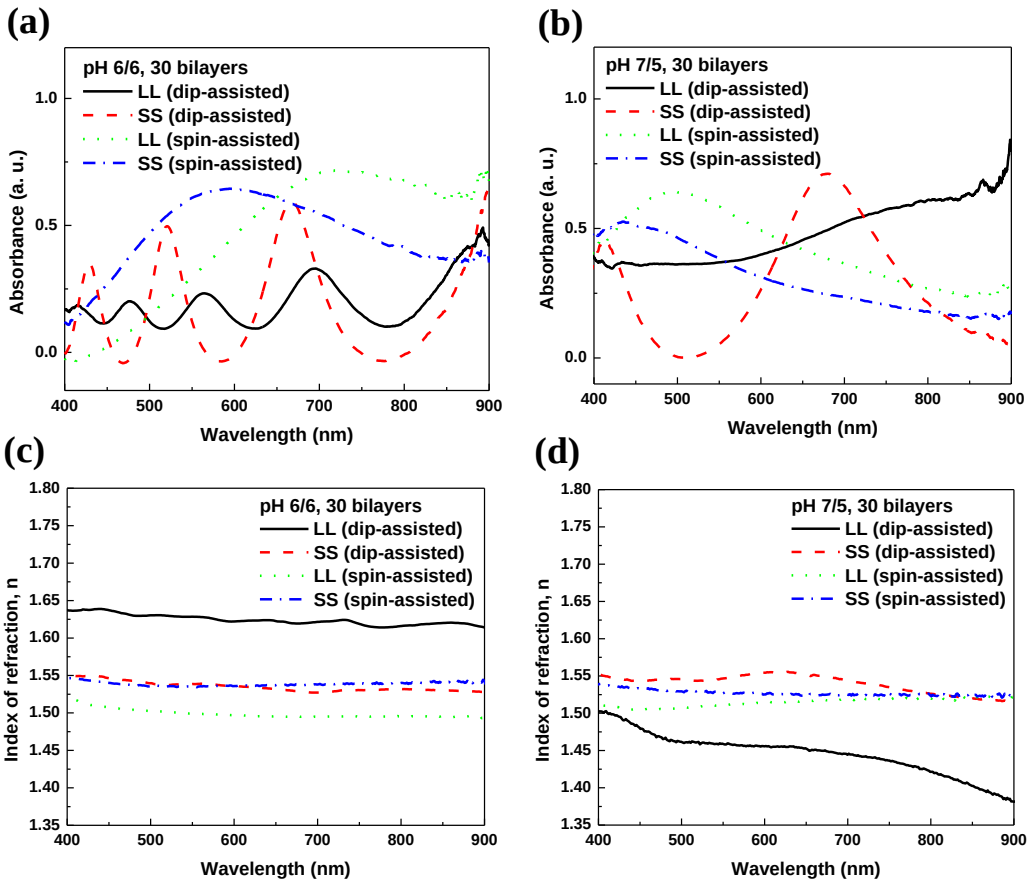

Figure 7.6: UV-Vis spectra in a reflective mode ((a) and (b)) and index of refraction ((c) and (d)) for LbL multilayer films with 30 bilayers prepared at different deposition pH pairs: pH 6/6 ((a) and (c)) and pH 7/5 ((b) and (d)).

As a result of the overall uniformity, linear and star LbL films display sharp and rich color variation with an increase in thickness due to interference phenomena for sub-micron films. For pH 6/6 and pH 7/5 the reflective star/star LbL films obtained with the dip-assisted method give a microscopically uneven surface with multiple colors of green and violet. Linear/linear LbL films look less reflective, which can be ascribed to their higher film inhomogeneities in the optical range (Figure S7.5). Spin-assisted LbL films with smaller thicknesses showed a relatively uniform bluish color for both linear and star components. LbL films at pH 7/5 showed similar results for the different assembly methods and pH conditions, but the overall color appearance is not well-developed due to the smaller thickness of the LbL films.

The UV-vis measurements, which were utilized to quantify the rich color appearance, clearly display a broad peak or a series of periodic peaks related to the light interference for thicker LbL films of linear/linear and star/star LbL films fabricated by the dip-assisted method at pH 6/6 (Figure 7.6). Multiple interference peaks with several harmonics is a peculiar feature of these films with thicknesses close to 1,000 nm that suggests that the LbL films remain optically clear and uniform at the micron scale despite the high level of surface corrugation observed with optical and AFM microscopies (Table 7.3). Apparently, the thickness of the LbL film has widespread local uniformity over large surface areas with regions of uniform thicknesses of a few microns across despite the surface corrugations. These large surface regions act as coherent domains not causing excessive light scattering in the visible range in contrast to most exponentially grown thick films. In fact, such an optical uniformity is a rare observation for exponentially

grown LbL films, which usually become opaque quickly with a growing number of layers due to the intense microphase separation and increased roughness on a sub-micron level. Remarkably, the estimation of the thickness of the LbL films from analyzing different orders of interference gives thicknesses which are close to independent AFM and ellipsometry measurements (Table 7.3).[317] This close correspondence confirms the true nature of the rich colors produced as coming from large microscopic domains with extremely uniform thickness over large surface areas.

Finally, the ellipsometry measurements of LbL films show refractive indices within a range of 1.52-1.63 for longer wavelengths (Figure 7.6). The significant decrease in the effective refractive index for linear/linear LbL films from 1.63 at pH 6/6 to 1.45 at pH 7/5 is caused by the formation of laterally non-uniform films due to microphase separation. However, all other LbL films show virtually unchanged refractive indices indicating that pH-triggered reorganizations do not result in significant changes in material properties.

7.3.4. Exponential growth for different star architectures.

To examine the effect of polymer components with different architectures on the exponential growth mode, linear/star pairs were further investigated at pH 6/6 and pH 7/5 (Table 7.2, Figure 7.7). Thicker LbL films display a linear buildup over a wide range from 9 to 30 bilayers, which can be described as $d = An + B$ where d is the thickness, n is the number of bilayers, A is the slope corresponding to the thickness of one bilayer, and B is d-intercept (Figure 7.7(a)). The rate of growth in the linear mode is similar for all LbL films with an around 100 nm/bilayer. Such extremely large growth rates in a linear

mode indicate a significant dependence of component diffusion during polyelectrolyte deposition on the amount of material deposited during a single step, which seems to have far exceeded the expected value for single monolayers of polyelectrolytes in non-disturbed conformations.

The exponential growth mode was analyzed by using the known equation: $d = A_0 e^{(n/\tau)}$ where d denotes thickness, A_0 is a scaling parameter, n is the number of bilayers, and τ corresponds to the characteristic growth time (Table 7.4).[298,318,319] Such an analysis shows that the growth mode for all polymer pairs is described by the exponential model with $R^2 \sim 0.98$ (Figure 7.7(b)). The linear/linear pairs show the highest growth rate while the star/star pairs possess the slowest rate of exponential growth. The linear/star combinatory pairs lie between the growth rates of linear/linear and star/star pairs. The overall characteristic growth parameter τ for LbL films studied here is within 1.2-1.5 for pH 6/6 and 2.2-3.0 for pH 7/5 (Table 7.4). These parameters indicate that the rate of exponential growth for pH 7/5 conditions is similar to those reported earlier for various LbL films (usually within 2-3).[298,313] In contrast, at pH 6/6 a much higher (twice) rate of exponential growth (two times lower τ) is observed for all component combinations studied here (Table 7.4).

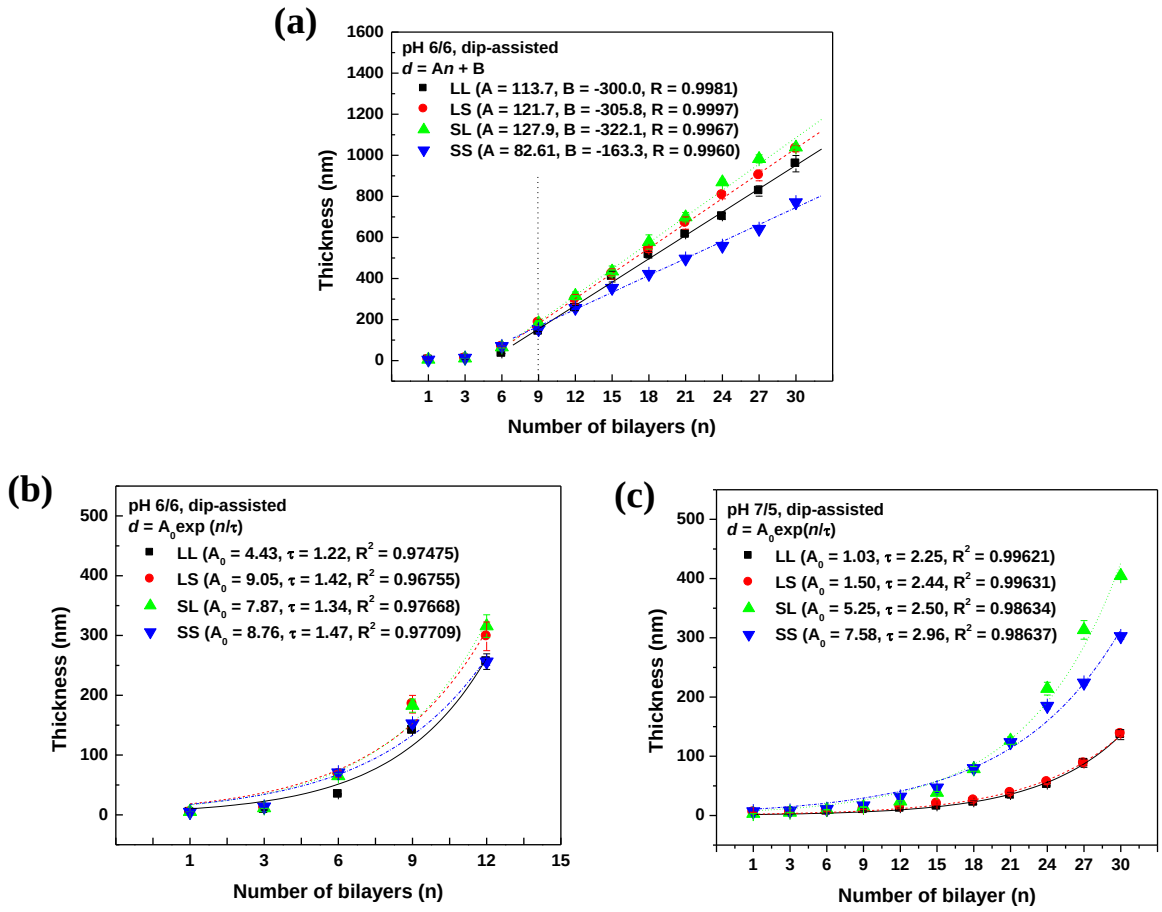

Figure 7.7: Buildup curve of the LbL multilayer films assembled with varying chain topology as a function of number of bilayers assembled by dip-assisting method at different pH conditions of pH 6/6 ((a) and (b)) and pH 7/5 (c): linear/linear (LL) (■), linear/star (LS) (●), star/linear (SL) (▲), and star/star (SS) (▼). (a) Linear growth curve is obtained by fitting date in the linear buildup region (n = 9 to 30) into a function of d = An + B for pH 6/6. (b) Exponential growth rate obtained by fitting the data into a function of $d = A_0\exp(n/\tau)$ (n = 1 to 12) for pH 6/6 (b) and (n = 1 to 30) for pH 7/5 (c).

In contrast to pH 6/6, at pH 7/5 exponential growth occurs for all linear and star pairs studied here after a period of slow growth during the initial few depositions (Figure 7.7(c)). Exponential analysis shows excellent fit with R^2 = 0.99 throughout the whole range of n from 1 to 30 bilayers (Figure 7.7(c), Table 7.4). Comparison of different assembling conditions reveals an overall lower rate of growth at 7/5 as compared to that

at pH 6/6 (Table 7.4). Such a difference can be related to the stronger intermolecular interactions at pH 7/5 than pH 6/6. The increased degree of ionic crosslinking can lead to the suppressed diffusion of polymer within LbL films. Also, the flat and smooth surface morphology due to the further extended conformation at pH 7/5 seems to contribute to the lower exponential growth.

Table 7.4: Exponential Growth Rate Parameters for dip-assisted LbL.

pH	polymer pair	τ	A_0
6 / 6	LL	1.22	4.43
	LS	1.42	9.05
	SL	1.34	7.87
	SS	1.47	8.76
7 / 5	LL	2.25	1.03
	LS	2.44	1.50
	SL	2.50	5.25
	SS	2.96	7.58

All results were obtained by fitting the thickness data versus the number of bilayers into the exponential growth formula represented by $d = A_0 e^{n/\tau}$ (d denotes the thickness of LbL film and n is the number of bilayers).

A summary of the morphological parameters (terminal thickness for 30 bilayers and large-scale roughness on the scale 10 μm x 10 μm) for all four polyelectrolyte pairs is presented in Figure 7.8 and corresponding AFM images are displayed in Figure 7.9. As apparent from this data, exponentially grown linear/linear p(AA)/p(DMAEMA) LbL films possess the most non-uniform morphology with large-scale microphase separation resulting in excessive roughness of about 50 nm on the scale 10 μm x 10 μm for both assembly conditions. Similar morphological features are observed for star/linear pairs

with the high surface roughness for these pair reaching 40 nm on the scale 10 μm x 10 μm (Figure 7.8). Such a difference for star-containing LbL films suggests that the linear components contribute to the exponential growth via surface roughening due to the faster diffusion and higher mobility caused by weak ionic interactions of the p(AA) or p(DMAEMA) chains.

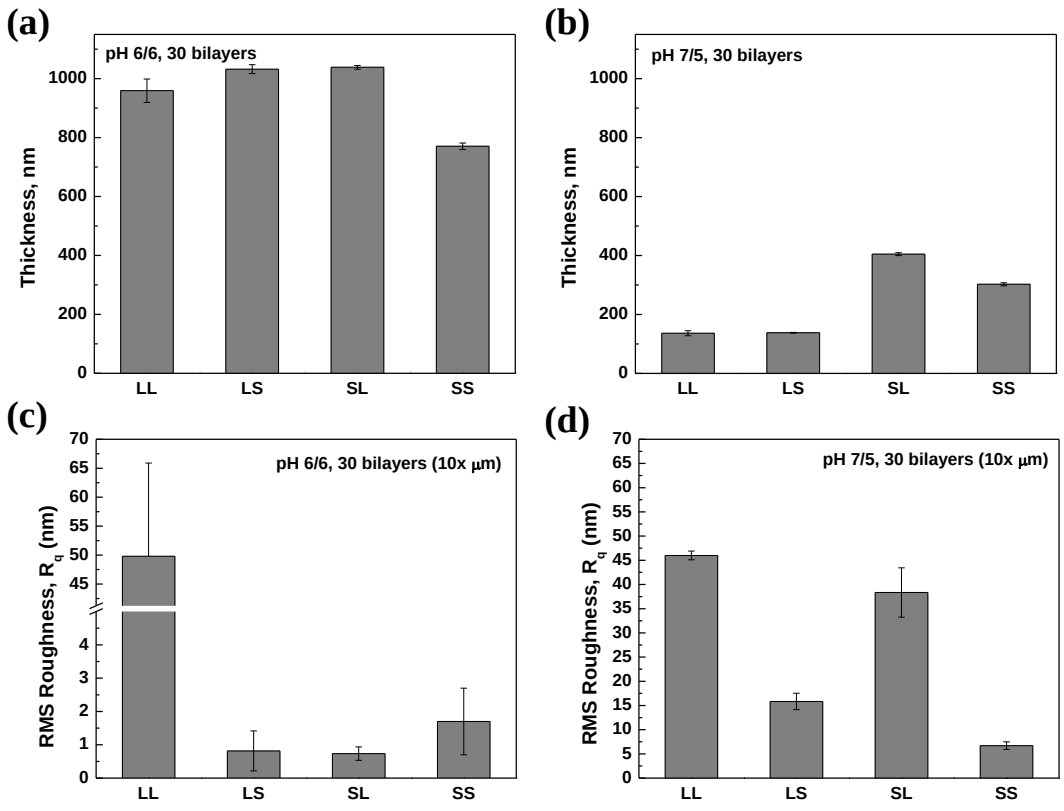

Figure 7.8: Variations of thickness ((a) and (b)) and RMS roughness (R_q) ((c) and (d)) of the 30 bilayered dip-assisted LbL films for different polymer pairs at pH 6/6 ((a) and (c)) and pH 7/5 ((b) and (d)).

In striking contrast, all star-containing LbL films show consistent exponential growth with the formation of thick and smooth films with surface roughnesses on the 10 μm x 10

μm not exceeding 2.0 nm for pH 6/6, a small value for LbL films (Figure 7.8). This value increases only modestly to 5-15 nm at 7/5 deposition conditions.

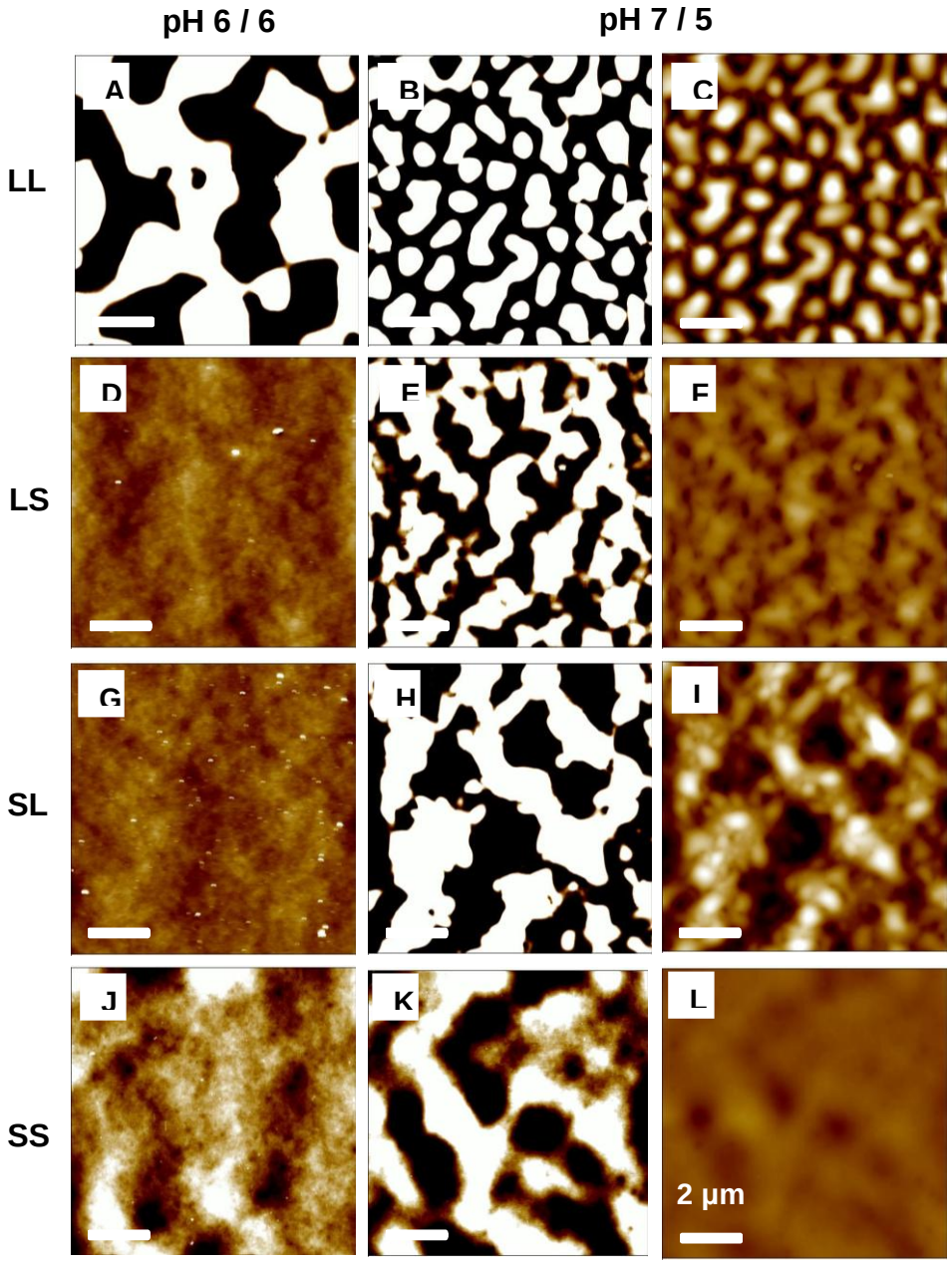

Figure 7.9: AFM topography images of the LbL multilayer films with different polymer pairs assembled at pH 6/6 (A-J, left) and 7/5 (B-K, middle and C-L, right) using dip-assisted method: linear/linear (LL) (A-C), linear/star (LS) (D-F), star/linear (SL) (G-I), and star/star (SS) (J-L). Scale bar is 2 μm and Z scale is 10 nm for all images and the Z scale is 10 nm (A-J, left and B-K, middle) and 200 nm (C-L, right).

Moreover, higher resolution AFM images show near uniform morphology at a sub-micron scale with a modest aggregation of components with the formation of network morphology with a mesh size of 100-200 nm (Figure 7.9, pay attention that the AFM images for 7/5 presented at two different Z-scales to show all details of rich surface morphology at different spatial scales).

These distinct and uniform morphologies, which do not occur in rough and microphase-separated exponentially grown linear/linear LbL films, might be attributed to the combination of high interdiffusion of star polyelectrolytes through the swollen matrix due to lower ionic crosslinking and a weak degree of ionization.

7.3.5. Shear rates and resulting spin-assisted LbL morphologies.

To probe the LbL assembly behavior under variable shear force, we studied the surface morphology of linear/linear and star/star pairs under selected conditions at increasing intervals of the rotational velocity up to 8,000 rpm during spin-assisted deposition. Figure 7.10 presents the thickness increase for these LbL films at 0 (dip-assisted), 1,000, 3,000, 6,000, and 8,000 rpm. For all spin-assisted LbL films shown here, the growth profiles is near-linear or slow exponential growth for both linear/linear and star/star pairs in contrast to the fast exponential growth observed for dip-assisted LbL films.

Overall, the resulting spin-assisted LbL films are 2 to 6 times thinner than their dip-assisted counterparts. This behavior is in a sharp contrast to that observed for other LbL

components such as p(SS) and p(AH) with much thicker films built via spin-assisted LbL assembly.[133] Such difference can be caused by the much weaker interactions between p(AA) and p(DMAEAMA) components under given pH conditions and the suppressed interdiffusion during spin-assisted LbL assembly.

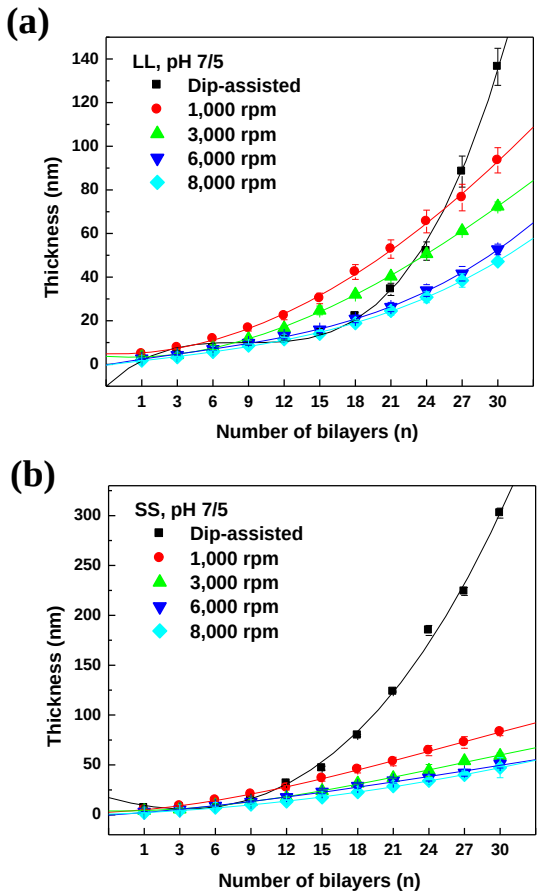

Figure 7.10: Buildup curve of the LbL films fabricated with dip- and spin-assisted methods for linear/linear (LL) (a) and star/star (SS) (b) polymer pairs at different spinning speeds in the range of 0 to 8,000 rpm at pH 7/5 (the lines are a guide to the eye).

It is also interesting that although dip-assisted LbL films from star/star pairs are much (twice) thicker than that from linear/linear pairs, the same star/star films prepared with spin-assisted LbL assembly are much (up to 50%) thinner (Figure 7.10). Such a dramatic

thinning of the star/star LbL films under intense shearing could be related to the fact that star polyelectrolytes retain their more compact shape and higher mobility in fluidic flow. Both contributions should result in a reduced amount of material tethered to the substrate in the course of spin casting. This effect is confirmed by the strong role of the increasing shear rates with the thinnest LbL films obtained at the highest rotational velocities (Figure 7.10).

To elucidate the true nature of structural changes occurring during spin-assisted assembly, AFM measurements were taken to examine the surface morphology versus the shear rate for these LbL films (Figures S7.6). As was discussed above, the surface morphology of dip-assisted linear/linear LbL films is non-uniform with microscopic

irregular surface domains and a worm-like morphology with high roughness reaching 45 nm for the 10 μm × 10 μm surface area (Figure S7.6(a)). In contrast, star/star LbL film show a more uniform morphology with some larger-scale surface corrugations, occasional holes, and much lower overall roughness of 7.0 nm on the scale 10 μm x 10 μm. The presence of holes may be attributed to either insufficient coverage or traces of draining solvent or air bubbles trapped within the multilayer film, which were not removed during the assembly process.

On the other hand, spin casting of both linear and star polyelectrolytes results in a much smoother surface morphology with a dramatically reduced roughness below 2.0 nm and a thickness down to 30-50 nm on the 10 μm x 10 μm (Figures S7.6, S7.7). Such thinning

and smoothing can be related to the removal of larger, weakly tethered aggregates clearly visible for LbL films obtained by the dip-assisted method and a suppression of lateral diffusion/microphase separation of components during fast (a fraction of a second) removal of solvent. Moreover, a further increase in the shear rate results in the progression of this reorganization with a gradually decreased film thickness and increased roughness on the scale 10 μm x 10 μm and domain size for both linear/linear and star/star polyelectrolytes (Figures S7.6, S7.7).

7.4. Conclusions

The assembly behavior, growth modes, and surface morphologies of LbL films composed of cationic p(DMAEMA) and anionic p(AA) weak polyelectrolyte stars at different deposition pH conditions close to the pK_a of the star polyelectrolytes (pK_a ~ 5.8 and 6.7 for respective components) were found to be critically dependent on the interplay of intermolecular interactions and conformational states as will be discussed in this section.

Firstly, we will discuss different modes of growth of the LbL films assembled with spin-assisted and dip-assisted routines. As we observed here, the spin-assisted method results in the stable and linear growth of LbL films from any combination of star and linear counterparts under all pH and shearing conditions tested here. The characteristic feature of this growth mechanism is the low rate of growth of 2-4 nm per bilayer. This growth rate is many times smaller than the unperturbed dimensions of the polymer chains exploited here (10-30 nm) indicating that both star and linear polyelectrolyte components

become highly flattened and compacted with excessive material removal under strong shearing forces and fast solvent removal.

The significant decrease in bilayer thicknesses observed here for spin-assisted LbL films is in striking contrast to that reported for conventional linear strong polyelectrolytes, which show much thicker spin-assisted LbL films obtained as compared to dip-assisted LbL films.[289,292] In the case of the strong polyelectrolytes studied earlier, the increased thickness was associated with a higher grafting density caused by enhanced attractive interactions between oppositely-charged polymer chains and very limited intermixing as was confirmed by neutron reflectivity of LbL films with deuterated components.[292] A similar phenomenon of the thinning of spin-assisted LbL films observed for p(EO) and p(AA) components was related to the suppression of the formation of a micellar morphology. The critical role of weak interactions in significant thinning was also demonstrated for short-range hydrogen-bonded spin-assisted LbL films.[320] Accordingly, the dramatic thinning of polyelectrolyte bilayers for weak polyelectrolytes studied in a pH range close to the isoelectric points of all components can be caused by weak interfacial interactions resulting in easy displacement of the adsorbed macromolecules by the fast removal of solvent and the strong shearing of polymer chains.

In fact, as has been suggested for branched, dendritic macromolecules a full range of shapes from highly spread, to pancake-like, to near-globular can be observed depending upon the strength of interfacial interactions and the type of surface assembly (grafting, Langmuir monolayers, or LbL films).[16,36,321,322,323,324] Indeed, star/star polymer pairs

were demonstrated to show a decreased extent of entanglement and limited molecular interdiffusion due to the compact and globular structure of branched molecules.[64] However, dendritic and hyperbranched macromolecules usually possess uniform chemical composition and surface-bonded functionalities. The occurrence of microphase separation of different long-chain arms within multiarm star block-copolymers and uniform ion distribution across loosely-packed star block copolymers are the most critical factors affecting their assembly behavior.

Apparently, the attachment of polycationic and polyanionic chains to a single, but relatively voluminous core, in star polymers does not significantly affect the resulting morphology of spin-assisted LbL films. Virtually identical thicknesses and surface morphologies of LbL films for all linear/linear, linear/star, and star/star polyelectrolyte pairs suggest that under low grafting density conditions, architectural confinement does not affect the ability of relatively long, flexible, and weakly charged arms to adapt a highly flattened, pancake-like conformation (Scheme 7.2). Histograms with actual film thicknesses and microroughnesses which are placed next to the film schematics clear quantify and scale dramatic changes in the LbL film morphologies for different compositions and different pH assembling conditions.

The overall morphology of spin-assisted LbL films remains stable over a wide range of assembling conditions within a pH range of 5-7, which can be related to the modest variation of macromolecular dimensions and degree of ionization. This is especially true for star polyelectrolytes in contrast to the dramatic changes usually observed for linear

polyelectrolytes within a narrow pH range.[278, 325] Therefore, this growth behavior supports the suggestion that the star structure limits the chain entanglements owing to steric hindrance, and as a result, suppresses the ionic crosslinking and reduces adherence to the substrate.

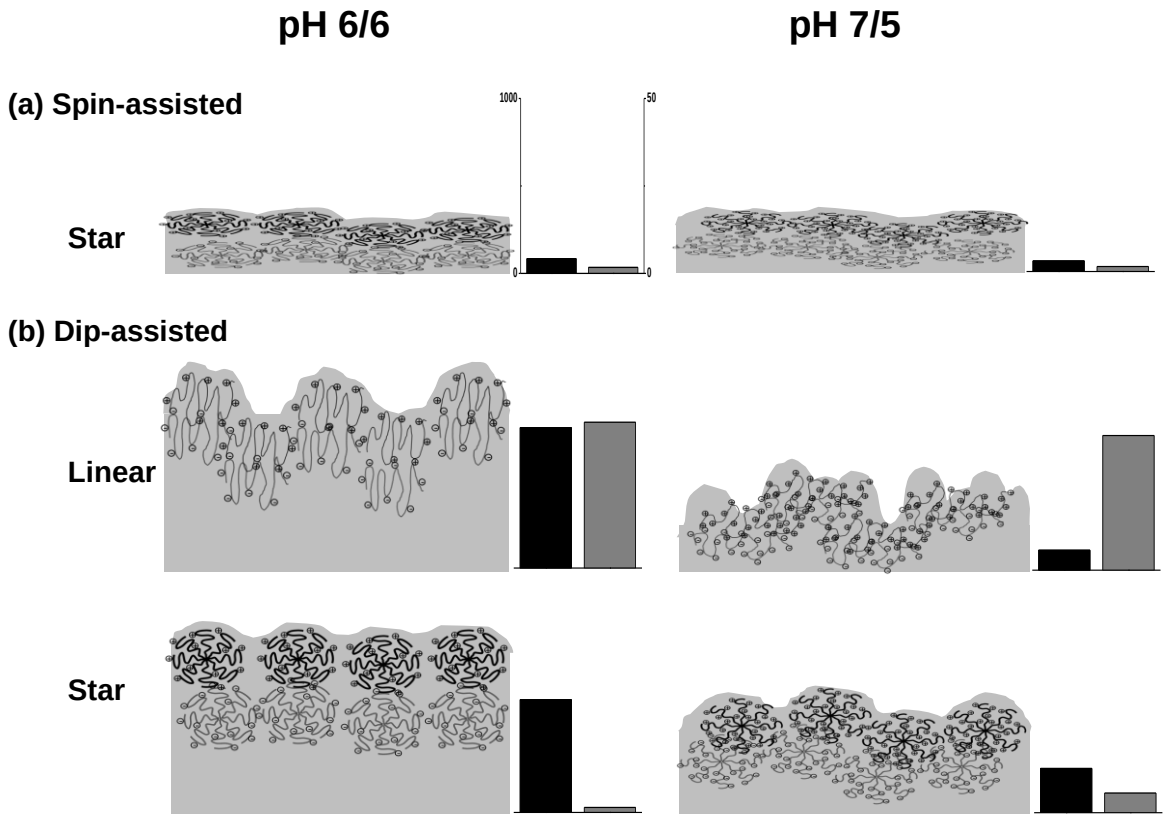

Scheme 7.2: Model structure of LbL multilayer films displaying the surface structure and expected molecular organization within the LbL assemblies: (a) spin-assisted LbL for star and (b) dip-assisted LbL for linear (top) and star (bottom) polymer at different pH condition of pH 6/6 (left) and pH 7/5 (right). Gray color-boxes represent the LbL films with different thicknesses and surface roughness, but their values are not set to the same length-scale for all drawings. The histograms on the right hand side of each drawing show the average thickness (black, left) and roughness (gray, right) with the left y-axis (1000 nm) for thickness and right y-axis (50 nm) for roughness for 30 bilayer LbL films. The bar graphs are all on the same scale.

In contrast to spin-assisted LbL films, the corresponding dip-assisted LbL films fabricated from star and linear p(DMAEMA) and anionic p(AA) show a rich pattern of different exponential growth modes controlled by the preparation conditions and molecular architecture (Scheme 7.2). Apparently, the dip-assisted environment with a long time available for swelling and interaction with solution is kinetically more favorable for extensive interdiffusion of components, large-scale molecular aggregation, and lateral diffusion of aggregates.

The first and most crucial conclusion is that weak star polyelectrolytes are capable of growing thick LbL films in an exponential growth mode. This result is even more surprising considering that star polyelectrolytes with high molecular weight and a large number of arms have been observed to be capable of growing only in the linear mode due to slow diffusion of star polyelectrolytes that prevents the common diffusion mechanism of fast exponential growth. Moreover, to date, only rough and thin LbL films have been fabricated via a linear growth mode with a small increment per bilayer (within 1-8 nm) with a few exceptions discussed below.[64,115] In contrast, the star/star and star/linear LbL assemblies studied here demonstrate an exponential growth mode with an increment per bilayer reaching 100 nm with without significant roughening.

The analysis of the experimental data with a generalized exponential function shows excellent correspondence of the growth kinetics to an extended slow growth phase and an exponential growth up to a very large number of bilayers (up to 30) in the case of the 7/5 LbL assemblies (Figure 7.7, Table 7.4). At milder pH 6/6 conditions, close to the pK_a for

both components, the LbL growth becomes even more dramatic with a narrow slow growth phase for the first few bilayers and then enters a fast exponential growth regime for n = 5 to 15, followed by linear growth for n = 15-30 (Figure 7.7). As a result, the LbL film reached 1 μm thickness which is many times higher than that for a dip-assisted LbL film fabricated earlier for star-based LbL films with an even higher molecular weight of components (30-80 nm for n = 10-16).[64,115]

At the pH 6/6 assembly condition, the rates of growth of star/star and linear/linear LbL films are similar although the total effective "molecular weight" of a bilayer of a stoichiometric composition is much lower for linear/linear pair (239,000 vs 680,000 g/mol) (Table 7.1). This effect suggests a more compact shape of star polyelectrolytes (per unit of mass) and probably less efficient uptake of star polyelectrolytes with much lower specific charge density per unit of volume during the buildup of LbL assemblies. On the other hand, the rate of growth at pH 7/5 is the highest for star/star LbL films with twice higher thickness as compared to that for linear/linear pairs (Figure 7.7). Such a difference can be associated with the slightly increased ionic interactions of the higher charged polycationic component with a dominating molecular weight contribution.

The investigation of the exponential growth rate for different component pairs such as linear/linear, linear/star, star/linear, and star/star LbL assemblies reveals that the pH 6/6 condition gives the highest growth rate with a resulting thicker film reflecting a stronger tendency toward the diffusion of star polyelectrolyte components during exposure to oppositely-charged polyelectrolytes, but without excessive roughening due to molecular

aggregation caused by lateral microphase separation after the completed deposition cycle (Scheme 7.2). It has been known that the exponential rate depends on the molecular weight and the mismatch in molecular size and ionic charge density.[298,297] This higher growth rates seem to be consistent with the lower ionic crosslink density of star polyelectrolytes at pH 6/6, thereby suggesting the weak ionic density is critical for the facilitation of an exponential growth mode even for the high molecular weight star polyelectrolytes employed in this study. That is, the larger number of "loosely-complexed" polymer chains at pH 6/6 could effectively contribute to the complexation because of mismatched ionic charges.[298,313,326] The retarded exponential buildup at the initial stages at pH 7/5 can be explained by the higher ionic density, and lower molecular weight of linear/linear and linear/star pairs than that for star/linear and star/star pairs. The compact branched architecture of the star polymer would limit the ionic complexation mainly in the outer shell, which might lead to large mismatching in ionic pairing. Thus, effective ionic charges that can contribute to ionic crosslinking may be lower than that for the linear counterpart, which might allow for high mobility within LbL films and facilitate the exponential growth of all star LbL films, a unique finding of this study.

However, the lower ionic density and higher ionic state mismatch between polyanionic and polycationic components at pH 6/6, particularly when incorporating the star component lead to thicker and more uniform LbL films. Notably, the resulting morphology of exponentially-grown star-containing LbL films is different from similar linear/linear pairs. The linear/linear pairs show well-developed "worm-like" surface

morphology with large surface roughness on the 10 μm x 10 μm. For star component containing LbL films the isolated and partially interconnected domain network appears to transform to a fully interconnected large-scale worm-like morphology which is, however, underpinned with a thicker material film. We suggest that the increased mass adsorption at pH 6/6 as well as the higher mobility of star polymer chains due to lower ionic density could lead to both a higher adsorption rate during the deposition step and, as a result, a reduced lateral aggregation due to the slow diffusion of star complexes.[103,326] This appears due to a combination of fast interdiffusion of components and their complexes followed by lateral microphase separation of dissimilar components and their complexes (Scheme 7.2).[103,286,295,298,308] The dramatically increased surface roughness enhances accelerated film buildup due to increased specific interfacial area and a higher probability of the interfacial adsorption during sequential exposure to solutions.[104,115] This model seems validated for linear/linear pairs of linear components, anionic p(AA) and cationic p(DMAEMA) by all experimental data acquired here.

It is important to note that to date very few studies attempted to exploit star polyelectrolyte for LbL assembly with a very limited selection of linear and star components and for a limited number of bilayers (below 10). In these studies, either the traditional linear growth mode was observed and associated with slow diffusion of high molecular weight star polyelectrolyte[64] or some evidences of the exponential growth have been noticed for few limited cases[115,309]. In contrast, in this study we introduced a far more comprehensive combination of linear and star polylectrolyte components with a wide range of molecular architectures and assembling conditions covering critical pH

combinations and an extended number of assembling cycles (up to 60). Such a comprehensive analysis unexpectedly revealed a uniquely rich LbL assembling behavior and morphologies of star polyelectrolytes with an extended combination of all linear, exponential, and linear/exponential modes of growth to be controlled by pH conditions and component nature.

In fact, we observed that the exponential growth of linear/linear pairs results in a rough (>50 nm roughness on the 10 μm x 10 μm) "worm-like" morphology caused by intense microphase aggregation of components, whereas the star/star LbL films from chemically identical polyelectrolyte components undergo very different growth mechanism. For star/star polyelectrolyte pairs thick, uniform, and molecularly smooth exponentially grown LbL films have been revealed in this study. We suggest that star polyelectrolytes with compact shape, partially screened charges and high diffusion mobility facilitate fast complexation and lead to exponential buildup of the LbL films. This fast buildup is likely to hinder efficient lateral diffusion of components and thus prevents large-scale microphase separation, which results in smooth, locally uniform, thick, and optically transparent LbL films with rich interference properties, a unique combination for exponentially grown LbL films from traditional linear polyelectrolytes.

Appendix. Supporting Information: Table S7.1 and Figure S7.1-S7.7.

Table S7.1: Thickness and Roughness of linear/star (LS) LbL FIlms at Different pH Deposition Conditions.

	Thickness (nm)[a]		RMS roughness (nm)		
pH[b]	6 bilayers	18 bilayers	6 bilayers (20 × 20 μm)	6 bilayers (1 × 1 μm)	18 bilayers (1 × 1 μm)
5 / 5	24.2 ± 0.5	79.2 ± 1.0	0.2	0.2	1.1
5 / 6	26.5 ± 0.5	80.8 ± 1.5	1.0	0.7	1.0
5 / 7	8.9 ± 1.0	18.3 ± 1.0	4.7	2.3	1.6
6 / 5	14.0 ± 0.5	59.7 ± 0.5	0.8	0.4	0.3
6 / 6	19.2 ± 1.0	62.4 ± 1.5	1.3	0.2	0.4
7 / 5	8.3 ± 1.0	31.8 ± 1.0	0.6	0.5	0.4
7 / 6	14.4 ± 1.0		1.7	0.5	
7 / 7	13.2 ± 0.5	60.1± 2.0	0.8	0.5	0.3

[a]All thickness values were obtained by fitting the ellipsometry data to the Cauchy model. [b]The first figure in notation corresponds to pH of p(AA) solution and the second one corresponds to pH of p(DMAEMA).

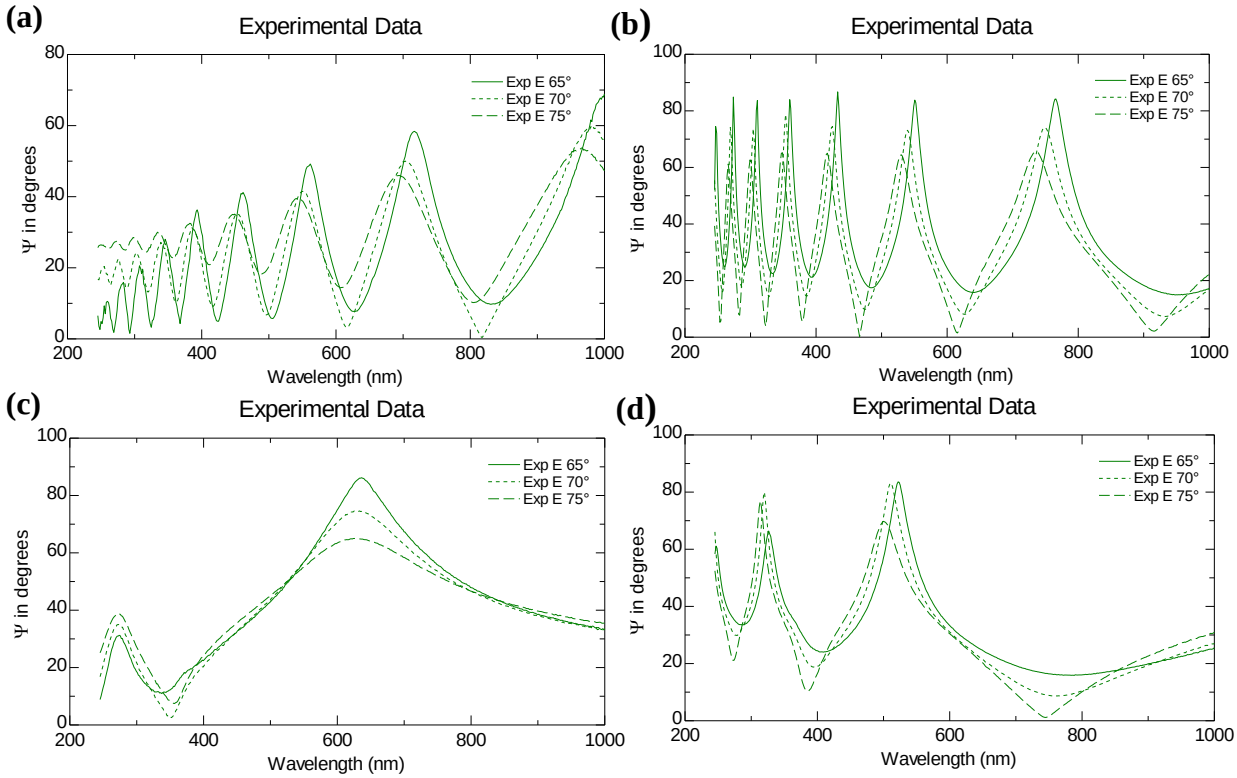

Figure S7.1: The ellipsometric raw data of Ψ (polarized angle) and Δ (phase) of dip-assisted LbL multilayer films on silicon oxide substrate measured at three incident angles 65, 70, and 75° for wavelengths from 200 to 1000 nm. (a) Linear/linear pair at pH 6/6, (b) star/star pair at pH 6/6, (c) linear/linear pair at pH7/5, and (d) star/star pair at pH 7/5.

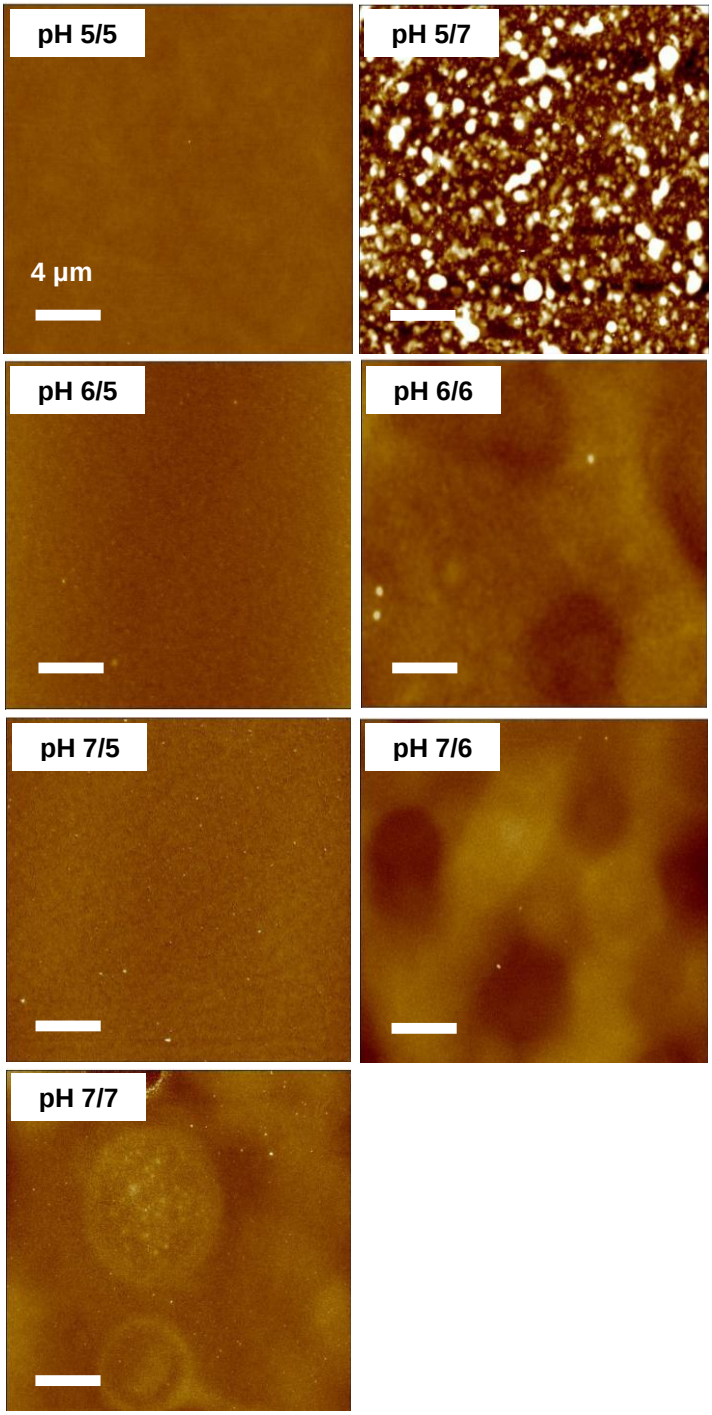

Figure S7.2. Large scale AFM topography images of linear/star LbL films (LS) with 6 bilayers assembled by using spin-assisted method at different pH pairs. Z scale is 20 nm.

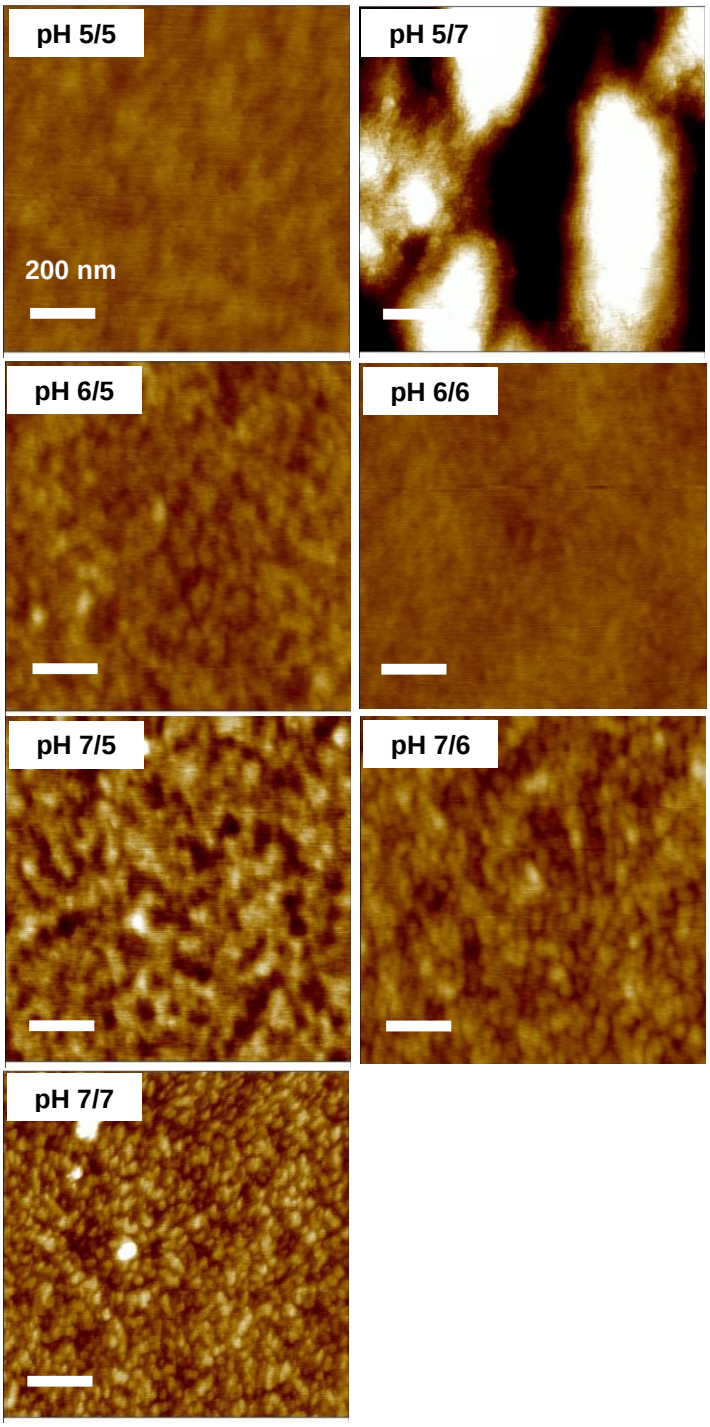

Figure S7.3: AFM topography images of linear/star LbL films (LS) with 6 bilayers assembled by using spin-assisted method at different pH pairs. Scan area for all is 1 μm × 1 μm and Z scale is 5 nm.

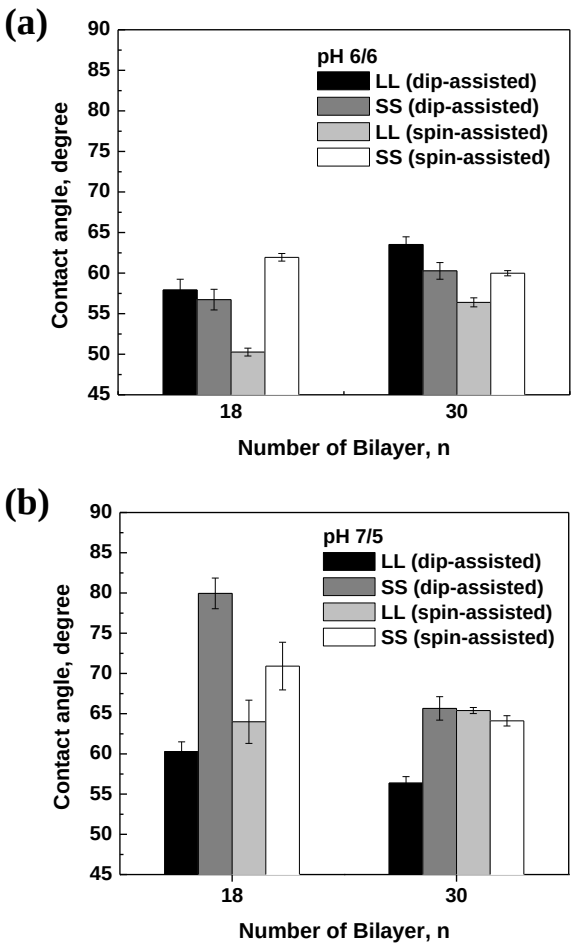

Figure S7.4: Contact angle of the LbL multilayer films composed of different components with different numbers of bilayers (18 and 30 bilayers): linear/linear (LL) (dip-assisted (black) and spin-assisted (light gray)) and star/star (SS) (dip-assisted (dark gray) and spin-assisted (white)) at different deposition pH pairs: (a) pH 6/6 (a) and (b) pH 7/5.

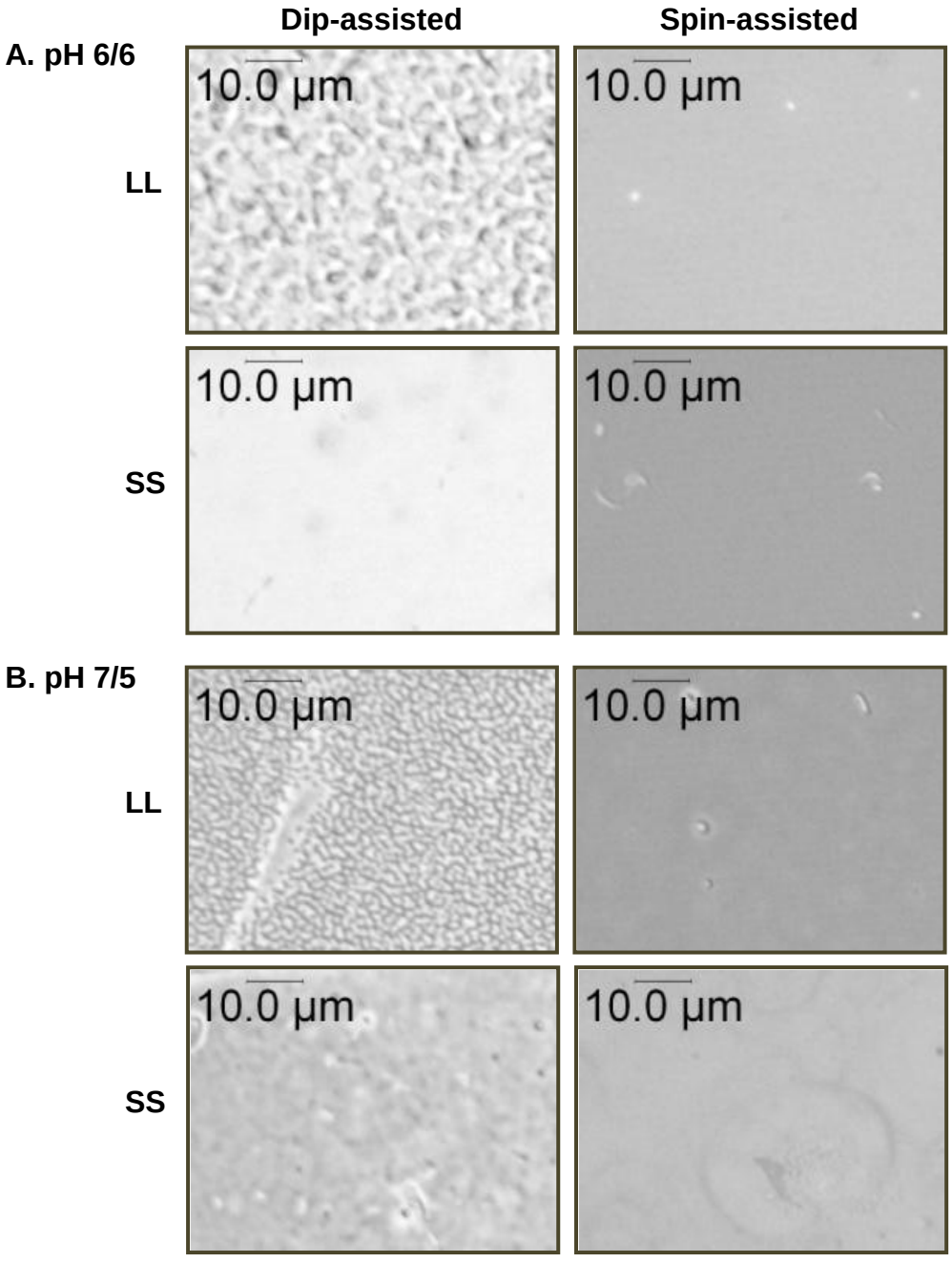

Figure S7.5: Optical microscopy images of LbL films with 30 bilayer films assembled at pH 6/6 using dip- (A) and spin-assisted (B) methods.

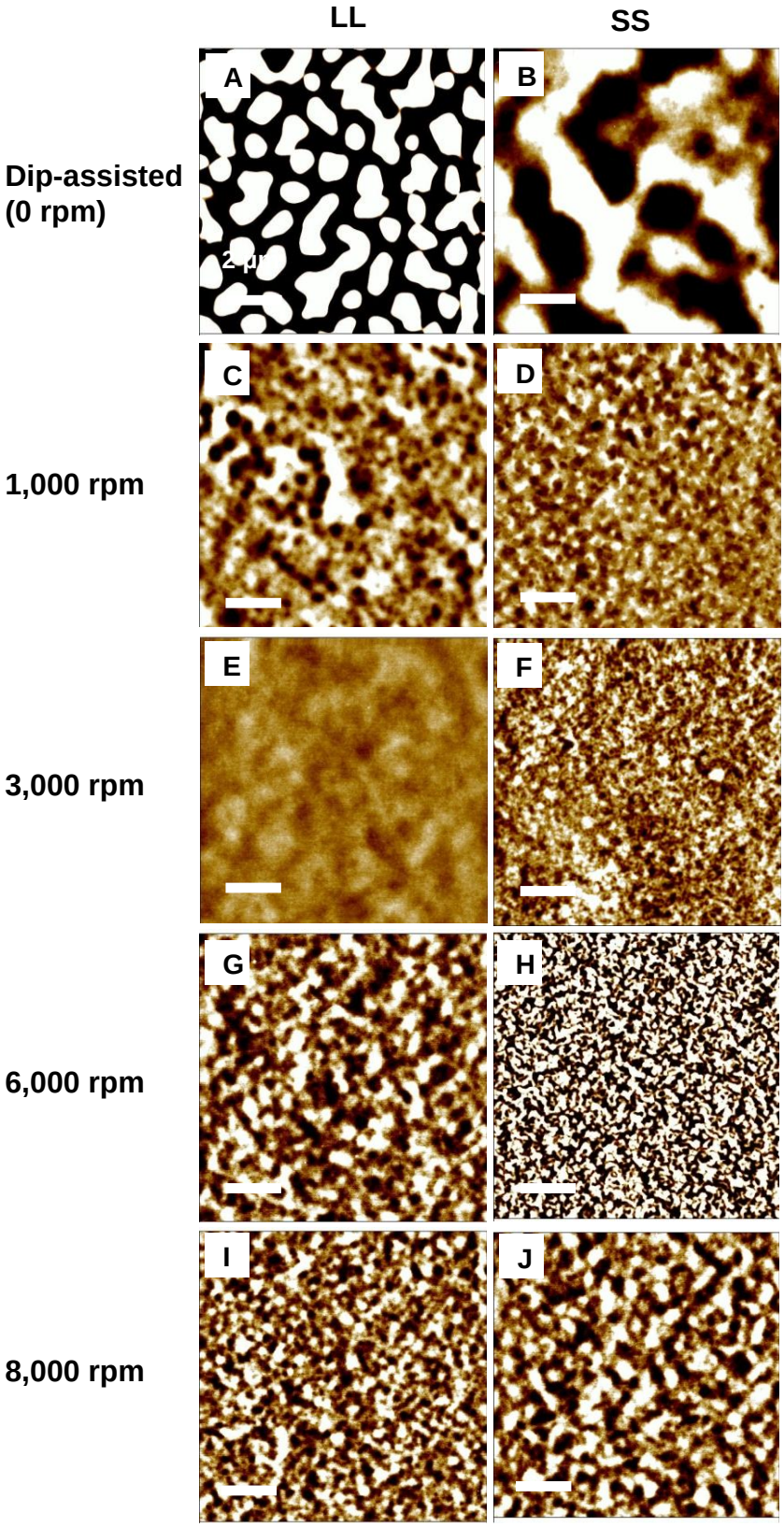

Figure S7.6:

Figure S7.6: AFM topography images of 30 bilayer LbL films: linear/linear (LL) (left) and star/star (SS) (right) assembled at different spinning speeds at pH 7/5. Scan area for all images is 10 μm × 10 μm and Z scale for height is 10 nm.

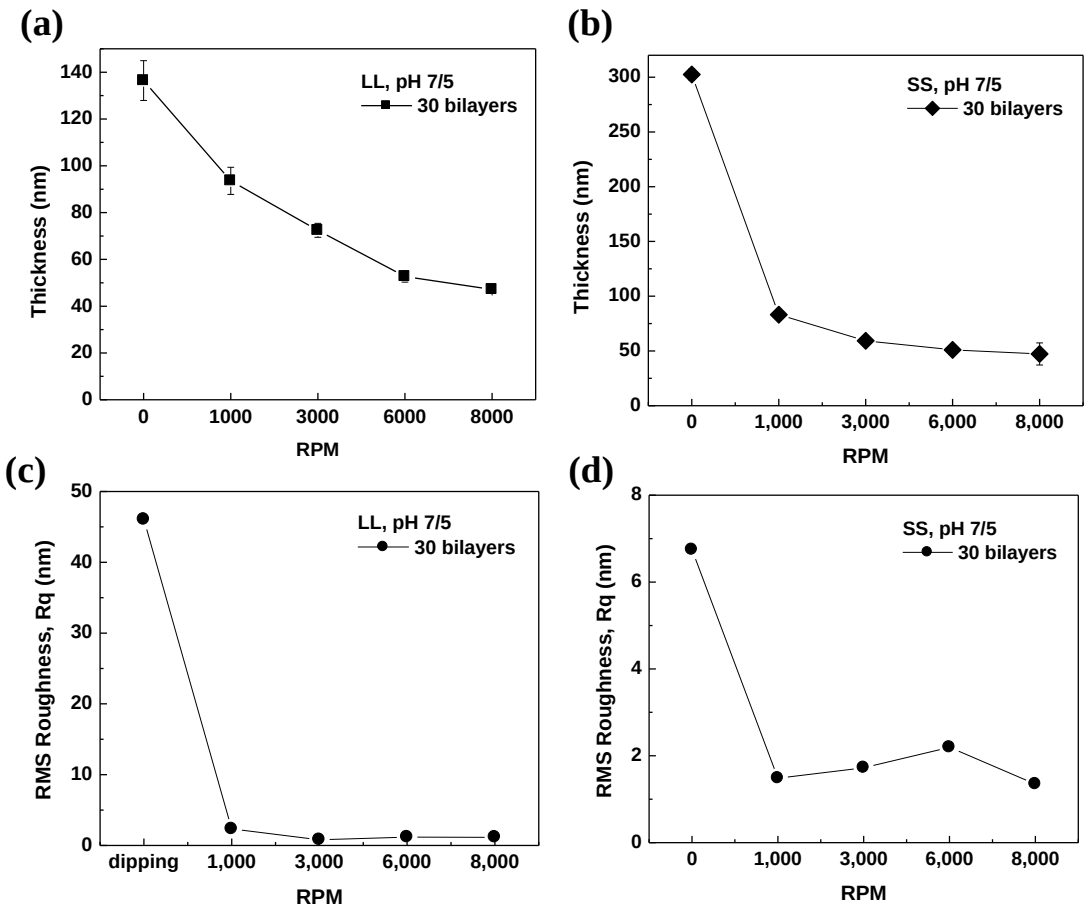

Figure S7.7: Variations of thickness ((a) and (b)) and RMS roughness (R_q) ((c) and (d)) of 30 bilayer LbL films of linear/linear (LL) (left) and star/star (SS) (right) polymer pairs as a function of shear rate (RPM) at pH 7 / 5 (the lines are a guide to the eye).

CHAPTER 8

MULTICOMPARTMENTAL MICROCAPSULES FROM STAR COPOLYMER MICELLES

8.1. Introduction

Amphiphilic star block copolymers can be of great interest for use as a nano-scale container, catalyst, and template.[47, 327, 328, 329, 330] In particular, star polymers bearing polyelectrolyte arms might act as colloidal nanoparticles and offer a rich phase behavior under various environments.[48,49] The charged arms on the polyelectrolyte stars show stretched or retracted configuration depending upon an interplay of long-range electrostatic repulsion between arms and osmotic pressure induced by confined counterions. Such an effective interaction of soft-sphere colloids leads to dynamic response (e.g. arm collective relaxation and self-diffusion) by deformation and interdigitation.[50,53,331,332] At the surfaces and interfaces, highly branched star polymers adapt different conformations (e.g. spreading and extending) due to the steric repulsion between crowded chains.[333,334,335]

Typically, star polymers are comprised of multiple polymeric arms chemically grafted onto one core.[16] Star architecture including spherical topology, multiple valence of charge, and a terminal functional end group can be easily tailored by advanced synthetic methods.[156,127,160,162,163,164,185,188,191,192, 336 , 337 , 338] The molecular organization of star polymers is similar to a spherical micelle of block copolymers with a thermodynamically frozen core, a polymer brush grafted onto spherical colloids, and hierarchical dendrimers.

Star polymers are known to have a small aggregation number and a high critical micelle concentration (CMC) compared to corresponding linear analogues. The thermodynamically enhanced stability stemming from steric repulsion between crowding arms enables colloidal star polymers to exist in the form of a single molecule, so called, "unimolecular micelle". Star block amphiphiles with pH-tunable multi-polyelectrolyte arms have been shown to be a promising building component for responsive ultrathin films.[149,151,152,153,154,193] The sequential surface assembly of star polymers can offer a versatile strategy to fabricate nanofilms with well-defined composition and stratified compartments.[22,339]

LbL assembly using a planar or colloidal template substrate has been a useful means for preparing tunable functional multilayer nanofilms, coatings, and membranes.[101] In particular, LbL hollow microcapsules assembled via electrostatic and/or hydrogen interactions create an alternately assembled multilayered shell wall and a hollow interior as a cargo carrier.[107,108] The permeability and pore structure of the microcapsules can be effectively tuned with a nanometer level accuracy by controlling the number of deposited layers and by an external field (e.g. pH, salinity, and temperature) due to the dynamically responsive and adaptive molecular transformations.

The dendrimers and linear block copolymers have been recently considered attractive building blocks for fabrication of functional LbL multilayer film and hollow microcapsules.[340] The ultrathin multilayer constructed from dendrimers have drawn a great deal of attention in drug delivery and sensor applications due to the polyvalency and

controllable physicochemical properties of dendritic units.[36,341,342] The incorporation of dendrimers into multilayer shell wall can affect the capsule stability, permeability, and elasticity as compared to linear architecture polyelectrolytes. Khodade et al. reported high yield hollow capsules based on poly(amidoamine) dendrimers.[343,344] Kim et al. probed the mechanical property of phosphorous dendrimer/polyelectrolyte microcapsules and demonstrated softening and the enhanced permeability.[345,346]

On the other hand, the use of polymeric micelles based on amphiphilic linear block copolymers for the construction of hollow microcapsules has been reported.[110,201,347,348,349,350,351,352] For instance, Ma et al. prepared LbL microcapsules from polymer micelles and demonstrated the ability of loading-unloading behavior.[353,354] Biggs et al. presented a novel strategy to assemble micelle-micelle films and microcapsules using zwitterionic diblocks.[355,356] Hong et al. found that star polymers can be used to fabricate microcapsules.[357] The multiarm star polymers with their well-defined periphery arms can thus be considered as a promising candidate for the fabrication of functional microcapsules owing to their well-defined hierarchical characteristics.[155,166]

In this chapter, we report on LbL microcapsules containing both pores and hydrophobic compartments in polyelectrolyte shells constructed from star-shaped heteroarm amphiphilic polystyrene/poly(2-pyridine) (PS_nP2VP_n) block copolymers (the subscript n denotes the number of arms (9 and 22 arms)). Specifically, the amphiphilic star coplymers with a high level of ionizable pyridine groups (Φ_{P2VP} = 80 wt %) were dispersed in an acidic aqueous environment, allowing for the formation of core/corona

micelles. The core/corona star copolymers with protonated pyridine units, which are positively charged at pH 3, can be successfully assembled with negatively charged linear poly(styrene sulfonate) (PSS) to form stable microcapsules. The surface morphology of collapsed microcapsules clearly reveals that the star copolymers remain as a unimolecular micelle within the shell. Moreover, the combination of confocal laser scanning microscopy and small angle neutron scattering (SANS) confirmed high porosity and fractal nature of these shells. Their enhanced colloidal stability and complex morphology of shells with nanopores and hydrophilic domains distributed in polyelectrolyte matrix facilitate the unique compartmental nature of these microcapsules that may enable controlled multicargo loading.

8.2. Experimental Details

Materials. Linear PSS (M_W = 70 kDa), and PEI (M_n = 10 kDa) from Aldrich were used as-received. 1.0M TRIS HCl was purchased from Rockland and was diluted to 0.01M in ultrapure pure water (Nanopure water with a resistivity of 18.2 MΩ cm) for use. 0.1M HCl (99.5% purity) and 0.1M NaOH (99.5%) solutions were utilized to adjust the pH of polyelectrolyte solutions. Fluorescence isothiocyanate (FITC) and FITC-dextrans with different molecular weights were purchased from Sigma-Aldrich.

Synthesis of star block copolymers. The amphiphilic heteroarm PS_nP2VP_n star block copolymers were synthesized by the "in-out method" via a multi-step, one pot, and sequential anionic living polymerization route.[126,128] All samples were characterized by a combination of gel permeation chromatography, ^{1}H NMR, and light scattering in

accordance with the approach published elsewhere and the results are summarized in Table 8.1.[126]

Table 8.1: Molecular Characteristics of Heteroarm PS_nP2VP_n Star Block Copolymers.

Chemical structures	Number of arms		PS_{arm}		$P2VP_{arm}$		Φ_{P2VP} [a]	$M_{w, tot}$
	n	Total	M_w	N_{PS}	M_w	N_{P2VP}		
PS_nP2VP_n	9	18	3,400	33	13,200	126	0.80	149,000
	22	44	3,500	34	14,300	136	0.80	386,000

a. Weight fraction of P2VP.

Preparation of LbL planar film and hollow microcapsules. As summarized in Table 8.1, amphiphilic heteroarm PS_nP2VP_n star block copolymers with different number of arms (9 versus 22 arms) and molecular weights (149,000 versus 386,000 Dalton) were employed to fabricate LbL films. All monolayer and multilayer films and microcapsules were obtained by a dip-assisted LbL method. PS_nP2VP_n heteroarm star block copolymers were dispersed in 0.2 mg/ml concentration mixed solution (4.0 vol % of dimethyformamide (DMF) and 94 vol % of 0.01 MTrisHCl buffer solution) at pH 3 under sonication. The monolayer of PS_nP2VP_n star copolymer monolayer was deposited on a silicon substrate without a prelayer by a 15 min dipping followed by a 2 min washing in the same buffer solution. The PEI adhesive pre-layer was used for all multilayer films. A polyanionic PSS layer was deposited first followed by polycationic PS_nP2VP_n star copolymer. The deposition cycle was repeated until the desired number of layers was obtained. The silicon substrate was placed in each polymer solution for 15 min followed by washing for

2 min in the same pH buffer solution. The monolayer and multilayer films were dried under mild nitrogen flow for ellipsometry and AFM measurement.

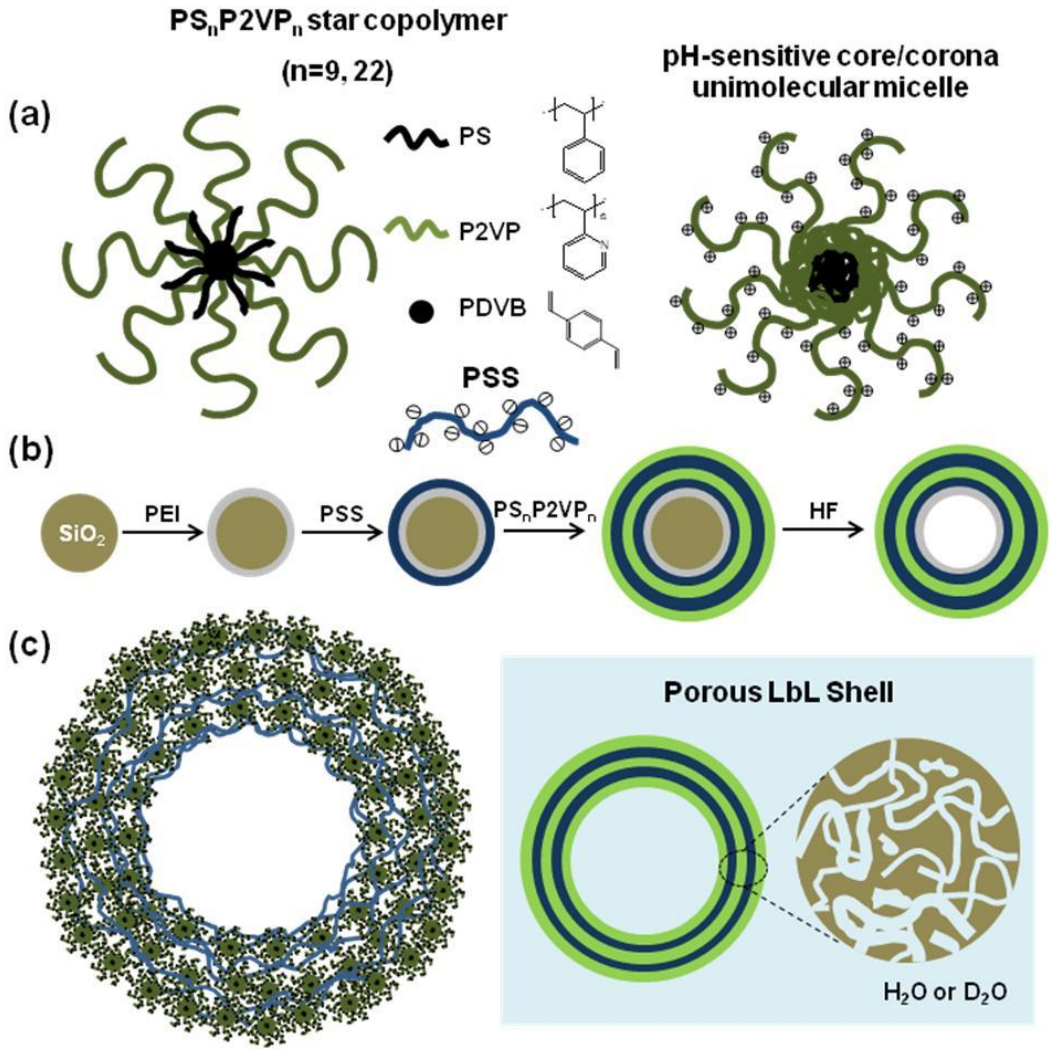

Figure 8.1: (a) Molecular structure and composition of amphiphilic heteroarm PS_nP2VP_n star block copolymers (left) and their core/corona unimolecular micelles (right); (b) fabrication procedure and (c) multilayer structure of an assembled star polymer hollow microcapsule (left) and its porous shell morphology (right).

The PS_nP2VP_n/PSS LbL hollow microcapsules were prepared using silica microsphere core (4.0 ± 0.2 μm in diameter, 10% dispersions in water, Polyscience, Inc.) as a

sacrificial template as illustrated in Figure 8.1b.[39,358] The silica cores were alternately immersed in 0.2 mg/ml polymer solution at pH 3 via repeated deposition cycles.

Characterization of LbL planar film and hollow microcapsules. Measurement of film thicknesses and refractive indices were made with a Woollam M2000U (J.A. Woollam Co, Inc., Lincoln, NE) multiangle spectroscopic ellipsometer at three incident angles 65, 70, and 75°. The Ψ (polarized angle) and Δ (phase) values were measured and used in conjunction with a Cauchy model (WVASE32 analysis software) to determine the thickness of the LbL films and their optical constants *n* and *k* over the wavelength range 245 to 1000 nm.

The morphological properties of the LbL film and capsule surface were probed under ambient conditions in the tapping and phase modes in air and fluid with nanometer resolution using a Dimension 3000 (Veeco Inc., Santa Barbara). For quantitative analysis of surface topography and roughness, AFM images were obtained with a Dimension-3000 in the "light" tapping mode with an amplitude ratio within 0.90-1.00 to avoid surface damage and film deformation.[135,136] The AFM cantilevers had spring constants in the range of 40-60 N/m. Scanning rates were between 1.0-2.0 Hz, depending on the scan area which ranged from 10 μm x 10 μm to 1 μm x 1 μm.[137]

To investigate capsule permeability to FITC-dextrans, hollow capsules were added to several Lab-Tek chambers, which were then half-filled and mixed with FITC-dextran solutions by a LSM 510 VLS META inverted confocal laser scanning microscope. To

confirm the alternating assembly of polymer pairs on the silica core, the surface potentials were monitored on Zetasizer Nano-ZS equipment (Malvern). Each value of the zeta-potential was obtained at ambient conditions by averaging three independent measurements of 35 sub-runs each.

SANS measurements. All samples were measured in D_2O to minimize the incoherent backscattering and increase contrast for hydrogenated shells.[146] For the 22 arm star polymer, the microcapsules with different shell thickness (5, 8, and 11 bilayers) in hydrogenated water were treated with deuterated water (D_2O) that was adjusted to pH3 using 0.1 M HCl. All SANS measurements were made at room temperature (22°) on the Extended-Q Small Angle Neutron Scattering (EQ-SANS) instrument of the Spallation Source at Oak Ridge National Lab (ORNL).[147]

8.3. Results and Discussion

8.3.1. Chemical composition and unimolecular micelles.

The heteroarm star block amphiphiles employed in this study are comprised of hydrophobic PS blocks and pH sensitive ionizable P2VP blocks that both emanate from a common single junction (Figure 8.1). Due to the pH induced ionization of pyridine moieties on the P2VP block arms (80 wt %), star copolymers can exist in the form of a core/corona state in acidic aqueous solution, analogous to the amphiphilic linear block copolymers with a thermodynamically frozen core. The dispersion of amphiphilic star copolymers in the aqueous environment was achieved by employing a DMF/water solvent mixture where the pH value was adjusted to be acidic (pH 3). The use of polar

DMF, which is a good solvent for both PS and P2VP segments, allows star amphiphiles to be solubilized with a corona/corona chain conformation.

The transparency of the solution was maintained indicating that there is no distinct large scale aggregation due to the increased solubility of the protonated pyridine groups of P2VP segments at sufficiently lower pH ($pK_{a,\ P2VP}$ ~4.3).[205] Since the value of pK_a is defined as the pH when 50% neutralization of total ionic monomer units occurs in a titration curve, the extent of ionization can be estimated to be around 25 % at pH 3 according to the literature.[155,347] Above pH 4.5 the solution becomes dramatically clouded because of the loss of hydrophilicity of pyridine units induced by their deprotonation. The solubility parameter (9.9 $(cal/cm^3)^{1/2}$) of P2VP at a unionized state is close to organic solvents such as chloroform (9.33) and tetrahydrofuran (9.51).[359]

Zeta-potential measurements show the apparent reduction in the electric potential of the polymer solution to be near pH 4.5, which is in good agreement with the observed change in the transparency at the same pH condition (Figure S8.1). However, the zeta-potential of star copolymer micelles shows the maximum positive value at pH2, which could be presumably due to different surface charge contribution from the outer-and inner ionic groups along the star polymer branch arms in contrast to solid nanoparticles. Since the z-potential is measured from the electrophoretic mobility and depends on the charges on the particle surface as well as the particle radius through, it is not easy to correlate the z-potential with the degree of ionization (pK_a). The colloidal stability of star polymer dispersant remains without pronounced precipitation over the long term. The multiarm

molecular conformation of star polymers provides a favorable colloidal stability owing to the steric repulsion of a dense chain structure. Therefore, the dispersed star copolymers take the form of a collapsed hydrophobic PS core which is screened by a positively charged stretched P2VP corona (Figure 8.1a).[166,359]

The association of amphiphilic heteroarm star copolymers with long chain polyelectrolyte depends on the preparation method, the number of arms, the hydrophobic content and the concentration (cmc). A $PS(3k)_{20}P2VP(23k)_{20}$ star prepared from a common good solvent forms unimolecular micelles in acidic aqueous solution due to the stabilization efficiency of the 20 polyelectrolyte arms.[155] Similarly, a $PS(20k)_7P2VP(56.5k)_7$ star with higher hydrophobic content was shown to exist as a unimer in very dilute solutions while it forms multimolecular micelles of low aggregation number (3 – 4) at higher concentration.[166] For the PS_9P2VP_9, which is similar to $PS(3k)_{20}P2VP(23k)_{20}$ some association that could lead to micelles comprising few stars (ca 2 or 3) cannot be excluded. However, because the PS_9P2VP_9 poses much less hydrophobic content with respect to $PS(20k)_7P2VP(56.5k)_7$, we assume that this star mainly stays as unimer micelles. These assumptions are corroborated from the fact that no turbidity or bluish tint (evidence of association) was observed after the slow addition of acidic water.

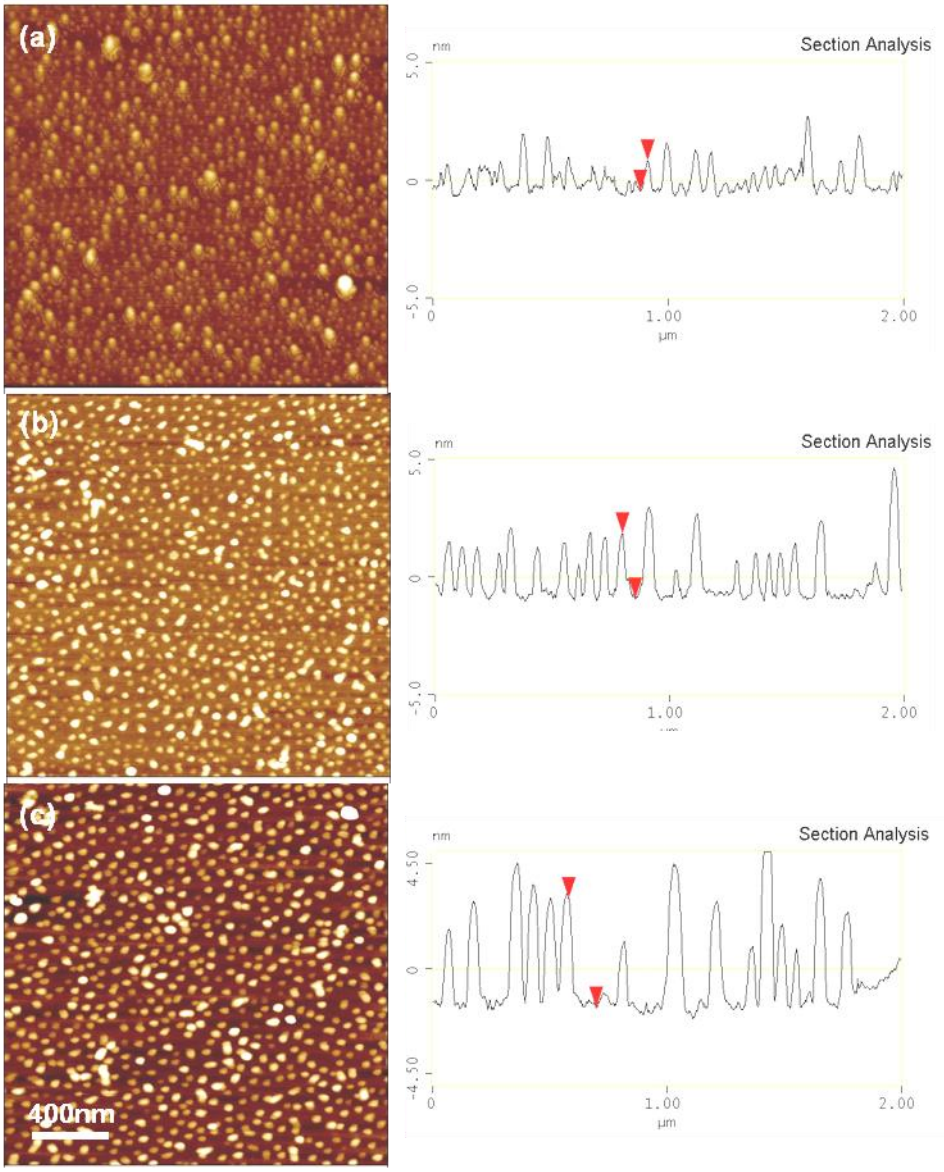

Figure 8.2. AFM topography image (left) and cross sectional analysis (right) of PS_nP2VP_n star block copolymer monolayer on planar silicon wafers in dry state obtained by dip-assisted deposition method at pH 3. (a) PS_9P2VP_9 in 4% DMF mixed aqueous solution. (b) $PS_{22}P2VP_{22}$ in 4% DMF mixed aqueous solution. (c) $PS_{22}P2VP_{22}$ in 4% acetone mixed aqueous solution. The z-scale of all AFM images is 10 nm.

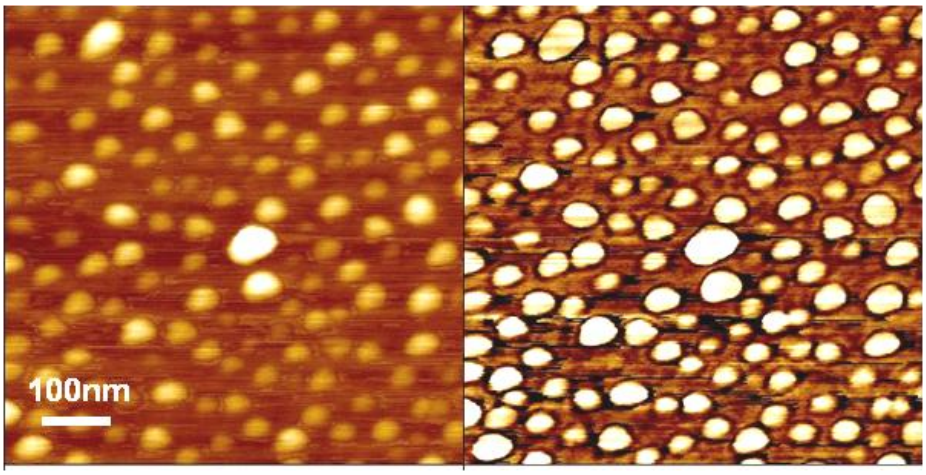

Figure 8.3: High resolution AFM topography (left) and phase (right) image of $PS_{22}P2VP_{22}$ star block copolymer unimolecular micelles on planar silicon substrate in dry state deposited by dip-assisted LbL method at pH 3. The z-scale is 10 nm and 60º.

8.3.2. Planar film morphology.

The planar LbL films possess a discrete spherical domain structure displaying collapsed circular molecular conformation in the dried state (Figure 8.2). A densely packed monolayer with a uniform size distribution is revealed from the high resolution AFM image in Figure 8.3. It is apparent that the size of aggregates depends on the number arms and the solvent, as illustrated by domain dimension results by AFM sectional analysis (Table 8.2). The 22 arm star polymers show larger domain height (2.4 ± 0.6 nm) than the 9 arm star polymer (1.5 ± 0.5 nm). A similar trend is observed with the domain width results (9 arms: 49.5 ± 6.0; 22 arms: 54.0 ± 5.7 nm). Moreover, such aggregation appears to depend on the solvent as seen from the different domain height for acetone and DMF, where the acetone mixture leads to slightly more swollen aggregation. This result is presumably due to the lower solubility of PS segments in acetone, leading to a larger aggregation number. In addition, the aggregation dimensional analysis and the uniform

surface morphology of the monolayer suggest that star polymers remain as a unimicellar state. This is particularly true for the star polymer with 22 arms owing to the enhanced steric stabilization effect, even at relatively high concentration (0.3 mg/ml).[359]

Table 8.2: Domain Height and Width of Star Copolymer Monolayer Films.

System	Domain height (nm)	Domain width (nm)
9 arms, DMF	1.5 ± 0.5	49.5 ± 6.0
22 arms, DMF	2.4 ± 0.6	54.0 ± 5.7
22 arms, acetone	3.3 ± 0.6	67.7 ± 5.6

All data were determined from cross-section analysis of AFM topography images (2 μm ×2 μm) for dried samples. Tip dilation effect is responsible for excessive domain width with actual values to be by 50% lower.

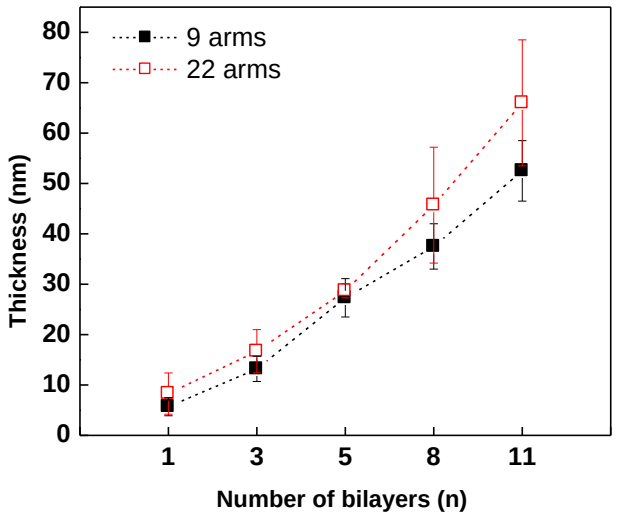

Figure 8.4: Build-up of PS_nP2VP_n/PSS LbL film on planar silicon wafer (9 arms (■) and 22 arms (□)).

The LbL multilayers on a planar substrate were investigated to examine the first (Figure 8.4). Both 9-arm and 22-arm star copolymers were found to build up uniform films with the increase in the number of bilayers (1, 3, 5, 8 and 11 bilayers) when sequentially assembled with PSS at pH 3. This linear growth behavior is an indication of strong electrostatic attraction of positively charged pyridium groups on P2VP with oppositely charged sulfonate groups on PSS.[360] Table S8.1 shows the average bilayer thickness for LbL films, in particular that the bilayer thickness is 5.0 ± 0.4 nm in the case of 9 arms while 5.8 ± 0.2 nm for 22 arms. The 22 arm star polymer appears to enable faster growth of multilayer LbL films than the 9 arm star polymer. This result is likely due to the difference in domain size for different arm numbers, as demonstrated by the arm dependency on their monolayer structure (Figure 8.2). The greater number of arms appears to have an advantage to form ionic bonds, which can be attributed to more stretched chain conformation of the arms due to the steric constrains. Further, the polyvalent binding of the multiarm star architecture with higher number of arms is likely due to the large molecular weight, which is similarly to the case of larger molecular weight linear polyelectroytes.[214]

To probe the fine morphology of LbL films, high resolution AFM topography images were collected for a varying number of bilayers (5, 8, and 11 bilayers), as displayed in Figure 8.5. The spherical aggregate structure is clearly observed for films with different numbers of layers, where an increase in the number of bilayers appears to lead to larger size aggregates. In the case of the 9 arm star copolymer, the domain size is observed to be similar to that of the 22 arm star copolymer. The multiarm star copolymers seem

likely to maintain stable micellar structures inside LbL multilayers after multiple deposition cycles. This observation implies the possibility to create a robust homogeneous multilayer assembly with discrete domain compartments based on star block copolymers.

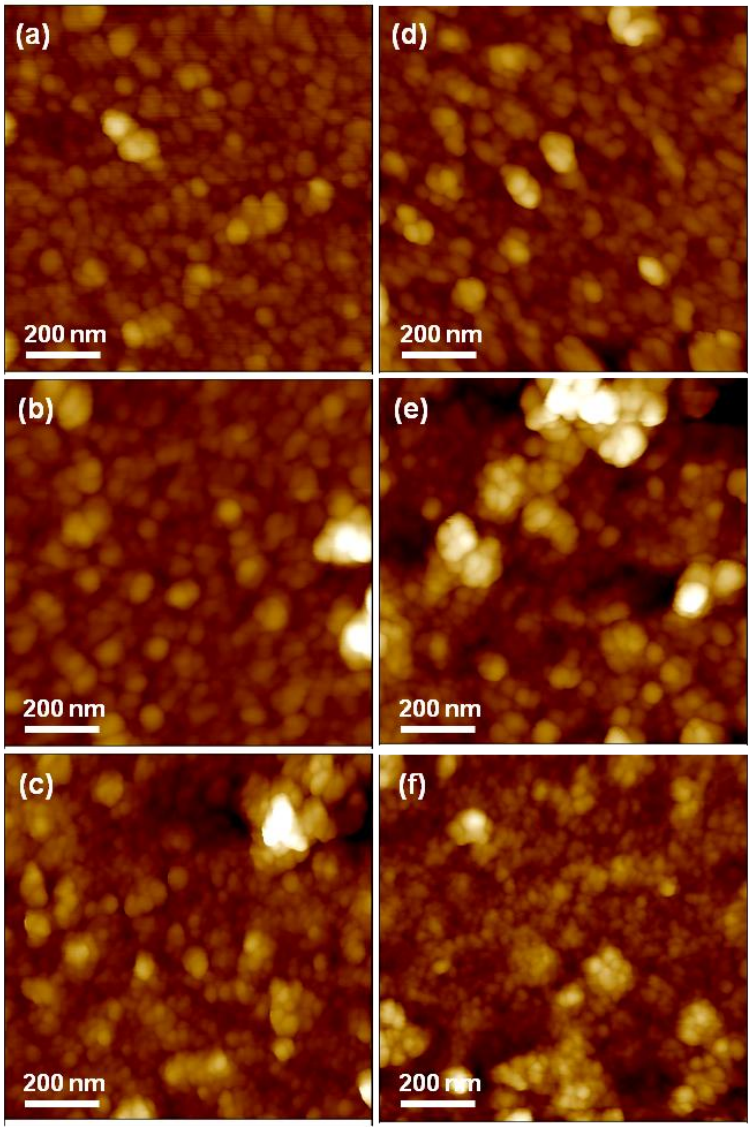

Figure 8.5: (a) AFM topography images of PS_nP2VP_n/PSS LbL multilayer film as a function of number of bilayers (5 (a,d), 8 (b,e), and 11 (c,f) bilayers) on planar silicon substrate in dry state (n = 9 arms (a,b,c) and 22 arms (d,e,f)). The z-scale is 120 nm.

8.3.3. Hollow microcapsule assembly and shell characteristics.

The zeta-potential measurement displayed in Figure 8.6 proves that the polyelectrolyte pair undergoes a successive charge reversal and overcompensation during sequential multilayer buildup thus indicating regular assembly on silica microparticles.

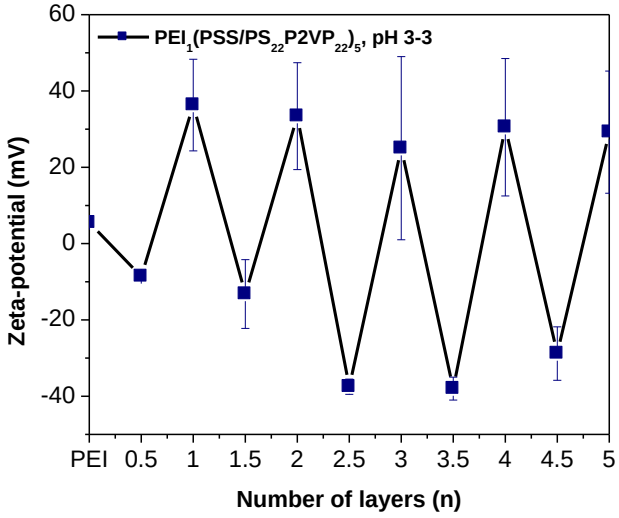

Figure 8.6: Zeta-potential measurements of $PS_{22}P2VP_{22}$/PSS LbL assemblies deposited on SiO_2 template core at pH 3.

Upon core dissolution intact hollow microcapsule can be successfully obtained as demonstrated by the CLSM microscopy images (Figures S8.2, 8.7). Distinct size reduction of whole microcapsules after dissolution of cores was observed regardless number of arms. For 5 bilayer shells, the capsule shrinkage appears prominent (50% reduction in diameter) with several wrinkles becoming visible (Figure S8.3). However, with increase in the number of bilayers (up to 50 nm in shell thickness), the microcapsule diameter is stabilized (less than 15 % reduction) because of uniform shells are formed.

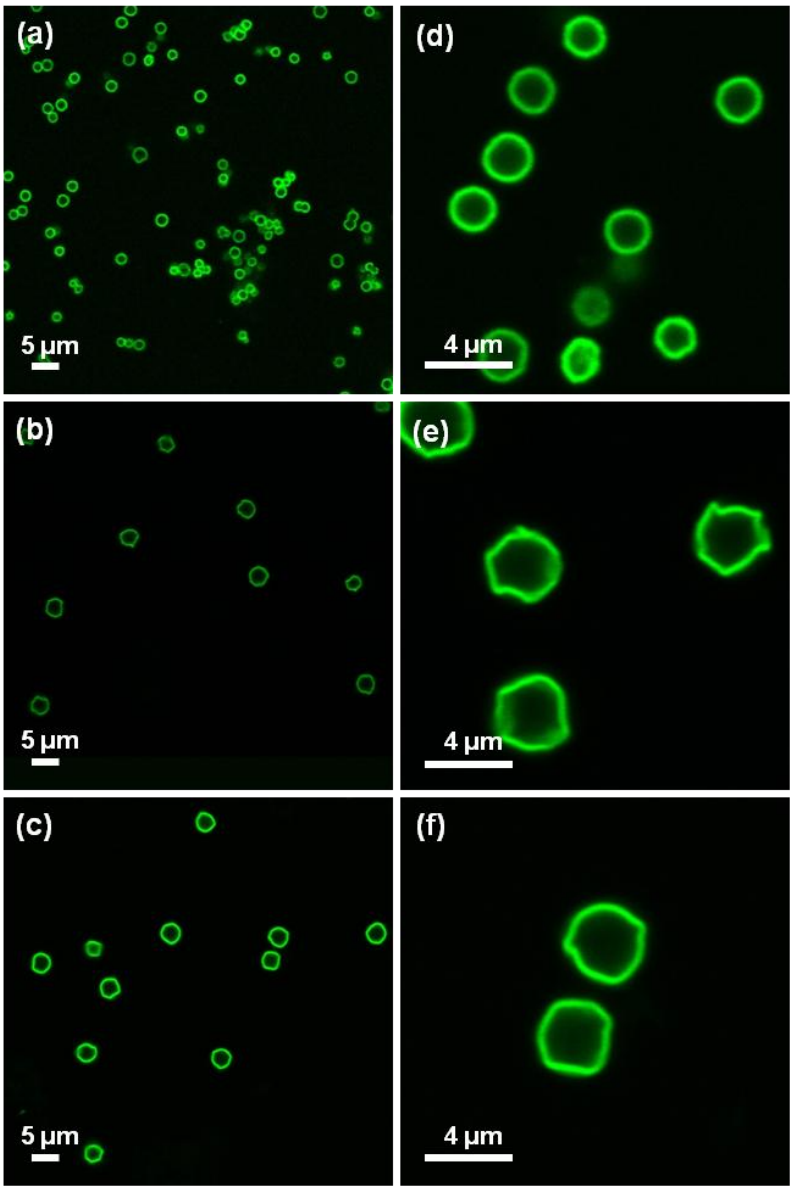

Figure 8.7: CLSM images (lower resolution (a,b,c) and higher resolution (d,e,f)) of $PS_{22}P2VP_{22}$/PSS microcapsules as a function of number of bilayers (5 (a,d), 8 (b,e), and 11 (c,f)).

Indeed, for 5 and 8 bilayers, the microcapsules were found to have a prominent buckled wall structure, which appears to be similar with the deformation of PSS/PDADMAC shells.[361] The degree of buckling appears to be decreased for thicker shells (Figures S8.2 and 8.7). This tendency of buckling is analogous to thin film on the patterned substrates

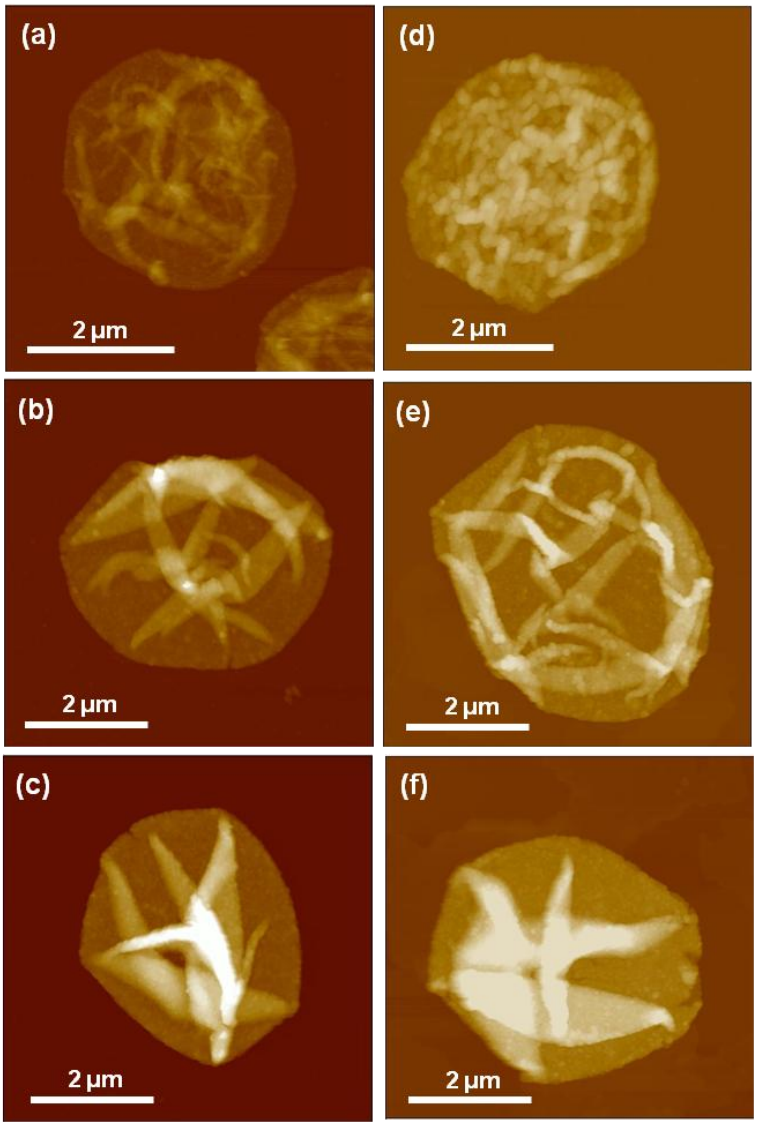

Figure 8.8: AFM topography images of PS_nP2VP_n/PSS microcapsules (9 arms (a,b,c) and 22 arms (d,e,f)) as a function of number of bilayers (5 (a,d), 8 (b,e), and 11 (c,f) bilayers) on silicon substrate in dry state. The z-scale of all images is 600 nm.

and on cores.[109,362,363] The possible driving force of the shrinkage of hollow capsules is the increased hydrophobic interaction in predominantly hydrophilic shells.[364,365] Upon compensation of cationically charged ionized pyridium on P2VP with anionic PSS counterpart, uncharged P2VP seems to no longer contribute for the solubilization of star

polymers. Such additional hydrophobic interactions can lead to the reduced surface tension at water/polyelectrolyte interface.

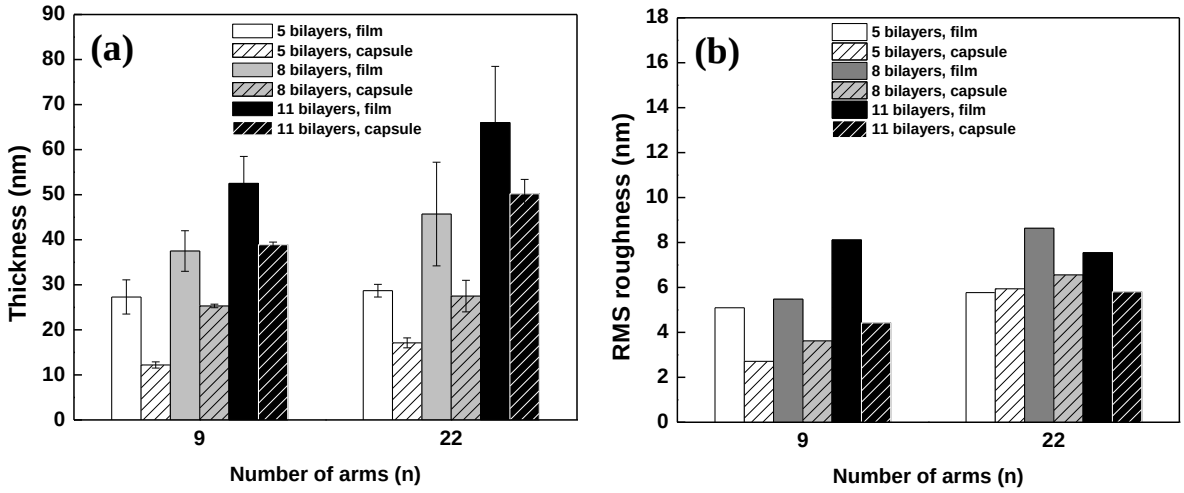

Figure 8.9: (a) Thickness and (b) RMS roughness of dried shell wall of PS_nP2VP_n/PSS microcapsules for different bilayers (5, 8, and 11 bilayers) compared to those of corresponding films on planar silicon wafer.

In order to further elucidate the shell morphology, the AFM images were collected for collapsed microcapsule walls (Figure 8.8). For both 9 arm and 22 arms star polymers, the number of wrinkles appears to be reduced whereas more pronounced folded structures were observed as the film thickness increases. These results suggest that the increased shell thickness leads to the formation of more rigid films and, thus, allow for being persistent against capillary deformation during the drying process. The stable microcapsule was obtained irrespective of number of arms but a similar trend in the folding phenomena was observed as illustrated in Figure S8.4. However, the microcapsules composed of 9 arms star copolymer showed thinner shells as expected due to the difference in molecular weights as discussed above for planar films (Figure 8.9a, Table S8.1).[214] The thickness of microcapsules was found to be lower than that of planar

film, which is attributable to fabrication process during the capsule assembling.[366] The overall morphology of microcapsules is relatively smooth and indicates modest aggregation (microroughness of 3-8 nm) (Figure 8.9b).

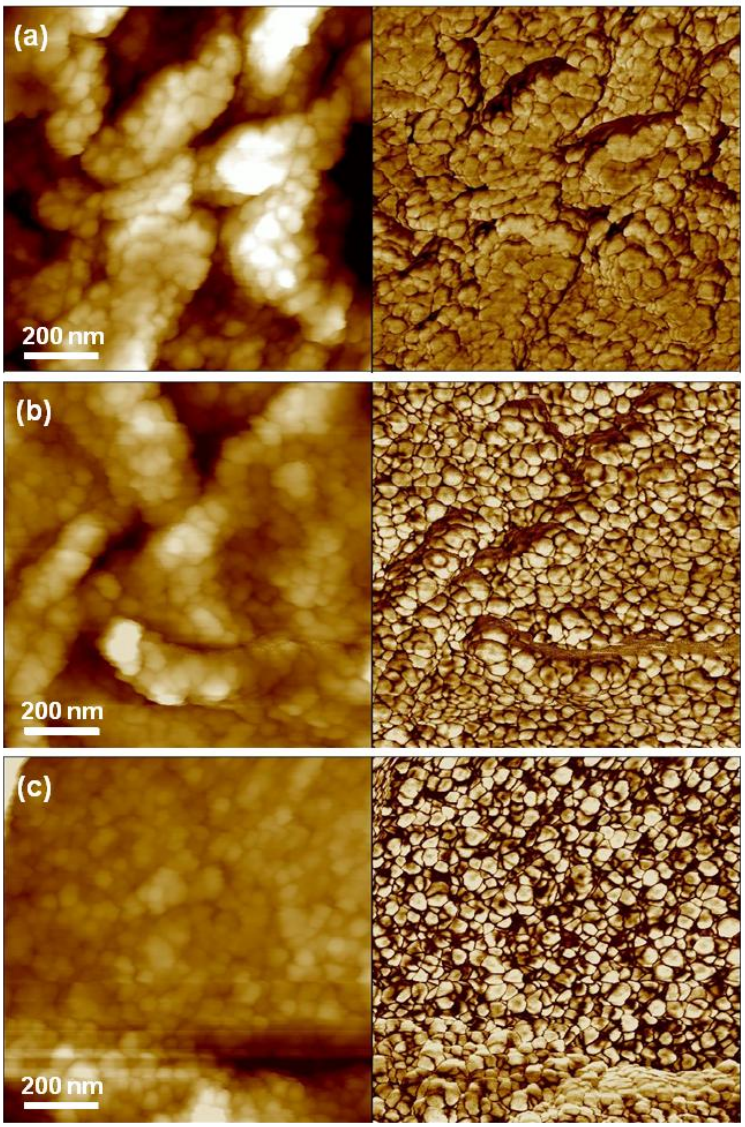

Figure 8.10: High resolution AFM images (topography (left) and phase (right)) of $PS_{22}P2VP_{22}$ /PSS microcapsules as a function of number of bilayers (5 (a), 8 (b), and 11 (c) bilayers) on silicon substrate in dry state. The Z scale of all images is 120 nm (topography) and 30° (phase).

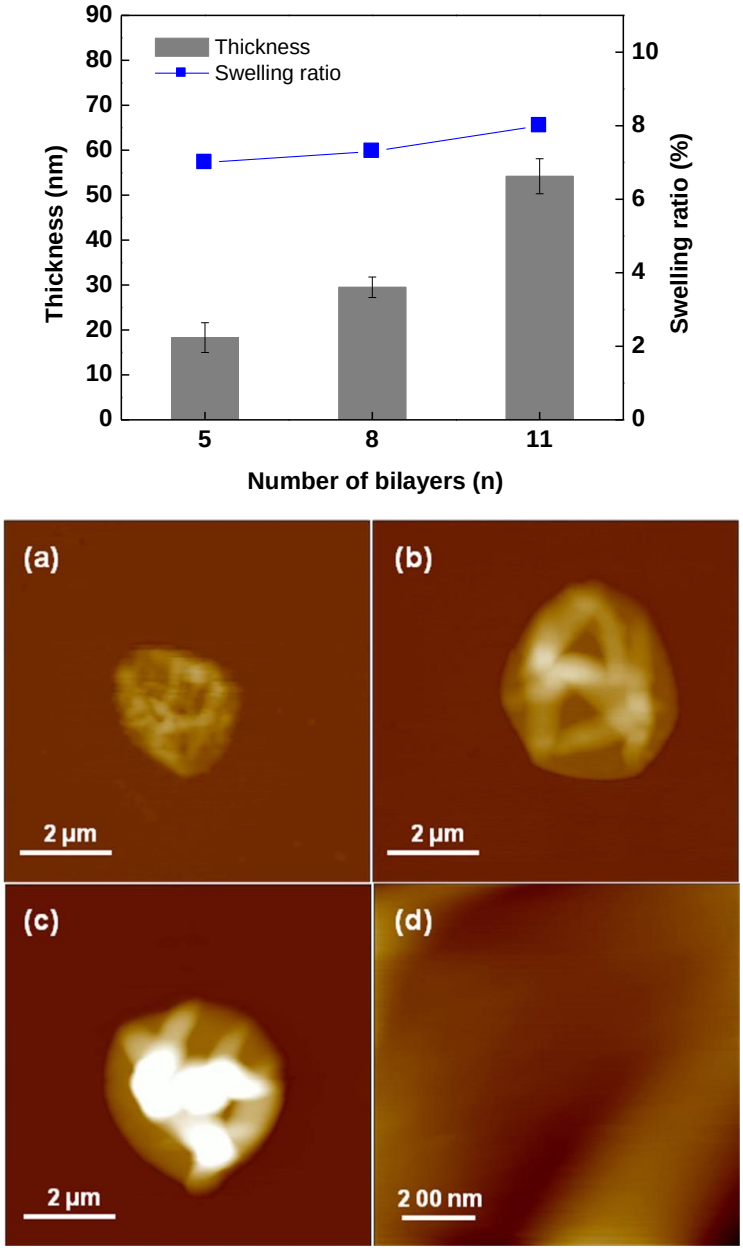

Figure 8.11: (Top) Shell thickness and swelling ratio and (bottom) AFM images of rehydrated $PS_{22}P2VP_{22}$ /PSS LbL hollow microcapsules as a function of number of bilayers (5 (a), 8 (b), and 11 (c) bilayers) and (d) high resolution image of the surface of capsule (c) using liquid cell scan under pH3 Tris-buffer of 0.01 M. The Z scale of images is 600 nm for (a-c) and 120 nm for (d).

The high resolution AFM topography images (1 × 1 µm) of the microcapsules composed of 22 arms star block copolymer show the uniform surface morphology of shells with

compact spherical domains (Figure 8.10). Regardless of change in the number of deposition layers, the similar grainy morphology as that typically seen in the dried collapsed LbL microcapsules with weak interaction of components.[214, 367 , 368] The aggregate dimensions remain to be close to the ones of the unimolecular star copolymer monolayers (Figure S8.5). These results confirm that star polymers can exist as a single molecular micelle without undergoing large-scale microphase separation. This enhanced colloidal stability of multiarm star polymers can be ascribed to the multivalent arms in contrast to the case of dendrimers or conventional micelles.[344,355,357,369]

Figure 8.11 shows the thickness change and surface morphology for rehydrated microcapsules composed of 22 arms star block copolymers. The liquid AFM scan was performed to probe shell swelling properties. The swelling ratio was determined from measuring the difference in thickness between dried and rehydrated capsule shells. The rehydrated microcapsules under liquid cell setup with filled with the pH3 Trisbuffer solutions of 0.01 M concentration are found to swell up to on average 8 % and reveal that the smooth surface morphology due to the highly hydrated surface in contrast to the granular texture of the dry shell. Notably, the low increment in the shell thickness in the wet state suggests that the capsules assembled from strong electrolyte at low ionic strength (0.01 M) stay neutral due to the high charge compensation and strong ionic bonding, leading to hydrophobic shell with the low level of free ionic groups.[370,371,372]

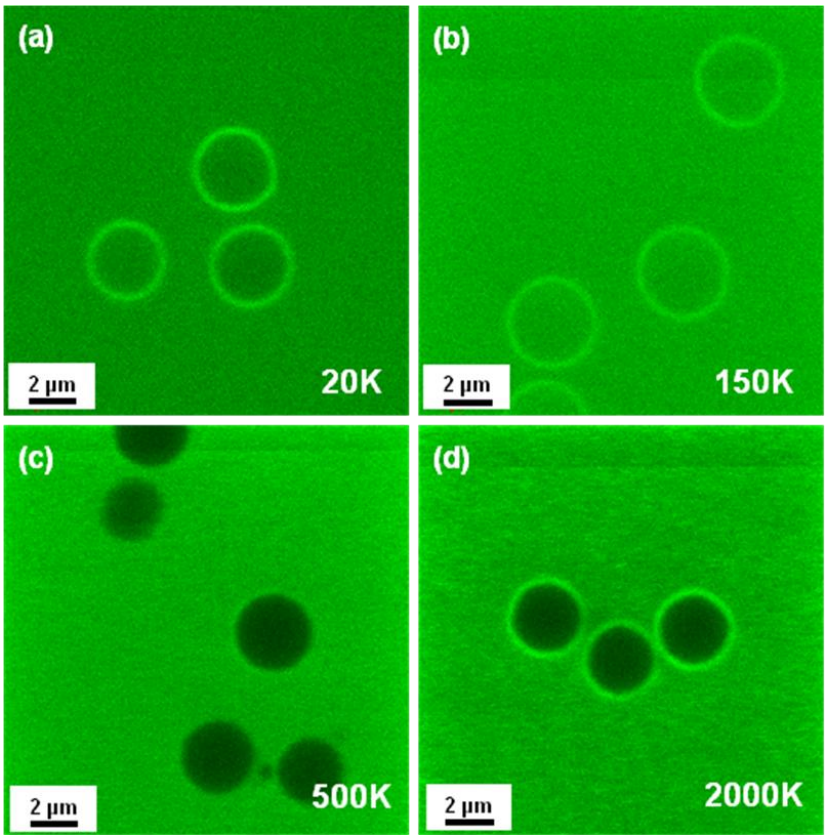

Figure 8.12: CLSM images of $PS_{22}P2VP_{22}$/PSS microcapsules (11 bilayers) using FITC-labeled dextran with varying molecular weights: (a) 20,000, (b) 150,000, (c) 500,000, and (d) 2000,000.

8.3.4. Porosity of LbL shells.

In order to probe the porous structure of the microcapsules as a function of deposited number of bilayers, measurements of the permeability were conducted using fluorescence dye labeled dextran with varying molecular weights, which correspond to the pore size of the shell.[373] Figure 8.12 depicts the CLSM images of microcapsules placed in solutions with different dextrans labeled with FITC dye. High contrast (no interior fluorescence) indicates non-permeable shell state and permeation results in uniform fluorescence. Table 8.3 summarizes the permeability behavior found for the 22 arms star copolymer

microcapsules and demonstrates the ability to tailor its permeability by varying the number of deposition layers. Either permeable or non-permeable state for dextrans with different molecular weights can be achieved by changing the shell thickness. The 5 bilayer microcapsules appear to be a complete permeable while the microcapsule show reduced permeability against the larger molecular weight dextran (Table 8.3). In striking contrast, the 9 arm star copolymer microcapsules are highly permeable regardless of the number of deposition layers which indicates less dense, open porous structure with larger pore dimensions even for thicker shells.

Table 8.3: Permeability of $PS_{22}P2VP_{22}$/PSS Microcapsules.

System	Dextran-20 kDa	Dextran-150 kDa	Dextran-250 kDa	Dextran-500 kDa	Dextran-2000 kDa
$PEI(PSS/PS_{22}P2VP_{22})_5$	+	+	+	+	+
$PEI(PSS/PS_{22}P2VP_{22})_8$	+	+	+/-	-	-
$PEI(PSS/PS_{22}P2VP_{22})_{11}$	+	+	+/-	-	-

Fluorescein isothiocyanate (FITC) -labeled dextrans with different molecular weights (kDa). "+" permeable, "+/-" partially permeable, and "-" non-permeable.

The pore dimensions estimated from hydrodynamic diameter of permeating dextran macromolecules correspond to the value of around 23 nm for thicker shells.[374] The pores stay larger than 35 nm for the thinnest shells and for all microcapsules fabricated from 9 arm star copolymer. However, even if the estimation of the pore dimensions from permeability experiments is popular, in fact, it is too coarse and does not provide

comprehensive information on true pore shapes, their distribution, and intrinsic morphology.

Therefore, in order to elucidate the porous morphology of the shells, SANS measurements were conducted for the deuterated water (D_2O) solutions. Here, we report SANS results on microcapsules made from the 22 arm star copolymer since the microcapsules from the 9 arm star copolymer do not show a high enough contrast for these experiments.

A significant increase in neutron scattering was observed for all microcapsules in a q-range of 0.04 to 0.5 nm^{-1} (Figure 8.13a). The scattering intensity increases with an increase in the number of bilayers, indicating that the scattering is directly related to the volume fraction of shells in the deuterated solution. The cross-over between the 8 and 11 bilayer scattering curves at 0.07 nm^{-1} could be due to a general decrease in the 11 bilayer scattering intensity due to the solution having a lower concentration than the 5 and 8 bilayer microcapsule solutions. This reduction in intensity does not affect the data fitting since it affects the entire scattering curve and is simply a scale factor for the intensity.

It is important to note that the q-range for the scattering effects in this experiment corresponds to distances of 1-100 nm which includes all the characteristic dimensions of several important structural features of our microcapsules known from independent measurements: total thickness of shells within 30-50 nm, domains size within 20-30 nm, and pore dimensions around 20 nm. However, considering the differences in scattering

densities and the fact that deuterated water can readily diffuse into hydrogenated shells, we can conclude that the scattering contrast is highest between pores filled with deuterated water and the hydrogenated shell material while the contrast within hydrogenated material is much lower. Therefore, we suggest that the scattering in this region is likely dominated by the pores with the lower-q contribution coming also from the shell thickness.

Non-linear fitting analysis was applied to the scattering data to confirm the trends observed for capsule thickness and the pore size dimensions as measured independently. In order to analyze scattering data, first, we suggested that the pores could be represented by individual objects with the scattering contrast determined by the hydrogenated polymer media and the pure deuterated water in the pores (Figure 8.1). In this analysis we varied the pore shape, their dimensions, and their polydispersity in attempts to fit experimental data. However, no such model provided satisfactory data fits. Therefore, the model of shell morphologies with distributed, individual, and well defined closed pores can be excluded from further consideration.

Second, two shape-independent models which are based upon the representation of scattering media as highly randomized interconnected morphologies with diffuse contributions of weakly-contrasted inhomogeneities at multiple length scales were applied to determine general trends. Initially, the scattering data were fitted with a power law model to determine the fractal dimension of randomized, network-like morphologies (Figure 8.13a).[375,376] In contrast to the model of individual scattering elements, the power

law model yielded a good fit for the data sets over their entire q-range for all microcapsules studied here (Figure 8.13a). The fractal dimensions for each system determined from this analysis are shown in the Figure 8.14a inset.

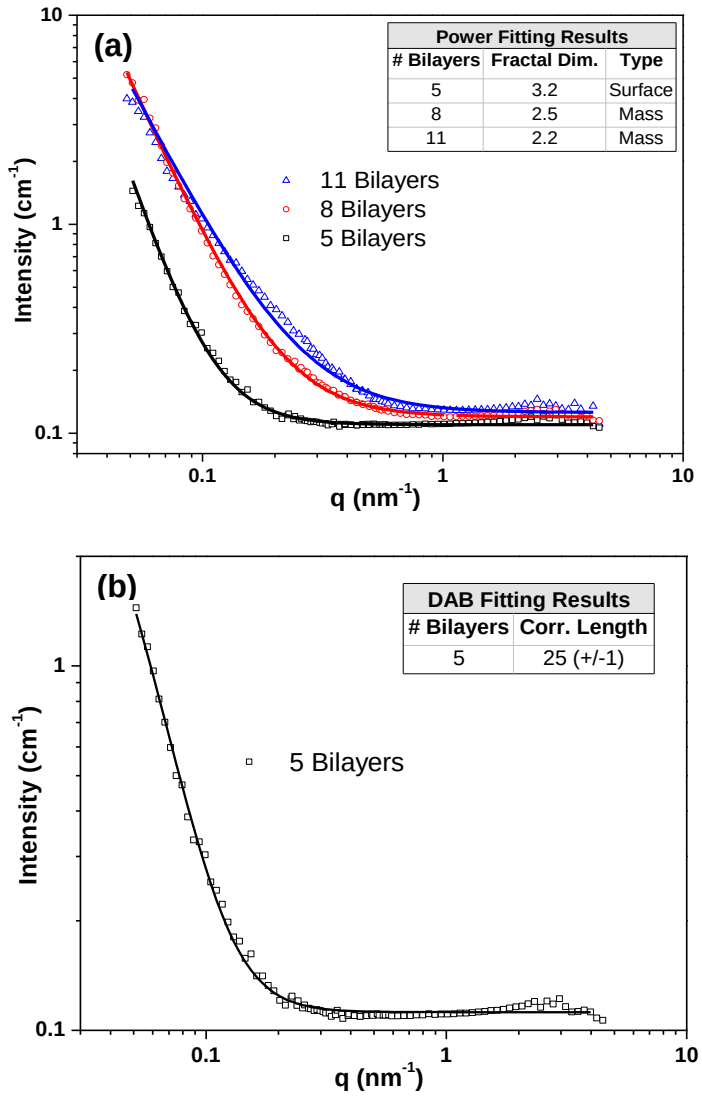

Figure 8.13: SANS data of fully hydrated $PS_{22}P2VP_{22}$/PSS microcapsules with (a) (square) 5 bilayers, (circle) 8 bilayers, and (triangle) 11 bilayers in D_2O solution that have been fitted with a power law model to determine the evolution of the fractal dimension, and (b) the 5 bilayer sample with a DAB fit.

Importantly, significant differences in power law fits were observed for microcapsules with different shell thickness. The 5 bilayer microcapsules show a fractal dimension of 3.2 which strongly suggests a surface fractal morphology, i.e, a rough and highly-folded uneven surface. This fractal distribution correlates well with the models of polymer distribution under modestly favorable adsorption conditions for LbL films with a limited number of layers as has been directly observed in AFM studies.[377] In contrast, the shells with an increased number of bilayers (8 and 11 bilayers) have a significantly reduced fractal dimension of 2.5 and 2.2, respectively, which suggests a mass fractal structure. Such a model corresponds to a network-like porous morphology with network elements randomly oriented within the shell. This combination is likely indicative of a denser system which can be approximated by a randomly clustered network with major elements of high contrast formed by the swollen hydrogenated polyelectrolyte matrix and the nanopores filled with deuterated water.

Such a transition from the surface fractal to the mass fractal for shell thickness increasing from 5 to 8 bilayers revealed here corresponds to general trends in morphological changes with the increasing number of layers as suggested based upon microscopic observations.[4,377, 378] The gradual filling of the initial two-dimensional network by subsequent polymer layers results in the formation of more uniform films with diminishing through-pores and decreasing pore dimensions. The occurrence of such reorganization is also supported by the results from fluorescence microscopy and AFM that are discussed above which demonstrate a densification of the surface morphology and a consistent decrease in the permeability. Moreover, significant shrinkage of

microcapsules with only a few bilayers can be naturally related to the initial open surface network formation followed by collapse during core removal.

Finally, another model for multilength scale random morphologies, the Debye-Anderson-Brumberger (DAB) model, was also exploited to determine a correlation length in spatial distribution of density inhomogeneities within the shells (Figure 8.13b).[379] The DAB model assumes that the scattering objects have random sizes and shapes and show an exponentially decaying correlation in their spatial distribution.[380] Initial results show that The DAB model fits the 5 bilayer data quite well over the entire q-range and provides a correlation length of about 25 nm which can be interpreted as the characteristic dimension of density inhomogeneities represented by pores. It is worth it to note that this value is very close to that estimated from dextran permeability measurements that additionally facilitate our interpretation of the SANS data. However, the DAB model does not describe properly the data from the thicker shell capsules, which presumably have smaller pore dimensions and denser shells contributing to the scattering in this q-range, likely because the assumptions regarding random pore sizes, shapes, and distributions are less accurate. Although these fitting results are preliminary and do not provide specific geometrical information on the capsule pores, they have provided an initial foundation for additional studies. Future investigation on pore geometries in these star polymer LBL microcapsules will be targeted toward capsules that have a large difference in size between microcapsule wall thickness and pore size. This design will make it possible to clearly isolate the scattering from each of these structures which will allow for more reliable fitting with the shape-dependent models.

To sum, we presented that the star copolymer unimolecular micelles can be successfully utilized to form unique multicompartamental LbL microcapsules with shells of coexisted network-like morphology of hydrophobic domains, hydrophilic polyelectrolyte matrix, and nanoscale water-filled pores. The polyvalent strong electrostatic interaction of core/corona multiarm architecture enables spherical star micelles to be incorporated into microcapsules with the ability to control shell morphology and the porous network structure.

Appendix. Supporting Information: Table S8.1 and Figure S8.1-S8.5.

Table S8.1: Average Bilayer Thickness of LbL Multilayer Films.

	Average bilayer thickness (nm)	
LbL multilayers	films[a]	Capsules[b]
PSS/PS_9P2VP_9	5.0 ± 0.4	3.0 ± 0.6
PSS/PS_{22}P2VP_{22}	5.8 ± 0.2	3.8 ± 0.7

All data were determined from dried samples. a. Measured with ellipsometry. b.

Measured with AFM topography analysis. In all systems, PEI was used as a pre-layer.

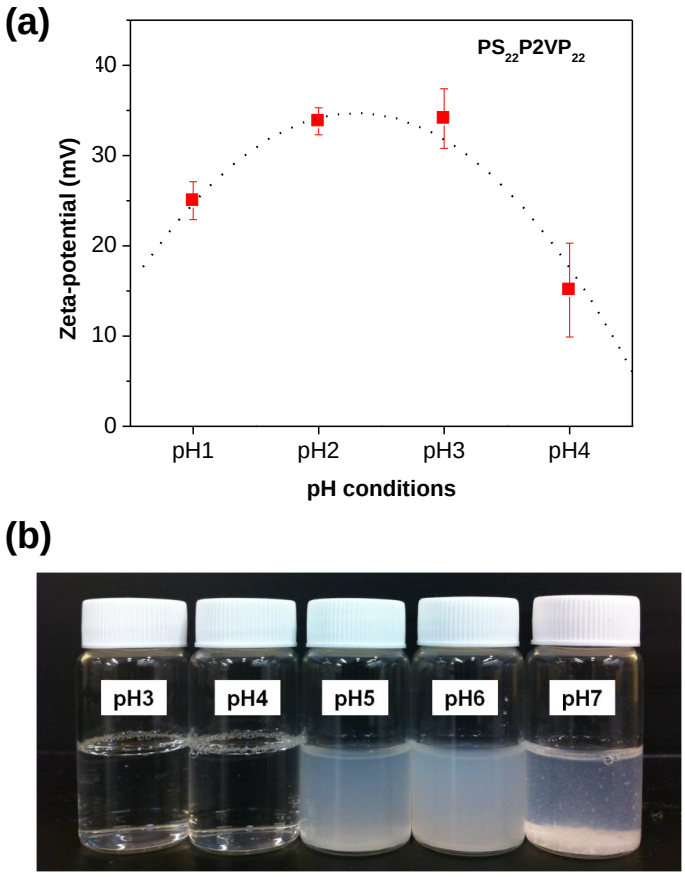

Figure S8.1: (a) Zeta-potential measurements of $PS_{22}P2VP_{22}$ star block copolymer solution with varying pH conditions. (b) Variation of transparency of $PS_{22}P2VP_{22}$ star block copolymer solution with pH.

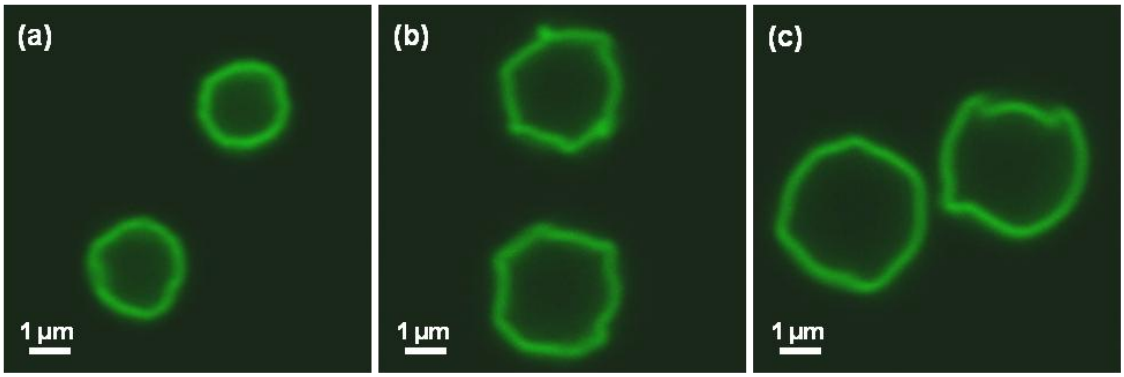

Figure S8.2: CLSM images of PS_9P2VP_9/PSS LbL microcapsules as a function of number of bilayers (5 (a), 8 (b), and 11 (c) bilayers).

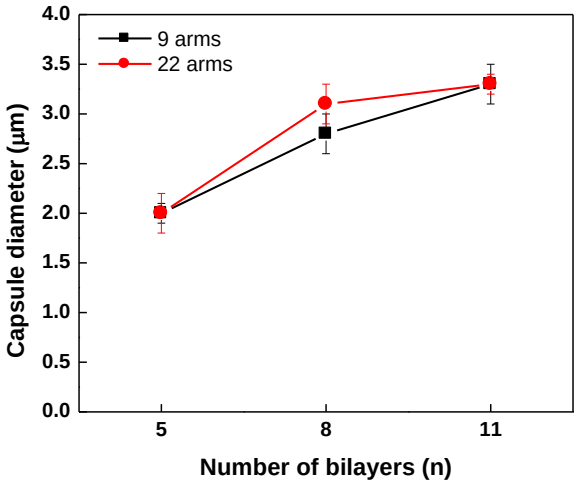

Figure S8.3: Variations of the diameter of PS_nP2VP_n/PSS LbL microcapsules (n=9 (■) and 22 (●) arms) a function of number of bilayers (5, 8, and 11).

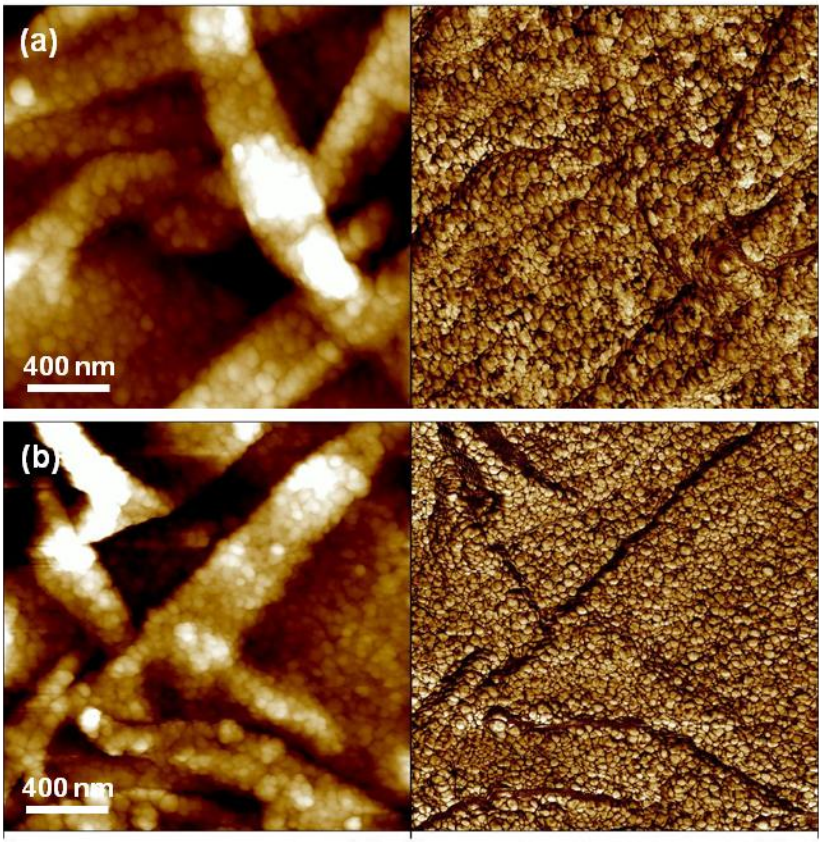

Figure S8.4: AFM images (topography (left) and phase (right)) of shell wall of (a) PS_9P2VP_9/PSS and (b) $PS_{22}P2VP_{22}$/PSS LbL hollow microcapsule for 8 bilayers on silicon substrate in dry state. The data scale of all images is 120 nm (topography) and 30° (phase).

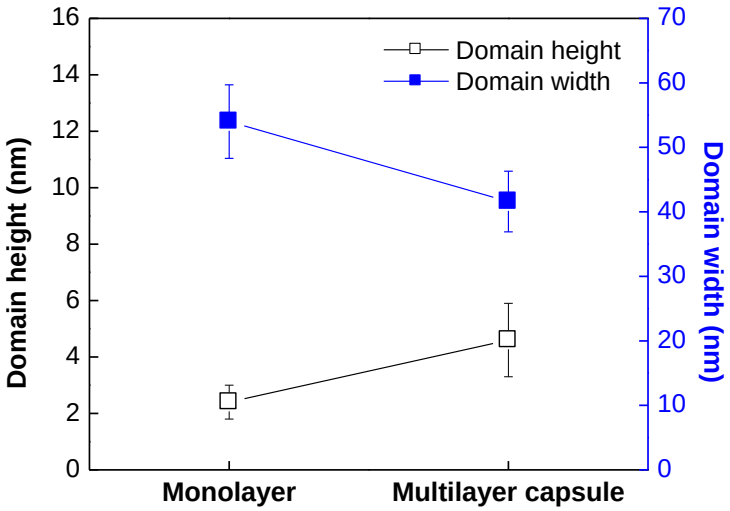

Figure S8.5: Domain height (□) and width (■) of the shell wall of $PS_{22}P2VP_{22}$/PSS LbL multilayer microcapsule in dry state as compared to $PS_{22}P2VP_{22}$ unimolecular micelle monolayer films on silicon wafers.

CHAPTER 9

STAR POLYMER UNIMICELLES ON GRAPHENE OXIDE FLAKES

9.1. Introduction

Graphene oxide (GO), which is derived from oxygenated graphene lattice, is an emerging two-dimensional material with its intriguing electronic, electrochemical, and biological activity. [381, 382, 383] Modification of graphene oxide chemistry with metal nanoparticles, [384, 385] DNA aptamers, [386] peptides, [387, 388] and polymers [389, 390] through covalent/non-covalent interactions (e.g., various chemical groups such as hydroxyl, amine, charged glutamic acid, and aromatic amino acid) is an area of current research interest in an electrochemical and bio-sensing devices with enhanced sensitivity and selectivity. Graphene oxide, as a graphene precursor, can be dispersed in water and thus enables wet chemistry and solution processes for a variety of thin film fabrication. The monolayer graphene oxide flake is considered a single atom layer carbon material with a wide range of sizes and shapes, which comprises hydrophobic graphitic domains (irregular regions of 1-6 nm^2 across) randomly distributed in hydrophilic oxygenated regions with the overall average ratio of graphitic : oxygenated : vacancy areas of 16 : 82 : 2 %, which is concerted with the popular Lerf-Kilnowshik (LK) model.[391]

The exact source of high acidity of graphene oxide and localization of acidic groups still remains arguable.[392] The presence of polar bondings including hydroxyl, phenol, epoxide, and carboxylic acid groups on the edge and basal plane is an evident cause of compelling solubility of graphene oxide flakes, enabling diverse chemical interactions such as

electrostatic, van der Waals, hydrogen bonding and π-π interactions available for interfacial assemblies.[393,394] Control over interactions and assemblies between graphene oxide and functional components is crucial because it affects complexation behavior, interfacial structure and overall integrity, morphology, and ultimate nanocomposite performance.[395,396]

The geometrically anisotropic (i.e., large aspect ratio in lateral and vertical direction) and unique in-plane random heterogeneous character due to the distribution of hydrophobic and hydrophilic domain are known to be critical for the stabilization of graphene oxide sheets at fluid-fluid interface (e.g., air-water and solvent-water).[382] Specifically, in the recent work, Huang and his colleagues have demonstrated a facile and versatile approach to control assembly of monolayer graphene oxide (i.e., up to micrometer scale uniformity) on the Langmuir trough. The in-plane amphiphilic feature combined with the use of methanol/water (5:1) mixed solvent system allowed graphene oxide to spread on the water surface and subsequently remain afloat via "edge-to-edge" repulsion after evaporation of methanol, which experimentally validated its amphiphilic nature.[397,398] While hydrated pliable graphene oxide in solution and bulk has a corrugated configuration due to the presence of vacancy and compositional inhomogeneity, it is able to transform into a stretched flat structure driven by capillary force and surface tension when incorporated at the interface.[399] For example, assembly of graphene oxide as two-dimensional filler for polymer nanocomposites has been explored for the fabrication of ultrathin nano-membranes in our research group. Surface-assisted assembly approach via electrostatic and hydrogen bonding interactions between graphene oxide and synthetic

polyelectrolyte or silk fibroin led to highly integrated hierarchical multilayer films with minimized folding and wrinkling showing dramatically enhanced mechanical properties of flexible nanocomposites with low graphene oxide content (8-20 vol %).[400,401]

Surface active properties of graphene oxide have been further manifested in the graphene oxide-assisted emulsification of toluene in aqueous media, and the interfacial entrapment of graphene oxide induced by air-bubbles in aqueous solution.[402] At the fluid-fluid interface (i.e., non-aromatic polar solvent chloroform/water interface), in particular, the organic solvent-driven enrichment of graphene oxide sheets from the bulk solution is another example to support their surface activity.[403] These findings are indeed extending the ability of graphene oxide flakes for assembly and functionalization, which are important for the fabrication of organized nanocomposites. In this regard, interfacial-driven assembly through non-covalent interactions can be considered for large area fabrication of flexible organized nanocomposite materials with anisotropic structure, controlled adsorption, and minimized wrinkling and folding.

Recently, non-covalent attachments based on self-assembly of amphiphilic star polymers have been considered for stabilizing carbon-based materials in solution.[22] Latridi et al. has demonstrated that polystyrene/(poly(2-vinylpyridine)-*b*-poly(acrylic acid)) star terpolymer (PS_{22}(P2VP-*b*-$PAA)_{22}$) enabled the pH tunable stabilization of carbon nanotubes in aqueous media, leading to controlled dispersion of colloidal nanotube-star hybrid via non-covalent bonding interactions.[404] Gröschel et al. has proved the concept that polymer-based Janus micelles can be utilized as effective colloidal dispersants in a

variety of solvents.[405] However, no attempts to assembly of star polymers with heterogeneous chemical composition on graphene oxide sheets have been reported to date.

Here, we discuss assembly of graphene oxide sheets with surface-active macromolecular surfactant, amphiphlic star copolymer at the air-water surface (Scheme 9.1). The highly branched poly(styrene)-poly(2-vinlypyridine) $(PS\text{-}P2VP)_n$ star copolymers comprising hydrophobic (PS) and hydrophilic arms (P2VP with ionizable pyridine groups)[128] were chosen to pair with heterogeneous graphene oxide surface. The binding, spreading, and assembly behavior of the star copolymers in the form of unimicelles at the edge and on the basal plane of graphene oxide flakes was investigated using LB technique for different polymer/graphene oxide mixing ratios, surface pressure and spreading solvent polarity. This surface-mediated assembly led to a stable micelle-graphene oxide bilayers. Incompressible and highly ordered micelle morphology on the graphene oxide surface is caused by strong affinity between two components and stable polymer-graphene oxide complexes.

9.2. Experimental Details

Materials. Graphene oxide was prepared from natural graphite flakes (325 mesh, 99.8% metal basis) purchased from Alfa Aesar through Hummer's method.[381] The dispersion of graphene oxide in a solution mixture of methanol/water (5:1 volume ratio) was subjected to ultrasonication for 15 min followed by centrifugation at 3000 rpm for 45 min. The supernatant (concentration 0.01 wt %) was decanted and used for all experiments.

Star block copolymers. The "in-out" methodology for star polymer synthesis was followed for the preparation of PS_{28}(P2VP-*b*-P*t*BA)$_{28}$ heteroarm star block terpolymer and its $PS_{28}P2VP_{28}$ copolymer precursor as reported elsewhere.[126] The results are presented in Table S9.1.[126]

Fabrication of graphene oxide/star polymer structures. Interfacial assembly of graphene oxide sheets and star polymers at the air-water interface were conducted on a KSV2000 mini trough equipped with a Wilhelmy plate for pressure sensing according to the usual procedure.[406] All experiments were made at a constant temperature of 25°C in a clean environment. Nanopure water was used as the subphase for all experiments. The pH of the water subphase was adjusted by using hydrochloric acid and sodium hydroxide without a buffer system.

Solutions of 0.2-0.1mg/ml of a star copolymer was dissolved in various solvent including chloroform, tetrahydrofuran, toluene, and dichloromethane (HPLC grade) and spread 70 µL of the polymer solution uniformly at the air-water interface. The graphene oxide sheets were spread first at air-water interface followed by depositing star polymer solution and then waiting for 30 min for evaporation of spreading solvent. The compression of GO/star polymer thin films was conducted at a speed of 5 mm/min and then transferred onto a silicon wafer by a vertical dipping method at a dipping rate of 2 mm/min and different surface pressures for different monolayer states (0, 15, and 30 mN/m). Specifically, graphene oxide-dispersed methanol/aqueous solution was spread first at the air-water interface on the Langmuir trough followed by addition of

amphiphilic polystyrene-poly(2-vinylpyridine), $PS_{28}P2VP_{28}$, star copolymer in chloroform (Scheme 9.1).[166] Upon solvent evaporation, lateral compression was applied to obtain different surface pressures at which subsequently GO/star copolymer Langmuir film at the air-water interface was transferred onto air-solid interface using vertical dipping method.

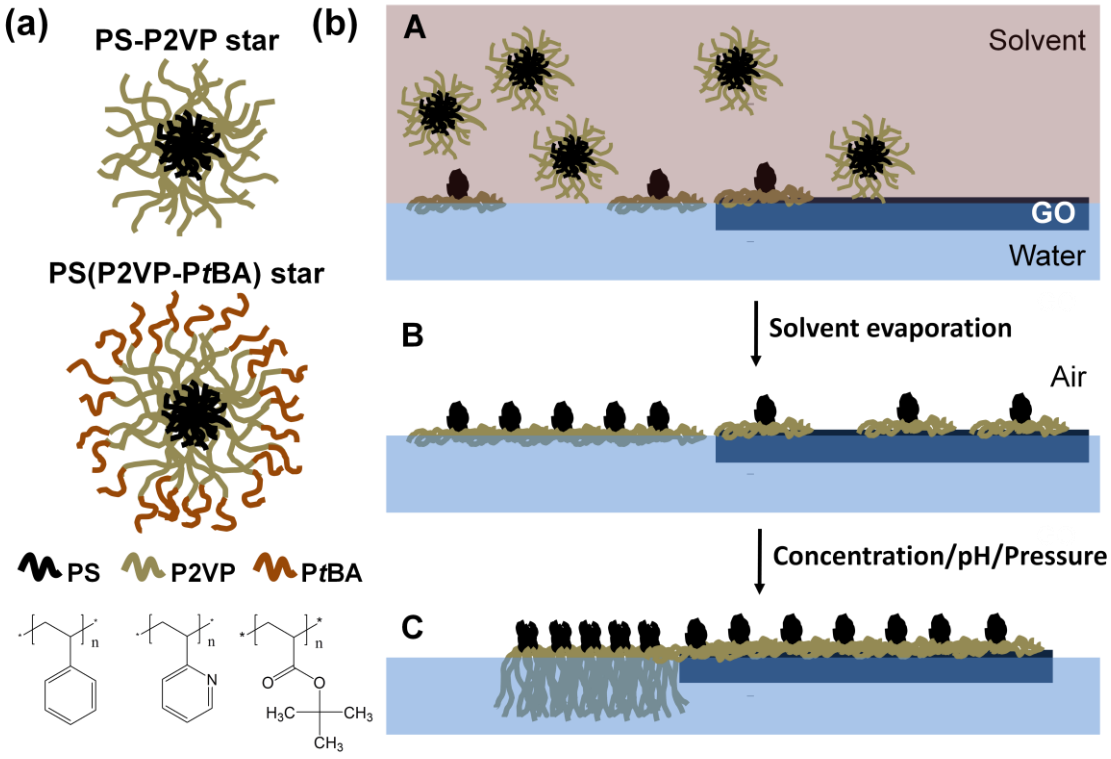

Scheme 9.1: (a) Chemical structure of amphiphilic heteroarm $PS_{28}P2VP_{28}$ and PS_{28}(P2VP-*b*-P*t*BA)$_{28}$ star copolymers. (b) Assembly and suggested molecular conformation of star polymer surface unimicelles on graphene oxide sheets at solvent/water and air-water interfaces for different conditions on a Langmuir trough (A-C).

9.3. Results and discussion

9.3.1. Effect of concentration and surface pressure

According to previous reports, the amphiphilic $PS_{28}P2VP_{28}$ star copolymer used in this study has been known to show pH-dependent surface aggregation behavior and a stable Langmuir monolayer composed of unimolecular micelles (or unimicelles) at the air-water interface.[155,162,164,165,188,191199] The pressure-area (π-A) Langmuir-isotherm of GO/$PS_{28}P2VP_{28}$ star copolymer showed gradual compression up to 40 mN/m, which is higher than individual graphene oxide and star copolymer, indicating the formation stable surface assembly at the air-water interface (Figure S9.1).

In order to investigate the binding behavior of star copolymer unimicelles, lower concentration of star copolymer solution (0.02 mg/ml $PS_{28}P2VP_{28}$ star copolymer in chloroform) was spread without external compression ("apparent" surface pressure = 0 mN/m). Acidic pH conditions was chosen (pH = 2) which allowed the pyridine units of P2VP segment to protonate and impart a positive charge on the arms (degree of ionization up to 60%, $pK_{a,P2VP}$ ~5.2).[155] The zeta-potential of graphene oxide at pH = 2 fall in the range of -10~-20 mV.[394] Thus, sufficient Columbic repulsion can be achieved to stabilize the graphene oxide monolayer film at the air-water interface.

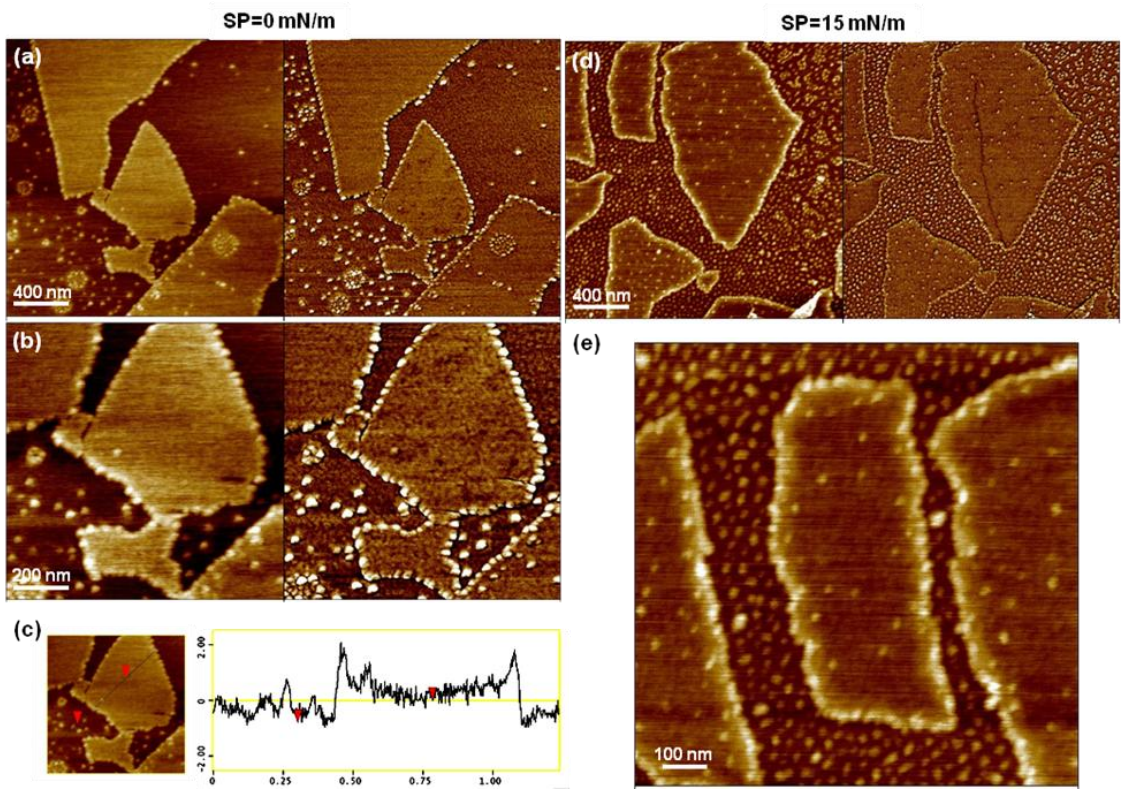

Figure 9.1: AFM topography (left) and phase (right) of GO (0.01 wt %, 0.5 ml)/$PS_{28}P2VP_{28}$ star copolymer (0.02 mg/ml in chloroform, 70 μL): (a) large area scan, (b) high resolution zoomed in image, and (c) topography height profile of corresponding image from (b) at surface pressures of 0 mN/m (a-c); (d) large area scan and (e) high resolution zoomed in for surface pressure 15 mN/m (d-e). The subphase pH was adjusted at pH 2. z-scale: 5 nm (topography) and 30° (phase) for a, d; 3 nm (topography) and 20° (phase) for b, c, e.

At zero pressure, deposition of star copolymers resulted in decoration of the polygonal periphery of graphene oxide sheets with star copolymer unimicelles while a small number of star polymer unimicelles were found on the basal plane (Figure 9.1). High resolution AFM image shows that the spherical micelles bonded predominantly along the edges of graphene oxide sheet with sparse concentration on the basal plane, especially on top of edge (total graphene oxide/micelle thickness: 2.0 ± 0.3 nm) (Figures 9.1b, c). Moreover, single micelle-string features were observed without aggregation along the edges of the

graphene oxide. This interesting morphology suggests that star copolymer unimicelles tend to move closer to the edge of graphene oxide sheets upon evaporation of star copolymer solution. Solution spreading/evaporation might trigger accumulation at the edge in combination with relatively hydrophobic graphene oxide basal plane compared to the water surface. Also, graphene oxide under acidic conditions (pH ~2) is known to show a higher contact angle (~70°) with water than the graphene oxide at higher pH (60° for basic water of pH 10). This suggests a reduced wettability of graphene oxide by water under the conditions employed in our study.[407]

Upon compression to a surface pressure of 15 mN/m, the surface density of star copolymer unimicelles formed at air-water interface increased significantly while the density at the surface of graphene oxide sheets still remained very low (Figure 9.1d, e). It is worth to note that the AFM images shown in Figure 9.1 and following figures were obtained by transferring the LB monolayer on a solid silicon oxide substrate but represent different scenarios at the original fluid interface: polymer monolayer is formed on either graphene oxide sheets or directly at fluid surface (Scheme 9.1). The density of star polymer unimicelles at the graphene oxide edge increased upon compression, as evident from the high resolution AFM topography image in Figure 9.1e. Meanwhile, comparing Figure 9.1a and 9.1d, no significant difference in micelle density is observed on the basal plane of the graphene oxide sheets.

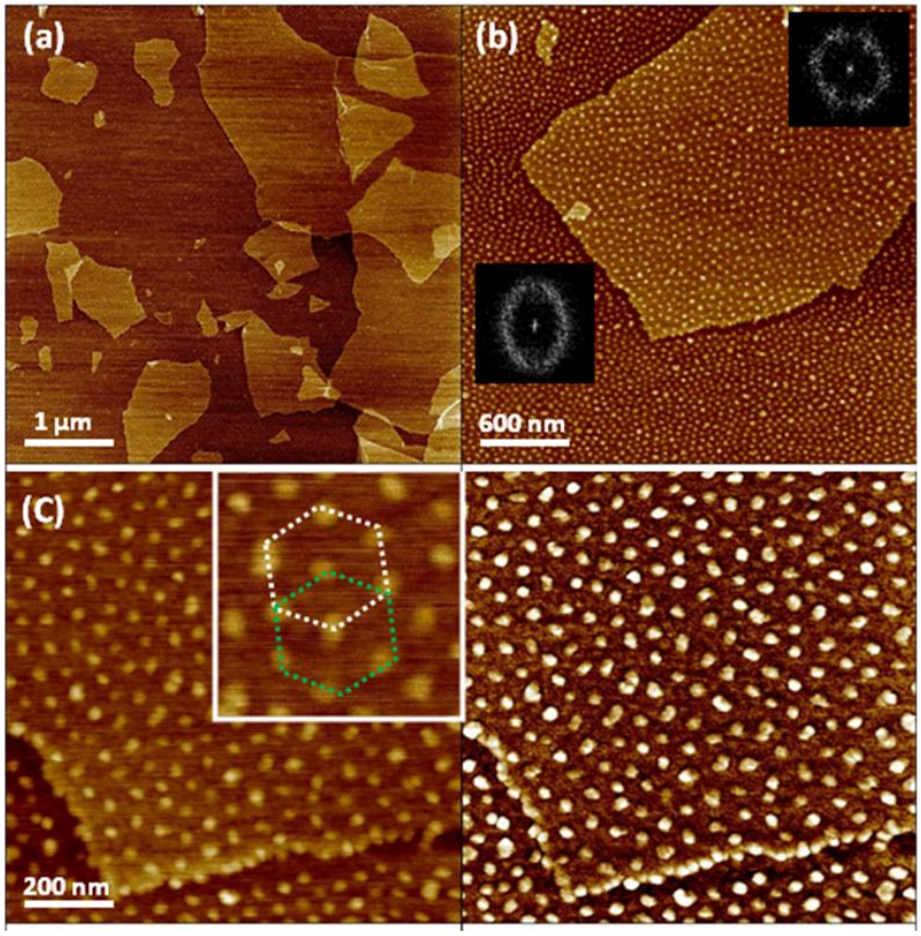

Figure 9.2: AFM topography (left, a,b,c) and phase (right, c) of GO (0.01 wt %, 0.5 ml)/$PS_{28}P2VP_{28}$ star copolymer (0.1 mg/ml in chloroform, 70 µL) at pH 2 for surface pressures of 0 mN/m. The inset in (C) indicates lattice analysis from the corresponding topography image in Figure 9.2c. z-scale: 5 nm (topography) and 20° (phase).

For further comparison of the effect of star copolymer concentration on preferential binding and assembly on the graphene oxide surface, high concentration of the star copolymer solution was deposited (0.1 mg/ml of $PS_{28}P2VP_{28}$ star copolymer in chloroform) at the same subphase pH of 2. These conditions resulted in a uniform surface coverage with compact organization across both graphene oxide and water surface. A local six-fold symmetry of star copolymer domain packing on the graphene

oxide sheets was observed indicating a uniform behavior under compression and corresponds to the dense surface packing of symmetrical disc-like molecules with a central core height of 1.3 ± 0.3 nm (Figure 9.2 and 9.3). The protonated stretched P2VP arms is expected to dominate the spacing and ordering of spherical polymer micelles due to intra-/intermolecular electrostatic and entropic repulsion. It has been demonstrated previously that the star copolymer unimicelles having a core-shell structure induced by phase segregation at pH 2 with the collapsed PS core on top of the extended P2VP shell (single PS_7P2VP_7 copolymer with P2VP molecular weight ($M_{w,\ P2VP\ arms}$) of 56500 Da) had an average diameter of 126 nm (highly stretched state) and 2.9 nm domain height.[65,166] Based on these results and the assumption that the chain dimensions are directly proportional to the molecular weight, we can estimate that the diameter of $PS_{28}P2VP_{28}$ star copolymer ($M_{w,\ P2VP\ arm}$ = 16,000 Da) used in this study to be around 36 nm. Taking into account the higher number of arms (28 versus 7 arms), this value can be increased presumably due to increased intramolecular repulsion.

As apparent from Figure 9.2b and 9.2c, spacing between the spherical surface micelles was larger (69 ± 12 nm) on graphene oxide surface than on the water surface (43 ± 8 nm), indicating packed state of star macromolecules suited on the fluidic subphase (about two times smaller cross-sectional surface area per molecule). In the previous study, we have observed that the dimension of $PS_{28}P2VP_{28}$ star copolymer from LB monolayer was 64 ± 5 nm in diameter with effective thickness of 0.5 nm.[338] Thus, the star polymer on the graphene oxide sheets seems to have a similar stretched conformation, however, a decrease in size of star polymers was observed at the water surface. On the other hand,

the pre-deposition of graphene oxide sheets at the air-water interface results in a reduced free surface and thereby more densely packed state of the star polymers at the same concentration. As illustrated in Scheme 9.1b (A-C), amphiphilic star copolymers can be predicted to undergo different extent of conformational transition on graphene oxide sheets and water surface (from initial planar surface micelle into compressed and compact structure with vertical orientation under external environments). Also, the AFM imaging directly visualized the interface line along which the edge of graphene oxide sheet meets the continuously organized star copolymer monolayer (0 mN/m) at the air-water interface (Figure 9.2).

The sharp interface between graphene oxide sheets and highly compressed star copolymer unimicelles was more pronounced at higher pressure (15 mN/m) (Figure 9.3). Polymer micelles appear to be ordered along the graphene oxide edge while more symmetrical hexagonal packing was prominent on the basal plane farther from the edges (Figures 9.2b,c and 9.3b,d). We note that the average domain spacing (66 ± 13 nm) on the graphene oxide remained almost unchanged during compression. However, the packing of the star polymers was very dense on the water surface. This observation revealed that the star polymer micelles stay incompressible on the surface of graphene oxide sheets under compression with reduced surface area "adsorbed" by polymer monolayer between sheets.

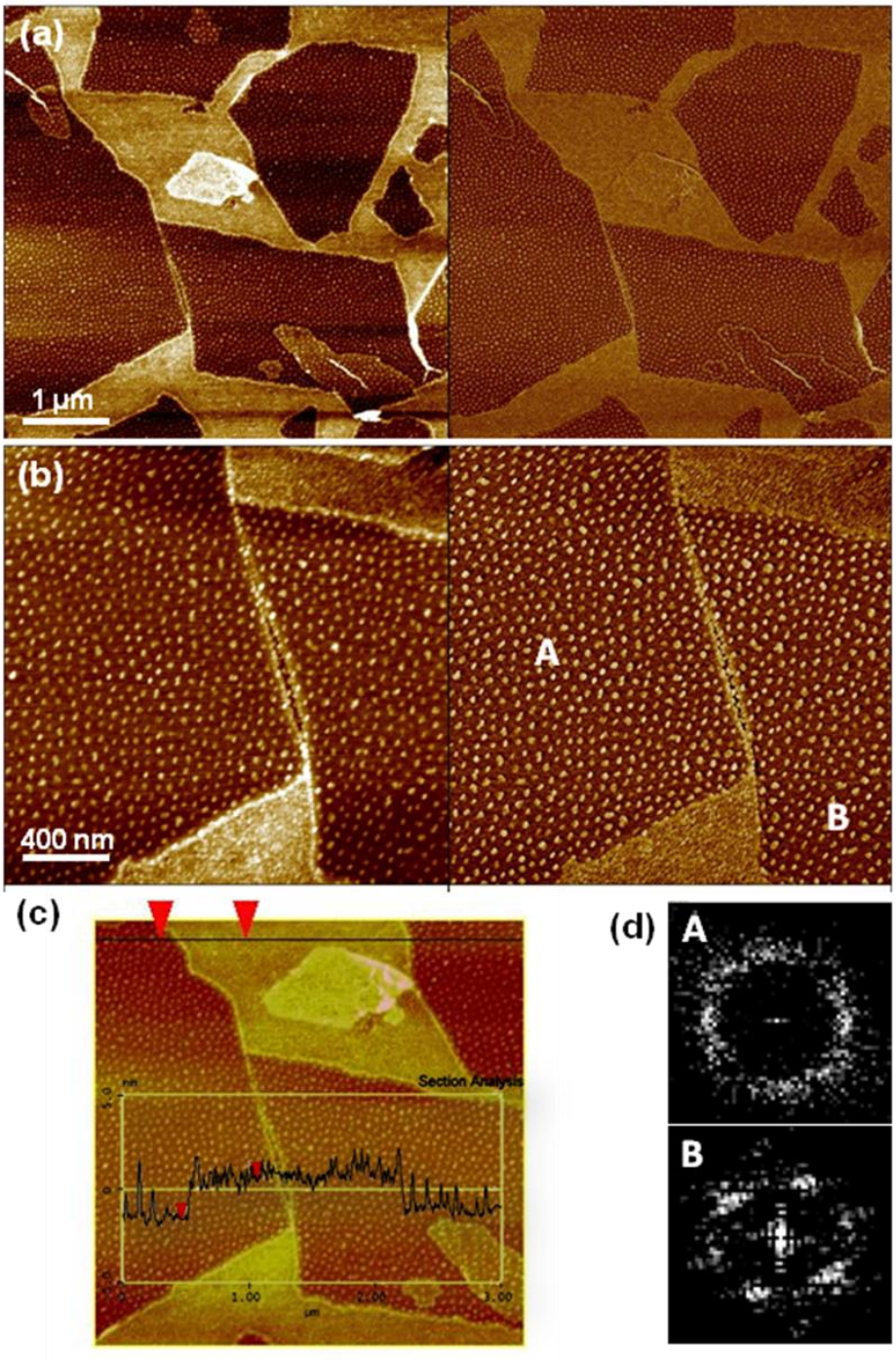

Figure 9.3: AFM topography (left,) and phase (right) of (a, b) GO (0.01 wt %, 0.5 ml)/$PS_{28}P2VP_{28}$ star copolymer (0.1 mg/ml in chloroform, 70 µL) at pH 2 for surface pressures of 15 mN/m; (c) The height profile of corresponding topography image; (d) FFT of domain morphologies for A and B regions from Figure 9.3b where A is corresponding to the center region while B, the near edge region of GO sheet. z-scale: 5 nm (topography) and 30° (phase).

Also, it is interesting that the polymer monolayer thickness difference on the basal plane of graphene oxide sheets and at the water surface is more pronounced upon compression. The AFM sectional analysis revealed that top surface of compressed polymer monolayer on water surface is around 1.5 nm thicker than that on graphene oxide surface indicating that a change in molecular conformation of the star copolymers occurs as a response to external compression with arms extending into the water subphase (Figure 9.3c). Further, a clearly distinguished interface between graphene oxide sheets and densely packed polymer monolayer indicates that there is no occurrence of buckling or folding of polymer monolayer along the edges of graphene oxide sheets under high compression. This result also suggests that the edges of graphene oxide sheets locate at the air-water interface rather than sinks into the subphase during compression (Scheme 9.1).

In order to further investigate the characteristics of the edge/basal plane of the graphene oxide sheets and the polymer monolayer, high resolution QNM measurements were carried out over a selected area under the same conditions (Figure 9.4 and S9.2). The topographical image shows interconnected star copolymer micelles on the water surface whereas the star copolymers retain a spherical structure on the graphene oxide basal plane. It is important to note that at the borderline between graphene oxide and water surface, star copolymer micelles appear to be highly crowded but no obvious invasion of polymer micelles towards the graphene oxide basal plane is observed. The adhesion images clearly differentiate the polymer micelles and graphene oxide surface, showing low adhesive forces on hydrophobic PS domains and much higher adhesion for surrounding hydrophilic polar regions of spread P2VP arms (Figure 9.4b). Also, the

apparent modulus mapping confirms higher stiffness of central domains as compared to the stiffness of surrounding matrix of spread arms. It is worth to note that the elastic modulus cannot be measured correctly owing to the high stiffness of the graphene oxide and the oxide substrate underneath.

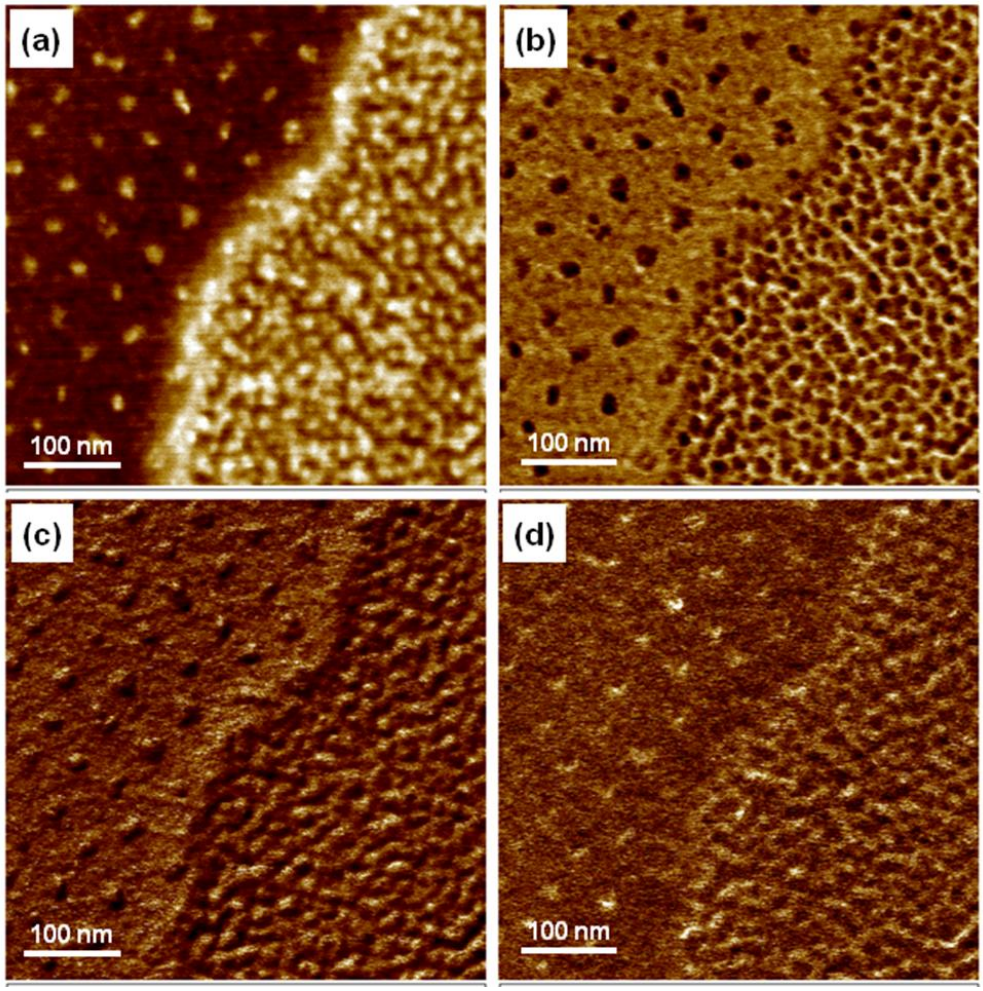

Figure 9.4: High resolution QNM analysis of (a) topography, (b) adhesion, (c) apparent modulus, and (d) deformation for GO (0.01 wt %, 0.5 ml)/$PS_{28}P2VP_{28}$ star copolymer (0.1 mg/ml in chloroform, 70 μL) at pH 2 for surface pressures of 15 mN/m. z-scale: 4 nm (topography), 2.5 nN (adhesion), 1.61 GPa (modulus), and 1.3 nm (deformation).

Further increase in the surface pressure does not change the symmetry and spacing of polymer domain morphology on the graphene oxide surface (see high resolution images in Figures 9.2 and 9.3). However, patterned spherical micelle morphology of polymer monolayer was found to transform into interconnected lamellar or layered continuous morphology on the water surface thus indicating dominant compression of polymer monolayer located between sheets (Figure 9.3 and 9.4). It is apparent that compressive stresses are not directly transferred to polymer monolayers on graphene oxide sheets, thus preserving "star-fish" global conformation and the polymer-graphene oxide complexes become more stable against compression.

Reduction of surface area at the air-water interface is facilitated by the transformation of the highly ionized P2VP segments at the water surface which can easily sink into the water subphase to form brush-like conformation as was demonstrated in previous studies on similar star block copolymers.[65,91,92,93,94,95,168] This is likely due to the pH-sensitivity of the P2VP blocks ($pK_{a,P2VP}$ ~5.2) which protonate under acidic pH conditions (pH = 2), and are prone to submerge into water subphase upon modest compression. These properties facilitate the conformational transition from "star-fish" to "jelly-fish" global conformation if star macromolecules are located at water surface.[91,92,93,94,95] We suggest that as a result of such heterogeneous morphology with different lateral and vertical segregation of star macromolecules, vertically segregated unimicelles can not cross over the elevated graphene oxide sheet edges and homogenize the conformational state of star macromolecules across the whole film. We believe that such stable surface micelles on graphene oxide sheet results from decreased configurational entropy of branched arms

confined on the attractive and non-diffusive graphene oxide surface. Overall, such "engineered" biphase morphology of Langmuir polymer monolayer represents a non-trivial example of tailored bi-component polymer monolayers rarely observed for Langmuir monolayers.

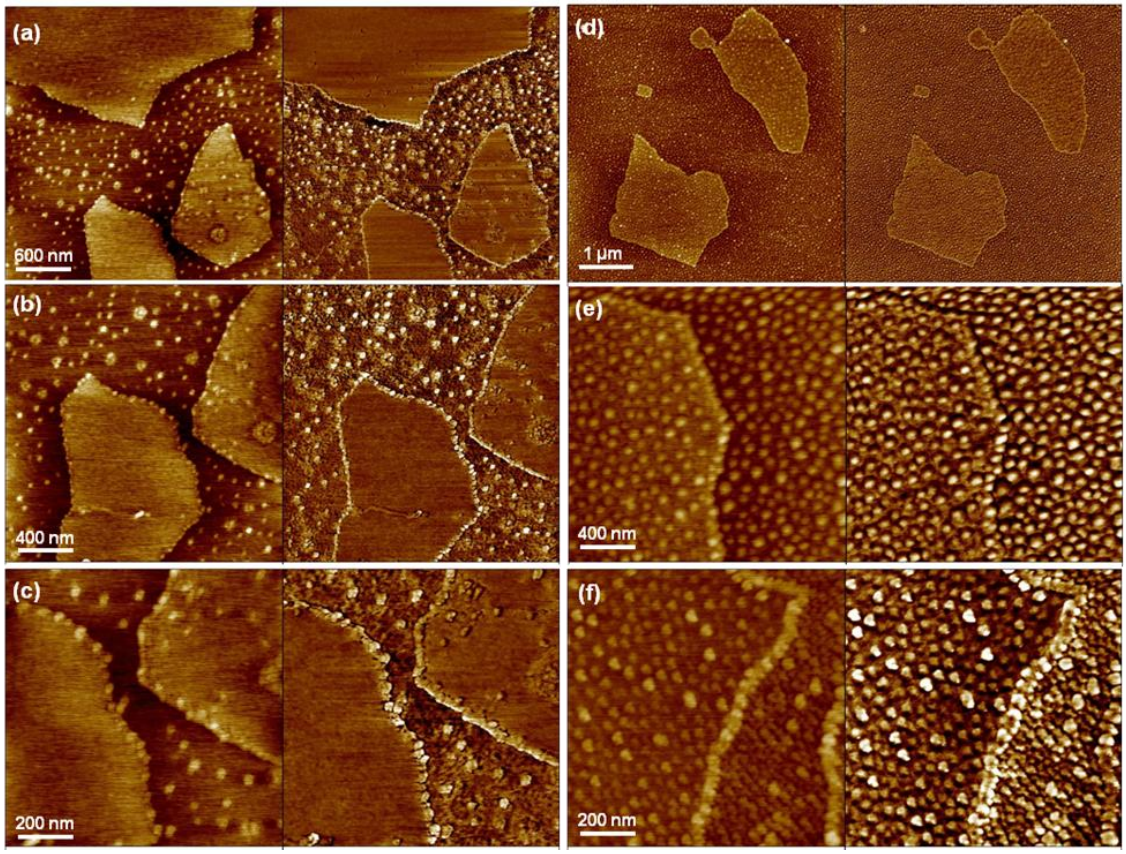

Figure 9.5: AFM topography (left) and phase (right) of (a-c) GO (0.01 wt %, 0.5 ml)/PS_{28}(P2VP-P*t*BA)$_{28}$ star terpolymer (0.02 mg/ml in chloroform, 70 µL) at surface pressures of 0 mN/m, (d-e) GO (0.01 wt %, 0.5 ml)/PS_{28}(P2VP-*b*-P*t*BA)$_{28}$ star block terpolymer (0.1 mg/ml in chloroform, 70 µL) at surface pressures of 0 mN/m, (f) GO (0.01 wt %, 0.5 ml)/PS_{28}(P2VP-*b*-P*t*BA)$_{28}$ star block copolymer (0.1 mg/ml in chloroform, 70 µL) at surface pressures of 15 mN/m. All depositions were conducted at pH 2. z-scale: 5 nm (topography) for a-f and 30° for a; 20° for b, c; 10° for d-f (phase).

9.3.2. Effect of molecular composition

Another intriguing feature of these biphasic monolayers was the preferential decoration of the sheet edges with individual polymer micelles of different star terpolymer, PS_{28}(P2VP-*b*-P*t*BA)$_{28}$ having a hydrophobic non-aromatic end block (P*t*BA) (Figure 9.5, Table S9.1). It is noteworthy that star terpolymers were prominently bound along the edge of graphene oxide at low concentrations (Figure 9.5a-c) while a dense coverage of star terpolymer micelles was observed everywhere at high polymer concentration with the edges still maintaining a dense chain-like morphology of the star polymers (Figure 9.5d-f).

Such a behavior can be related to the presence of hydrophobic P*t*BA end blocks of star terpolymer which restrain the preferential strong binding of polar arms by promoting additional vertical segregation of the stars with hydrophobic end anchors.[188] Heterogeneous graphene oxide surface seems to partially compromise preferential binding of polymer unimicelles on the basal plane. When unimicelles are added, hydrophilic P2VP segments with highly negatively charged ionic groups spread on the water surface and decorated the edges, further preventing the star macromolecules with hydrophobic end blocks to spread across the entire flake. We suggest that the preferential edge binding phenomena can be driven by decrease in high surface energy of graphene oxide edge via balancing the attraction force and reducing conformation entropy of star polymers. Notably, in case of small molecules (e.g., oxygen and nitrogen gas), the graphene provide active edge sites for strong binding due to partial charges at the edges.[408] On the other hand, a preferential binding of small peptides to graphene can be

induced by non-covalent bonding i.e., electrostatic or π-π interactions in solution. For instance, negatively charged amino acid on peptide attracted to the edge of graphene sheets while aromatic amino acid containing peptide were found to dominantly bind on the basal plane.[409]

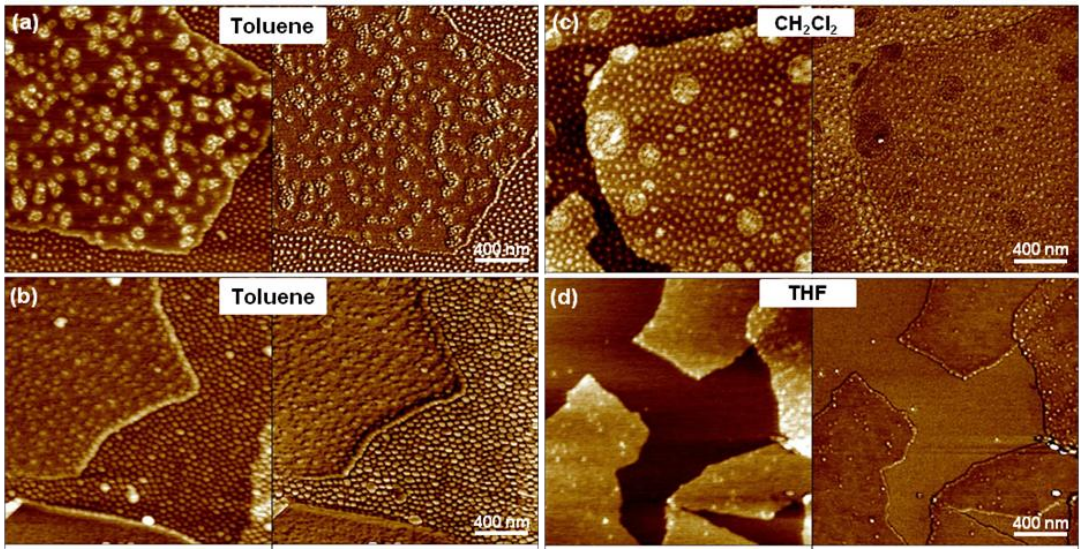

Figure 9.6: AFM topography (left) and phase (right) of GO (0.01 wt %, 0.5 ml)/$PS_{28}P2VP_{28}$ star copolymer (0.1 mg/ml, 70 μL) at pH 2 for different spreading solvents at surface pressure 0 mN/m): (a,b) toluene, (c) dichloromethane (CH_2Cl_2), and (d) tetrahydrofuran (THF). z- scale: 5 nm for a-d (topography) and 10° for a, c, d; 30° for b (phase).

9.3.3. Effect of spreading solvent polarity and subphase pH

The coverage of star copolymer on the surface of graphene oxide might be also related to solvent characteristics. It has been demonstrated that amphiphilic graphene oxide can stabilize the oil-water interface (e.g., aromatic and non-aromatic solvents) due to the graphitic domain.[403] In particular, a non-aromatic volatile organic solvent such as chloroform spreads on the graphene oxide and make it suspended on the water surface even after evaporation. Thus, further investigation of influence of spread organic solvent

on interface assembly was conducted by employing different organic polar solvents such as toluene, dichloromethane (CH_2Cl_2), and tetrahydrofuran (THF) for spreading star copolymer micelles in comparison with non-selective good solvent, chloroform ($CHCl_3$) (Figure 9.6). Chloroform can play an important role in assembling because it is a good solvent for both PS and P2VP blocks and thus star macromolecules possess random coil-coil conformation in solution. Upon the spreading at air-water interface, it can facilitate to induce the vertical phase segregation of star copolymers with collapsed hydrophobic PS core and ionized hydrophilic P2VP corona at the interface. This is beneficial for hydrophilic aromatic pyridine group on star copolymer to interact with hydrated graphene oxide sheets through ionic interaction.[80,166]

In contrast to non-selective polar organic solvent, the aromatic polar ones such as toluene are bad solvents for P2VP, and since P2VP arms are much longer than PS arms, we expect multimolecular micelle formation as was observed in Figures 9.6a and b. In the case of toluene, the star copolymer surface micelles dewetted owing to contact of hydrophobic PS outer layer with the polar graphene oxide surface. It was shown that that toluene can be mixed with graphene oxide aqueous solution, producing graphene oxide-stabilized toluene/water emulsion and multimolecular micelles.[402]

In the case of dichloromethane, large aggregates were observed with a similar morphology like the ones with chloroform (Figure 9.6c). However, the lower boiling temperature of dichloromethane (39.6°C) (61.2°C for chloroform) seems to limit single

molecular level dispersion upon deposition. Finally, tetrahydrofuran (THF) endowed sparse star copolymer micelles both on graphene oxide and water surface (Figure 9.6d).

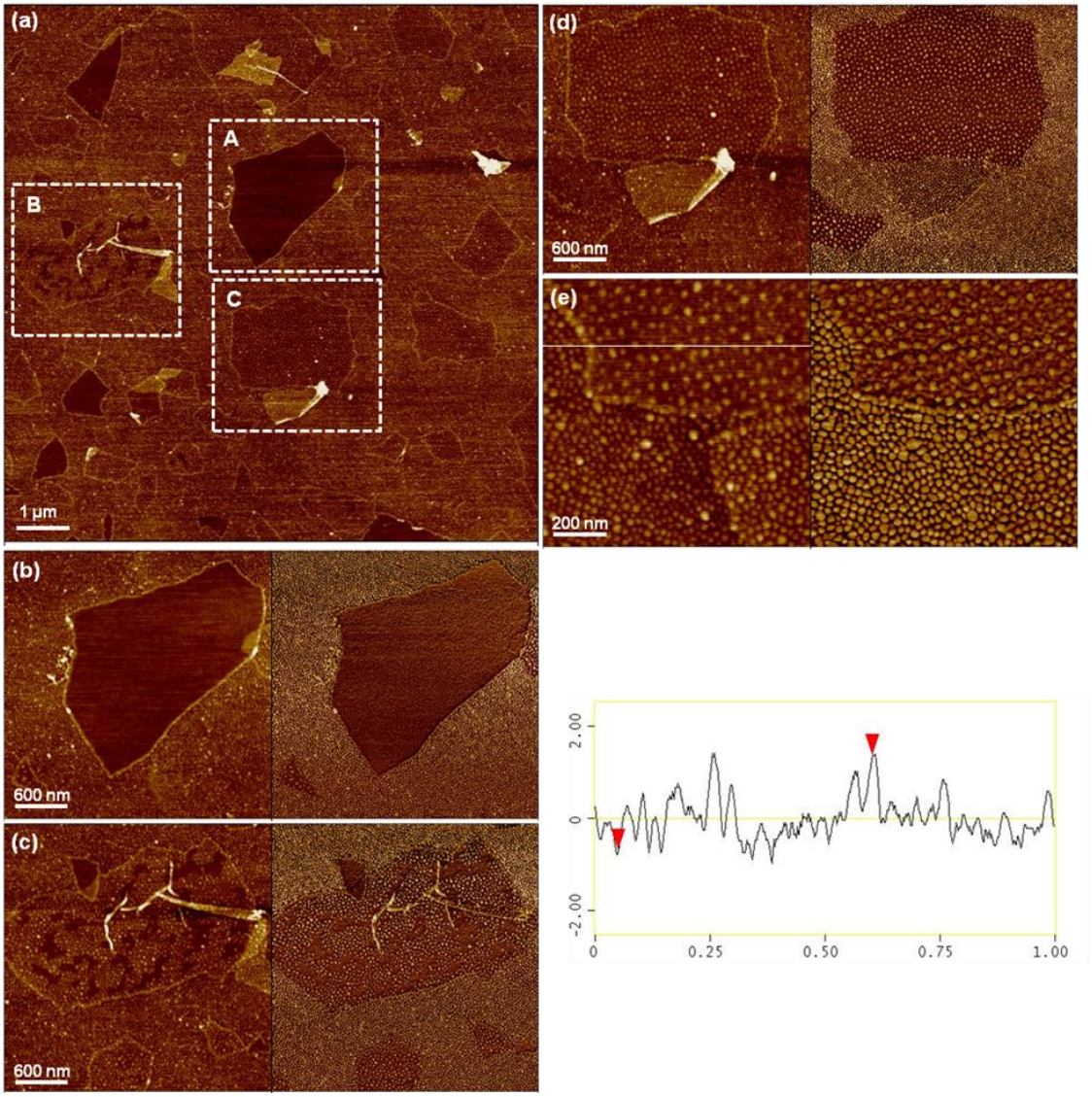

Figure 9.7: AFM topography images at low (a) and high (b-e) magnification images; AFM topography (left) and phase (right) of (b-e) GO (0.01 wt %, 0.5 ml)/$PS_{28}P2VP_{28}$ star copolymer (0.1 mg/ml, 70 µL) at pH 6 for surface pressure 15 mN/m. The height profile of corresponding topography image (e) is placed in bottom right. z-scale: 5 nm (topography) and 30° (phase).

One possible reason is that THF is a non-selective good solvent for both PS and P2VP and renders non-segregated structure of star copolymers, which seem unfavorable for surface adsorption.[410] It is in contrast to more selective-solvent for P2VP such as chloroform: induced 'Janus-like' PS and P2VP phase segregation favorable for hydrophilic P2VP bottom layer to orient toward the surface of graphene oxide sheets. In addition, it has been known that the significant dipole moment of THF (1.75 D, as high as water 1.82 D) can enable the formation of stable dispersions of graphene oxides and adversely affect their interfacial stability. Also, the water miscible THF seems to be insufficient to sustain star copolymer micelle at the interface with star copolymer micelles sinking into water sub-phase during deposition.

In order to study the effect of pH on the assembly, a weakly acidic subphase pH condition was considered (pH = 6) since the pyridine unit become highly deprotonating at basic pH regimes (apparent p$K_{a,P2VP}$ 5.2) (Figures 9.7 and 9.8). Compared to acidic pH of 2, the surface morphology of graphene oxide showed less coverage and ordering of the star polymers (Figure 9.7). Some graphene oxide flakes with high density of star copolymer micelle were observed which were similar to the density obtained at the air-water interface while others were left empty or showed less ordered morphology. This observation indicates that reduced ionization of P2VP affects charge density of star copolymer micelles, resulting in a decrease in their colloidal stability and subsequent variation of interaction between graphene oxide and star copolymer micelle. Also, it could be possible that that the apparent p$K_{a,P2VP}$ of star copolymers on the surface of graphene oxide sheets could be shifted to lower values likely due to the limited ionization

of pyridine units as a result of a lower level of hydration on the surface of relatively hydrophobic graphene oxide sheets compared to the air-water interface.

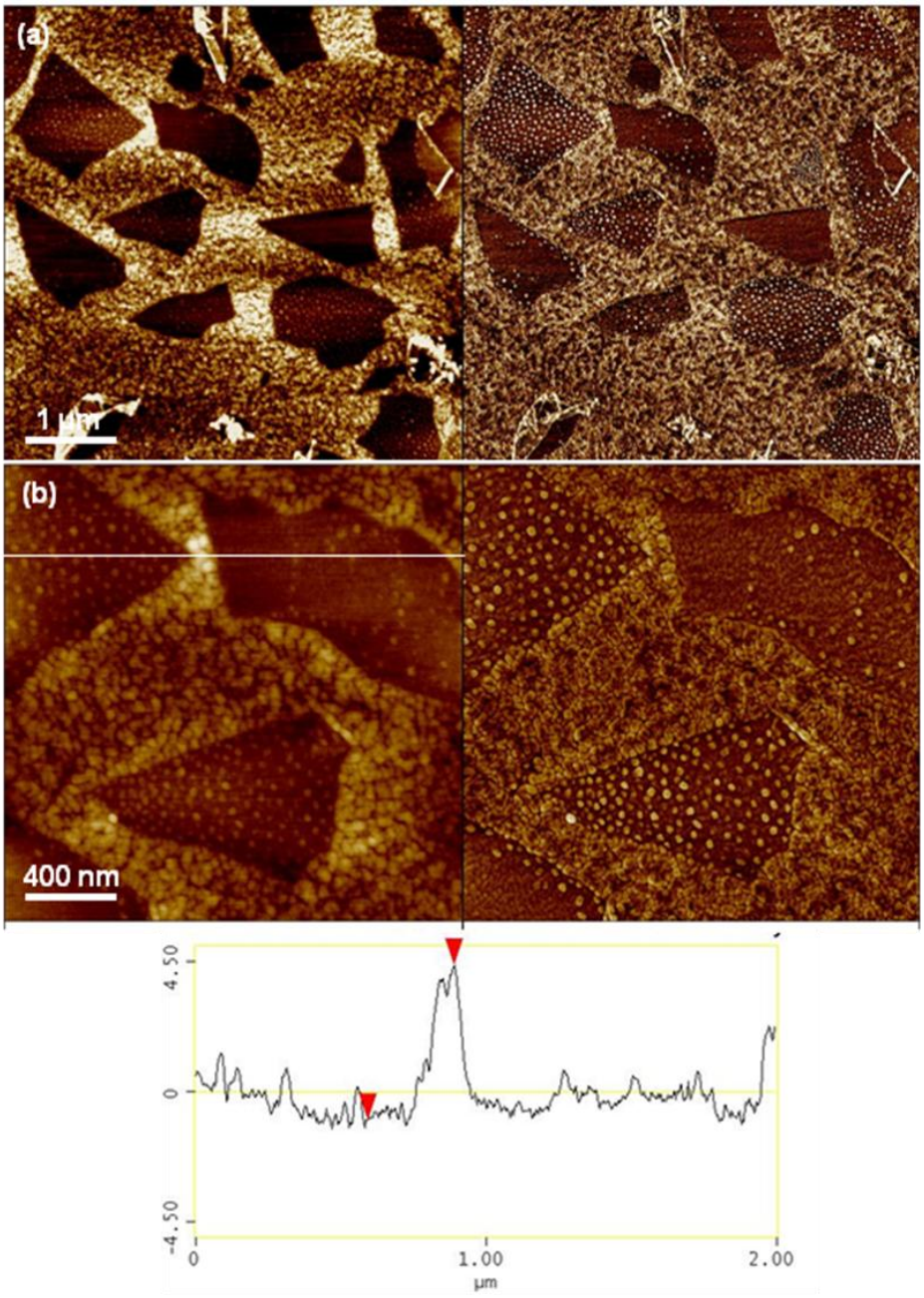

Figure 9.8: AFM topography images at low (a) and high (b-e) magnification images; AFM topography (left) and phase (right) of GO (0.01 wt %, 0.5 ml)/$PS_{28}P2VP_{28}$ star copolymer (0.1 mg/ml, 70 μL) at pH 6 for surface pressure of 30 mN/m. The height profile of topography image is obtained from Figure 9.8b (bottom). z-scale: 5 nm for a; 10 nm for b (topography) and 10° for a; 20° for b (phase).

Upon further compression to 30 mN/m unusual biphasic "tile-like" morphology was noted where graphene oxide sheets retain integrated flat configuration surrounded by polymer micelle domains with pronounced difference in domain height (Figures 9.8 and S9.3). The higher domains are correspond to the laterally compressed star polymer monolayer on the solid substrate transferred from the air-water interface (Figure 9.8, topography height profile) while the lower parts are graphene oxide-star polymer complex domains. In previous study, we observed that effective thickness of star copolymers was highly affected by compression force at the air-water interface for the same acidic condition (pH 2): the effective thickness dramatically increased from 0.5 nm at surface pressure 0.5 mN/m to 3.7 nm at 10 mN/m.[199] The lateral compression-driven orientation of star copolymer in vertical direction across the air-water interface seems to be responsible for the large increment in thickness of star polymer domains. However, the star copolymers on graphene oxide surface retain the initial flat conformation irrespective of external pressure due to the hindered chain transformation of star copolymers confined on the graphene oxide sheets which can sustain without sinking or folding due to interfacial stability of polymer-graphene oxide complexes. However, above the pK_a of P2VP stable micelle morphology was not observed because of the low extent of ionization of P2VP arms. In addition, the increase of pH closer to basic regime (7-10) seems to result in reduction of the surface activity of graphene oxide against additional polymer deposition because of increase in the hydorphilic nature as indicated by more negative zeta potential.[394]

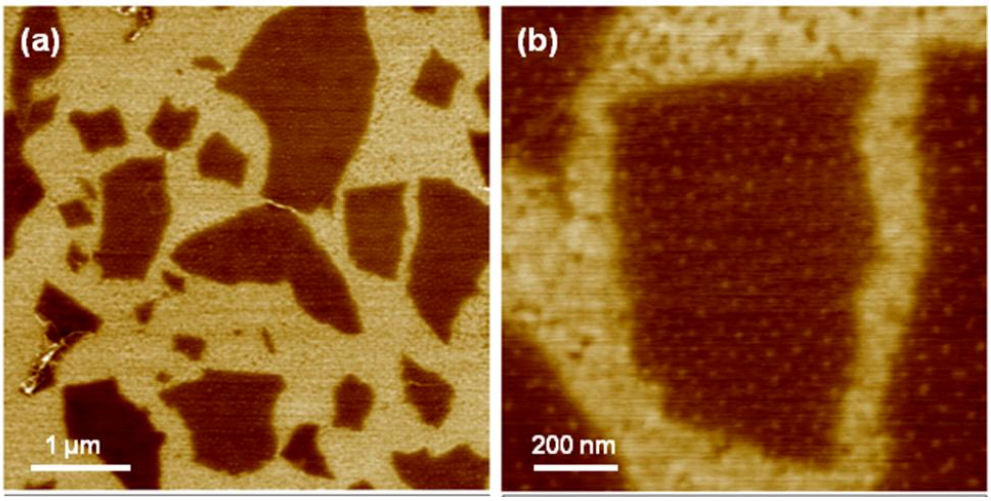

Figure 9.9: EFM images of GO (0.01 wt %, 0.5 ml)/$PS_{28}P2VP_{28}$ star copolymer (0.1 mg/ml, 70 µL) at pH 6 for surface pressure of 30 mN/m. z-scale: 2.5° for (a) and 2.0° for (b).

Finally, electrostatic force microscope (EFM) measurements were also performed to reveal surface charge distribution for biphasic morphology (Figure 9.9). The graphene oxide sheets not covered with the star polymer showed a higher EFM phase shift than the surface areas covered only with the star polymer monolayer. This contrast indicates that the uncovered graphene oxide sheets possess higher negative potential.[411] We suggest that the positively charged star polymer partially neutralizes the negatively charged surface (oxygenated functionalities) of the graphene oxide sheets. The heterogeneous biphasic morphology and intact state of graphene oxide sheets was also confirmed by Raman microscopy (Figure S9.4). The peak positions and D/G band ratio further confirmed the unchanged chemical composition and vibrational states of the graphene oxide sheets in complexes with star polymer micelles.

In summary, adsorption, spreading, and ordering of star polymer surface micelles on the basal plane and edge of in-plane amphiphilic monolayer graphene oxide were examined

using a Langmuir trough. The tunable preferred binding behavior and extent of coverage of these star polymers was demostrated. The micelles on the basal plane of graphene oxide sheets were found to remaine incompressible under lateral compression due to the confined arm status on their polar surface of graphene oxide. Well-organized discrete micelle assembly on the basal and edge of graphene oxide sheets is an evidence for the presence of strong affinity between star polymers and graphene oxide.

Appendix. Supporting Information: Table S9.1 and Figure S9.1-S9.4.

Table S9.1: Molecular Characteristics of the Star Polymers.

Polymer	Number of arms (average)	M_w	Degree of polymerization
$PS_{(arm)}$		3000[a]	29
PS_{28}	28	84000[b]	
$PS_{28}P2VP_{28}$	56	529000[b]	
$P2VP_{(block, arm)}$		16000[c]	152
PS_{28}(P2VP-*b*-P*t*BA)$_{28}$	56	843000[b]	
P*t*BA$_{(block,arm)}$		11000[d]	86

[a] Determined by SEC using PS standards. [b] Determined by SLS. [c] Calculated by subtracting the M_w of the PS_{28} from that of $PS_{28}P2VP_{28}$ and dividing by the number of arms (28). [d] Calculated by subtracting the M_w of the $PS_{28}P2VP_{28}$ from that of PS_{28}(P2VP-*b*-P*t*BA)$_{28}$ and dividing by the number of arms (28).

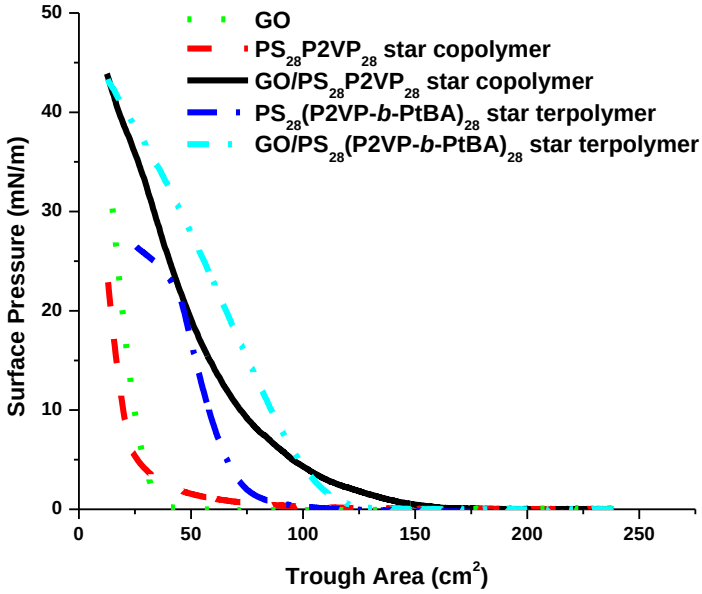

Figure S9.1: Pressure-area (π-A) Langmuir-isotherm versus trough area of GO (Dot, Green), $PS_{28}P2VP_{28}$ star copolymer (Dash, Red), GO/$PS_{28}P2VP_{28}$ star copolymer (Line, Black), PS_{28}(P2VP-*b*-PtBA)$_{28}$ star terpolymer (Dash-Dot, Blue), and GO/PS_{28}(P2VP-*b*-PtBA)$_{28}$ star terpolymer (Dash-Dot-Dot, Sky-Blue) at water subphase pH 2.

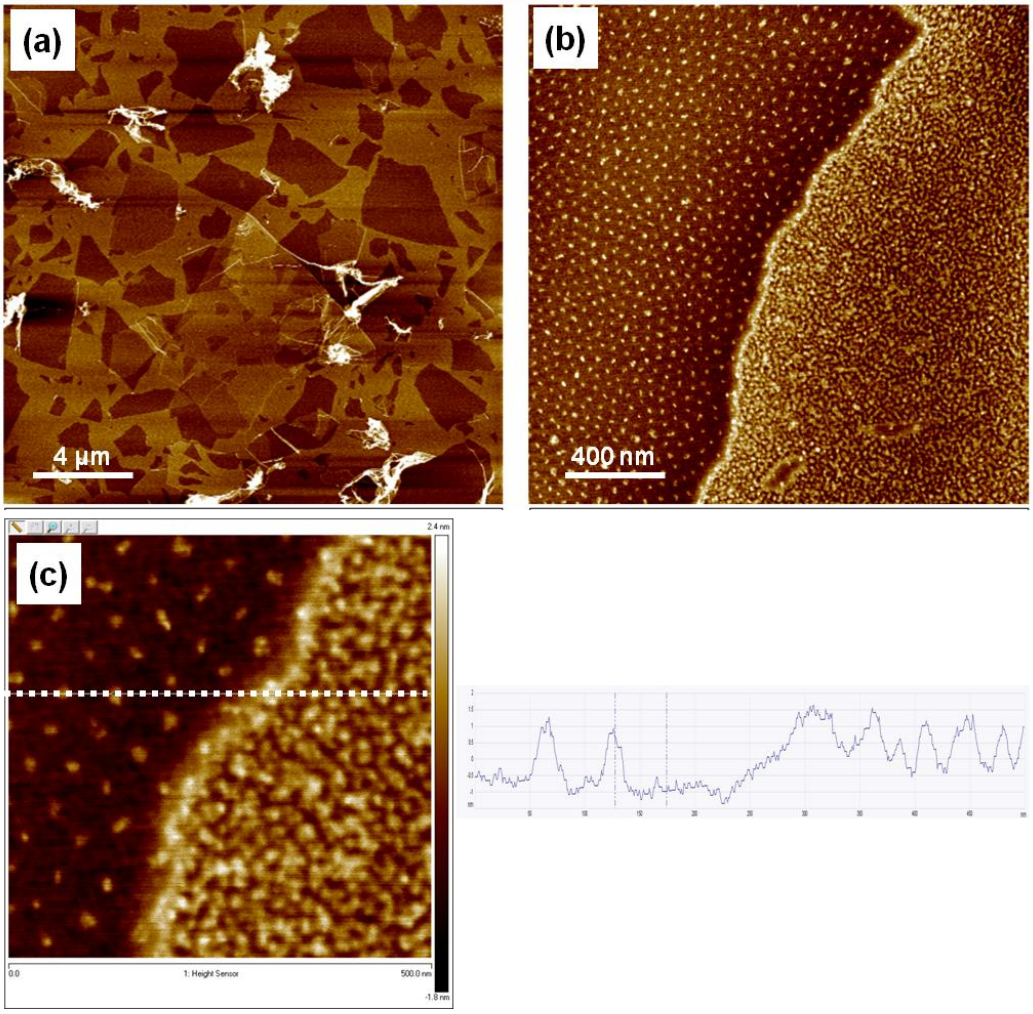

Figure S9.2: High resolution AFM topography of GO (0.01 wt %, 0.5 ml)/$PS_{28}P2VP_{28}$ star copolymer (0.1 mg/ml in chloroform, 70 µL) at pH 2 for surface pressures of 15 mN/m: (a) low magnification (20 × 20 µm), (b) high magnification (2 × 2 µm), and (c) height profile analysis of high solution image (500 × 500 nm). z-scale: 10 nm for (a), 4 nm for (b), and 4.2 nm for (c).

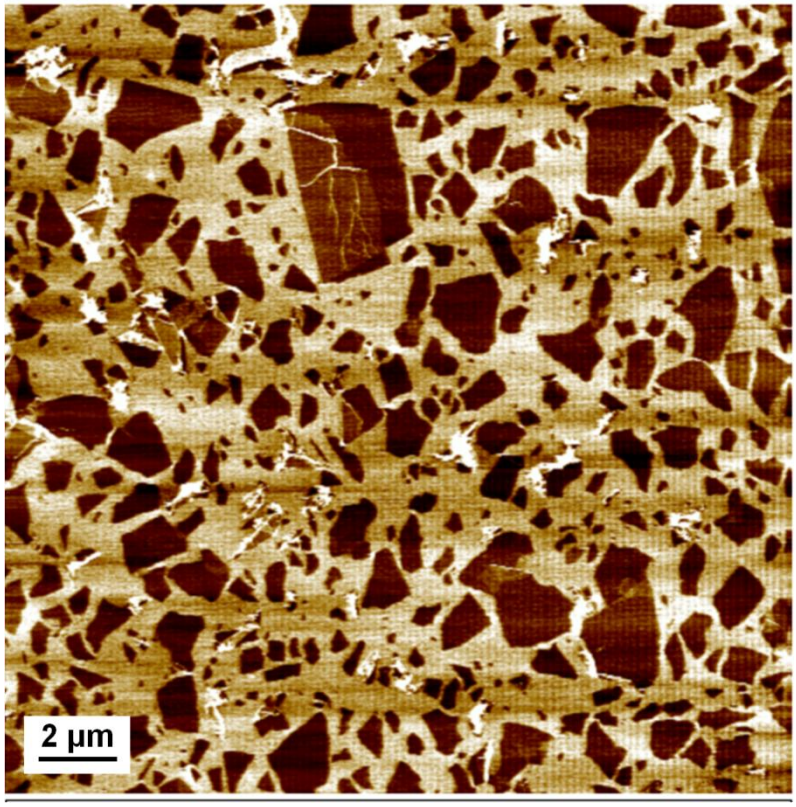

Figure S9.3: Low magnification AFM topography of GO (0.01 wt %, 0.5 ml)/$PS_{28}P2VP_{28}$ star copolymer (0.1 mg/ml, 70 µL) at pH 6 for surface pressure of 30 mN/m. z-scale: 6.5 nm

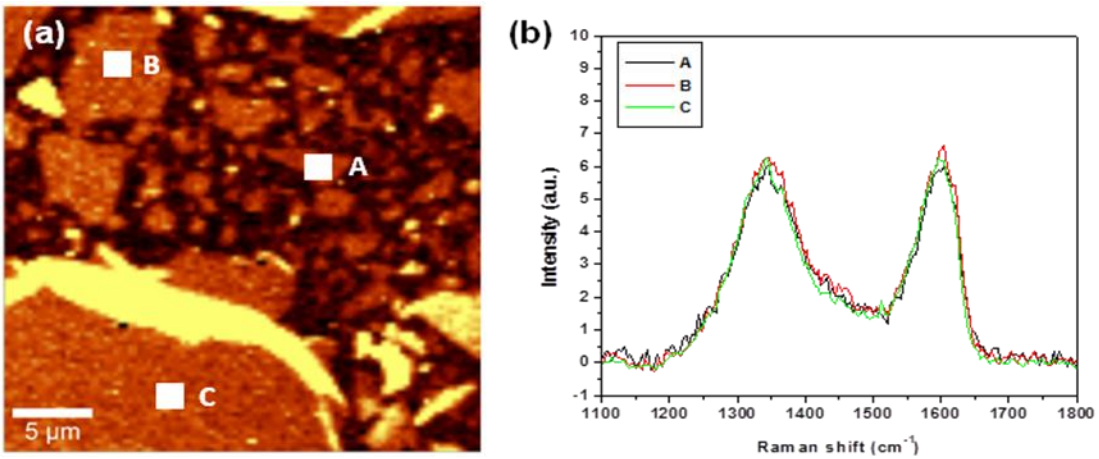

Figure S9.4: Raman mapping (a) and spectra of G and D bands of GO (0.01 wt %, 0.5 ml)/$PS_{28}P2VP_{28}$ star copolymer (0.1 mg/ml, 70 µL) at pH 6 for surface pressure of 30 mN/m.

CHPATER 10

GENERAL CONCLUSIONS AND BROADER IMPACT

10.1. Summary of Major Results

In this work, we have addressed the central issues related to the surface and interfacial behavior of novel highly-branched macromolecules. Primarily, we focused on their chain structures and phase transformations in nanoscale ultrathin films assembled from stimuli-sensitive star-shaped polymers: star amphiphilic block copolymers (s-BCP) and star polyelectrolytes (s-PE). The star macromolecules considered includes pH-sensitive amphiphilic heteroarm star copolymers, star block terpolymers with hydrophobic end blocks, star polyampholytes possessing zwitteric diblock arms, and pH and salinity responsive weak polycationic and polyanionic polyelectrolytes (Scheme 10.1). These star architectures have ability to transforme into complex nanostructures such as well-defined ultrasoft nanoparticles, nanogels, quasi two-dimensional circular micelles, core/shell type single molecular micelles, pankcake & brush micelles, or Janus-like molecular particles by responding to external environments (pH, salinity, solvent polarity, surface pressure, and concentration) through molecular deformations and phase segregations. These ultrasoft colloidal branched polymeric molecules with weak but multivalent interactions can be directly assembled into a variety of supramolecular ultrathin nanofilms with lateral uniformity or heterogeneous morphology, as well as fractal nanoporous multicompartmental shells.

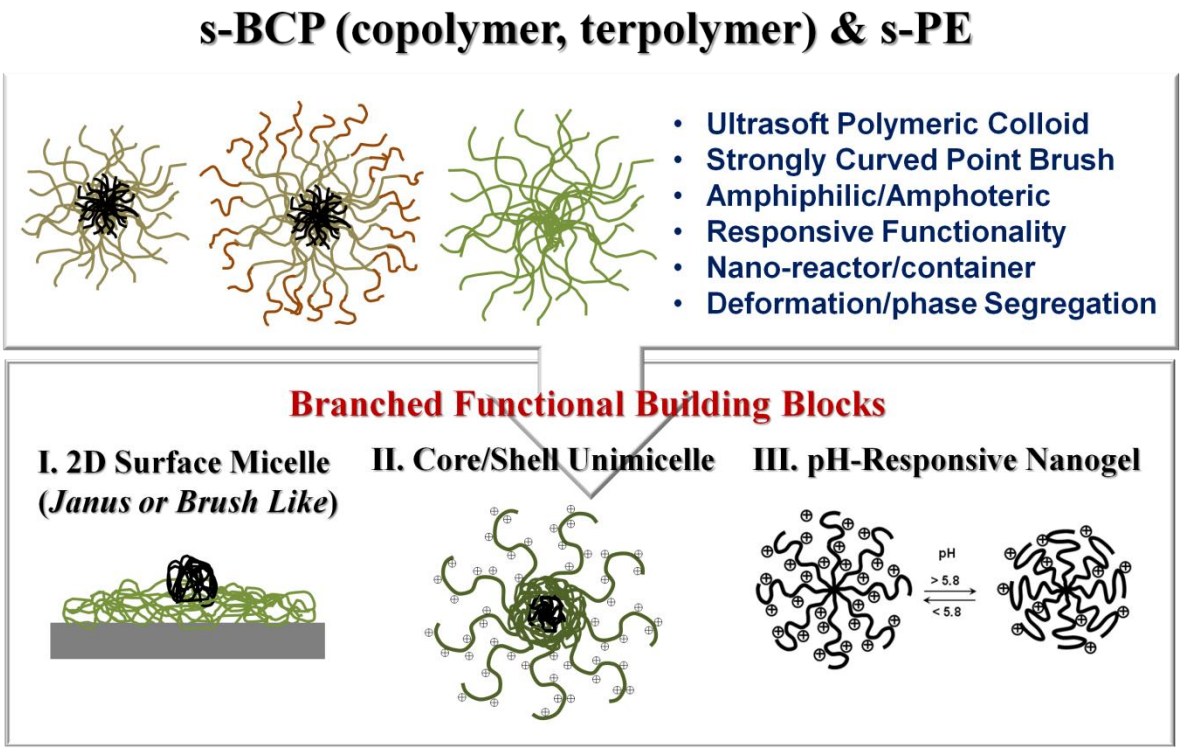

Scheme 10.1: Various types of novel branched functional building blocks based on star-shaped polymers (s-BCP & s-PE) for supramolecular ultrathin nanofilm assemblies studied here.

Fundamental questions were addressed here regarding how molecular architecture and chemical composition influences directed assembly behavior with emphasis on the role of surface and molecular confinement. We explored aggregation behavior, morphological properties, and microstucture in the monomolecular and multilayer ultrathin films prepared from star-like branched architectures using LB and LbL techniques in conjunction with comprehensive surface characterization methods. The responsive surface assembly behavior was elaborated from the viewpoint of adsorption,

intra/interchain diffusion, and conformation change of complex multi-arm architectures as a function of topology, number of arms, arm length, and nature of interactions.

The limited interdiffusion and entanglement, compact structure, and stronger stretched arms and repulsive interactions of non-linear highly-branched molecular architecture remain a challenge for controllable organized ultrathin film assembly, as compared to traditional linear polymers, especially, in the case of interfacially confined conditions. To circumvent this intrinsic molecular characteristic of highly branched architectures, it is crucial to consider chain architectures, interactions, and phase transformations. These surface-mediated star polymer assemblies and interfaces can offer a powerful design platform to craft a tunable surface and interface for precisely engineered functional polymer ultrathin films. The detail summary on the work concerning important technical developments and findings in this study are presented below.

Firstly, we studied the surface behavior and morphologies of two series of novel pH-responsive amphiphilic heteroarm star polymers, which differ in architecture, block topology, arm lengths, and number of arms. The π-A isotherms of Langmuir monolayers at different subphase pH exhibited strong pH-dependence leading to the different limiting molecular area and surface micelle stability. Due to the pH-sensitive ionization of P2VP block, the morphology of star copolymers bearing the free P2VP arms was strongly dependent on the pH of the subphase, while the star terpolymer containing the protonated hydrophilic P2VP block as midblocks and terminal hydrophobic P*t*BA blocks,

maintained nearly constant organization at low pH. The surface morphology studies suggested that star copolymers without end blocks can form circular micelles with larger sizes, which can be readily transformed to labyrinth morphologies with dense interpenetrating structures by compression and pH variation.

On the other hand, the presence of two oppositely ionizable polyelectrolytes blocks in the same diblock arms of complex amphoteric star-shaped terpolymers, namely PS_n(P2VP-PAA)$_n$ led to variety of inter/intra molecular interactions triggered by changing the pH of the subphase. The effect of pH on the assembly behavior was more distinct for the polymer with smaller arm density because of easy chain reorganization feasible in the polymer. In contrast, star copolymer with large number of arms exhibit a similar molecular area at the air-water interface and hence retained their circular micellar structure in the LB films at different subphase pH and surface pressures due to the restriction of chain reorganization in the polymer.

The surface morphology of the LB films fabricated at different pH and surface pressures indicate the microphase separation of amphoteric star terpolymers due to inter/intra molecular interactions facilitated by the presence of amphoteric nature of the polymer chains. The extent and nature of ionization of the oppositely charged blocks make it possible to tune the molecular conformation and hence the morphology in the thin films. This novel strategy to design functional surfaces with diverse morphology composed of their hydorphobic and dual pH responsive domains can allow for the creation of

multiresponsive and multicompartement nanostructures and for the immobilization of proteins with different isoelectric points.

Secondly, we demonstrated *in situ* synthesis of individual gold nanoparticles on monolayers of PS_nP2VP_n star copolymers at the liquid-solid interface. In this approach, electrostatic interactions were utilized to incorporate $AuCl_4^-$ into the protonated P2VP chains, which form continuous film underneath PS aggregate to interact with hydrophilic substrate. We found indeed that LB monolayer comprised of star copolymer surface micelles can act as a template for nanoparticle growth in one-sided P2VP microphase. The gold nanoparticle (average size of 6 ± 1 nm) growth can be controlled by surface pressure, $HAuCl_4$ concentration, domain morphology, and the number of P2VP arms.

Thirdly, the unique multilayer assembly behavior of pH-sensitive star-shaped polyelectrolytes with both linear and exponential growth modes controlled by star architecture and assembly conditions was discovered and explored as a function of deposition pH, number of layers, and the method of assembly. For dip-assisted LbL assembly, the pH-dependent exponential growth was observed for both linear and star polyelectrolytes. In the case of linear/linear components, the exponential buildup was accompanied with a notable surface segregation which resulted in dramatic surface non-uniformity, "worm-like" heterogeneous morphology, and dramatic surface roughening.

In contrast, star/linear and star/star LbL films showed very uniform and smooth surface morphology with much larger thickness reaching up to 1.0 μm for 30 bilayers and rich

optical interference effects. We suggest that star polyelectrolytes with compact shape, partially screened charges and high diffusion mobility facilitate fast complexation and lead to exponential buildup of the LbL films. This fast buildup is likely to hinder efficient lateral diffusion of components and thus prevents large-scale microphase separation, which results in smooth, locally uniform, thick, and optically transparent LbL films with rich interference properties, a unique combination for exponentially grown LbL films from traditional linear polyelectrolytes.

Fourthly, the star copolymer unimolecular micelles can be successfully utilized to form unique multicompartamental LbL microcapsules with shells of coexisted network-like morphology of hydrophobic domains, hydrophilic polyelectrolyte matrix, and nanoscale water-filled pores. Such unique morphology of extra thin-shell microcapsules might facilitate the ability for concurrent storage of hydrophobic, hydrophilic, and charged species in different compartments of shells based upon highly branched block-copolymer macromolecules. The buildup of such microcapsules is controlled by star copolymer architecture with the enhanced hydrophobic characteristics and is efficient for star copolymers with a larger number of arms. We suggest that highly branched star copolymers maintain a core/shell unimolecular micelle within the shell with a granular morphology while effectively contributing to the buildup of stable multilayer shells with a complex network-like morphology. The polyvalent strong electrostatic interaction of core/corona multiarm architecture enables spherical star micelles to be incorporated into microcapsules with the ability to control shell morphology and the porous network structure.

Finally, the formation of peculiar biphasic morphology of star copolymers combined with graphene oxide sheets in Langmuir monolayers was caused by spreading, and ordering of star polymer surface micelles on the basal plane and edge of in-plane amphiphilic monolayer graphene oxide. It was demonstrated that surface activity of solvated graphene oxide sheets makes it possible for star polymer surfactants to adsorb on the pre-suspended graphene oxide surface. As a result, this interface-mediated assembly led to micelle-decorated graphene oxide bilayer complexes with uniform spacing and organized morphology due to the strong affinity between star polymers and graphene oxide. Electrostatic, hydrogen bonding, and π-π interactions between partially protonated heterocyclic pyridine units and negatively charged polar graphene oxide surface facilitate their assembly.

Importantly, we found that the surface coverage of star polymer unimicelles on the graphene oxide sheets was not affected by external assembly conditions after evaporative deposition in contrast to pressure-sensitive air-water interface. Incompressible monolayer of surface micelles on graphene oxide sheet is due to intra/intermolecular electrostatic repulsion between positively charged pyridine groups as well as entropic barrier of highly branched arms. The conformational transformations are hindered by the non-diffusive and attractive graphene oxide surface in contrast to water surface. Vertically segregated polymer arm chain conformation across the air-water interface prevents the star polymers from sliding over the functionalized edge onto the surface of amphiphilic graphene oxide. Remarkable ability of graphene oxide to sustain high lateral

surface pressure without sinking or folding is attributed to the intrinsic stiffness as well as conformal surface tension upwardly applied on the continuous single sheets. The surface-assisted assembly strategy can facilitate large scale film fabrication with peculiar biphasic "tile-like" morphology.

10.2. Critical Findings and Conclusions

The work in this dissertation elucidates the surface related-conformational transformations and responsive assembly behavior of star polymers. This non-covalent surface assembly can offer a facile approach to fabrication of ultrathin functional films for potential applications in heterogeneous catalysis and as highly sensitive sensing materials. This study also offers a practical view on fabricating novel polymer nanostructures, such as star unimolecular monolayers, gold-star polymer ultrathin hybrid films, graphene oxide-star polymer biphasic composite nanofilms, pH-mediated exponentially grown stratified multilayers, and nanoporous multidomain multilayered microcapsules, as summarized (Scheme 10.2 and 10.3). This approach presents a promising strategy to fabricate a variety of responsive organized ultrathin polymer film and coating materials. This nanoscale "bottom-up" processing of polymers in combination with wet fabrication methods (LB and LbL methods) and self-assembly at the surface enables ultrasoft polymeric colloids to assemble into supramolecular thin films in a controlled way on the monomolecular level.

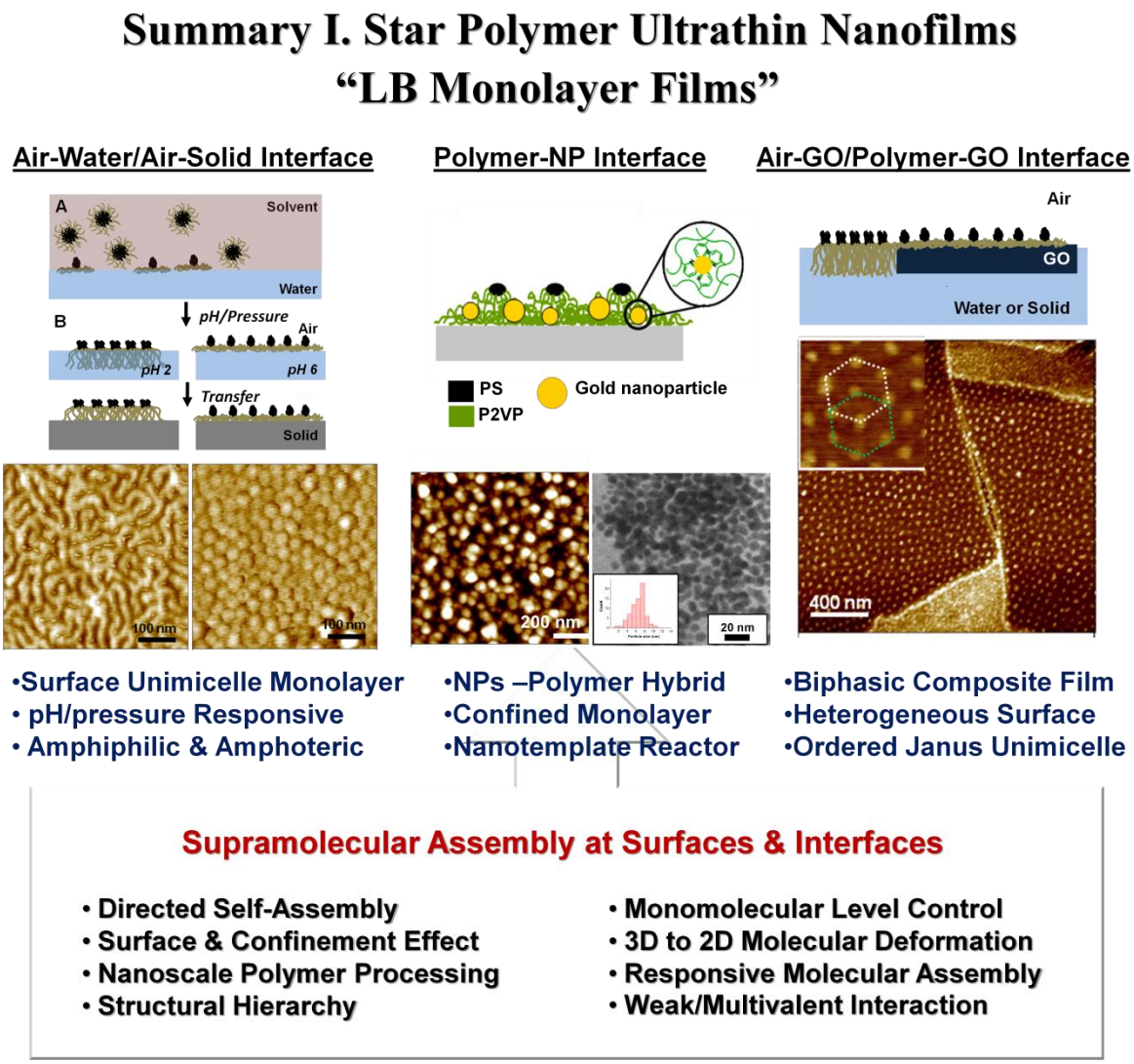

Scheme 10.2: Summary I of the controlled interfacial assembly of highly-branched star-shaped polymers into organized LB monolayer films through a directed assembly at various surfaces and interfaces.

The most novel and significant advancements from material science and surface engineering perspectives on fabrication, characterization, and applications of ultrathin film polymer materials can be highlighted (Scheme 10.2 and 10.3).

Here, we demonstrated that a directed supramolecular self-assembly strategy in conjunction with stimuli-sensitive molecular design can be a powerful approach for fabrication of organized ultrathin nanofilms based on well-defined functional branched star architectures. For instance, amphiphilic heteroarm star block copolymers and terpolymers containing ionizable blocks were assembled into densely pack ordered monolayers of surface unimicelles with controllable circular or lybrinth nanodomain structures through pH/pressure responsive molecular switching in chain conformation and phase transformation (Scheme 10.2). The incorporation of amphoteric arms into amphiphilic star terpolymers offers a richer phase behavior and more complex morphology at an extened range of pH region through complex inter/intra arm interactions compared to a single component charged arms.

Star polymers with higher arm number tend to retain larger and discrete spherical micelle structures and stable unimicelle morphology indicating stronger stretched arms due to their increased intramolecular repulsions and limited interpenetration compared to their counterparts with lower arm number. Larger number of arms retains three-dimensional conformations by more effectively resisting the surface confinemet. Also, these star polymer unimicelle can provide increased interstitial binding sites for precurors used in nanoparticle synthesis.

Moreover, the preferred adsorption and binding behavior of amphiphilic star copolymers on a chemically heterogeneous graphene oxide surface at the air-water interface led to peculiar biphasic graphene-polymer hybrid films with ordered micelle spacing and

morphology (Scheme 10.2). The solvent mediated Janus-like vertical phase segregation of heteroarm star polymers resulted in controlled intermolecular interaction with graphene oxide sheets and determined the surface ordering and coverage in bilayered hybrid films. Assembly of the incompressible micelles on the in-plane amphiphilic graphene oxide surfaces with limited crossing from water surface to graphene oxide sheets provided a profound understanding of the geometric and dimensional nature of surface active graphene oxide flakes at the air-water interface.

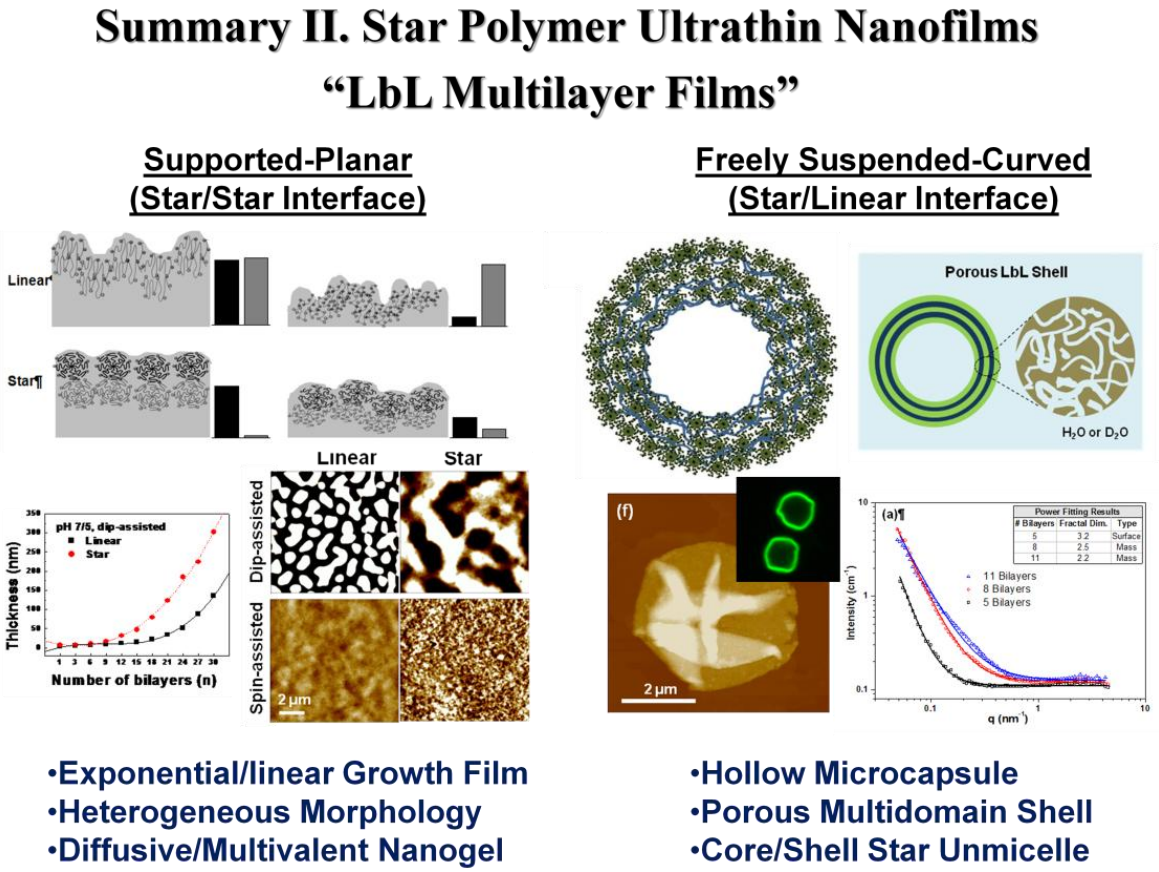

Scheme 10.3: Summary II of the controlled interfacial assembly of highly-branched star-shaped polymers into organized LbL multilayer films through a directed assembly at various surfaces and interfaces.

On the other hand, we proposed a facile approach to assemble the hierarchical multilayer structure based on pH-controlled self-diffusion of oppositely charged weak star polyelectrolyte components (Scheme 10.3). In particular, we found that exponentially grown films rendered stable stratified multilayer and heterogeneous surface morphology. This is a first report on the tunable switching between exponential and linear growth mode in multilayer assemblies that elucidated molecular architecture dependent adsorption and diffusion of colloid-like star polyelectrolyte nanogel. Weak yet polyvalent interactions of star polyelectrolytes can be controlled by external ionic strength and degree of ionization during the consective LbL deposition, as a result, yielding unique and unreported multicompartmental nanostructures with different extent of intermixing and complexation.

A multicompartmental multilayer capsules from core/shell type unimolecular micelles on curved template substrates showed mass fractal transition in the multilayer shells with a clear evidence of evolution of three-dimensional interconnected network pore structure transitioned from two-dimensional large pores (Scheme 10.3). Multilayered shell composed of large arm star polymers showed smaller effective pore dimension in contrast to lower arm counterpart because of more efficient stretched conformations due to multivalent interactions and enhanced colloidal stability to prevent large scale rearrangement and reorganization during template core removal and repeating deposition cycles.

10.3. Significance and Broader Impact

The results presented in this study provide a fundamental insight and practical strategy for the fabrication and characterization of advanced supramolecular polymer thin films in diverse environments and interfacially confined conditions. Adopting highly-branched polymeric materials as emerging building blocks offers a new approach for fabrication of adaptive and stimuli-responsive functional coatings and films due to their intriguing molecular architectures and properties. The directed assembly method of stimuli-sensitive highly-branched molecules at the interface enables the ability to achieve tunable surface and interfacial organization.

Star-shaped polymeric molecules can provide a wide range of choices in the construction of flexible yet stable ultrathin nanostrucutres in diverse forms of new assembly components, namely environmentally sensitive quasi-two-dimensional surface micelles (i.e., pancake or brush-like conformation), pH and salinity responsive ultrasoft ionic nanoparticles or nanogels, core/shell type compartment unimolecular micelles, and "Janus-like" biphasic amphiphiles.

The advantage of novel supramolecular polymers is to control multivalent interaction at different length and time scales and thereby provide richer phase states and more complex morphology behavior, as well as high level of mobility in design of programmable responsive polymer devices. Furthermore, star polymers at the surface can rearrange into two dimensional conformations with strong peripherially stretched or compressed arms under geometrically confined conditions and the degree of adsorption

determine the final molecular structure. This surface confinement effect leads to enhanced surface ordering due to strong repulsion and can control brush-like structure by varying surface interactions between the star polymer and the substrate.

We suggest that the fundamental viewpoint of surface related rearrangements and interactions of soft hybrid nanoscale building blocks based on star-shaped polymeric molecules will ultimately be translated to inspire an advanced design concept for miniaturized polymeric thin film devices. Also a single molecular level surface manipulation will allow for a high performance soft functional bio-interfaces with fast and reliable signal transduction in actuators. The combination of a "bottom-up" assembly approach with sophisticated wet fabrication technology and surface engineering will ensure enhanced accuracy and specificity on a nanometer length scale for the controlled organization of functional ultrathin polymer films and coatings.

Furthermore, diverse and active attempts in synthesis and material sciences is urged to tailor the design of advanced star architectures, such as arm structures and compositions and controlled interactions between polymers and various surfaces and interfaces. This synthetic strategy could contribute to current important problems, such as an uncontrolled release of the payload in drug containers, bio-compatible and bio-degradable monomeric components, and incorporation of functional and environmental signal sensing moieties, for example, conductive conjugated or high dielectric arms for multifunctional polymeric materials.

As a next step, design of more sensitive and selectively responsive polymer ultrathin films can be envisioned. To realize richer phase behavior and diverse responsive dynamics, anisotropic arm structures and multiresponsive novel star architectures might be addressed by breaking molecular symmetry, for example, by adopting multicompartmental Janus-like star polymers or patchy star polymers as novel building components. Also, the multivalent binding and interstitial space of star structures can be considered to be a platform for single molecular inorganic-organic functional hybrid nanocomposites by association with functionalized nanoparticles by chemically grafting conjugated fluorescent dyes to the multiple free chain ends for imaging and optical sensing materials. The creation of star core/shell type star unimicelles with biocompatible and biodegradable monomer units coupled with a facile crosslinking system will be pushed as a top priority for controlled encapsulation and release of *in vivo* drug carriers.

These efforts present a versatile paradigm for a synthetic and assembly platform of the rationally designed stimuli-responsive functional hierarchical polymer ultrathin nanomaterials for prospective applications in biosensing, self-healing coatings, drug delivery, tunable catalysis, and imaging. More specifically, these assemblies can find a wide range of use in manipulating surface adhesion, friction, and wetting properties of bio-surfaces and interfaces, stratified layered nanocomposites, multicompartmental functional carriers or films for controlled release and encapsulation, nanomembranes with

tunable permeability and pore structure, and synthetic templates of nanoparticles or scaffolds for catalysis and biomolecules.

DISSEMINATION OF WORK

The work presented in this dissertation has been summarized in the following publications:

1. **I. Choi,** D. D. Kulkarni, W. Xu, C. Tsitsilianis, V. V. Tsukruk, Star Polymer Unimicelles on Graphene Oxide, *Langmuir* **2013**, *29*, 9761-9769.

2. **I. Choi,** S. Malak, W. Xu, W. T. Heller, C. Tsitsilianis, V. V. Tsukruk, Multicompartmental Microcapsules from Star Copolymer Micelles, *Macromolecules* **2013**, *46*, 1425-1436.

3. R. Kodiyath, **I. Choi,** B. Patternson, C. Tsitsilianis, V. V. Tsukruk, Interfacial Behavior of pH Responsive Ampholytic Heteroarm Star Block Terpolymers, *Polymer* **2013**, 54, 115-1159.

4. W. Xu, **I. Choi**, F. A. Plamper, C. V. Synatschke, A. H. E. Müller, V. V. Tsukruk, Nondestructive Light-Initiated Tuning of Microcapsule Permeability, *ACS Nano* **2012**, 7, 598-613.

5. **I. Choi**, R. Suntivich, F. A. Plamper, C. V. Synatschke, A. H. Müller, V. V. Tsukruk, pH-Controlled Exponential and Linear Growing Modes of LbL Assemblies of Star Polyelectrolytes, *J. Am. Chem. Soc.* **2011**, *133*, 9592-9606.

6. R. Suntivich, **I. Choi**, M. K. Gupta, C. Tsitsilianis; V. V. Tsukruk, Gold Nanoparticles Grown on Star-Shaped Block Copolymer Monolayers, *Langmuir*, **2011**, *27*, 10730-10738.

7. D. Kulkarni, **I. Choi**, S. Singamaneni, V. V. Tsukruk, Large and Nano-scale Free-Standing Graphene oxide-Polyelectrolyte Membranes, *ACS Nano* **2010**, *4*, 4667-4676.

8. **I. Choi**, R.; Gunawidjaja, R. Suntivich, C. Tsitsilianis, V. V. Tsukruk, Surface Behavior of PS_n(P2VP-*b*-P*t*BA)$_n$ Heteroarm Stars, *Macromolecules* **2010**, *43*, 6818-6828.

The following publications are related to the work in this dissertation:

9. V. V. Shevchenko; A. V. Dorokhin; **I. Choi**; N. S. Klimenko; V. V. Tsukruk, Synthesis of Amphiphilic Systems of Polyhedral Oligomeric Silsesquioxanes with Phenolic Azo Dye Disperse Yellow, *Proceedings of the National Academy of Sciences of Ukraine* **2013**, submitted.

10. R. Suntivich, O. Shchepelina, **I. Choi,** V. V. Tsukruk, Inkjet-Assisted Layer-by-Layer Printing of Encapsulated Arrays, *ACS Applied Materials & Interface* **2012**, *4*, 3102-3110.

11. S. T. Krishnaji, W. Huang, O. Rabotyagova, E. Kharlampieva, **I. Choi**, V. V. Tsukruk, R. Naik, P. Cebe, D. L. Kaplan, Thin Film Assembly of Spider Silk-like Block Copolymers *Langmuir* **2011**, *27*, 1000-1008.

12. R. Gunawidjaja, E. Kharlampieva, **I. Choi**, V. V. Tsukruk, Bimetallic Nanostructures as Active Raman Markers, Gold-Nanoparticle Assembly on 1D and 2D Silver Nanostructure Surfaces, *Small* **2009**, *5*, 2460-2466.

Conference presentations on dissertation topic:

1. **I. Choi,** S. Malak, W. Xu, W. T. Heller, C. Tsitsilianis, V. V. Tsukruk, Multicompartmental Microcapsules from Star Copolymer Micelles, *ACS National Meeting in Indianapolis, Indiana* (2013), submitted.

2. W. Xu, **I. Choi**, F. A. Plamper, C. V. Synatschke, A. H. E. Müller, V. V. Tsukruk, Nondestructive Light-Initiated Tuning of Microcapsule Permeability, *AkzoNobel Student Award in Applied Polymer Science, ACS National Meeting in Indianapolis, Indiana* (2013), submitted.

3. W. Xu, **I. Choi**, F. A. Plamper, C. V. Synatschke, A. H. E. Müller, V. V. Tsukruk, Nondestructive Light-Initiated Tuning of Microcapsule Permeability, 2013 MSE POSTER SESSION, April 12, 2013.

4. W. Xu, **I. Choi**, F. A. Plamper, C. V. Synatschke, A. H. E. Müller, V. V. Tsukruk, Nondestructive Light-Initiated Tuning of Microcapsule Permeability, GEORGIA TECH RESEARCH & INNOVATION CONFERENCE, February 12, 2013.

5. **Choi, I.**; Suntivich, R.; Plamper, F. A.; Synatschke, C. V. Müller, A.H.E.; Tsukruk. V. V. pH-Controlled Exponential and Linear Growing Modes of Layer-by-Layer

Assemblies of Star Polyelectrolytes, *The Materials Research Society (MRS) National Meeting*, Boston, MA, USA, November 28-December 1, (2011).

6. **Choi, I.**; Gunawidjaja, R.; Suntivich, R.; Tsitsilianis, C.; Tsukruk. V. V. Surface Behavior of $PS_n(P2VP\text{-}b\text{-}PtBA)_n$ Heteroarm Stars, *The Materials Research Society (MRS) National Meeting*, Boston, MA, USA, November 28-December 1, (2011).

7. Suntivich, R.; **Choi, I.**; Gupta, M. K.; Synatschke, Tsitsilianis, C.; Tsukruk. V. V. Gold Nanoparticles Grown on Star-Shaped Block Copolymer Monolayers, *The Materials Research Society (MRS) National Meeting*, Boston, MA, USA, November 28-December 1, (2011).

8. Suntivich, R.; Shchepelina, O.; **Choi, I.**; Tsukruk, V. V. Inkjet-Assisted Layer-by-Layer Printing of Encapsulated Arrays, *The Materials Research Society (MRS) National Meeting*, Boston, MA, USA, November 28-December 1, (2011).

9. **Choi, I.**; Gunawidjaja, R.; Tsitsilianis, C.; Tsukruk, V. V. Assembly Behavior of pH-responsive Heteroarm Star Block Terpolymers, *The Materials Research Society (MRS) National Meeting*, San Fransico, CA, USA, April 5-9, (2010).

10. Gunawidjaja, R.; Kharlampieva, E.; **Choi, I.**; Tsukruk, V. V. Assembly of Bimetallic Plasmonic Nanostructures as Active Raman Markers, *The Materials Research Society (MRS) National Meeting*, San Fransico, CA, USA, April 5-9, (2010).

REFERENCES

[1] Granik, S.; Kumar, S. K.; Amis, E. J.; Antonietti, M.; Balazs, A. C.; Chakraborty, A. K.; Grest, G. S.; Hawker, C.; Janmey, P.; Kramer, E. J.; Nuzzo, R.; Russell, T. P.; Safinya, C. R. *J. Polym. Sci. Part B. Polym. Phys.* **2003**, *41*, 2755.

[2] Jones, R.; Kumar, S. K.; Ho. K. L.; Briber, R. M.; Russell, T. P. *Nature* **1999**, *400*, 146.

[3] Soles, C. L.; Ding, Y. *Science* **2008**, *322*, 689.

[4] Tsukruk, V. V. *Prog. Polym. Sci.* **1997,** *22*, 247.

[5] Forster, S.; Konrad, M. *J. Mater. Chem*. **2003,** *13*, 2671.

[6] Hadjichristidis, N.; Pitsikali, M.; Pispas, S.; Iatrou, H. *Chem. Rev.* **2001**, *101*, 3747-92.

[7] Hadjichristidis, N.; Iatrou H.; Pitsikalis M.; Sakellariou G. *Chem. Rev*. **2009**, *109*, 5528-78.

[8] Matyjaszewski, K. *Prog. Polym. Sci.* **2005**, *30*, 858-75.

[9] Matyjaszewski, K.; Spanswick, J. *Materials Today.* **2005**, *8*, 26-33.

[10] Luzinov, I.; Minko, S.; Tsukruk, V. V. *Prog. Polym. Sci.* **2004**, *29*, 635.

[11] Magerle, R.; Krausch, G. *Adv. Mater*. **2002,** *14*, 1579.

[12] Jacob. N.; Israelachvli, D.;Michell, J.; Ninham, B. W. *J. Chem. Soc., Faraday Trans. 2***, 1976**, *72*, 1525.

[13] Fasolka, M. J.; Mayes, A. M. *Annu. Rev. Mater. Res*. **2001**, *31*, 323.

[14] Riess, G. *Prog. Polym. Sci*. **2003**, *28*, 1107.

[15] Forster, S.; Zisenis, M.; Wenz, E.; Antonietti, M. *J. Chem. Phys*. **1996**, *104*, 9956.

[16] Pelelshanko, S.; Tsukruk, V. V. *Prog. Polym. Sci.* **2008,** *33*, 523.

[17] Kataoka, K.; Harada, A.; Nagasaki, Y. *Adv Drug Deliv Rev* **2001**, *47*, 113-131.

[18] Adams, M. L.; Lavasanifar, A.; Kwon, G. S.; *J. Pharm. Sci.* **2003**, *92*,1343-1355.

[19] Kakizawa, Y.; Kataoka, K. *Adv Drug Deliv Rev* **2002**, *54*, 203-22

[20] Percec, V.; Ahn, C. –H.; Ungar, G.; Yeardley, D. J. P; Möller, M.; Sheiko, S. S. *Nature* **1998**, *391*, 161-64.

[21] Sheiko, S. S.; Möller, M. in Topics in Polymer Chemistry. Dendrimers III. 2001, 212, 137F. Vögtle, (Ed.) Springer-Verlag, Heidelberg.

[22] Peleshanko, S.; Tsukruk, V. V. *J. Polym. Sci.: Polymer Phys.*, **2012**, *50*, 83-100

[23] Van der Poll, D. G.; Kieler-Ferguson, H. M.; Floyd, W. C.; Guillaudeu, S. J.; Jerger, K.; Szoka, F. C.; Fréchet, J. M. J. *Bioconjug. Chem.* **2010***; 21,* 764-73.

[24] Tully, D. C.; Fréchet, J. M. J. *Chem. Commun*. **2001**, 1229-1239.

[25] Tsukruk, V. V. Rinderspacher, F.; Bliznyuk, V. N. *Langmuir* **1997**, *13*, 2171-2176.

[26] Sidorenko, A.; Zhai, X. W.; Peleshanko, S.; Greco, A.; Shevchenko, V. V.; Tsukruk, V. V. *Langmuir* **2001**,*17*, 5924-5931.

[27] Shulha, H.; Zhai, X.; Tsukruk. V. V. *Macromolecules* **2003**, *36*, 2825-2831.

[28] Stuart, M. A. C.; Huck, W. T. S.; G. J.; Müller, M.; Ober, C.; Stamm, M.; Sukhoruko, G. B.; Szleifer, I.; Tsukruk, V. V.; Urban, M.; Winnik, F.; Zauscher, S.; Luzinov, I.; Minko, S. *Nature Mater*. **2010**, *9*, 101.

[29] Khanna, K.; Varshney, S.; Kakkar, A. *Polym. Chem.* **2010**, *1*, 1171-1185.

[30] Iatridi, Z.; Tsitsilianis, C. *Polymers* **2011**, 3, 1911-1933.

[31] Jacob, S.; Majoros, I.; Kennedy, J. P. *Macromolecules* **1996**, *29*, 8631-8641.

[32] Ornatska, M.; Peleshanko, S.; Genson, K. L.; Rybak, B.; Bergman, K. N.; Tsukruk, V. V. *J. Am. Chem. Soc.* **2004**, *126*, 9675-9684.

[33] Choi, I.; Suntivich, R.; Plamper, F. A.; Synatschke, C. V.; Müller, A. H. E.; Tsukruk, V. V. *J. Am. Chem. Soc.* **2011,** *133*, 9592-9606.

[34] Ornatska, M.; Bergman, K. N.; Rybak, B.; Peleshanko, S.; Tsukruk, V. V. *Angew. Chem. Int. Ed*. **2004**, *43*, 5246-5249.

[35] Ornatska, M.; Peleshanko, S.; Rybak, B.; Holzmueller, J.; Tsukruk, V. V. *Adv. Mater.* **2004,** *16*, 2206-2212.

[36] Tsukruk, V. V. *Adv. Mater*. **1998**, *10*, 253.

[37] Plamper, F.; Becker, H.; Lanzendorfer, M.; Patel, M.; Wittemann, A.; Ballauff, M.; Müller, A. H. E. *Macromol. Chem. Phys*. **2005**, *206*, 1813.

[38] Jiang, C.; Markutsya, S.; Pikus, Yu.; Tsukruk, V. V. *Nature Mater.* **2004,** *3*, 721.

[39] Jiang, C.; Tsukruk, V. V., *Adv. Mater*. **2006**, *18*, 829.

[40] Lavalle, P.; Voegel, J.-C.; Vautier, D.; Senger, B.; Schaaf, P.; Ball, V. *Adv. Mater.* **2011**, *23*, 1191.

[41] Mamedov, A. A.; Kotov, N. A. *Langmuir* **2000**, *16*, 5530.

[42] Chen, K. M.; Jiang, X.; Kimerling, L. C.; Hammond, P. T. *Langmuir*, **2000**, *16*, 7825.

[43] Caruso, F.; Susha, A. S.; Giersig, M.; Mohwald, H. *Adv. Mater*. **1999**, *11*, 950.

[44] Jaber, J. A.; Schlenoff, J. B. *Curr. Opin. Colloid. Interface Sci*. **2006**, *11*, 324.

[45] Peleshanko, S.; Tsukruk, V. V. *Prog. Polym. Sci.* **2008**, *33*, 523.

[46] Lin, Z.; Zhao, L. *Soft Matter* **2011**, *7*, 10520.

[47] Gao, H. *Macromol. Rapid Commun.* **2012**, *33*, 722

[48] Likos, C.N.; Löwen, H.; Watzlawek, M.; Abbas, B.; Jucknishke, O.; Allgaier, J.; Richter, D. *Phys. Rev. Lett.* **1998**, *20*, 4450.

[49] Jusufi, A.; Likos, C.N.; Löwen, H. *Phys. Rev. Lett.* **2002**, *88*, 018301-1.

[50] Vlassopoulos, D. J. *Polym. Sci. Part B. Polym. Phys.* **2004**, *42*, 2931.

[51] Bobrynin, A. V.; Colby, R. H.; Rubinstein, M. *J. Polym. Sci.: Part B.: Polym. Phys.* **2004**, *42*, 3513.

[52] Dobrynin, A.; Rubinstein, M. *Prog. Polym. Sci*. **2005**, *30*, 1049.

[53] Shusharina, N. P.; Rubinstein, M. *Macromolecules* **2008**, *41*, 203.

[54] Polotsky, A. A.; Birshtein, T. M.; Daoud, M.; Borisov, O. V. *Macromolecules* **2011**, *44*, 8999.

[55] Rud, O. V.; Mercurieva, A. A.; Leermakers, F. A. M.; Birshtein, T. M. *Macromolecules* **2012** DOI 10.1021/ma202201m.

[56] Egorov, S. A.; Paturej, J.; Likos, C. N.; Milchev, A. *Macromolecules* **2013** DOI 10.1021/ma400188s.

[57] Albrecht, K.; Mourran, A.; Moeller, M. *Adv. Polym. Sci*. **2006**, *200*, 57.

[58] Epps, III, T. H.; Albert, J. N. L. *Material Today* **2010**, *13*, 24.

[59] Li, Z.; Marc, A.; Hillmyer, M. A.; Lodge, T. P. *Langmuir* **2006**, *22*, 9409.

[60] He, E.; Yue, C. Y.; Tam, K. C. *Langmuir* **2009**, *25*, 4892.

[61] He, E; Ravi, P.; Tam, K. C. *Langmuir* **2007**, *23*, 2382.

[62] Dong, W.; Zhou, Y.; Yan, D.; Mai, Y.; He, L.; Jin, C. *Langmuir* **2009**, *25*, 173.

[63] Connal, L. A.; Vestberg, R.; Hawker, C. J.; Qiao, G. G. *Adv. Funct. Mater.* **2008**, *18*, 3706.

[64] Kim, B. -S.; Gao, H.; Argun, A. A.; Matyjaszewski, K.; Hammond, P. T. *Macromolecules* **2009**, *42*, 368.

[65] Kiriy, A.; Gorodyska, G.; Minko, S.; Stamm, M.; Tsitsilianis, C. *Macromolecules* **2003**, *36*, 8704.

[66] Qin, S.; Matyjaszewski, K.; Xu, H.; Sheiko, S. S. *Macromolecules* **2003**, *36*, 605.

[67] Schappacher, M.; Deffieux, A. *Macromolecules* **2005**, *38*, 4942.

[68] Nunez, E.; Vancso, G. J.; Gedde, U. W. *J. Macromol. Sci. Part B: Phys.* **2008**, 47, 589.

[69] Stavrouli, N.; Triftaridou, A. I.; Patrickios, C. S.; Tsitsilianis, C. *Macromol. Rapid. Commun.* **2007**, 28, 560.

[70] Stavrouli, N.; Kyriazis, A.; Tsitsilianis, C. *Macromol. Chem. Phys*. **2008**, 209, 2241.

[71] Plamper, F. A.; Walther, A.; Muller, A. H. E.; Ballauff, M. *Nano Lett.* **2007**, *7*, 167.

[72] Walther, A.; Yuan, J.; Abetz, V.; Muller, A. H. E. *Nano Lett*. **2009**, *9*, 2026.

[73] Plamper, A. E.; Ruppel, M.; Schmalz, A.; Borisov, O.; Ballauff, M.; Muller, A. H. E. *J. Am. Chem. Soc.* **2007**, *40*, 14538.

[74] Hammond, M. R.; Li, C.; Tsitsilianis, C.; Mezzenga, R. *Soft Matter* **2009**, 5, 2371.

[75] Logan, J. L.; Masse, P.; Dorvel, B.; Skolnik, A. M.; Sheiko, S. S.; Francis, R.; Taton, D.; Gnanou, Y.; Duran, R. S. *Langmuir* **2005**, *21*, 3424.

[76] Francis, R.; Skolnik, A. M.; Carino, S. R.; Logan, J. L.; Underhill, R. S.; Angot, S.; Taton, D.; Gnanou, Y.; Duran, R. S. *Macromolecules* **2002**, *35*, 6483.

[77] Matmour, R.; Lepoittevin, B.; Joncheray, T. J.; El-khouri, R. J.; Taton, D.; Duran, R. S.; Gnanou, Y. *Macromolecules* **2005**, *38*, 5459.

[78] Matmour, R.; Francis, R.; Duran, R. S.; Gnanou, Y. *Macromolecules* **2005**, *38*, 7754.

[79] Joncheray, T. J.; Denoncourt, K. M.; Mathieu, C.; Meier, M. A. R. Schubert, U. S.; Duran, R. S. *Langmuir* **2006**, *22*, 9264.

[80] Lupitskyy, R.; Roiter, Y.; Tsitsilianis, C.; Minko, S. *Langmuir* **2005**, *21*, 8591.

[81] Kiriy, A.; Gorodyska, G.; Minko, S.; Tsitsilianis, C.; Jaeger, W.; Stamm, M. *J. Am. Chem. Soc.* **2003**, *125*, 11202.

[82] Chatterjee, J.; Jain, S.; Bates, F. S. *Macromolecules* **2007**, *40*, 2882.

[83] Elbs, H.; Drummer, C.; Abetz, V.; Krausch, G. *Macromolecules* **2002**, *35*, 5570.

[84] Thompson, R. B.; Ginzburg, V. V.; Matsen, M. W.; Balazs, A. C. *Science* **2001**, *292*, 2469.

[85] Bockstaller, M. R.; Lapetnikov, Y.; Margel, S.; Thomas, E. L. *J. Am. Chem. Soc.* **2003**, *125*, 5276.

[86] Acharya, S.; Hill, J. P.; Ariga, K. *Adv. Mater*. **2009**, *21*, 2959.

[87] Guo, Y.; Geng, W.; Sun, J. *Langmuir* **2009**, *25*, 1004.

[88] Morgan, S.; Jones, P.; Lamont, A. S.; Heidenreich, A.; McCormick, C. L. *Langmuir* **2007**, *23*, 230.

[89] Petty, M. C.; Langmuir-Blodgett Film: A Introduction; Cambridge University Press: New York, NY, 1996.

[90] Sheiko, S. S.; Prokhorova, S. A.; Beers, K. L.; Matyjaszewski, K.; Potemkin, I. I.; Khokhlov, A. R.; Möller, M. *Macromolecules* **2001**, *34*, 8345.

[91] Zhu, J.; Lennox, R. B.; Eisenberg, A. *Langmuir* **1991,** *7*, 1579.

[92] Zhu, J.; Eisenberg, A.; Lennox, R. B. *J. Am. Chem. Soc.* **1991,** *113*, 5583.

[93] Zhu, J.; Einsenberg, A.; Lennox. R. B. *Macromolecules* **1992,** *25*, 6556.

[94] Zhu, J.; Lennox, R. B.; Einsenberg, A. *J. Phys. Chem*. **1992,** *96*, 4727.

[95 Zhu, J.; Einsenberg, A.; Lennox, R. B. *Macromolecules* **1992,** *25*, 6547.

[96] Israelachvili, J. *Langmuir* **1994**, *10*, 3774.

[97] Borner, H. G.; Beer, K.; Matyjaszewski, K. ; Sheiko, S. S.; Moeller, M. *Macromolecules* **2001**, *34*, 4375.

[98] Rybak, B. M.; Bergman, K. N.; Ornatska, M.; Genson, K. L.; Tsukruk, V. V. *Langmuir* **2006**, *22*, 1027.

[99] Genson, K. L.; Holzmueller, J.; Jiang, C.; Xu, J.; Gibson, J. D.; Zubarev, E. R.; Tsukruk, V. V. *Langmuir* **2006** *22*, 7011.

[100] Milner, S.; T. Chain Architecture and Asymmetry in Copolymer Microphases, *Macromolecules* **1994**, *27*, 2333.

[101] Decher, G. *Science*, **1997**, 277, 1232.

[102] Decher, G.; Schlenoff, J. B. *Multilayer Thin Films: Sequential Assembly of Nanocomposite Materials;* WILEY-VCH Verlag GmbH&Co. KGaA: Weinheim, 2003.

[103] Picart, C.; Lavalle, P.; Hubert, P.; Guisinier, F. J. G.; Decher, G. Schaaf, P.; Voegel, J.-C. *Langmur* **2001**, *17*, 7414.

[104] Picart, C.; Mutterer, J.; Richert, L.; Luo, Y. Prestwich, G. D.; Schaaf, P.; Voegel, J. –C. Lavalle, P. *PNAS* **2002,** *99,* 12531.

[105] Lavalle, P.; Picart, C.; Mutterer, J.; Gergely, C.; Reiss, H.; Voegel, J.-C.; Senger, B.; Schaaf, P. *J. Phys. Chem. B* **2004**, *108*, 635.

[106] Porcel, C.; Lavalle, P.; Ball, V.; Decher, G.; Senger, B.; Voegel, J.-C.; Schaaf, P. *Langmuir* **2006**, *22*, 4376.

[107] Donath, E; Sukhorukov, G. B.; Caruso, F.; Davis, S. A.; Mohwald, H. *Angew. Chem*. **1998**, *110*, 2323.

[108] Antipov, A. A.; Sukhorukov, G. B. *Adv. Colloid Interface Sci.* **2004**, *111*, 49.

[109] Peyratout, C. S.; Dähne, L. *Angew. Chem. Int. Ed*. **2004**, *43*, 3762.

[110] Biggs, S.; Sakai, K.; Addison, T.; Schmid, A.; Armes, S. P.; Vamvakai, M.; Butun, V.; Webber, G. *Adv. Mater*. **2007**, 19, 247.

[111] Kim, B. -S.; Park, S. W.; Hammond, P. T. *ACS Nano* **2008**, 2, 386.

[112] Kozlovskaya, V.; Kharlampieva, E.; Chang, S.; Muhlbauer, R.; Tsukruk, V. V. *Chem. Mater.* **2009**, *21,* 2158.

[113] Chang, S.; Singamaneni, S.; Kharlampieva, E.; Young, S. L.; Tsukruk, V. V. *Macromolecules* **2009**, *42*, 5781.

[114] Yang, S.; Zhang, Y.; Wang, Li.; Hong, S.; Xu, J.; Chen, Y. *Langmuir* **2006**, 22, 338.

115] Connal, L. A.; Li, Q.; Quinn, J. F.; Tjipto, E.; Caruso, F.; Qia, G. G. *Macromolecules* **2008**, 41, 2620.

[116] Schlenoff, J. B. *Langmuir* **2009**, *25*, 14007.

[117] Interdisciplinary Globally-leading Polymer Science and Engineering, NSF Polymer Workshop, Arlington VA, **2007**.

[118] Frechet, J. M. J.; Tomalia, D. A. Eds. *Dendrimers and Other Dendritic Polymers*; John Wiley & Sons, Inc.: New York, 2002.

[119] Newkome, G. R.; Moorefield, C. N.; Vogtle, F. *Dendritic Molecules*; VCH Verlagsgesellschaft mbH.: Weinheim; New York; Basel; Cambridge; Tokyo, 1996.

[120] Hay, G.; MacKay, M. E.; Hawker, C. J. *J. Polym. Sci.* **2001**, *39*, 1766.

[121] Zhao, J.; Swinnen, A.; Assche, G. V.; Mancha, J.; Vanderzande, D.; Van Mele, B. *J. Phys. Chem. B* **2009**, *113*, 1587.

[122] Savenije, T. J.; Kroeze, J. E.; Yang, X.; Loos, J. *Thin Solid Films* **2006**, *2*, 511.

[123] Jing, C.; Xu, X.; Zhang, X.; Liu, Z.; Chu, J. *J. Phys. D.: Appl. Phys.* **2009**, *42*, 075402.

[124] Younes, A. H.; Ghaddar, T. H. *Inorg. Chem.* **2008**, *47*, 3408.

[125] Son, S.; Dodabalapur, A.; Lovinger, A. J.; Galvin, M. E. *Science* **1995**, *269*, 376.

[126] Tsitsilianis, C.; Voulgaris, D. *Macromol. Chem. Phys*. **1997,** *198*, 997.

[127] Voulgaris, D.; Tsitsilianis, C.; Esselink, F. J.; Hadziioannou, G. *Polymer*, **1998**, *39*, 6429.

[128] Tsitsilianis C, Chaumont P, Rempp P. *Makromol. Chem* **1990**, *191*, 2319.

[129] Schnitter, M.; Engelking, J.; Heise, A.; Miller, R. D.; Menzel, H. *Macromol. Chem. Phys*. **2000**, *201*, 1504.

[130] Plamper, F. A.; Schmalz, A., Penott-Chang, E.; Drechsler, M.; Jusufi, A.; Ballauff, M.; Müller, A. H. E. *Macromolecules* **2007**, *40*, 5689.

[131] Larson, K.; Vaknin, D.; Villavicencio, O.; McGrath, D.; Tsukruk, V. V. *J. Phys. Chem. B* **2002**, *106*, 7246.

[132] Ulman, A. *An Introduction to Ultrathin Organic Films: From Langmuir-Blodgett to Self-Assembly*; Academic Press.: Boston, MA, 1991.

[133] Kharlampieva, E.; Kozlovskaya, V.; Chan, J.; Ankner, J. F.; Tsukruk, V. V. *Langmuir*, **2009**, *25*, 14017.

[134] Markutsya, S.; Jiang, C.; Pikus, Y.; Tsukruk, V. V. *Adv. Funct. Mater.* **2005**,*15*, 771.

[135] Tsukruk, V. V. *Rubber Chem. Technol*. **1997**, *70*, 430.

[136] McConney, M. E.; Singamaneni, S.; Tsukruk, V. V., *Polym. Rev.* **2010**, *50*, 235.

[137] Magonov, S. N.; Elings, V.; Whangbo, M. H. *Surf. Sci.* **1997,** *375*, L385.

[138] Tsukruk, V.V.; Singamaneni, S., *Scanning Probe Microscopy of Soft Matter: Fundamentals and Practices*, Wiley-VCH, Weinheim, 2012.

[139] Young, S. L.; Utilizing *Biomacromolecules* **2012**, 13, 3189.

[140] Singamaneni, S.; Gupta, M.; Yang, R.; Tomczak, M. M.; Naik, R. R.; Wang, Z. L.; Tsukruk, V. V. ACS Nano 2009, 3, 2596.

[141] Wang, H.; Xu, T.; Das, N. C. *Silver Nanoparticle Inks for Printable Electronics*. Abstracts, 35th Northeast Regional Meeting of the ACS: Binghamton, NY, October 5-7, **2006**.

[142] Groehn, F; Bauer, B.; Akpalu, YA.; Jackson, CL.; Amis, EJ., *Macromolecules* **2000**, *33*, 6042.

[143] Mandell, J.; Baerga-Ortiz, A.; Falick, A.; Komives, E. *Methods in Mol. Biol.* **2005**, *305*, 65.

[144] Norman, A. L.; Ho, D. L.; Greer, S. C. *Macromolecules* **2007**, *40*, 9628.

[145] Cheng, G.; Graessley, W. W.; Melnichenko, Y. B. *Phys. Rev. Lett.* **2009**, *102*, 157801.

[146] Wang, D.; Moses, D.; Bazan, G. C.; Heeger, A. J.; Lal, J. *J. Macromol. Sci. – Pure Appl. Chem.* **2001**, *A38(12)*, 1175.

[147] Zhao, J. K.; Gao, C. Y.; Liu, D. *J. Appl. Cryst.* **2010**, *43*, 1068.

[148] Wignall, G. D.; Bates, F. S. *J. Appl. Cryst.*, **1987**, *20*, 28.

[149] Pitsikalis, M.; Pispas, S.; Mays, J. W.; Hadjichristidis, N. *Adv. Polym. Sci.* **1998,** *135*, 1.

[150] Hirao, A.; Hayashi, M.; Loykulnant, S.; Sugiyama, K.; Ryu, S. W.; Haraguchi, N.; Matsuo, A.; Higashihara, T. *Prog. Polym. Sci.* **2005,** *30*, 111.

[151] Hadjichristidis, N. *J. Polym. Sci. Part A. Polym. Chem*. **1999,** *37*, 857.

[152] Beyer, F. L.; Gido, S. P.; Poulos, Y.; Avgeropoulos, A.; Hadjichristidis, N. *Macromolecules* **1997,** *30*, 2373.

[153] Beyer, F.; Gido, S. P.; Uhrig, D.; Mays, J. W.; Tan, N. B.; Trevino, S. F. *J. Polym. Sci. Part B, Polym. Phys.* **1999,** *37*, 3392.

[154] Grayer, V.; Dormidontova, E.; Hadziioannou, G.; Tsitsilianis, C. *Macromolecules* **2000,** *33*, 6330.

[155] Stepanek, M.; Matejicek, P.; Humpolickova, J.; Havrankova, J.; Podhajecka, K.; Spirkova, M.; Tuzar, Z.; Tsitislianis, C.; Prochazka, K. *Polymer* **2005,** *46*, 10493.

[156] Kanaoka, S.; Omura, T.; Sawamoto, M.; Higashimura, T. *Macromolecules* **1992,** *25*, 6407.

[157] Tsitislianis, C. Graff, S.; Rempp, P., *Eur. Polym. J*. **1991,** *27*, 243.

[158] Avgeropoulos, A.; Poulos, Y.; Hadjichristidis, N. *Macromolecules* **1996,** *29*, 6076.

[159] Tsitsilianis, C.; Voulgaris, D. *Macromol. Reports* **1995,** *A32*, 569.

[160] Ge, Z.; Xu, J.; Wu, D.; Narain, R.; Liu, S. *Macromol. Chem. Phys*. **2008,** *209*, 754.

[161] Kyriazis, A.; Thierry, A. Burchard, W.; Tsitsilianis, C. *Polymer* **2009,** *50*, 3204.

[162] Peleshanko, S.; Gunawidjaja, R.; Jeong, J.; Shevchenko, V. V.; Tsukruk, V. V. *Langmuir* **2004,** *20*, 9423.

[163] Genson, K. L.; Hoffman, J.; Teng, J.; Zubarev, E. R.; Vaknin, D.; Tsukruk, V. V. *Langmuir* **2004,** *20*, 9044.

[164] Gunawidjaja, R. Peleshanko, S.; Kirsten L. G.; Tsitsilianis, C.; Tsukruk, V. V. *Langmuir* **2006,** *22*, 6168.

[165] Pispas, S.; Hadjichristidis, N.; Potemkin, I.; Khokhlov, A. *Macromolecules* **2000,** *33*, 1741.

[166] Gorodyska, G.; Kiriy, A.; Minko, S.; Tsitsilianis, C.; Stamm, M. *Nano Lett*. **2003,** *3*, 365.

[167] Yu, Y.; Chien, W.; Chen, S. *Polym. Int.* **2008,** *57*, 1369.

[168] Cox, J. K.; Yu, K.; Constantine, B.; Eisenberg, A.; Lennox, R. B. *Langmuir* **1999,** *15*, 7717.

[169] Logan, J. L.; Masse, P. Gnanou, Y.; Taton, D.; Duran, R. *Langmuir* **2005,** *21*, 7380.

[170] Zheng, W.; Wang, Z. *Macromolecules* **1995,** *28*, 7215.

[171] Hadjichristidis, N.; Iatrou, H.; Pitsikalis, M.; Pispas, S.; Avgeropoulos, A. *Prog. Polym. Sci.* **2005,** *30*, 725.

[172] Zhang, L; Eisenberg, A. *J. Am. Chem. Soc*. **1996,** *118*, 3169.

[173] Discher D. E.; Eisenberg, A. *Science* **2002,** *297*, 967.

[174] Li, Z.; Kesselman, E.; Talmon, Y.; Hillmyer, M. A.; Lodge, T. P. *Science* **2004,** *206*, 98.

[175] Pochan D. J.; Chen, Z.; Cui, H.; Hales, K.; Qi, K.; Wooley, K. L. *Science* **2004,** *306*, 94.

[176] Cornelissen, J.; Fischer, M.; Sommerdijk, N.; Nolte, R. J. M. *Science* **1998,** *280*, 1427.

[177] Fustin, C. A.; Abetz, V.; Gohy, J. F. *Eur. Phys. J.* **2005,** *E16*, 291.

[178] Sheller, N. B.; Petrash, S.; Foster, M. D.; Tsukruk, V. V. *Langmuir* **1998,** *14*, 4535.

[179] Li, S.; Clarke, C. J.; Eisenberg, A.; Lennox, R. B. *Thin Solid Films* **1999,** *354*, 136.

[180] Shin, K.; Rafailovich, M. H.; Sokolov, J.; Chang, D. M.; Cox, J. K.; Lennox, R. B.; Eisenberg, A.; Gibaud, A.; Huang, J.; Hsu, S. L.; Satija, S. K. *Langmuir* **2001,** *17*, 4955.

[181] Wen, G.; Chung, B.; Chang, T.; *Polymer* **2006,** *47*, 8575.

[182] Goncalves da Silva, A. M.; Filipe, E. J. M.; dOliveira, J. M. R.; Martinho, J. M. G. *Langmuir* **1996,** *12*, 6547.

[183] Chung, B.; Choi, M.; Ree, M.; Jung, J. C.; Zin, W. C.; Chang, T. *Macromolecules* **2006,** 39, 684.

[184] Voulgaris, D.; Tsitsilianis, C.; Grayer, V. Esselink, F. J.; Hadziioannou, G. *Polymer* **1999,** 40, 5879.

[185] Voulgaris, D.; Tsitsilianis, C. *Macromol. Chem. Phys*. **2001**, *202*, 3284-3292.

[186] Tsitsilianis, C.;Alexandridis, P.; Lindman, B. *Macromolecules* **2001**, *34*, 5979-5983.

[187] Wu, Z.; Liang H.; Lu, J. *Macromolecules* **2010**, *43*, 5699-5705.

[188] Gunawidjaja, R.; Peleshanko, S. Tsukruk, V. V. *Macromolecules*, **2005,** *38*, 8765-8774.

[189] Zhou, Z.; Li, Z.; Ren, Y.; Hilmyer, M. A.; Lodge, T. *J. Am. Chem. Soc*. **2003**, *125*, 10182-10183.

[190] Saito, N.; Liu, C.; Lodge, T. P.; Hilmyer, M. A. *ACS Nano* **2010**, *4*, 1907-1912.

[191] Peleshanko, S.; Jeong, J.; Gunawidjaja, R.; Tsukruk, V. V. *Macromolecules* **2004**, *37*, 6511-6522.

[192] Iatridi, Z.; Roiter, Y.; Stavrouli, N.; Minko, S.; Tsitsilianis, C. *Polym. Chem*. **2011**, *2*, 2037-2044.

[193] Iatridi, Z.; Tsitsilianis, C. *Chem. Commun*, **2011**, *47*, 5560-5562.

[194] Linardatos, G.; Tsoukleri, G.; Parthenios, J.; Galiotis, C.; Monticelli, O.; Russo, S.; Tsitsilianis, C. *Macromol. Rapid Commun*. **2011**, *32*, 371-377.

[195] Sfika, V.; Tsitsilianis, C; Kiriy, A.; Gorodyska, A. Stamm, M. *Macromolecules* **2004**, *37*, 9551-9560.

[196] Lowe, A. B.; McCormick, C. L. *Chem. Rev*. **2000**, *102*, 4177-4189.

[197] McCormick, C. L.; Lowe, A. B. *Acc. Chem. Res*. **2004**, *37*, 312-325.

[198] Zelikin, A. N. *ACS Nano*, **2010**, *4*, 2494-2509.

[199] Choi, I.; Gunawidjaja, R.; Suntivich, R.; Tsitsilianis, C.; Tsukruk, V. V. *Macromolecules* **2010**, *43*, 6818-6828.

[200] Suntivich, R.; Choi, I.; Gupta, M. K.; Tsitsilianis, C.; Tsukruk, V. V. *Langmuir* **2011**, *27*, 10730-10738.

[201] Cho, J.; Hong, J.; Char, K.; Caruso, F. *J. Am. Chem. Soc*. **2006**, *128*, 9935-9942.

[202] Okubo, T. J. *Colloid Interface Sci*. **1988**, *125*, 281-386.

[203] Sperling L. H. *Introduction to physical polymer science*; Wiley-Interscience: New York, 1986.

[204] JonCheray, T. J.; Bernard, S. A.; Matmour, R.; Lepoittevin, B.; El-Khouri, R. J.; Taton, D.; Gnanou, Y.; Duran, R. S. *Langmuir* **2007**, *23*, 2531-2538.

[205] Mauser, T.; Dejugnat, C.; Sukhorukov, G. B. *J. Phys. Chem. B* **2006**, *110*, 20246-20253.

[206] Mann, S. *Biomineralization*, 1st ed.; Oxford University Press, USA, 2002.

[207] Dickerson, M. B.; Sandhage, K. H.; Naik, R. R. *Chem. Rev*. **2008**, *108*, 4935.

[208] Stupp, S. I.; Donners, J.; Li, L-S.; Mata, A. *MRS Bulletin* **2005**, *30*, 864.

[209] Aizenberg, J. *Adv. Mater*. **2004**, *16*, 1295.

[210] Iyer, K. S.; Zdyrko, B.; Malynych, S.; Chumanov, G.; Luzinov, I. *Soft Matter* **2011**, *7*, 2538.

[211] Kharlampieva, E.; Zimnitsky, D.; Gupta, M.; Bergman, K. N.; Kaplan, D. L.; Naik, R. R.; Tsukruk, V. V. *Chem. Mater*. **2009**, *21*, 2696.

[212] Kharlampieva, E., Kozlovskaya, V., Gunawidjaja, R., Shevchenko, V. V., Vaia, R., Naik, R. R.; Kaplan, D. L.; Tsukruk, V. V. *Adv. Funct. Mater*. **2010**, *20*, 840.

[213] Kharlampieva, E.; Kozlovskaya, V.; Zavgorodnya, O.; Lilly, G. D.; Kotov, N. A.; Tsukruk, V. V. *Soft Matter* **2010** *6*, 800.

[214] Kozlovskaya, V.; Kharlampieva, E.; Drachuk, I.; Cheng, D.; Tsukruk, V. V. *Soft Matter* **2010**, *6*, 3596.

[215] Singamaneni, S.; Kharlampieva, E.; Jang, J.-H; McConney, M. E.; Jiang, H.; Bunning, T. J.; Thomas, E. L.; Tsukruk, V. V. *Adv. Mater.* **2010**, *22*, 1369.

[216] Shan, J.; Tenhu, H. *Chem. Commun.* **2007**,*44*, 4580.

[217] Wang, J.; Kong, L. T.; Guo,Z.; Xua, J. Y.; Liua, J. H. *J. Mater. Chem.* **2010**, *20*, 5271.

[218] Prime, D.; Paul, S.; Josephs-Franks, P. W. *Phil. Trans. R. Soc. A* **2009** *367*, 4215.

[219] Butterworth, K. T.; Coulter, J. A.; Jain, S.; Forker, J.; McMahon, S. J.; Schettino, G.; Prise, K. M.; Currell, F. J.; Hirst, D. G. *Nanotechnology* **2010**, *21*, 295101.

[220] Anderson, K. D.;Marczewski, K.;Singamaneni, S.;Slocik, J. M.; Jakubiak, R.; Naik, R. R.;Bunning, T. J.; Tsukruk, V. V. *ACS Appl. Mater. Interfaces* **2010**, *8*, 2269.

[221] Anderson, K. D.; Slocik, J. M.; McConney, M. E.; Enlow, J. O.; Jakubiak, R.; Bunning, T. J.; Naik, R. R.; Tsukruk, V. V. *Small* **2009**, *5*, 741.

[222] Sidorenko, A.; Tokarev, I.; Minko, S.; Stamm, M. *J. Am. Chem. Soc.* **2003**, *125*, 12211.

[223] Dong, H.; Fey, E.; Gandelman, A.; and Jones, W. E. Jr. *Chem. Mater.* **2006**, *18*, 2008.

[224] Youk, J. H.; Park, M.-K.; Locklin, J.; Advincula, R.; Yang, J.; Mays, J. *Langmuir* **2002**, *18*, 2455.

[225] Förster, S.; Antonietti, M. *Adv. Mater.* **1998**, *10*, 195.

[226] Zhu, H.; Pan, Z.; Hagaman, E. W.; Liang, C.; Overbury, S. H.; Dai, S. *J. Colloid Interface Sci.* **2005**, *287*, 360.

[227] Kuo, P. L.; Chen, C. C.; Jao, M. W. *J. Phys. Chem. B* **2005**, *109*, 9445.

[228] Sun, X.; Jiang, X.; Dong, S.; Wang, E. *Macromol. Rapid Commun.* **2003**, *24*, 1024.

[229] Zhang, J.; Gao, Y.; Alvarez-Puebla, R. A.; Buriak, J. M.; Fenniri, H. *Adv. Mater.* **2006**, *18*, 3233.

[230] Leff, D. V.; Brandt, L.; Heath, J. R. *Langmuir* **1996**, *12*, 4723.

[231] Peng, Z. A.; Peng, X. *J. Am. Chem. Soc.* **2001**, *123*, 1389.

[232] Shevchenko, E. V.; Talapin, D. V.; Rogach, A. L.; Kornowski, A.; Haase, M.; Weller, H. *J. Am. Chem. Soc.* **2002**, *124*, 11480.

[233] Spatz, J. P.; Mossmer, S.; Hartmann, C.; Mooller, M.; Herzog, T.; Krieger, M.; Boyen, H.-G.; Ziemann, P. *Langmuir* **2000**, *16*, 407.

[234] Filali, M.; Meier, M. A. R.; Schubert, U. S.; Gohy, J.-F. *Langmuir*, **2005**, *21*, 7995.

[235] Mossmer, S.; Spatz, J. P.; Moller, M.; Aberle, T.; Schmidt, J.; Burchard, W. *Macromolecules* **2000**, *33*, 4791.

[236] Lu, J., Q.; Yi, S., S. *Langmuir* **2006**, *22*, 3951.

[237] Ornatska; M.; Bergman, K. N.; Goodman, M.; Peleshanko, S.; Shevchenko, V. V.; Tsukruk, V. V. *Polymer* **2006**, *47*, 8137.

[238] Peleshanko, S.; Gunawidjaja, R.; Petrash, S.; Tsukruk, V. V. *Macromolecules* **2006**, 39, 4756.

[239] Mishra, M. K.; Kobayashi S, editors. *Star and hyperbranched polymers*; New York: Dekker; **1999.**

[240] Knecht, M. R.; Weir, M. G.; Myers, V. S.; Pyrz, W. D.; Ye, H.; Petkov, V.; Buttrey, D. J.; Frenkel, A. I.; Crooks, R. M. *Chem. Mater.* **2008**, *20*, 5218.

[241] Mogilevsky, A.; Jelinek, R. *Langmuir* **2011**, *27*, 1260.

[242] Tsitsilianis, C.; Voulgaris, D.; Stepanek, M.; Podhajecka, K.; Prochazka, K.; Tuzar, Z.; Brown, W. *Langmuir* **2000**, *16*, 6868.

[243] Luzinov, I.; Minko, S.; Tsukruk, V. V. *Soft Matter* **2008**, *4*, 714.

[244] Szunerits, S.; Boukherroub, R. *Langmuir* **2006**, *22*, 1660.

[245] Tsukruk ,V. V.; Bliznyuk, V. N. *Langmuir* **1998,***14*, 446.

[246] Peleshanko, S.; Sidorenko, A.; Larson, K.; Villavicencio, O.; Ornatska, M.; McGrath, D. V.; Tsukruk, V. V. *Thin Solid Films* **2002**, *406*, 233.

[247] Huglin, M. B.; Rego, J. M. *Polymer* **1990**, *31*, 1269.

[248] Tantavichet, N.; Pritzker, M. D.; Burns, C. M. *J. Appl. Polym. Sci*. **2001**, *81*, 1493.

[249] Swami, A.; Selvakannan, PR.; Pasricha, R.; Sastry, M. *J. Phys. Chem. B* **2004**, *108*, 19269.

[250] Jeonga, H.; Leeb, B.-J.; Choa, W.J.; Ha, C.-S. *Polymer* **2000**, *41*, 5525.

[251] Kiriy, A.; Gorodyska, G.; Minko, S.; Tsitsilianis, C.; Stamm, M. *Polym. Mater. Sci. Eng.* **2003,** *88*, 233.

[252] Kim, E.; Kang, C.; Baek, H.; Hwang, K.; Kwak, D.; Lee, E.; Kang, Y.; Thomas, E. L. *Adv. Funct. Mater.* **2010**, *20*, 1728.

[253] Kuo, P.,-L.; Chen, W., -F. *J. Phys. Chem. B*, **2003**, *107*, 11267.

[254] Mie, G., *Ann. Phys*. **1908**, *330*, 377.

[255] Service, R. F. *Science* **1996**, *271*, 920.

[256] Schmid, G.; Corain, B. *Eur. J. Inorg. Chem.* **2003**, *17*, 3081.

[257] Xu, L.; Yang, H.; Li, X.; Zhang, X.; Zhao, S.; Li, C.; Zhang, S. *J. Macromol. Sci. B.* **2010**, *49*, 770.

[258] Lvov, Y.; Decher, G.; Möhwald, H. *Langmuir* **1993**, *9*, 481.

[259] Lvov, Y.; Möhwald, H. *Protein Architecture: Interfacial Molecular Assembly and Immobilization Biotechnology*, Marcel Dekker, New York **2000**, 1-394.

[260] Mendelson, J. D.; Barret, C. J.; Chan, V. V.; Pal, A. J.; Mayes, A. M.; Rubner, M. F. *Langmuir* **2000**, *16*, 5017.

[261] Swiston, A. J.; Cheng, C.; Um. S. H.; Irvine, D. J.; Cohen, R. E.; Rubner, M. F. *Nano Lett.* **2008**, *8*, 4446.

[262] Hammond, P. T. *Adv. Mater*. **2004**, *16*, 1271.

[263] Jiang, C.; Tsukruk, V. V. *Soft Matter.* **2005**, *1*, 334.

[264] Nolte, M.; Schoeler, B.; Peyratout, C. S.; Kurth, D. G.; Fery, A. *Adv. Mater.* **2005**, *17*, 1665.

[265] Sukhishvili, S. A. *Curr. Opin. Colloid Interface Sci.* **2005**, *10*, 37.

[266] Ariga, K.; Ji, Q.; Hill, J. P. *Adv. Polm. Sci*, **2010**, *229*, 51.

[267] Zhai, L.; Nolte, A. J.; Cohen, R. E.; Rubner, M. F. *Macromolecules* **2004**, *37*, 6113.

[268] Kozlovskaya, V.; Harbaugh, S.; Drachuk, I.; Shchepelina, O.; Kelley-Loughnane, N.; Stone, M.; Tsukruk, V. V. *Soft Matter.* **2011**, *7*, 2364.

[269] Kharlampieva, E.; Sukhishvili, S. A. *Polymer Rev*. **2006**, *46*, 377.

[270] Kotov, N. A. *NanoStructured Materials*, **1999**, *12*, 789.

[271] Dubas, S.; Schlenoff. J. B. *Macromolecules* **1999**, *32*, 8153.

[272] Kozlovskaya, V.; Kharlampieva, E.; Khanal, B. P.; Manna, P.; Zubarev, E. R.; Tsukruk, V. V. *Chem. Mater*. **2008**, *20*, 7474.

[273] Wilson, J. T.; Cui, W.; Kozlovskaya, V.; Kharlampieva, E.; Pan, D.; Qu, Z.; Krishnamurthy, V. R.; Mets, J.; Kumar, V.; Wen, J.; Song, Y.; Tsukruk, V. V.; Chaikof, E. L. J. *Am. Chem. Soc*. **2011**, *133*, 7054.

[274] Caruso, F. *Adv. Mater.* **2001**, *13*, 11.

[275] Kharlampieva, E.; Sukhishvili, S. A. *Langmuir* **2003**, *19*, 1238.

[276] Choi, J.; Rubner, M. F. *Macromolecules* **2005**, *38*, 116.

[277] Itano, K.; Choi, J.; Rubner, M. F. *Macromolecules* **2005**, *38*, 3450.

[278] Philippova, O. E.; Hourdet, D.; Audebert, R.; Khokhlov, A. R. *Macromolecules*, **1997**, *30*, 8278.

[279] Wang, J. S.; Matyjaszewski, K. *J. Am. Chem. Soc*. **1995**, *117*, 5614.

[280] Matyjaszewski, K. Xia, J. *Chem. Rev*. **2001**, *101*, 2921.

[281] Muthukrishnan, S.; Plamper, F.; Mori, H.; Müller, A. H. E. *Macromolecules* **2005**, *38*, 10631.

[282] Plamper, F. A.; McKee, J. R.; Laukkanen, A.; Nykänen, A.; Walther, A.; Ruokolainen, J.; Aseyev, V.; Tenhu, H. *Soft Matter* **2009**, *5*, 1812.

[283] Plamper, F. A.; Murtomäki, L.; Walther, A.; Kontturi, K.; Tenhu, H. *Macromolecules* **2009**, *42*, 7254.

[284] Plamper, F. A.; Reinicke, S.; Elomaa, M.; Schmalz, H.; Tenhu, H. *Macromolecules* **2010**, *43*, 2190.

[285] Nguyen, P. M.; Zacharia, N. S.; Verploegen, E.; Hammond, P. T. *Chem. Mater*. **2007**, *19*, 5524-5530.

[286] Zacharia, N. S.; Modestino, M.; Hammond, P. T. *Macromolecules* **2007**, *40*, 9523.

[287] Zacharia, N. S.; Delongchamp, D. M.; Modestino, M.; Hammond, P. T. *Macromolecules* **2007**, *40*, 1598.

[288] Schlenoff, J. B.; Dubas, S. T.; Farhat, T. *Langmuir* **2000**, *16*, 9968.

[289] Cho, J.; Char, K.; Hong, J.-D.; Lee, K.-B. *Adv. Mater*. **2001**, *13*, 1076.

[290] Cho, J.; Lee, S.-H.; Kang, H.; Char, K.; Koo, J. Byoung, H. S.; Lee, K.-B. *Polymer* **2003**, *44*, 5455.

[291] Jiang, C.; Markutsya, S.; Tsukruk, V. V. *Langmuir* **2004**, *20*, 882.

[292] Jiang, C.; Markutsya, S.; Tsukruk, V. V. *Adv. Mater*. **2004**, *16*, 157.

[293] Schoeler, B.; Poptoshev, E.; Caruso, F. *Macromolecules* **2003**, *36*, 5253.

[294] Salomaki, M.; Vinokurov, I. A.; Kankare, J. *Langmuir* **2005**, *21*, 11232.

[295] Laugel, N.; Betscha, C.; Winterhalter, M.; Voegel, J.-C.; Schaaf, P.; Ball, V. *J. Phys. Chem. B* **2006**, *110*, 19443.

[296] Porcel, C.; Lavalle, Ph, Decher, G.; Senger, B.; Voegel, J.-C.; Schaaf, P. *Langmuir* **2007**, *23*, 1898.

[297] Sun, B.; Jewell, C. M.; Fredin N. J.; Lynn, D. M. *Langmuir* **2007**, *23*, 8452.

[298] Jiang, C.; Ko, H.; Tsukruk, V. V. *Adv. Mater.*, .**2005,** *17*, 2127.

[299] Jiang, C.; Markutsya, S.; Shulha, H.; Tsukruk, V. V. *Adv. Mater.* **2005,** *17*, 1669.

[300] Zimnitsky, D.; Shevchenko V. V.: Tsukruk, V. V. *Langmuir.* **2008**, *24*, 5996.

[301] Jiang, C.; Wang, X.; Gunawidjaja, R.; Lin, Y.-H.; Gupta, M. K.; Kaplan, D. L.; Naik, R. R.; Tsukruk, V. V. *Adv. Funct. Mater.* **2007,** *17*, 2229

[302] Kozlovskaya, V.: Kharlampieva, E.; Jones, K.; Lin, Z.; Tsukruk, V. V. *Langmuir*, **2010**, *26*, 7138.

[303] Kujawa, P.; Moraille, P.; Sanchez, J.; Badia, A.; Winnik, F. M. *J. Am. Chem. Soc*. **2005**, *127*, 9224.

[304] Kolasinska, M.; Krastev, R.; Gutberlet, T.; Warszynski, P. *Langmuir* **2009**, *25*, 1224.

[305] Chiarelli, P. A.; Johal, M. S.; Casson, J. L.; Roberts, J. B.; Robinson, J. M.; Wang, H.-L. *Adv. Mater*. **2001**, *13*, 1167.

[306] Lee, S.-S.; Hong, J.-D.; Kim, C. H.; Kim, K.; Koo, J. P.; Lee. K.-B. *Macromolecules* **2001**, *34*, 5358.

[307] Elbert, D. L.; Herbert, C. B.; Hubbell, J. A. *Langmuir* **1999**, *15*, 5355.

[308] Lavalle, P.; Picart, C.; Mutterer, J.; Gergely, C.; Reiss, H.; Voegel, J.-C.; Senger, B.; Schaaf, P. *J. Phys. Chem. B* **2004**, *108*, 635-648.

[309] Guo, Z.; Chen, X.; Xin, J.; Wu, D.; Li, J.; Xu, C. *Macromolecules* **2010**. *43*, 9087.

[310] Pincus, P. *Macromolecules* **1991**, *24*, 2912.

[311] Roiter, Y.; Minko, S. *J. Am. Chem. Soc*. **2005**, *127*, 15688.

[312] Yoo, D.; Shiratori, S. S.; Rubner, M. F. *Macromoelcules* **1998**, *31*, 4309.

[313] Shiratori, S. S.; Rubner, M. F. *Macromolecules* **2000**, *33*, 4213.

[314] Ono, S. S.: Decher, G. *Nanolett* **2006**, *6*, 592.

[315] Wong, J. E.; Zastrow, H.; Jaeger, W.; von Klitzing, R. *Langmuir* **2009**, *25*, 14061.

[316] Xu, C.; Wu, T.; Drain, C. M.; Batteas, J. D.; Fasolka, M. J.; Beers, K. L. *Macromolecules*, **2006**, *39*, 3359.

[317] Swanepoel, R. *J. Phys. E: Sci. Instrum*. **1983**, *16*, 1214.

[318] DeLongchamp, D. M.; Kastantin, M.; Hammond, P. T. *Chem. Mater*. **2003**, *15*, 1575.

[319] Gu, X.; Wang, G. *Appl. Surf. Sci*. **2011**, *257*, 1952.

[320] Seo, J.; Luthenhaus, J. L.; Kim, J.; Hammond, P. T.; Char, K. *Langmuir* **2008,** *24*, 7995.

[321] Mansfield, M. L. *Polymer* **1996**, *37*, 3835.

[322] Bliznyuk, V. N.; Rinderspacher, F.; Tsukruk V. V. *Polymer*, **1998**. *39*, 5249.

[323] Betley, T. A; Holl, M. M. B.; Orr, B. G.; Swanson, D. R.; Tomalia, D. A.; Baker, Jr. J. R. *Langmuir* **2001**, *17*, 2768.

[324] Li, J.; Piehler, L. T.; Qin, D., Baker, J. R.; Tomalia, D. A. *Langmuir* **2000**, *16*, 5613.

[325] Laguecir, A.; Ulrich, S.; Labille, J.; Fatin-Rouge, N.; Stoll, S.; Buffle, J. *Eur. Pol. J.*, **2006**, *42*, 1135.

326 Lavalle, Ph, Gergely, C.; Cuisinier, F. J. C.; Decher, G.; Schaaf, P.; Voegel, J. C.; Picart, C. *Macromolecules* **2002**, *35*, 4458.

[327] Elsabahy, M.; Wooley, K. L. *Chem. Soc. Re*. **2012**, *41*, 2545.

[328] Liu, X.; Jin, X.; Ma, P. X. *Nat. Mater*. **2011**, *10*, 398.

[329] Lee, V. Y.; Havenstrite, K.; Tjio, M. McNeil, M.; Blau, H. M.; Miller, R. D.; Sly J. *Adv. Mater*. **2011**, *23*, 4509.

[330] Barreto, J. A.; O'Malley, W.; Kubeil, M.; Graham, B.; Stephan, H.; Spiccia, L. *Adv. Mater*. **2011**, 23, H18.

[331] Jusufi, A. Likos, C. N.; Ballauff, M. *Colloid Polym. Sci*. **2004**, *282*, 910.

[332] Rud, O. V.; Mercurieva, A. A.; Leermakers, F. A. M.; Birshtein, T. M. *Macromolecules* **2012**, *45*, 2145.

[333] Sheiko, S.; Sun, F. C.; Randall A.; Shirvanyants, D.; Rubinstein, M.; Lee, H.-I; Matyjaszewski, K. *Nature* **2006**, *440*, 191.

[334] Panyukov, S.; Sheiko, S. S.; Rubinstein, M. *Phys. Rev. Lett.* **2009**, *102*, 148301-1

[335] Spatz, J. P.; Eibeck, P.; Mössmer, S.; Möller, M.; Kramarenko, E. Y.; Khalatur, P. G.; Potemkin, I. I.; Khokhlov, A. R.; Winkler, R. G.; Reineker, P. *Macromolecules* **2000**, *33*, 150.

[336] Tsitsilianis, C.; Voulgaris, D. *Macromol. Reports* **1995**, *A32*, 569.

[337] Peleshanko, S.; Jeong, J.; Shevchenko, V. V.; Genson, K. L.; Pikus, Yu.; Petrash, S.; Tsukruk, V. V. *Macromolecules*, **2004**, *37*, 7497.

[338] Choi, I.; Gunawidjaja, R.; Suntivich, R.; Tsitsilianis, C.; Tsukruk, V.V. *Macromolecules* **2010**, *43*, .

[339] Zhu, Z.; Sukhishivili, S. A.*J. Mater. Chem.* **2012**, *22*, 7667.

[340] Pavlukhina, S.; Sukhishvili, S. *Adv. Drug Deliv. Rev.* **2011**, *63*, 822.

[341] Bliznyuk, V. N.; Rinderspacher, F.; Tsukruk, V. V. *Polymer* **1998**, *39*, 5249.

[342] Nguyen, R. M.; Zacharia, N. S.; Verploegen, E.; Hammond, P. T. *Chem. Mater.* **2007**, *19*, 5524.

[343] Khopade, A. J.; Caruso, F. *Nano Lett* **2002**, *2*, 425.

[344] Khopade, A. J.; Caruso, F. *Biomacromolecules* **2002**, *3*, 1154.

[345] Kim, B.-S.; Lebedeva, O. V.; Kim, D. H.; Caminade, A.-M.; Majoral, J.-P.; Knoll, W.; Vinogradova, O. I. *Langmuir* **2005**, *21*, 7200.

[346] Kim, B.-S.; Lebedeva, O. V.; Koynov, K.; Gong, H.; Caminade, A.-M.; Majoral, J.-P.; Vinogradova, O. I. *Macromolecules* **2006**, *39*, 5479.

[347] Webber. G. B.; Wanless, E. J.; Armes, S. P.; Tang, Y.; Li, Y.; Biggs, S. *Adv. Mater*. **2004**, *16*, 1794.

[348] Hong, J.; Bae, W. K.; Lee, H.; Oh, S.; Char, K.; Caruso, F. *Adv. Mater*. **2007**, *19*, 4363.

[349] Sakai, K.; Webber, G. B.; Vo. C.-D.; Wanless, E. J.; Vamvakai, M.; Butun, V.; Armes, S. P.; Biggs, S. *Langmuir* **2008**, *24*, 116.

[350] Zhu, Z.; Sukhishvili, S. A. *ACS Nano* **2009**, *3*, 3595.

[351] Tan, W. S.; Zhu, Z.; Sukhishvili, S. A.; Rubner, M. F.; Cohen, R. E. *Macromolecules* **2011**, *44*, 7767.

[352] Son, K. J.; Yoon, H.-J.; Kim, J.-H.; Jang, W.-D. Lee, Y.; Koh, W.-G. *Angew. Chem. Int. Ed.* **2011**, *50*, 1.

[353] Ma, N.; Zhang, H.; Song, B.; Wang, Z.; Zhang, Xi. *Chem. Mater*. **2005**, *17*, 5065.

[354] Ma, N.; Wang, Y.; Wang, Z.; Zhang, Xi. *Langmuir* **2006**, *22*, 3906.

[355] Addison, T.; Cayre, O. J.; Biggs, S.; Armes, S. P.; York, D. *Langmuir* **2008**, *24*, 13328.

[356] Addison, T.; Cayre, O. J.; Biggs, S.; Arms. S. P.; York. D. *Langmuir* **2010**, *26*, 6281.

[357] Hong, J.; Cho, J.; Char, K. *J. Colloid & Interface Sci*. **2011**, *364*, 112.

[358] Shchepelina, O.; Kozlovskaya, V.; Singamaneni, S.; Kharlampieva, E.; Tsukruk, V. V. *J. Mater. Chem.* **2010**, *20*, 6587.

[359] Kiriy, A.; Gorodyska, G.; Minko, S.; Steamm, M.; Tsitsilianis, C. *Macromolecules* **2003**, *36*, 23.

[360] Lvov, Y.; Decher, G.; Moehwald, H. *Langmuir* **1993**, *9*, 481.

[361] Gao, C.; Leporatti, S.; Moya, S.; Donath, E.; Möhwald, H. *Langmuir* **2001**, 17, 3491.

[362] Singamaneni, S.; McConney, M. E.; Tsukruk, V. V. *Adv. Mater*. **2010**, *22*, 1263.

[363] Singamaneni, S.; Tsukruk, V. V. *Soft Matter* **2010**, *6*, 5681.

[364] Köhler, K.; Shchukin, D. G.; Möhwald, H.; Sukhorukov, G. B. *J. Phys. Chem. B* **2005**, *109*, 18250.

[365] Köhler, K.; Shchukin, D. G.; Sukhorukov, G. B.; Möhwald, H. *Macromolecules* **2004**, *37*, 9546.

[366] Kim, J. Y.; DeRocher, J. P.; Mao, P.; Han, J.; Cohen, R. E.; Rubner, M. F. *Chem. Mater*. **2010**, *22*, 6409.

[367] Leporatti, S.; Voigt, A.; Mitlöhner, R.; Sukhorukov, G.; Donath, E.; Möhwald, H. *Langmuir* **2000**, *16*, 4059.

[368] Gao, C.; Leporatti, S.; Donath, E.; Mohwald, H. *J. Phys. Chem. B* **2000**, *104*, 7144.

[369] Smith, E. G.; Webber, G. B.; Sakai, K.; Biggs, S.; Armes, S. P.; Wanless, E. J. *J. Phys. Chem. B.* **2007**, *111*, 5536.

[370] Decher, G.; Lvov, Y.; Schmitt, J. *Thin Solid Fims* **1994**, *244*, 772.

[371] Sukhorukov, G. B.; Schmitt, J.; Decher, G. *Ber. Bunsenges. Phys. Chem.* **1996**, *100*, 948.

[372] Dubas, S.; Schlenoff, J. B. *Langmuir* **2001**, *17*, 7725.

[373] Armstrong, J. K.; Wenby, R. B.; Meiselman, H. J.; Fisher, T. C., *Biophys. J.* **2004**, *87* , 4259

[374] Shchepelina, O.; Drachuk, I.; Gupta, M. K.; Lin, J.; Tsukruk, V. V. *Adv. Mater*. **2011**, *23*, 4655.

[375] Freltoft, T.; Kjems, J. K.; Sinha, S.K. *Phys. Rev. B* **1986**, *33*, 269.

[376] Schmidt, P. W. *J. Appl. Cryst.* **1991**, *24*, 414.

[377] Zimnitsky, D.; Shevchenko, V. V.; Tsukruk, V. V. *Langmuir*, **2008**, *24*, 5996

[378] Tsukruk, V. V.; Bliznyuk, V. N.; Visser, D. W.; Campbell, A. L.; Bunning, T.; Adams, W. W. *Macromolecules,* **1997**, *30,* 6615.

[379] Debye, P.; Bueche, A. M. *J.Appl. Phys.* **1949**, *20,* 518.

[380] Debye, P.; Anderson, H. R.; Brumberger, H. *J. Appl. Phys.* **1957**, *28,* 679.

[381] Hummers, W. S.; Offeman, R. E., Preparation of Graphitic Oxide, *J. Am. Chem. Soc.* **1958**, *80*, 1339.

[382] Kim, J.; Cote, L. J.; Huang, J., Two Dimensional Soft Material: New Faces of Graphene Oxide, *Acc. Chem. Res.* **2012**, *45*, 1356.

[383] Dreyer, D. R.; Park, S.; Bielawski, C. W.; Ruoff, R. S., The Chemistry of Graphene Oxide, *Chem. Soc. Rev*. **2010**, *39*, 228.

[384] Liu, J.; Fu, S.; Yuan, Bin,; Li, Y.; Deng, Z. *J., Am. Chem. Soc.* **2010**, *132*, 7279.

[385] Mao, S.; Lu, G.; Yu, K.; Bo, Z.; Chen, J., *Adv. Mater.* **2010**, *22*, 3521.

[386] Wang, Y.; Li, Z.; Hu, D.; Lin, C. –T.; Li. J.; Lin, Y., *J. Am. Chem. Soc.* **2010**, *132,* 9274.

[387] Wang, Z.; Huang, P.; Bhirde, A.; Jin, A.; Ma, Y.; Niu, G.; Neamati, N.; Chen, X., *Chem. Commun.* **2012**, *48*, 9768.

[388] Chou, S. S.; De, M.; Luo, J.; Rotello, V. M.; Huang, J.; Dravid, V. P., *J. Am. Chem. Soc.* **2012**, *134*, 16725.

[389] Liu, Z.; Robinson, J. T.; Sun, X.; Dai, H., *J. Am. Chem. Soc.* **2008**, *130*, 10876.

[390] Kim, B. H.; Kim. J. Y.; Jeong, S. –J.; Hwang, J. O.; Lee, D. H.; Shin, D. O.; Choi, S. –Y.; Kim, S. O., *ACS Nano* **2010**, *4*, 5464.

[391] Lerf, A.; He, H.; Rorster, M.; Kilnowski, J., *J. Phys. Chem. B.* **1998**, *102*, 4477.

[392] Dimiev, A.; Kosynkin, D. V.; Alemany, L. B.; Chaguine, P.; Tour, J. M., *J. Am. Chem. Soc*. **2012**, *134*, 2815.

[393] Erickson, K.; Erni, R.; Lee, Z.; Alem, N.; Gannett, W.; Zettl, A., *Adv. Mater.* **2010**, *40*, 4467.

[394] Wang, X.; Bai, H.; Shi, G., *J. Am. Chem. Soc.* **2011**.133, 6338.

[395] Gudarzi, M. M.; Sharif, F. *Soft Matter*, **2011**, *7*, 3432.

[396] Zou, J. Kim, F., *ACS Nano* **2012**, *6*, 10606.

[397] Cote, L. J.; Kim, f.; Huang, J., *J. Am. Chem. Soc.* **2009**, *131*, 1043.

[398] Gao, Y.; Chen, X.; Xu, H.; Zou, Y.; Gu, R.; Xu, M.; Jen, A. K. -Y.; Chen, H., *Carbon*, **2010**, *48*, 4475.

[399] Cheng, C.; Li, D., Solvated *Adv. Mater.* **2012**, *25*, 13-30.

[400] Kulkarni, D. D.; Choi, I.; Singamaneni, S. S.; Tsukruk, V. V., *ACS Nano* **2010**, *4*, 4667.

[401] Hu K.; Gupta, M. K.; Kulkarni, D. D.; Tsukruk, V. V., *Adv. Mater.* **2013**, DOI: 10.1002/adma.201300179.

[402] Kim, J.; Cote, L. J.; Kim, F.; Yuan, W.; Shull, K. R.; Huang, J., *J. Am. Chem. Soc.* **2010**, *132*, 8180.

[403] Kim, F.; Cote, L.; Huang, J. *Adv. Mater*. **2010**, *22*, 1954.

[404] Latridi, Z.; Tsitsilianis, C., *Soft Matter* **2013**, *9*, 184.

[405] Gröschel, A. H.; Löbling, T.; Petrov, P. D.; Müllner, M.; Kuttner, C. Wieberger, F.; Müller. A. H. E., *Angew. Chem. Int. Ed*. **2013**, *52*, 3602.

[406] Kodiyath, R.; Choi, I.; Patterson, B.; Tsitsilianis, C.; Tsukruk, V. V., *Polymer* **2012**, *54*, 1150.

[407] Cote, L. J.; Kim, f.; Zhang, Z.; Huang, J., *Soft Matter*, **2010**, *6*, 6096.

[408] Radovic, L., *J. Am. Chem. Soc*. **2009**, *131*, 17166.

[409] Kim, S. N.; Kuang, Z.; Slocik, J. M.; Jones, S. E.; Cui, Y.; Farmer, B. L.; MacAlpine, M. C.; Naik, R. R., *J. Am. Chem. Soc*. **2011**, *133*, 14480.

[410] Paredes,J. I.; Villar-Rodil, S.; Martínez-Alonso, A.; Tascón, J. M. D., *Langmuir* **2008**, *24*, 10560.

[411] Jaafar, M.; Lopez-Polin, G.; Gomez-Navarro, C.; Gomez-Herrero, J., *Appl. Phys. Lett.* **2012**, *101*, 263109-1.

VITA

IKJUN CHOI

Ikjun Choi was born in Deajeon, South Korea on May 1, 1976 to Yonghun Choi and Heeroh Park. He attended Daejeon Middle School and graduated from Chungnam High School in 1995. In 1999, he obtained a B.S. in Chemical Engineering from the Chungnam National University in Daejeon, and in 2002, completed a M.S. in Materials Science and Engeering from the Gwangju Institute of Science and Technology under the guidance of Prof. T. H. Yoon in Gwangju, South Korea. From 2002 to 2004, he worked at the Coreana Cosmetics R & D Center in Chungnam, South Korea, and from 2005 to 2008, worked in the Petroleum Chemcial Research Center at the LG Chem Research Park, in Deajeon, South Korea. In 2008, He began a Ph.D. in Materials Science and Engineering at the Georgia Institute of Technology with Prof. Vladimir Tsukruk.